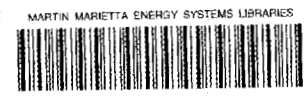

ORNL/TM-10508

ornl

OAK RIDGE NATIONAL LABORATORY

MARTIN MARIETTA

The Intergranular Segregation of Boron in Substoichiometric Ni_3Al

A. Choudhury

OPERATED BY
MARTIN MARIETTA ENERGY SYSTEMS, INC.
FOR THE UNITED STATES
DEPARTMENT OF ENERGY

ORNL/TM-10508
Distribution
Category UC-25

Metals and Ceramics Division

THE INTERGRANULAR SEGREGATION OF BORON IN SUBSTOICHIOMETRIC Ni_3Al

A. Choudhury

Date Published: December 1987

Prepared for the
Office of Basic Energy Sciences
KC 02 01 05 0

Prepared by the
OAK RIDGE NATIONAL LABORATORY
Oak Ridge, Tennessee 37831
operated by
MARTIN MARIETTA ENERGY SYSTEMS, INC.
for the
U.S. DEPARTMENT OF ENERGY
under Contract DE-AC05-84OR21400

TABLE OF CONTENTS

LIST OF TABLES

LIST OF FIGURES

ACKNOWLEDGMENTS

This dissertation would not have been possible without the assistance and encouragement of numerous people; I would like to express my sincere thanks and gratitude to them. The following list of people is probably not comprehensive and for any unwitting omissions, I extend my apologies.

The help and guidance of my advisors, Dr. C. L. White and Dr. C. R. Brooks, in matters both technical and personal are acknowledged with respect and gratitude. Dr. C. T. Liu of the Oak Ridge National Laboratory was immensely helpful in providing direction, assistance and encouragement in the course of this research; to him I shall remain indebted for this. The encouragement, in terms of personal attentiveness to the progress of the research, provided by Dr. J. O. Stiegler is also gratefully acknowledged. Dr. E. E. Stansbury provided help and insight on numerous occasions and for this I offer my sincere thanks to him.

The members of the Alloy Behavior and Design group at Oak Ridge National Laboratory deserve thanks for their help and patience in what must often have appeared to be pesky "graduate student problems." The following deserve special mention in this regard: R. A. (Ray) Padgett, E. H. (Elmer) Lee, S. M. (Maggie) Winsbro, D. H. (Herschel) Pierce, J. O. (Jim) Scarbrough, G. M. (Gwen) Sims, and C. L. (Connie) Dowker.

Dr. R. E. Clausing and Lee Heatherly earned my respect and gratitude on occasions too numerous to mention with their help in terms of putting problems in perspective. The respite from these provided by Lee and Ray on our numerous fishing trips shall remain with me as very pleasant memories.

J. Nave and Carolyn Angel deserve my thanks for the frequent occasions when I tried their patience in terms of photographic work.

Alma R. McDonald, Patsy T. Thornton and Patricia H. Wilson must surely have drawn from their enormous reserves of patience, for while I gave enough instigation for exasperation, I came through the preparation of this dissertation without crutches. They deserve my sincere thanks for a job excellently executed in the typing and preparation of this dissertation. Mary Threat from their office deserves my thanks for the many "rush jobs" I put her through.

At the University of Tennessee, the following people have put up with me for six years; to them I owe thanks and gratitude: Bobby L. McGill, Ted A. Long, Ron L. Johnson, Steve A. Stiner, Michael R. Neal, Howell B. Thompson and his entire staff, I. F. (Sancy) Hail, Betty K. Frazier, Phyllis R. Davis, Elizabeth S. Turner, Phyllis L. Klindt, Inez C. McDonald, Kay B. Davis, Aileen W. Cagle and Albert W. Carter.

My fellow graduate students were instrumental in making my stay at U.T. enjoyable.

The financial support provided by Dr. J. E. Spruiell in terms of a graduate teaching assistantship during the initial part of my Ph. D. effort is gratefully acknowledged. The present research was financially supported by Subcontract No. 7685 PAS90 with The University of Tennessee and Metals and Ceramics Division of the Oak Ridge National Laboratory operated by Martin Marietta Energy Systems, Inc., under contract DE-AC05-84OR21400 with the U.S. Department of Energy.

THE INTERGRANULAR SEGREGATION OF BORON IN SUBSTOICHIOMETRIC Ni_3Al*

A. Choudhury

ABSTRACT

The intermetallic compound Ni_3Al offers promise as an excellent candidate material for high temperature applications. In addition to its unusual property of increasing strength with temperature (until ~700°C), it has excellent corrosion and oxidation resistance. Microalloying the alloy with boron has been shown to be dramatically effective in improving its inherent intergranular brittleness. It has also been observed that this improvement results from the strong tendency of boron to segregate to the grain boundaries of Ni_3Al. This research deals with the first detailed study of the segregation behavior of this beneficial segregant. By virture of its surface sensitivity, Auger electron spectroscopy was chosen as the technique adopted to study this segregation. The strong effect of segregant level on the grain boundary strength level can be controlled by thermal history variations and by variations in the level of solute in the bulk. Cathodic hydrogen charging was shown to be a potent tool in opening up otherwise cohesive boundaries for analysis. At a more fundamental level, the effective binding energy of boron at the grain boundaries of Ni_3Al was calculated from experimental data; it was found to vary between 0.2 and 0.45 eV. The kinetics of segregation have been investigated; the present set of kinetic studies were shown to be inadequate to find a diffusion coefficient and that temperatures lower than those studied here need to be used. As an associated investigation, a set of elemental standards were developed for the particular scanning Auger microprobe used in this study.

---

*Research sponsored by the Division of Materials Sciences, U.S. Department of Energy under contract DE-AC05-84OR21400 with the Martin Marietta Energy Systems, Inc.

CHAPTER 1

INTRODUCTION

I. GENERAL COMMENTS

Ordered intermetallic alloys have been studied for over 30 years. They form long-range ordered (LRO) crystal structures (composed of sublattices of the various atomic species) below their critical ordering temperature (T_C). The term "ordered alloys" commonly refers to alloys which form LRO crystal structures at relatively low temperatures and become disordered at higher temperatures. The term "intermetallic compounds" is generally applied to strongly ordered alloys having specific stoichiometric formulae.

Since their lattices are ordered, intermetallic alloys possess dislocations having large Burgers vectors, which often split into pairs or groups. This decomposition can impose considerable constraints on their motion. Strongly ordered alloys also tend to exhibit low atomic mobility, which leads to lower rates for diffusion controlled processes such as creep. It is mainly for these reasons that ordered intermetallics exhibit very attractive high temperature properties. In some cases, as in the Ni_3Al alloy studied here, the yield stress actually increases with temperature (Refs. 1,2,3,4). In addition to this, ordered intermetallic aluminides and silicides are very oxidation and corrosion resistant by virtue of their ability to form compact, adherent oxide surface films.

Because of their extreme intergranular brittleness there used to be warranted skepticism in the materials community about the commercial feasibility of ordered intermetallic compounds. However, significant

progress has been made in recent years and very high ductilities have been achieved. Section III of this chapter gives a short overview of the problem of brittleness in intermetallic compounds.

Extensive investigations have been carried out on several intermetallics with a view towards commercial applications. The range of such applications extends through such varied fields as advanced heat engines (e.g., Stirling engines, adiabatic diesel engines); high temperature heat recovery systems; and structural materials for hot components such as coal gasifiers, coal liquefaction, fluidized bed combusters and fuel cells (Ref. 5). To date, the systems showing maximum promise are surely the aluminides and Fe-Co-Ni-V systems. Both NiAl and Ni_3Al have fascinating properties; however, it is Ni_3Al which (as a base alloy) shows the better commercial promise.

II. THE Ni - Al SYSTEM

As can be seen from the Ni - Al phase diagram in Figure 1-1, there are four intermetallics in this system:

β ---- $NiAl_3$

γ ---- Ni_2Al_3

δ ---- NiAl

γ' ---- Ni_3Al

The intermetallic γ' is the strengthening phase in a number of high temperature nickel-base superalloys. It is to be noted that γ' is not a strict chemical compound but does possess some range of solid solubility.

AC-100

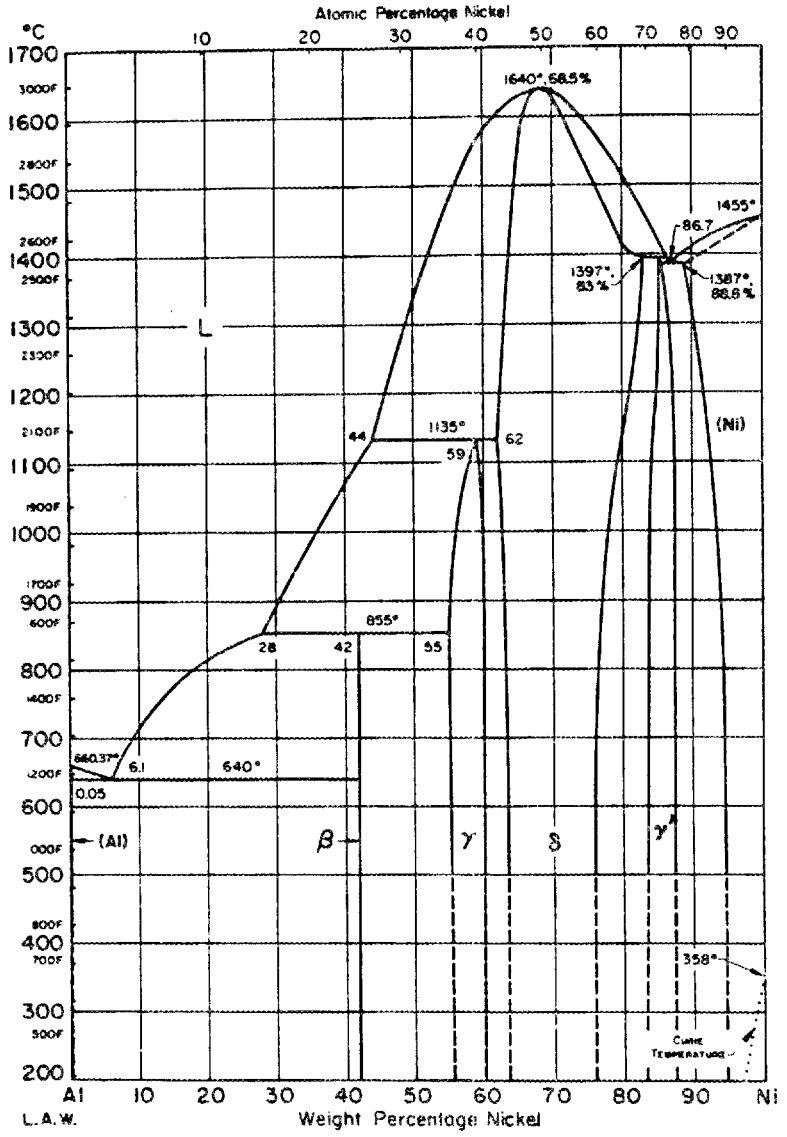

Figure 1-1. The Al - Ni phase diagram (Ref. 6).

It has been extensively studied, but to date its use as the primary phase in structural materials has been precluded due to its extreme inherent intergranular brittleness in the polycrystalline form. It has been shown that this brittleness can be ameliorated by the addition of boron and control of aluminum content. These observations have proven useful in the design of "Advanced Aluminides," where solid solution strengthening can be achieved by the addition of elements like Fe and Hf. Such aluminides have extremely good high temperature strength, as shown in Figures 1-2 and 1-3. Figure 1-3 also illustrates another attribute of the aluminides – their low density as compared to common superalloys.

III. BRITTLENESS OF ORDERED INTERMETALLICS

There are two factors that can lead to brittleness in ordered intermetallics such as Ni_3Al: an insufficient number of slip systems and grain boundary brittleness. Unalloyed Ni_3Al deforms by $\{111\}$ <110> slip at all temperatures, and at temperatures above 400°C some slip along $\{100\}$ is also observed; at 700°C $\{100\}$ slip predominates (Ref. 2). Von Mises' criterion of five independent slip systems for arbitrary shape change under constant volume is thus readily satisfied by Ni_3Al at all temperatures. Hence the brittleness of Ni_3Al cannot stem from a restriction on the number of slip systems. Further, single crystals of Ni_3Al are highly ductile, while polycrystals are extremely brittle and display primarily intergranular fracture (Refs. 8,9). Such intergranular brittleness can stem from two sources – inherent brittleness of the grain boundaries, or segregation of harmful impurities to these boundaries. Several

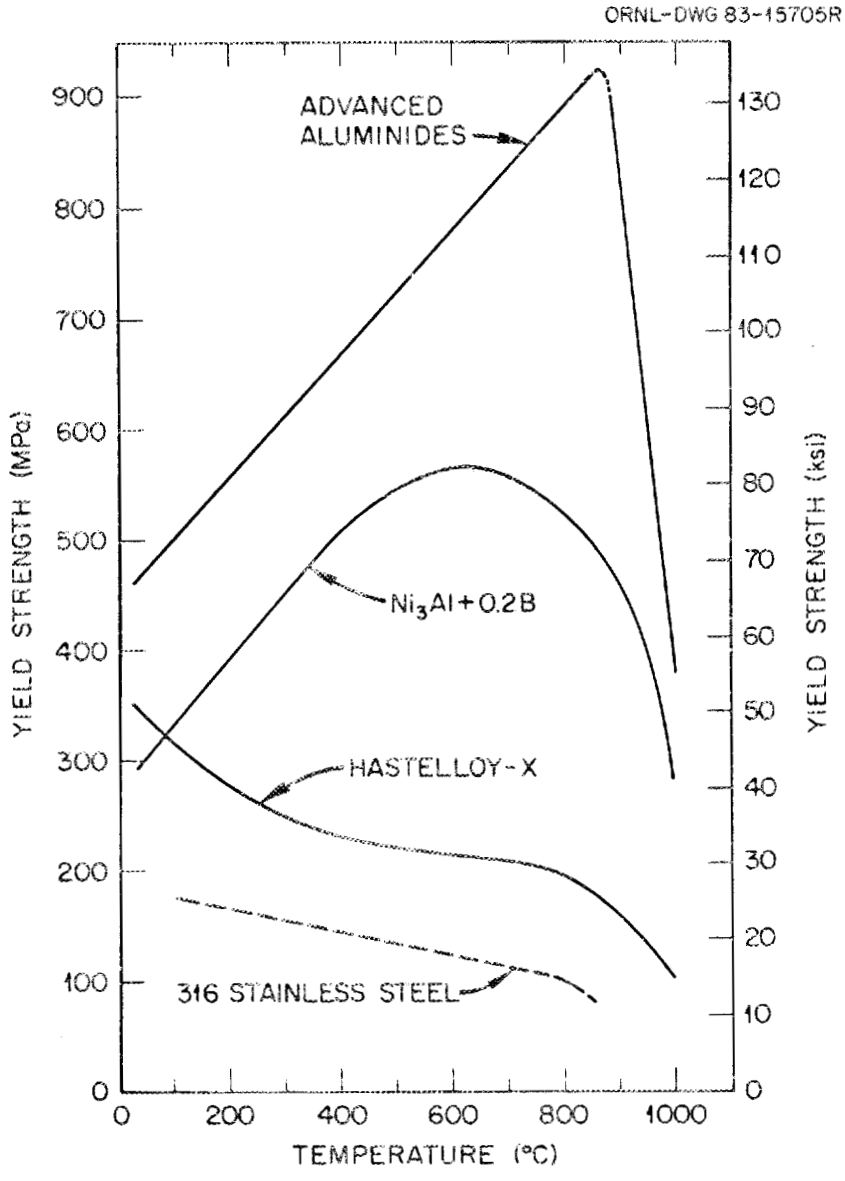

Figure 1-2. Yield stress as a function of test temperatures for Ni_3Al-base aluminide alloys, Hastelloy X, and type 316 stainless steel (Ref. 7).

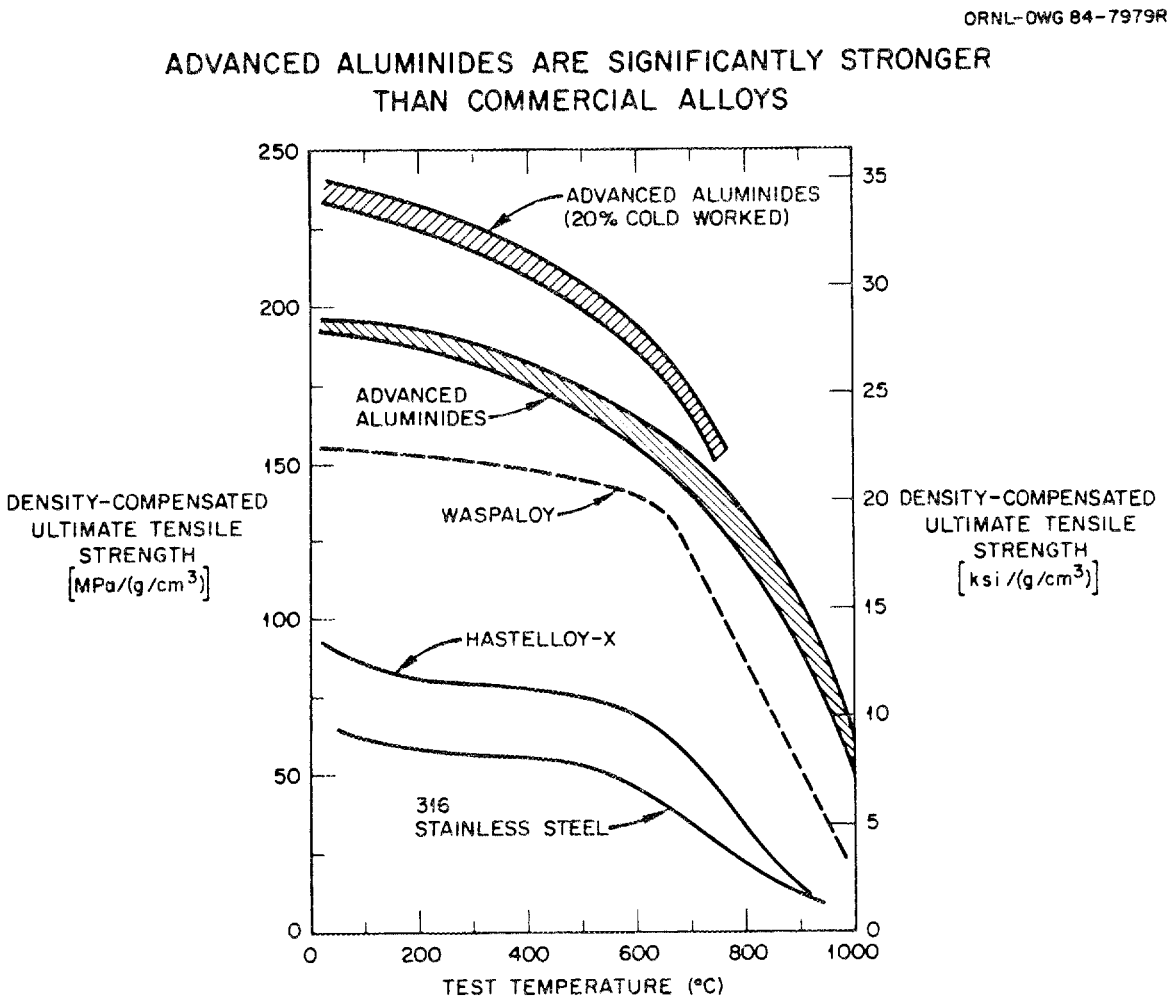

Figure 1-3. Comparison of density compensated ultimate tensile strength (as a function of temperature) of advanced aluminides (B-doped Ni_3Al + 0.5 - 1.0 at. % Hf) with commercial alloys (Ref. 7).

authors (Refs. 10,11,12) have shown that in the case of Ni_3Al, the grain boundaries are inherently brittle.

Improvements in ductility and fabricability of intermetallics have been achieved by both macroalloying and microalloying. In macroalloying, the ordered crystal structures and bulk properties are controlled by the addition of major concentrations (typically > 1%) of alloying elements. These property changes are essentially attributable to changes in electron to atom ratio (e/a). Using this approach, excellent ductility and fabricability have been realized in $(Co,Fe)_3V$, $(Ni,Co,Fe)_3V$ and $(Ni,Fe)_3V$ (Refs. 13,14).

Microalloying, on the other hand, involves control of defect structure and composition by the addition of minor concentrations (in the ppm range) of elements. This approach has the distinct advantage of obviating expensive processing techniques.

As mentioned earlier, intergranular brittleness in ordered systems stems from two sources - intrinsic brittleness and segregation of harmful impurities to grain boundaries. In view of this, two types of microalloying additions (dopants), depicted schematically in Figure 1-4, have been used to improve the ductility of these alloys. Type I dopants are scavengers of harmful impurities from grain boundaries. They usually accomplish this effect by precipitation processes which lower the amount of harmful impurities available for segregation. Type II dopants, on the other hand, enhance grain boundary cohesion by altering the atomic bonding characteristics at the grain boundaries. Optimum results are usually obtained by a combination of both of these approaches, as has been demonstrated in Ni_3Al (Ref. 7).

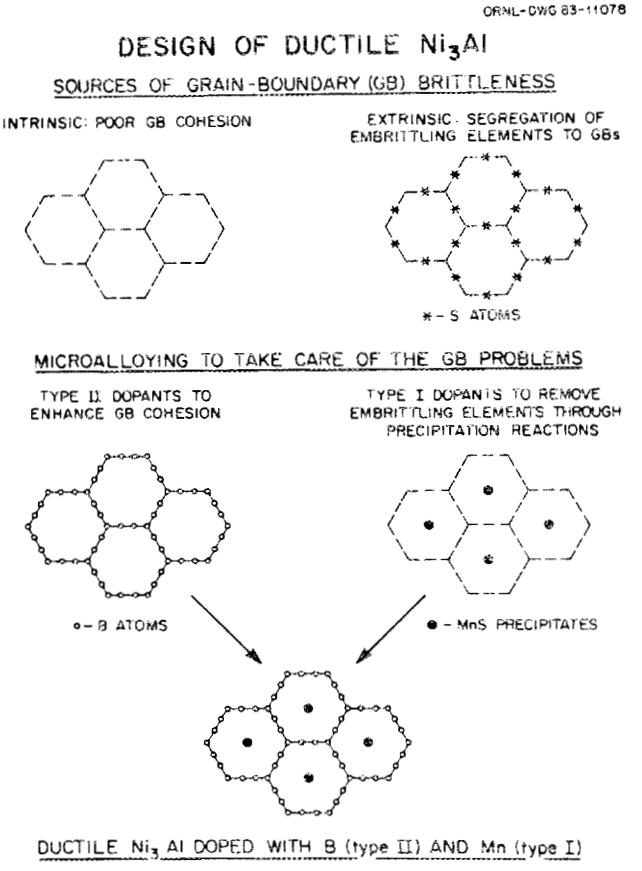

Figure 1-4. Sources of grain boundary brittleness and design of ductile Ni_3Al by microalloying with Type I and Type II dopants (Ref. 7).

Rapid solidification does provide one potential means of circumventing the problem of intergranlular brittleness. The beneficial effects of rapid solidification are improvement in alloy homogeneity, reduction of grain boundary segregation and reduction in the degree of order. The disadvantages of rapid solidification are the restriction that products must be thin in at least one dimension and that they may lose all or part of their favorable behavior during hot consolidation or subsequent heat treatment at elevated temperatures (Ref. 7).

CHAPTER 2

STRUCTURE AND PROPERTIES OF Ni_3Al

I. INTRODUCTION

The intermetallic compound Ni_3Al (γ' phase) has a $L1_2$ ordered structure (Cu_3Au prototype) where the Al atoms occupy the corner positions while the Ni atoms are at face-centered positions (Figure 2-1). Ni_3Al and some other $L1_2$ alloys exhibit rather unusual mechanical properties as a result of their LRO structure and retention of the same to very high temperatures. Ni_3Al remains ordered up to its melting temperature (Ref. 16) and hence the temperature dependence of the Bragg-Williams (LRO) parameter, S, cannot be used to explain the mechanical properties.

II. TEMPERATURE AND ORIENTATION DEPENDENCE OF YIELD STRENGTH

Several workers have shown that, like other $L1_2$ alloys, the yield (flow) stress of Ni_3Al increases as a function of temperature, and goes through a maximum at some elevated temperature (Refs. 15,17,18). This is illustrated in Figure 2-2 for an alloy of 20% Al, 10% Fe and 70% Ni. The reason for this anomalous behavior has been the subject of debate for about 25 years. In a recent review, Pope and Ezz (Ref. 19) described the various mechanisms (Table 2-1) proposed to explain this behavior.

There now appears to be a general agreement that Takeuchi and Kuramoto's model (Ref. 1) as modified by Lall, Chin and Pope (Ref. 23) most adequately explains the observed experimental results. Takeuchi and

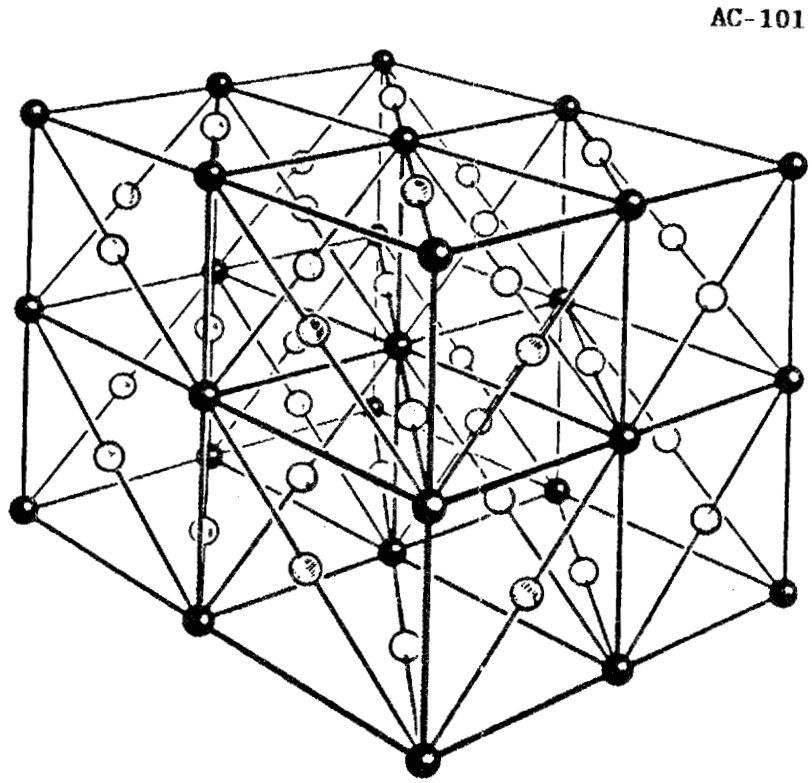

Figure 2-1. The ordered Ni_3Al structure ($L1_2$). ○ – Ni, ● – Al (Ref. 15).

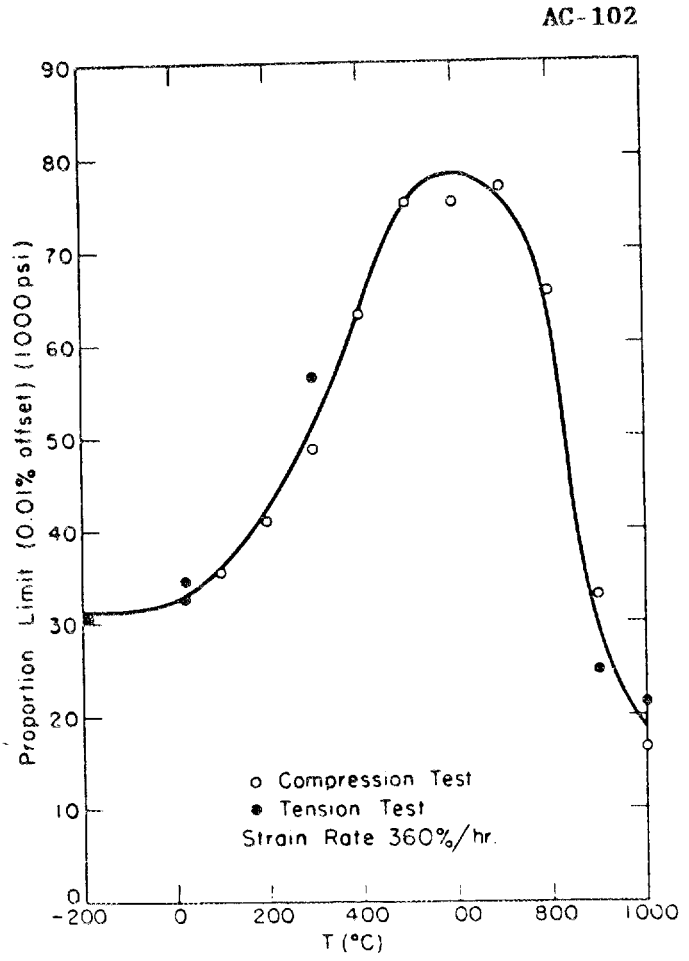

Figure 2-2. Proportional limit as a function of temperature for an ordered nickel-base alloy (20% Al, 10% Fe, 70% Ni) (Ref. 15).

Table 2-1. Chronological listing of proposed mechanisms for the anomalous yield strength vs temperature and work hardening behavior of $L1_2$ ordered alloys

Year	Author(s)	Reference Number	Mechanism and Remarks
1960	Flinn	15	Minimum in energy of APB between superpartials occurs in plane other than slip plane – causes pinning of APB as diffusive mechanisms become operative.
1962	Kear & Wilsdorf	20	Cross slip of 1/2 $[\bar{1}01]$ (111) from (111) to (010) planes renders them immobile – explains high work hardening rate.
1965	Davies & Stoloff	18	Intrinsic effect of lattice – dislocation interaction.
1967	Copely & Kear	3	Difference in core widths of dissociated superpartials – at low temperatures – wide cores – at high temperatures – constricted cores – restriction on shear.
1970	Thornton et al.	2	Low temperature – Exhaustion hardening. High temperature – Debris hardening.
1972	Pope et al.	4	Changes in LRO parameter – proven wrong since then.
1973	Takeuchi & Kuramoto	1	CRSS differences – pinning of cross slipped segments.
1975	Staton-Bevan & Rawlings	21 22	Disproved "Debris hardening" conclusively.
1974	Lall et al.	23	Improved and refined Takeuchi and Kuramoto's model.

Kuramoto (Ref. 1) observed the following with regard to the flow stress of Ni_3Ga (which, like Ni_3Al, has a $L1_2$ structure) as a function of temperature:

(a) The flow stress vs temperature curve goes through a maximum.

(b) Below the temperature at which the maximum in flow stress occurs, slip occurs primarily on the (111) $[\bar{1}01]$ system.

(c) Below the temperature at which the maximum in flow stress occurs, a preponderance of screw dislocations exist.

(d) Above the temperature at which the maximum in flow stress occurs, flow occurs mostly by (001) $[\bar{1}10]$ slip.

(e) Schmid's law does not hold for (111) $[\bar{1}01]$ slip but does hold for (001) $[\bar{1}10]$ slip.

(f) At constant temperature, the CRSS for (111) $[\bar{1}01]$ slip increases as the orientation of compression axis is moved away from the [001] direction.

These authors observed that the CRSS for (111) $[\bar{1}01]$ slip is independent of orientation at -196°C. Hence, for (111) $[\bar{1}01]$ slip at any temperature, the increase in CRSS, $\Delta\tau_{PB}$ [slip in primary (111) slip plane in direction of burgers vector], over the value at -196°C, is caused by cross slip of screw dislocations from (111) to (010) planes. As screw dislocations move on (111) planes, short segments cross slip to (010) planes - these provide local pinning points on the moving dislocation as shown in Figure 2-3. In order to continue moving, the dislocation must bow between these points. Below the temperature for peak stress, $\Delta\tau_{PB}$ is controlled by these cross slipped segments and is given by:

$$\Delta\tau_{PB} \propto \exp\left(\frac{-H + \tau_{CB}V}{3kT}\right) \qquad \text{Equation (2-1)}$$

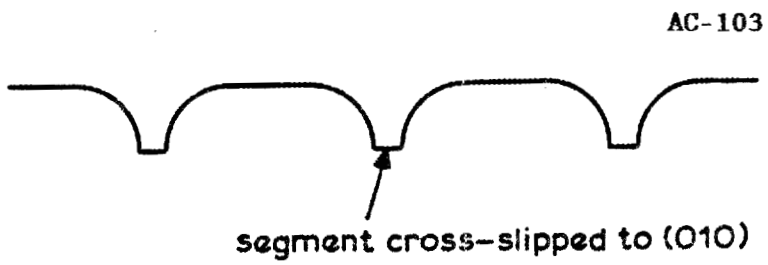

Figure 2-3. Schematic diagram of [$\bar{1}$01] dislocation bowing between cross slipped segments on (111) slip plane (Ref. 19).

where

T = Temperature

V = Activation volume

H = Activation enthalpy

τ_{CB} = Resolved shear stress on (010) $[\bar{1}01]$; i.e. stress which promotes cross slip from (111) to (010) planes.

It is the presence of τ_{CB} which leads to the breakdown of Schmid's law.

Lall et al. (Ref. 23) found that the CRSS for (111) $[\bar{1}01]$ slip is dependent not only on temperature and RSS on (010) $[\bar{1}01]$ but also on the RSS (τ_{PE}) that expands on contracts the Shockley partials which comprise the (1/2) (111) [101] superpartials (i.e., (1/12) $[1\bar{2}1]$). This leads to:

$$\Delta\tau_{PB} \propto \exp\left(\frac{-H + \tau_{CB}V_1 + \tau_{PE}V_2}{kT}\right) \qquad \text{Equation (2-2)}$$

where

V_1, V_2 = Activation volumes

τ_{PE} = Resolved shear stress on (111) along $[1\bar{2}1]$.

It is believed that an expression like Equation (2-2) adequately explains the temperature and orientation dependence of the flow stress of Ni_3Al which is similiar to Ni_3Ga not only in crystal structure but also in that it remains ordered until its melting point. In Liang and Pope's (Ref. 16) nomenclature Ni_3Al is a Type II $L1_2$ ordered alloy (Type I being alloys in which $T_C \ll T_M$).

III. PLANAR FAULTS AND DISLOCATION DISSOCIATIONS

Four distinct types of planar faults can form in the $L1_2$ structure (all on the $\{111\}$ planes):

(a) Antiphase Boundaries (APBs)

(b) Superlattice Intrinsic Stacking Faults (SISFs)

(c) Superlattice Extrinsic Stacking Faults (SESFs)

(d) Complex Stacking Faults (CSFs)

Figure 2-4 shows how each of these may be formed. Table 2-2 ranks these faults in terms of fault energy and indicates the structural consequences of formation of these faults in the lattice.

As is to be expected, the dissociation of dislocations in the $L1_2$ lattice is extremely complicated; however, only a few are important. These are mentioned below and are shown schematically in Figure 2-5.

(i) Figure 2-5(*a*): Dissociation by APB and CSF on (111) planes

(Ref. 24) $[\bar{1}01] = 1/6\ [\bar{1}\bar{1}2] + 1/6\ [\bar{2}11] + 1/6\ [\bar{1}\bar{1}2] + 1/6\ [\bar{2}11]$

(ii) Figure 2-5(*b*): Dissociation by APB, CSF and SISF on (111) planes (Ref. 25)

$[\bar{1}01] = 1/6\ [\bar{1}\bar{1}2] + 1/6\ [\bar{2}11] + 1/6\ [\bar{1}2\bar{1}] + 1/6\ [1\bar{2}1] +$

$1/6\ [\bar{1}\bar{1}2] + 1/6\ [\bar{2}11]$

(iii) Figure 2-5(*c*): Dissociation by APB on (111) planes

$[\bar{1}01] = 1/2\ [\bar{1}01] + 1/2\ [\bar{1}01]$

(iv) Figure 2-5(*d*): Dissociation by SISF on (111) planes

$[\bar{1}01] = 1/3\ [\bar{2}11] + 1/3\ [\bar{1}\bar{1}2]$

AC-104

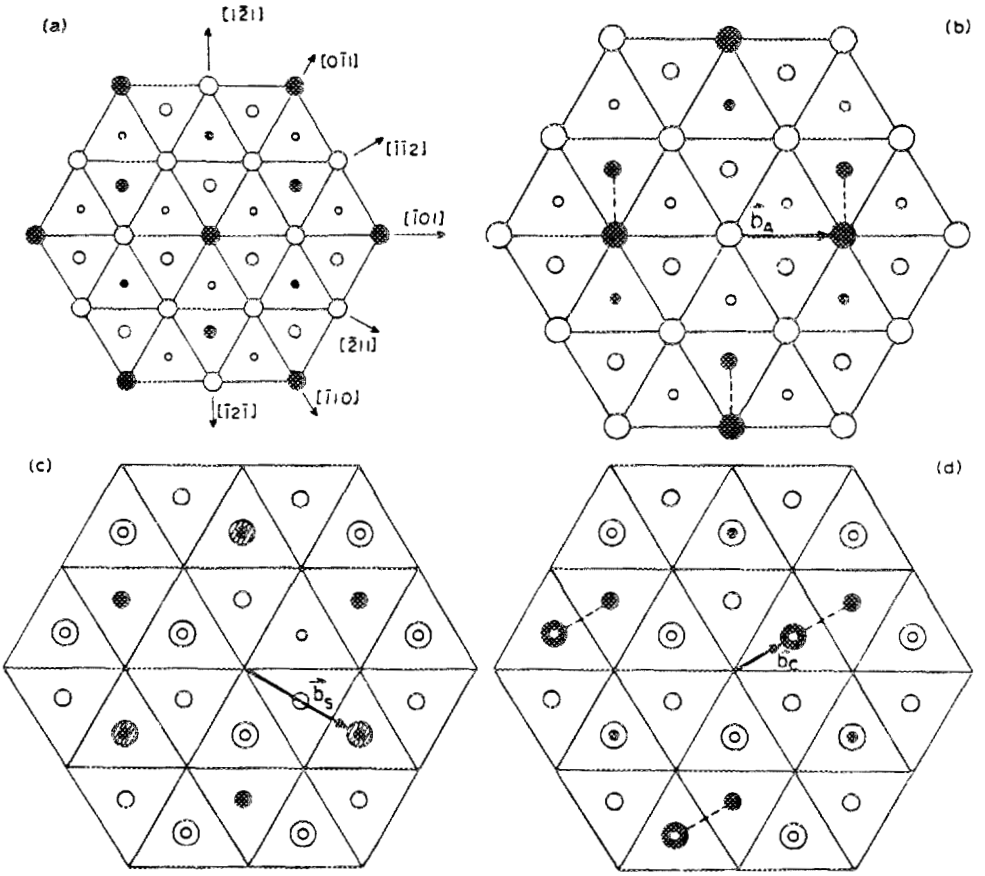

a three (111) planes; *b* after sliding top layer in *a* by $b_A = \frac{1}{2}[\bar{1}01]$ to produce APB, dashed lines indicating 'incorrect' B—B nearest-neighbour bonds; *c* after sliding top layer in *a* by $b_S = \frac{1}{3}[\bar{2}11]$ to produce SISF; *d* after sliding top layer in *a* by $b_C = \frac{1}{6}[\bar{1}\bar{1}2]$ to produce CSF

Figure 2-4. Four types of faults in A_3B alloy with $L1_2$ structure. Three successive (111) planes are shown, large, medium and small circles representing atoms in upper, middle and lower planes respectively and open and closed circles representing majority and minority atoms respectively (Ref. 19).

Table 2-2. Planar faults in $L1_2$ structures ranked in order of decreasing fault energy (CSF - highest fault energy)

Type of Fault	Remarks	
	Stacking Sequence	Nearest Neighbors
CSF	Changed	Violated
APB	Unchanged	May be violated
SESF & SISF	Changed	Not violated

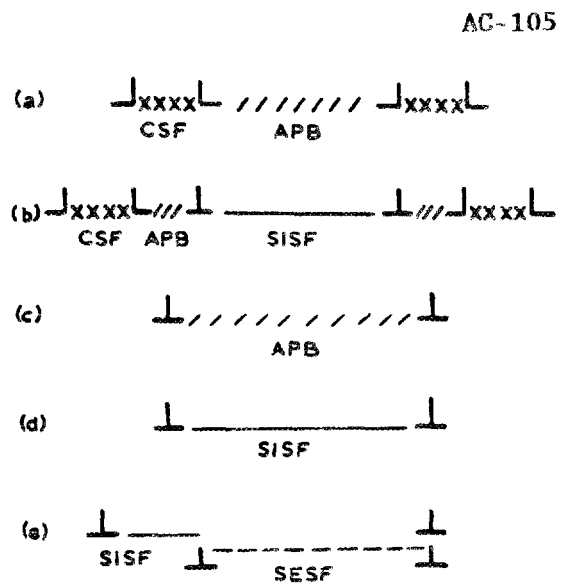

a $[\bar{1}01]$ dislocation with $\frac{1}{2}[\bar{1}01]$ superpartials dissociated into Shockley partials; *b* as in *a* but with equal and opposite $\frac{1}{6}\langle 112\rangle$ partials added, converting APB to SISF; *c* as in *a* but with undissociated superpartials; *d* $[\bar{1}01]$ dislocation dissociated into $\frac{1}{3}\langle 112\rangle$ superpartials separated by SISF; *e* $[\bar{2}11]$ dislocation dissociated into four $\frac{1}{3}\langle 112\rangle$ superpartials, producing SISF and SESF, on two adjacent planes

Figure 2-5. Dislocation dissociations on (111) planes that appear to be important in $L1_2$ ordered alloys (Ref. 19).

(v) Figure 2-5(*e*): Dissociation by SISF and SESF on (111) planes (Ref. 26)

$$[\bar{2}11] = 1/3\ [\bar{1}2\bar{1}] + 1/3\ [\bar{1}\bar{1}2] + 1/3\ [\bar{2}11] + 1/3\ [\bar{2}11]$$

(vi) Dissociation by APB on (010) planes (Ref. 15)

$$[\bar{1}01] = 1/2\ [\bar{1}01] + 1/2\ [\bar{1}01]$$

Pope and Ezz (Ref. 19) conclude that there is direct and indirect experimental evidence that dissociation follows schemes (i) or (iii), (v) and (vi) but none for (ii) or (iv).

IV. COMPOSITIONAL EFFECTS ON FLOW OF GAMMA PRIME

Two types of compositional effects can be envisaged: off-stoichiomety effects and effects of third element.

Lopez and Hancock (Ref. 27) showed that off-stoichiometry results in higher flow stress in the Ni_3Al structure. They also found that excess Al has a much more marked effect than does excess Ni. A similiar effect of the excess of minority element being more potent in increasing flow strength than an excess of the majority element was also seen by Noguchi et al. (Ref. 28) in both Ni_3Ga and Ni_3Al.

Guard and Westbrook (Ref. 29) pointed out that elements which dissolve substitutionally in Ni_3Al can be divided into three groups:

(a) Those which substitute for Ni - viz, Co and Cu

(b) Those which substitute for Al - viz, Si, Ti, Mn and V

(c) Those which substitute for both Ni and Al - viz. Fe, Cr and Mo

They found that the solubility of alloying additions is governed by both electronic and atomic size factors. The solubility of alloying elements in Ni_3Al was found to increase with decreasing temperature.

Curwick (Ref. 30) measured the CRSS of $Ni_3(Al,X)$ single crystals as a function of temperature and orientation of the compression axis, for X = Mo,Nb,Ta,Ti,W. He found that all the elements tested increased the CRSS for (111) [101] slip but decreased it for (001) [$\bar{1}$10] slip, relative to pure Ni_3Al.

Guard and Westbrook (Ref. 29) attributed their results to a combination of solid solution strengthening and defect hardening. Curwick (Ref. 30), however, realized the complicated manner in which his results were connected to temperature and orientation effects. He thus could not correlate the strengthening effect with any theory of solid solution strengthening.

Rawlings and Staton-Bevan (Ref. 31) and Aoki and Izumi (Ref. 32) studied the strengthening effect of alloying additions in polycrystalline Ni_3Al. The former authors concluded that the extent of strengthening resulting from an addition depends on the atomic misfit parameter, the stoichiometry of the alloy and the sublattice on which the element resides. The latter authors arrived at similiar conclusions with the additional assertion that the modulus parameters are important in determining the degree of strengthening.

Wee and co-workers (Refs. 33,34) pointed out that the introduction of periodic faults on (111) or (010) planes of the $L1_2$ lattice can produce other ordered structures like DO_{19} and DO_{22}. They put forward an APB

argument to show that elements which make the $L1_2$ structure unstable with respect to the DO_{19} or DO_{22} structures lead to strengthening of the $L1_2$ structure. This model has been used by Noguchi et al. (Ref. 28) to explain their off-stoichiometry effects.

Although the model proposed by Wee and co-workers (Refs. 33,34) appears to offer a reasonable explanation for compositional effects, it is by no means problem free. A discussion of some of these can be found in Pope and Ezz's (Ref. 19) review.

In a series of papers, Takasugi, Izumi and Masahashi (Refs. 35,36,37) have investigated the correlation between mechanical properties and fracture behavior of a number of $L1_2$ A_3B compounds. In particular, they have addressed the effects of ternary alloy additions, deviations from stoichiometry and the boron effect in Ni_3Al. While discussion about the boron effect will be postponed until Chapter 3, their findings related to the other topics may be summarized as follows:

(a) Due to a lack of conclusive proof to the contrary, they discounted the possibility of metallurgical and crystallographic factors playing a major role in the intergranular brittle behavior among the $L1_2$ alloys studied.

(b) In the A_3B alloys studied, brittleness was observed when the element corresponding to B was an element in the b subgroup of the periodic table.

(c) In the nickel-base A_3B alloys studied, intergranular brittleness was more pronounced as the valency difference between A and B increased. In addition to this a relative size effect was observed.

(d) From a structural standpoint, using the coincident site lattice (CSL) (discussed in Chapter 4) model for grain boundary structure, the authors deduced:

(i) In $L1_2$, A_3B compounds, there was a preponderence of A-A bonds while A-B bonds were in the minority. In addition, B-B bonds were quite scarce.

(ii) In most cases, the A-B bonds had a covalent character and thus were very strong. However, since they were a minority compared to the A-A bonds at grain boundaries, the grain boundaries were expected to be weak.

(iii) Also, in the formation of A-B covalent bonds, B atoms drew charge from A atoms, thereby weakening the more prevalent A-A bonds leading to further weakening of the grain boundaries.

(e) In terms of the ternary element effects in Ni_3Al, the authors categorized ternary additions with respect to the element they substituted for in Ni_3Al. The authors deduced that intergranular brittleness was enhanced as the valency difference between the ternary additions and the solvent species increased.

(f) Using the above arguments, these authors concluded that intergranular brittleness in the systems studied stemmed from grain boundary structural considerations and the effect of this on the bonding nature at the grain boundaries. The latter is also affected by the electronic nature of the constituent elements. This approach was used to rationalize the effects of deviations from stoichiometry.

(g) The effects of interstitials such as H and B on the inherent grain boundary strength in these alloys was deduced to be superimposed on their latent potency for grain boundary weakness.

CHAPTER 3

EFFECT OF BORON ON PROPERTIES OF Ni_3Al

I. INTRODUCTION

As has been noted previously, in spite of its attractive density, strength, creep and corrosion properties, the applicability of Ni_3Al (as in the case of many other intermetallics) has been severely limited by its extreme brittleness in its polycrystalline form both at room temperature and at elevated temperatures. In 1978, Aoki and Izumi (Ref. 9) reported that boron improves the ductility of polycrystalline Ni_3Al. The following paragraphs contain a brief historical survey of the developments leading to and from this important finding.

Aoki and Izumi (Ref. 9) realized that while other intermetallics may be intrinsically brittle due to noncompliance with the Von Mises' criterion of five independent slip systems for arbitrary shape change under constant volume, such was not the case with Ni_3Al. Since the operative slip system at room temperature is $\{111\}$ <110>, Von Mises' criteria is satisfied. In agreement with this, they found, as had earlier investigators (Refs. 2,3,15,17,29), that single crystals of Ni_3Al exhibited over 100% elongation at and below room temperature but this markedly decreased with increasing temperature, reaching a minimum at the temperature where the peak in yield strength occurred (Figure 3-1). The fracture surfaces of such samples exhibited ductile dimple fracture.

Per contra, polycrystalline specimens processed similarly (cast and homogenized) exhibited no elongation in tension at any temperature.

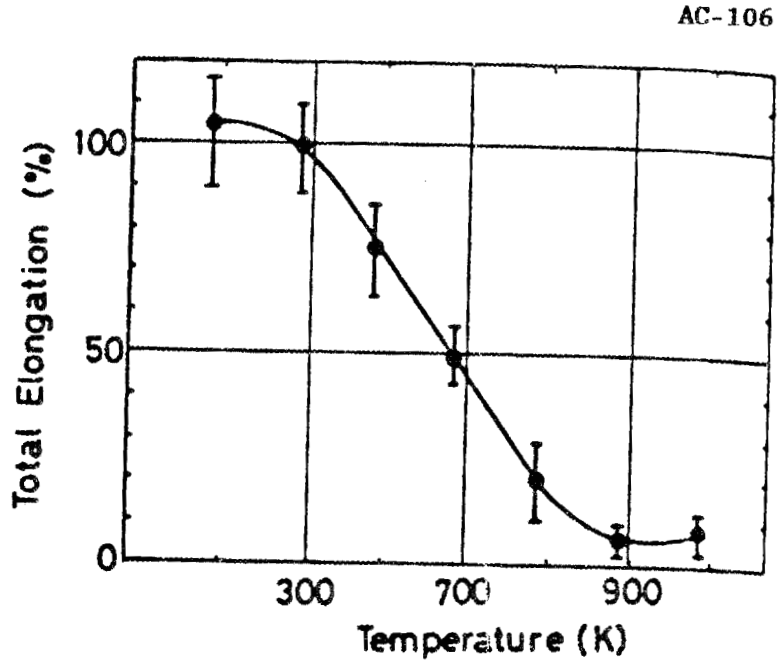

Figure 3-1. Temperature dependence of total elongation of Ni_3Al single crystal (Ref. 9).

However, some ductility was exhibited under compression. In both cases, as an example, the boron free polycrystals underwent brittle fracture prior to yielding, and no elongation was observed. Addition of 0.1 wt. % boron, however, resulted in a 35% elongation under tension without causing any loss in the yield strength found by compressive loading. SEM fracture surface observations revealed that boron significantly suppresses grain boundary fracture and leads to a mixed inter-transgranular fracture as opposed to exclusively intergranular fracture in the boron-free polycrystals.

Using ion microanalysis, they did find boron in the grain boundaries of boron-doped material but were unable to determine whether the segregation of boron to the boundaries or reduction of grain boundary impurities by boron addition was responsible for the enhanced ductility.

In a subsequent paper (Ref. 10) they discredited the segregation of impurities explanation, having examined both zone refined and deoxidized and desulphurized materials and found no improvement in ductility.

In a subsequent AES study of fracture surfaces (Ref. 11) Ogura et al. have shown the absence of segregated impurities in the intergranular facets of boron-free Ni_3Al (to the detectability limit 0.1 at. %). They thus suggest the role of boron as being that of a modifier of some intrinsic nature of grain boundary atomic bonds. From SEM fractographs, the authors found evidence of slip traces on intergranular facets. Further evidence of plastic deformation to a depth of about 120 μm from the facet surfaces was found from sequential back reflection pin hole patterns obtained after electropolishing. This agrees well with an earlier observation made by Schulson et al. (Ref. 12).

Liu, White and coworkers (Refs. 38,39,40,41) systematically doped Ni_3Al with two types of dopants:

Type I: Grain boundary impurity scavengers like Ce, Mn, and Ti.

Type II: Grain boundary cohesiveness improvers like C and B; further explanation of this will be given later.

Included in this study was off-stoichiometry effects.

In brief, the following results were obtained:

(a) Boron is the most effective dopant for improving ductility of Ni_3Al.

(b) The room temperature ductility of boron-doped Ni_3Al is critically dependent on deviations from stoichiometry. Above 25 at. % Al, no amount of boron will render the aluminide ductile and fabricable. Substoichiometric (24 at. % Al) compositions were the best for studies on this system. Figure 3-2 shows ultimate tensile strength and percent elongation as a function of Al concentration between 24 and 25 at. % Al. As is to be expected, the fracture mode changes from intergranular through a mixed mode to transgranular as Al content decrease from 25 to 24 at. % Al in the boron-doped material. This is shown in Figure 3-3.

(c) The solubility limit of boron in Ni_3Al is roughly 0.3 ± 0.05 wt. %; beyond that level, second phase particles with a composition of $Ni_{20}Al_3B_{10}$ were observed. This is the Tau phase reported by Stadelmaier et al. (Refs. 42,43). The room temperature ductility of Ni - 24 at. % Al increases sharply with

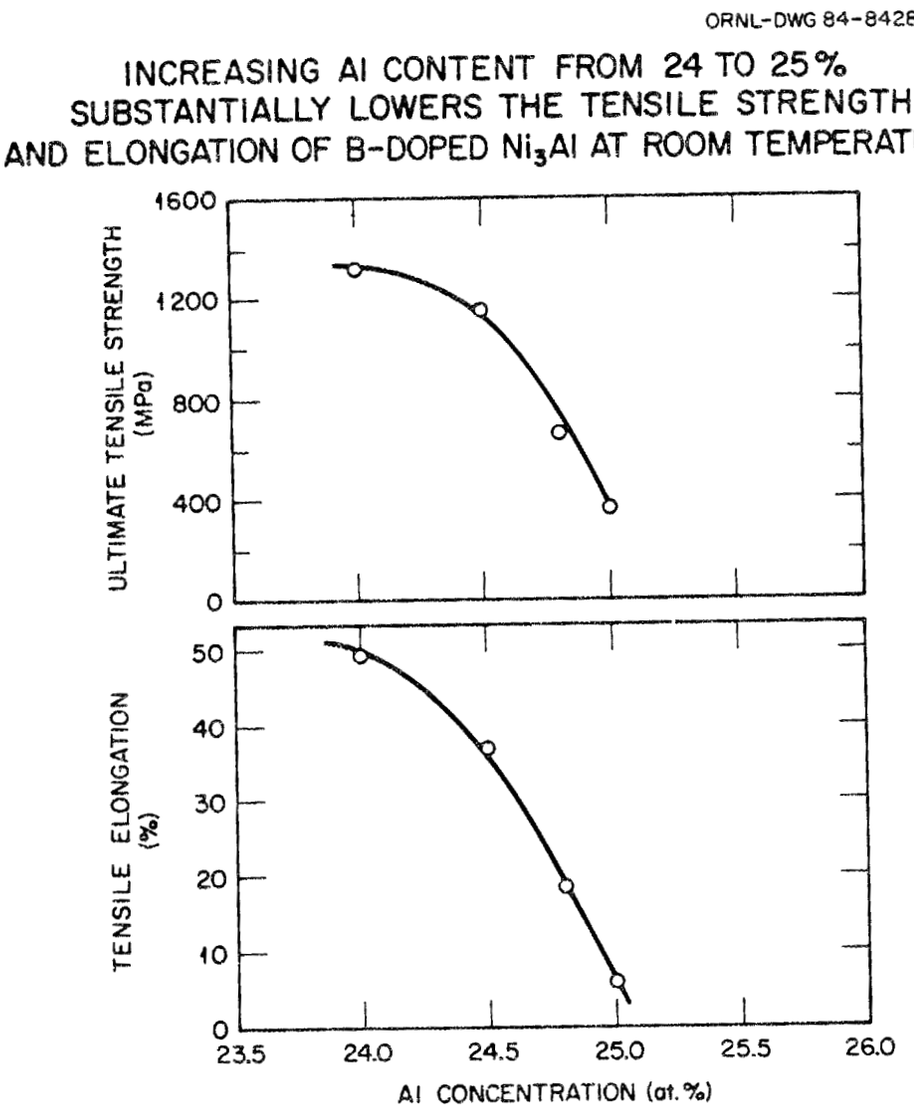

Figure 3-2. Plot of room temperature tensile elongation and ultimate tensile strength as a function of aluminum concentration to show the alloy stoichiometry effect (Ref. 40).

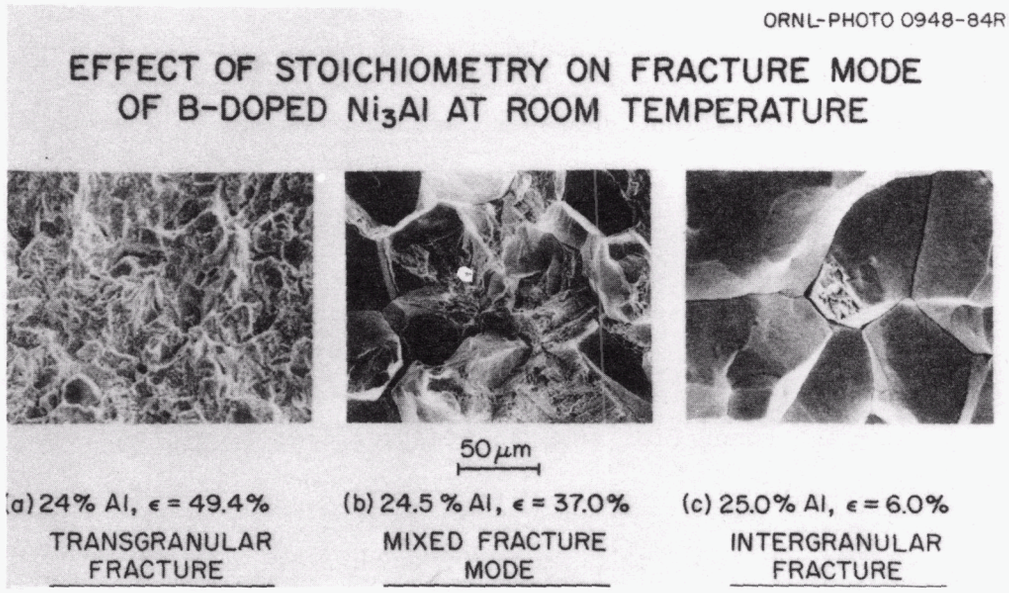

Figure 3-3. SEM fractographs of Ni_3Al doped with 0.05 wt. % B, showing the effect of alloy stoichiometry on fracture behavior at room temperature. (*a*) 24 at. % Al, tensile fractured; (*b*) 24.5 at. % Al, tensile fractured; (*c*) 24.8 at. % Al, tensile fractured (Ref. 40).

boron concentration reaching a broad maximum of about 50% for the 0.1 wt. % boron aluminide – the highest ever achieved in a a polycrystalline aluminide. With a further increase in boron, the ductility exhibits a modest decrease to 40% at 0.2 wt. % boron. Figure 3-4 shows this effect.

(d) Using Peak Height Ratios (PHRs) of AES spectra as comparative measures of degree of segregation on freshly fractured surfaces of boron-doped Ni_3Al, they found no effect of Al content on C, O and S segregation. However, with decreasing bulk Al content, the amount of grain boundary Al decreases while the intensity of segregation of grain boundary boron increases, as shown in Figure 3-5. Tied with this is the finding that boron displays an unusual segregation behavior in that it segregates more strongly to grain boundaries than to free surfaces (e.g., cavities). Conversely, S, an embrittling impurity, segregates more strongly to free surfaces than to grain boundaries, as shown in Figure 3-6. As shall be discussed later, these authors have correlated these observations with theories of solute segregation and strength.

(e) The yield strength of boron-doped Ni_3Al decreases with increasing grain size, following a Hall-Petch (Refs. 44,45) type of relation:

$$\sigma_y = \sigma_{o,y} + K_y d^{-\frac{1}{2}}$$

with $\sigma_{o,y} = 163$ MPa

$K_y = 8.2$ MPa $cm^{\frac{1}{2}}$

This is shown in Figure 3-7.

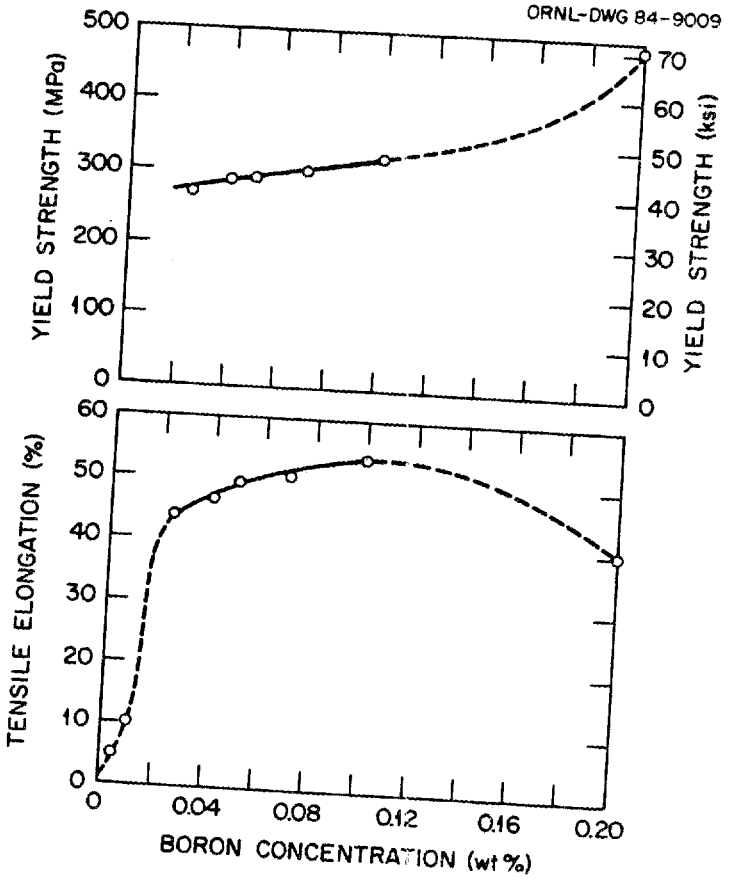

Figure 3-4. Plot of room temperature tensile properties as a function of boron concentration for Ni_3Al (24 at. % Al). All specimens were recrystallized for 30 minutes at 1000°C (Ref. 40).

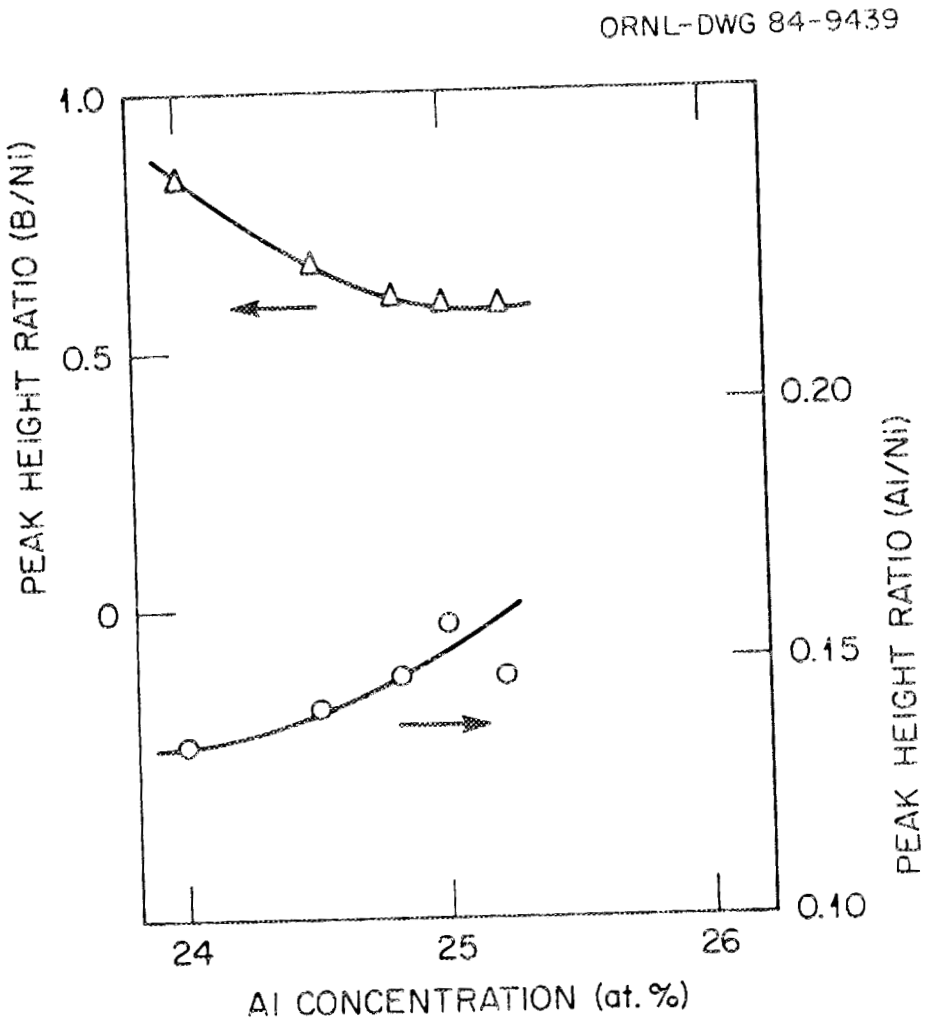

Figure 3-5. Correlation of PHR (B, 180 eV/Ni, 102 eV) and PHR (Al, 1396 eV/Ni, 848 eV) with aluminum concentration. The peak height ratios were obtained from intergranular portions of fracture surfaces of Ni_3Al – 0.05 wt. % B (Ref. 40).

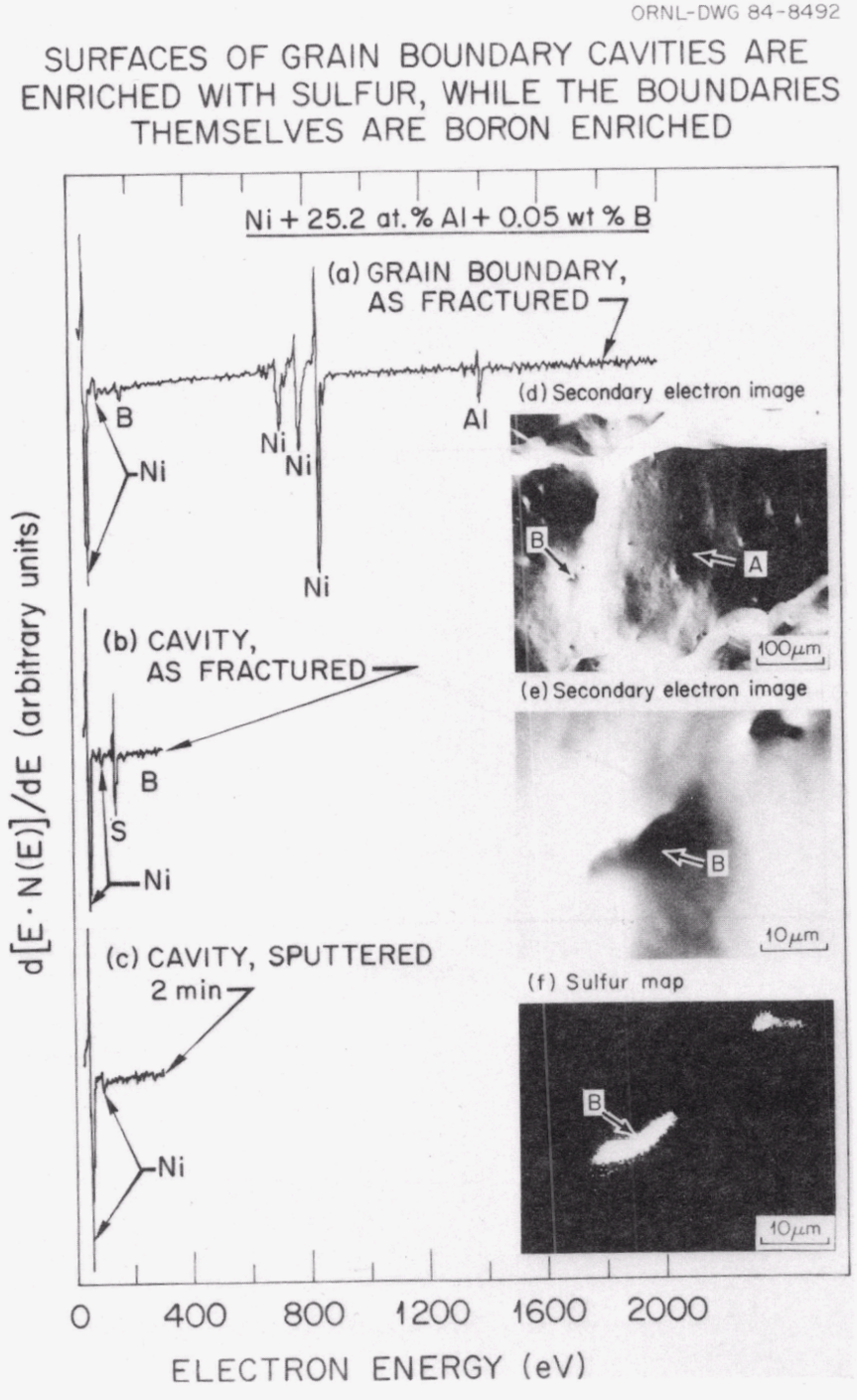

Figure 3-6. Auger spectra [(*a*) – (*c*)], secondary electron images [(*d*) and (*e*)], and a sulphur elemental map (*f*), describing a region on a fracture surface of Ni – 25.2 at. % Al – 0.05 wt. % B. The Auger spectrum in (*a*) was obtained from the smooth grain boundary region at point "A" in image (*d*), and the partial spectrum was from the feature at point "B" in image (*e*) (Ref. 40).

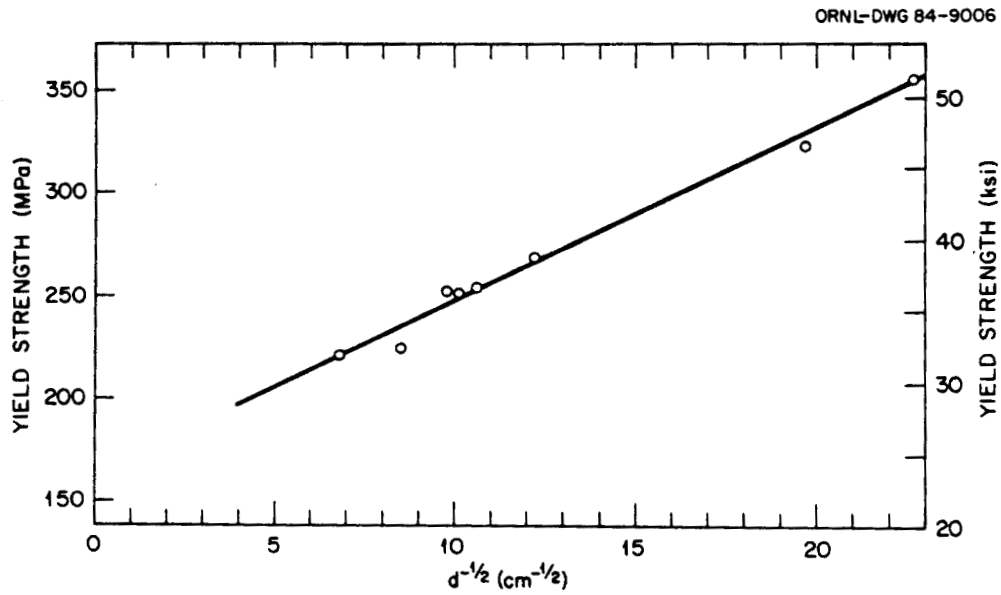

Figure 3-7. The Hall-Petch plot of yield stress of boron-doped Ni_3Al (24 at. % Al) as a function of $d^{-\frac{1}{2}}$ (d = grain diameter) (Ref. 40).

(f) At small grain sizes, the tensile elongation of boron-doped Ni_3Al (24 at. % Al) was independent of grain size and kept constant at about 50%. With an increase in grain size above 110 μm in diameter, however, the aluminide showed only a moderate drop in ductility but no change in fracture mode, i.e., transgranular fracture persisted.

Schulson and coworkers (Refs. 46,47), however, have claimed a better fit for the yield strength – grain size behavior of undoped and boron-doped (800 wppm B) as:

$$\sigma_y = \sigma_o + kd^{-0.8}$$

where

σ_o = 93 ± 14 MPa for undoped

= 241 ± 9 MPa for doped

k = 2080 ± 105 MPa . $\mu m^{0.8}$ for undoped

= 1200 ± 22 MPa . $\mu m^{0.8}$ for doped.

It is interesting to note that Takasugi et al. (Ref. 48) have recently reported an improvement in the ductility of cast substoichiometric Ni_3Al with the addition of beryllium. Within the solubility limit for beryllium (~1 at. %), the yield strength increases linearly with beryllium content.

From the above it is amply evident that an in-depth study of boron segregation behavior in Ni_3Al is important to understanding and predicting its effects on grain boundary cohesion. So far most of the work has concentrated on one bulk boron level (0.05 wt. %) and one basic thermal history (annealing for 30 minutes at 1000°C). Additional information on

the thermodynamics and kinetics of the segregation process is clearly needed. It is this aspect of the problem on which attention has been focused in this dissertation.

CHAPTER 4

GRAIN BOUNDARY STRUCTURE

I. MACROSCOPIC DESCRIPTION

The following description of grain boundaries is due to Cahn (Ref. 49); while it will not be used in the subsequent treatment, it has been included for completeness. He has considered a system containing a boundary lying along some plane in the bulk phase consisting of two adjoining crystals 1 and 2. In such a case the boundary may be described in terms of temperature, pressure, composition and the following nine geometrical factors:

(a) three to describe crystal misorientation,

(b) three to describe position of boundary with respect to any one of the crystals, and

(c) three to describe the translational mismatch of the two crystals.

If the last three variables and the position of the grain boundary normal to itself is relaxed to equilibrium then the number of variables required to specify the system is $(C + 1) + 5 = C + 6$, where C is the number of chemical components in the system. Thus the structure of a boundary may be represented in the abstraction of a $C + 6$ variable hyperspace.

II. GEOMETRICAL ASPECTS

The following section is derived from Balluffi's treatment of this topic (Ref. 50).

A planar grain boundary between lattices 1 and 2 can be thought of as a core region of "bad material" sandwiched between two relatively perfect crystals which are imperfect only in so far as they are elastically strained. "Bad material" is defined as material where the atomic structure is highly disorganized in terms of nearest neighbors and interatomic distances. Although the exact positions of the atoms at the core are uncertain, several geometrical descriptions have been put forward; these are at best convenient models and by no means exact descriptions. Three of these will be described here.

(A) Coincidence Site Lattice (CSL)

This lattice describes the basic periodicity of the atomic structure of the core region. Such a lattice may be constructed if the two lattices adjoining the boundary are imagined to extend throughout all space and one of these is translated with respect to the other, without rotation, such that atoms of each crystal lattice coincide at one point which is the origin of the CSL. The space lattice then made up of all points in space at which atoms coincide is the CSL - e.g., Figure 4-1 shows the CSL in two dimensions for cubic lattices rotated around [001].

The quantity $\sum$ is defined as the reciprocal of the fraction of lattice atoms associated with CSL points. The misorientation or tilt angle between two crystals may thus be given in terms of $\sum$ for a known crystal type. A grain boundary of any given misorientation may now be constructed

AC-107

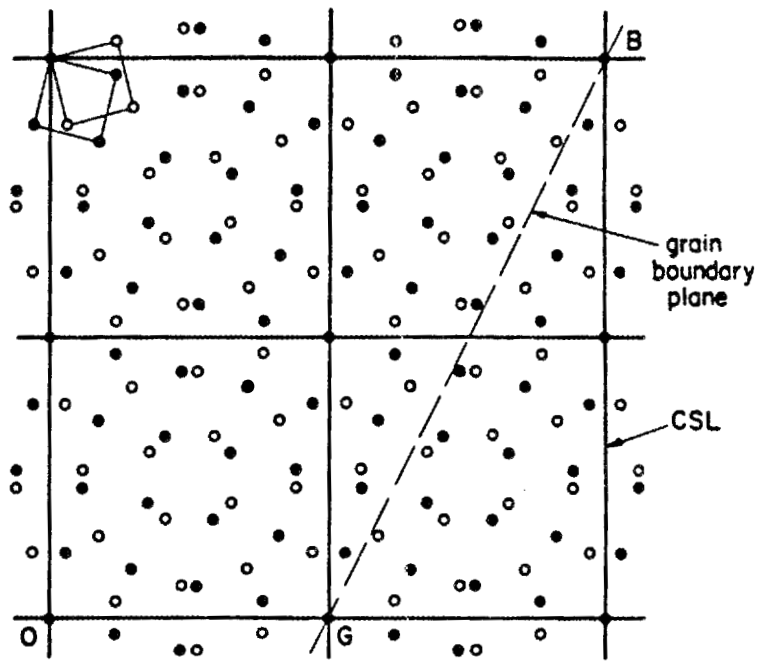

Figure 4-1. (001) planes of two interpenetrating simple cubic lattices rotated with respect to one another around [001] by θ - 28.1° ($\sum$ = 17). Coincidence Site Lattice indicated by the square mesh. The quantity $\sum$ is defined as the reciprocal of the fraction of lattice atoms associated with CSL points (Ref. 50).

by passing a plane through the two interpenetrating lattices and discarding all atoms of lattice 1 on one side of the plane and all atoms of lattice 2 on the other. This rigid lattice grain boundary configuration formed is then allowed to relax to a minimum energy equilibrium structure. Hence the CSL model shows the dependence of grain boundary structure on the relative orientation of the two crystals but ignores the effects of boundary inclination.

(B) O-Lattice

The O-Lattice is defined (Ref. 51) as the array of points in space where points in lattices 1 and 2 with the same internal unit cell coordinates coincide, if both lattices are assumed to extend throughout all of space. For a given misorientation of two grains, many alternative O-Lattices may be constructed; however, for any given O-Lattice, each O-Lattice point can serve as the origin for the transformations linking the two lattices - i.e., the O-Lattice is a "lattice of origins." Figure 4-2 shows the O-Lattice for the case given in Figure 4-1, the CSL being denoted by the intersection of lines marked C in Figure 4-2. As can be seen, the CSL is a sublattice of the O-Lattice. The structure of the boundary is periodic with CSL period rather than O-Lattice period. The O-Lattice spacing varies continuously with misorientation as opposed to the discontinuous behavior of the CSL.

(C) DSC Lattice

The DSC lattice for a particular grain boundary defines all the vector displacements of lattice 1 and lattice 2 relative to each other which are possible under the condition that the overall pattern of atoms produced by the two interpenetrating lattices remains unchanged. It is

AC-108

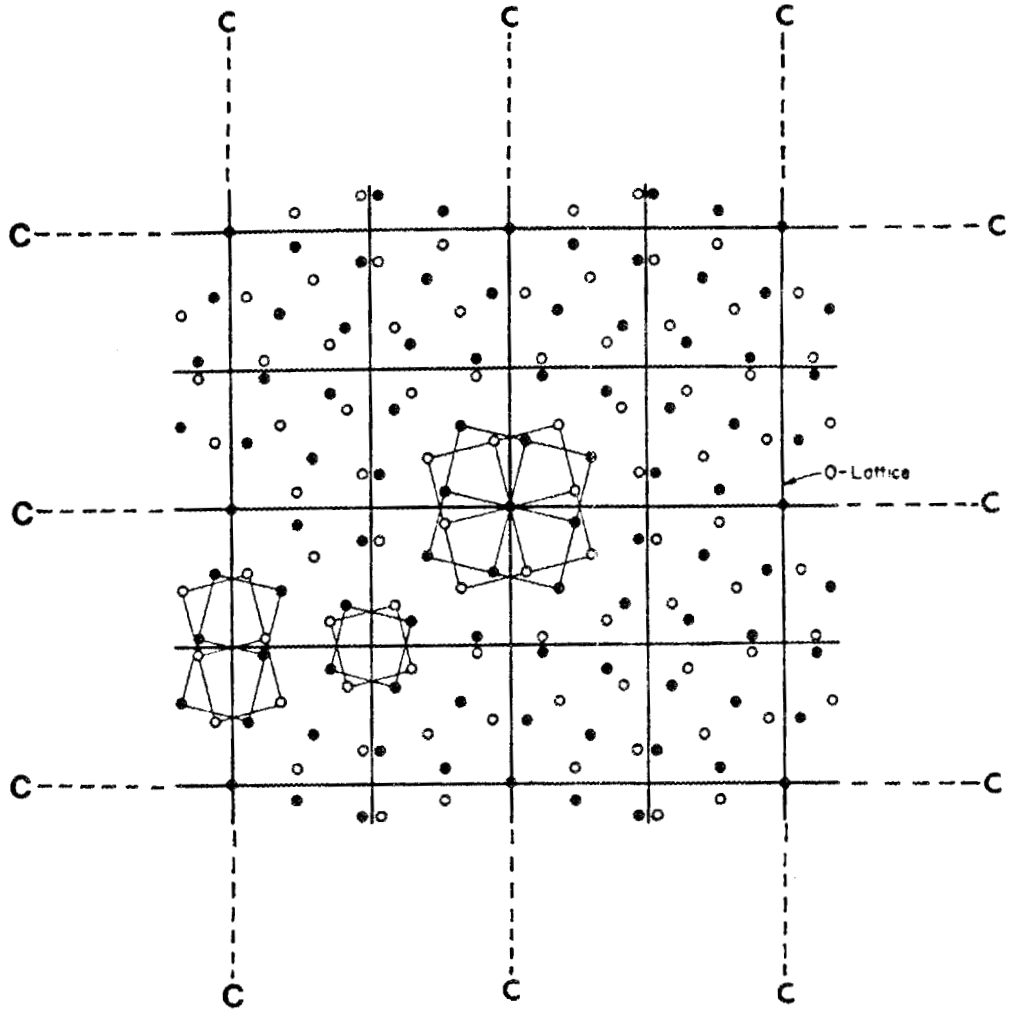

Figure 4-2. (001) planes of two interpenetrating simple cubic lattices rotated with respect to one another around [001] by $\theta = 28.1°$ ($\sum = 17$) as in Figure 4-1. 0-Lattice indicated by the square mesh. Note that three different atomic patterns (illustrated) exist around the different 0-Lattice points. Also each 0-Lattice point may be used as an origin for the rotational transformation of one lattice into the other (Ref. 50).

thus the lattice of pattern conserving displacements, i.e., Displacement of lattice 2 with respect to lattice 1 by a DSC lattice vector causes a pattern Shift which is Complete. The lattice defines the possible Burgers Vectors of all perfect grain boundary dislocations (GBDs) which may exist in the boundary. The lattice spacing of the DSC lattice in the plane normal to the axis of misorientations tends to vary reciprocally with the spacing of the CSL. A simple graphical way to find the DSC lattice vectors is to find the set of vectors connecting atoms of lattice 1 with lattice 2; this is shown for the same case as Figures 4-1 and 4-2 on Figure 4-3.

Hence as the degree of lattice coincidence matching ($1/\sum$) decreases, the CSL becomes larger and the DSC lattice becomes smaller.

III. DISLOCATION MODELS

Although it is possible to represent all grain boundaries as arrays of lattice dislocations, such representations are accurate portrayals of low angle boundaries but less so of high angle ones. In its original form, the model incorporated a linear array of dislocations of which the core was indescribable in terms of energy. Although the description has undergone significant modifications, the model is still mainly valid for low angle ($<15°$) boundaries. Use of nonlinear dislocation models have suggested that in low energy boundaries, the dislocation cores have sizes comparable to lattice dislocations whereas this core diameter increases as the boundary energy increases. Other approaches have suggested that there is a marked delocalization of dislocations at the boundaries (Ref. 52).

AC-109

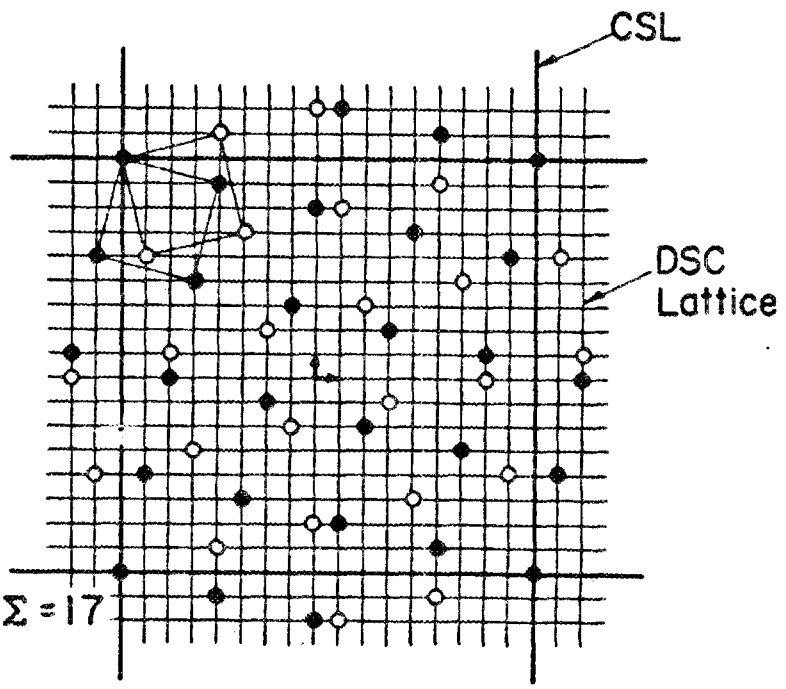

Figure 4-3. DSC-Lattices formed by interpenetrating (001) planes of simple cubic lattices rotated with respect to one another by angle θ around [001] (θ = 28.1° or $\sum$ = 17). The base vector of the DSC lattice is shown at the center of the diagram; also shown is the CSL (Ref. 50).

IV. PLANE MATCHING MODELS

These models were developed to explain fringes appearing on electron microscopy photographs of high angle boundaries which had been disproven as Moire' fringes. It is not clear that these models are not alternative descriptions of dislocation models since these fringes are explained in terms of strain fields (Ref. 52).

V. STRUCTURAL/POLYHEDRAL UNIT MODELS

Such models have attempted to describe the structure and properties of grain boundaries in terms of a two-dimensional array of one or several types of "structural unit," which is defined as a small group of atoms arranged in a characteristic configuration. These individual structural units assume certain deltahedral shapes - most often an adequate description of the misorientation in addition to space filling requirements necessitates the use of more than one type of these deltahedra. It so turns out that the descriptions in terms of a mixture of deltahedra are alternative forms of descriptions in terms of secondary GBDs (Ref. 52).

Computer simulations of grain boundaries using certain interatomic potentials have been instrumental in popularizing this concept of grain boundaries.

VI. EQUILIBRIUM DEFECTS IN GRAIN BOUNDARIES

The following treatment is derived from Ref. 50.

(a) Perfect GBDs: these may be introduced in a boundary by making a

suitable cut and then displacing one half along a DSC lattice vector. Such dislocations generally have grain boundary ledges associated with them (Figure 4-4).

(b) Pure Grain Boundary Ledges: these are steps in the boundary plane which completely lack any extrinsic dislocation character.

(c) Partial GBD: such dislocations arise as a consequence of the possibility of several orientations giving rise to the types of relaxation of CSLs called for by minimum energy considerations. Such degenerate regions in the same boundary are separated by partial dislocations.

(d) Facet Dislocations: when the effect of increasing the total area is overcome by the effect of reducing energy per unit area, a flat boundary can degenerate into a faceted one. Dislocations can exist along the lines of intersection of facets due to differences in the relative displacements of lattices 1 and 2 across adjacent facets.

Balluffi and Olson (Ref. 53) have recently shown that it is possible to describe a given grain boundary by means of several alternative primary dislocation arrays. However, lack of a unique description of the static equilibrated dislocation structure does not pose any problems as far as determination of physical properties is concerned.

They have developed a hierarchy of four types of interfacial dislocations which are sufficient to represent all interfacial dislocation structures:

(a) Primary Interfacial Dislocations: perfect GBDs.

AC-110

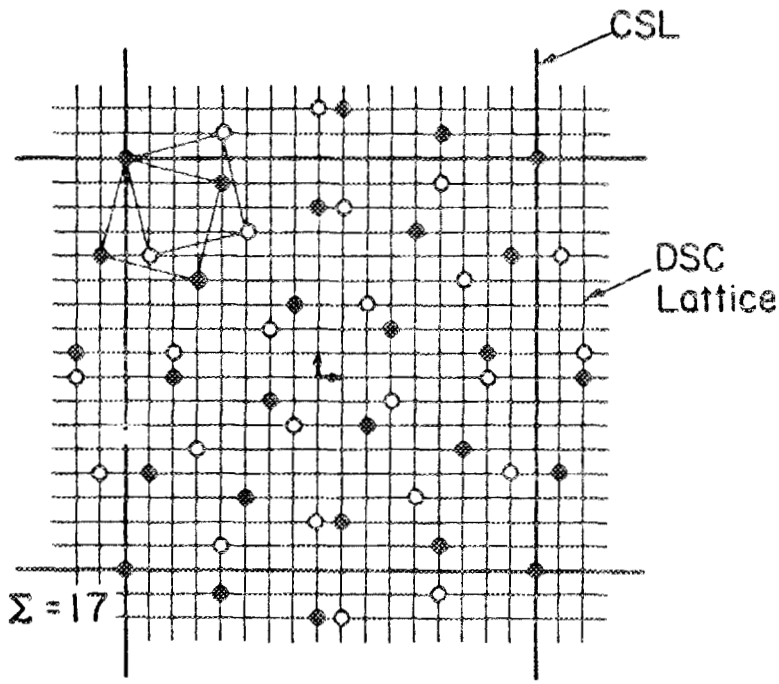

Figure 4-4. Perfect grain boundary edge dislocation in a tilt boundary formed by rotating simple cubic lattices with respect to one another around [001] by $\theta = 28.1°(\sum = 17)$. Grain boundary dislocation (encircled) is seen as a dislocation in the DSC lattice (square mesh). Burgers Vector of dislocation is one mesh spacing of DSC-Lattice (Ref. 50).

(b) Secondary Interfacial Dislocations: at high angle misorientations, GBD cores overlap requiring relaxations from CSL/DSC lattice positions; the periodic mismatch associated with such relaxations are called Secondary Interfacial Dislocations.

(c) Coherency Interfacial Dislocations: generally found in interphase boundaries; they are always associated with an interfacial step.

(d) Translational Interfacial Dislocations: these arise due to rigid body translations of the two crystals; they are a form of partial GBDs.

VII. NONEQUILIBRIUM DEFECTS IN GRAIN BOUNDARIES

Gleiter (Ref. 52) has given an account of nonequilibrium defects in grain boundaries and the following treatment is adapted from this.

(A) Point Defects

Computer simulation techniques and dynamic hard sphere models have yielded two kinds of vacancy structures:

(i) Vacancies in short period boundaries of good fit are described by a localized boundary vacancy surrounded by a displacement field which extends only a few lattice constants from the vacancy.

(ii) Vacancies in random boundaries induce a displacement field which is much more extended than in the previous case.

(B) Dislocations

A detailed description of models proposed for understanding the structure of extrinsic dislocations in grain boundaries is not of direct

interest here; suffice it to state that there are three such models:

(i) the dissociation model,

(ii) the core delocalization model, and

(iii) the strain sharing model.

VIII. SPECIAL BOUNDARIES VS GENERAL BOUNDARIES

Boundaries possessing a considerable amount of order as a result of a higher degree of periodic matching have coarse DSC lattices and hence have GBDs with large and distinguishable Burgers vectors. Such boundaries, having physically significant degree of order, are called special bound aries. General boundaries, on the other hand, have low degrees of matching and hence fine DSC lattices. As can be imagined, such a categorization is extremely subjective.

IX. GRAIN BOUNDARIES IN $L1_2$ SUPERLATTICE ALLOYS

The geometrical aspects of grain boundaries in $L1_2$ superlattices have been worked out by Takasugi and Izumi (Ref. 54). They note the following points about grain boundaries in intermetallic alloys:

(a) intergranular embrittlement of high angle boundaries is enhanced with increasing ordering energy of the alloys;

(b) superlattice grain boundaries are very susceptible to liquid metal and oxidation embrittlement; and

(c) the grain boundary embrittlement, accompanied by grain boundary hardening and shift in the ductile-to-brittle transition

temperature, occurs only with a stoichiometric excess of the more electropositive element.

These authors used the CSL theory to find the possible geometrical configurations of atoms in the grain boundary region. Pair bonding defects were identified and classified into several types. Next to nearest neighbors were used to find the fault energies of these defects. They characterized these defects as antiphase boundaries (APBs), stacking faults (SFs) and APB + SF faults. The authors reached the conclusion that these faults do not follow any system based on $\sum$ (i.e., θ) or on microscopic orientation. The grain boundary energy is a sum of two terms:

(a) defect bonding energy term, and

(b) lattice distortion term.

The grain boundary energy in ordered lattices is controlled by the first term. The authors identified two types of relative translations between the sublattices:

(i) Symmetrical (S) Boundaries: fully symmetrical tilt boundaries - in these the sublattices in one half of the crystal is truly symmetrical to the other half, forming with the same kind of atoms.

(ii) Pseudo-Symmetrical (PS) Boundaries: the sublattice in one half of the crystal is symmetrical to the sublattice but forming with the different atoms in the other half.

In the $L1_2$ lattice, these authors contend, the S boundaries do not always form the low energy configuration. Farkas (Ref. 55) in reinterpreting Takasugi and Izumi's (Ref. 54) results has shown that if the grain boundary structure is considered as a two phase structure, each

phase having a different composition but the same grain boundary energy, then on the average the S boundaries do indeed have lower energy than PS boundaries in the $L1_2$ structures, as predicted from symmetry considerations.

Farkas (Ref. 56) has dealt with the structural unit model for $L1_2$ structures and has reached the following conclusions:

(a) The grain boundary structure is composed of two phases (i.e., two types of structural unit combinations) of differing composition but identical grain boundary energy.

(b) If the equilibrium distances of atoms are similar for all types of bonds [i.e., "soft" interatomic potentials (e.g., Cu_3Au)], then the grain boundary structures that are densest for the pure FCC metals are also densest for the $L1_2$ structure.

(c) If the equilibrium distances of atoms (bond lengths) are different types of bonds [i.e., "hard" interatomic potentials (e.g., Ni_3Al)], then the grain boundary structure that is densest for the pure FCC metals is not the densest for the $L1_2$ structure. The author claims this may be part of the grain boundary brittleness problem.

X. GRAIN BOUNDARY STRUCTURE AND SEGREGATION

As compared to free surfaces, there is more freedom at grain boundaries for the formation of new structures which are independent of the details of the original structure. This is because a grain boundary is a smaller perturbation in the lattice than a free surface and has a much more complex structure. A grain boundary segregant must try to be compatible with both the adjoining lattices whereas a surface segregant need

only be compatible with a single lattice (Ref. 50). Studies have shown that solute atoms segregated to grain boundaries are localized to within a few atomic distances from the center plane of the boundary. The extent of segregation at grain boundaries is often considerably less than that at free surfaces since the energy of binding a solute (binding energy) to the average grain boundary core should be lower than to the average free surface.

The study of segregation to grain boundaries is extremely complicated and some of these complications are:

(a) The existence of a range of segregation sites is associated with a range of solute atom binding energies.

(b) Segregated solute atoms of the same type do interact.

(c) Solute atoms of different types may either enhance or retard each each other's segregation. There is also segregation site competition between these.

(d) More than a monolayer of solute atoms could lead to the formation of complex segregate structures.

(e) The degree of segregation to special boundaries is lower than to general boundaries.

Structural unit models have shown (Ref. 57) that grain boundaries of superlattices are inherently more amenable to segregation than those of pure metals or random solutions. The structure of superlattice grain boundaries is characterized by faulted bondings and certain combinations of structural (polyhedral) units. These cause heterogeneity of stress fields at the boundaries which in turn affect the segregation both of the

constituent atoms and impurities. Thus segregation is intrinsically tied in with grain boundary structure.

CHAPTER 5

INTERFACIAL SEGREGATION AND THERMODYNAMICS

I. INTRODUCTION

Segregation is defined as solute enrichment at interfaces in the absence of second phase formation. If interfaces in crystalline solids are considered to be two dimensional arrays of crystal defects, then the various kinds of interfaces that may be formed are depicted schematically in Figure 5-1. Lattice distortions and excess energies are associated with both interfaces and solute atoms, and substantial reductions in defect energy may occur when a solute atom on a bulk lattice site exchanges positions with a solvent atom on a distorted interfacial site. Interfacial regions, therefore, often have solute concentrations several orders of magnitude higher than the bulk crystal. This chapter deals with the physical and thermodynamical basis for this interfacial segregation while the next chapter deals with the effect of this segregated solute on interfacial properties in general and interfacial cohesion in particular.

II. INTERFACIAL ENERGY

The interfacial energy (F_b) of a grain/crystal boundary is defined as the excess free energy per unit area of the boundary surface. The concept of excess quantities is discussed in Section IV of this chapter.

The existence of an interfacial energy may be rationalized on the following basis. The bulk crystals are the lowest energy arrangement of

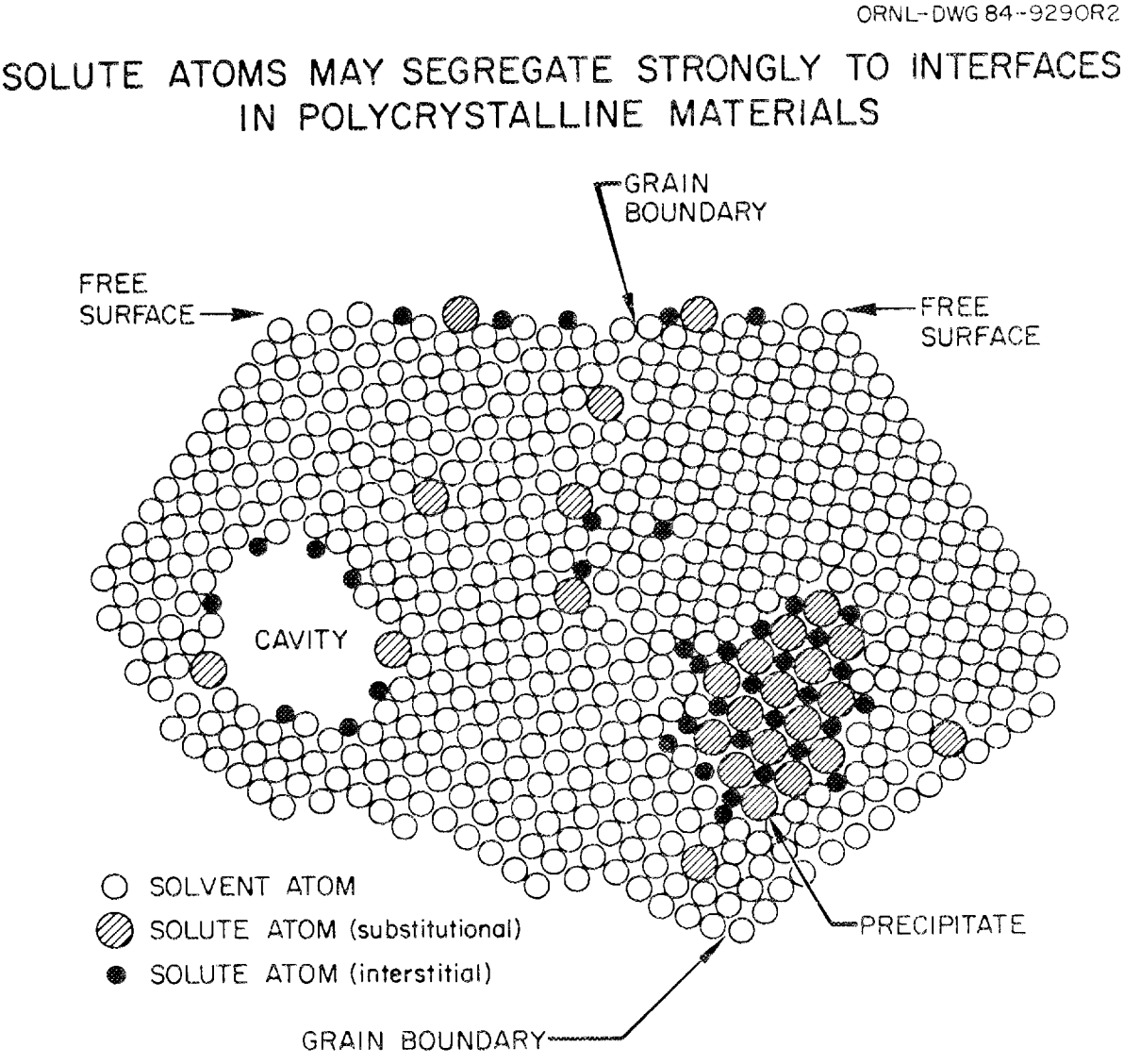

Figure 5-1. Schematic illustration of the various types of interfaces that may exist in crystalline materials (Ref. 58).

the atoms. Since the boundary exists between two such single crystals of different orientation, the boundary must consist of atoms displaced from their lowest free energy positions - i.e., the boundary atoms must possess a higher free energy. If the boundary is considered to have associated with it all the excess free energy due to these displaced atoms, it follows that the boundary must have a higher free energy than the adjoining crystals. If, however, a grain boundary is considered as a surface, then the grain boundary tension, γ_b (analogous to surface tension), is defined (Ref. 59) as the reversible work of formation (dW) of an unit area (dA) of the boundary at constant temperature, volume and chemical potentials:

$$\gamma_b = \frac{dW}{dA} \qquad \text{Equation (5-1)}$$

At this point it is to be realized that, unlike the situation in liquids, the grain boundary tension, γ_b, is NOT equal to the interfacial energy, F_b. Grain boundary tension, experiments are generally conducted at temperatures high enough to lead to high atomic mobility, however, so that γ_b can be considered to be numerically equal to F_b.

It is known (Ref. 59) that the following factors affect the grain boundary energy:

(a) the orientation relationship between the two crystals,

(b) the boundary inclination,

(c) the solute content, and

(d) the temperature.

As shown in Figure 5-2, grain boundary energy as a function of both misorientation angle and inclination angle (Ref. 60) generally exhibits cusps. Thus certain high angle boundaries exhibit low energy.

The temperature dependence of grain boundary energy arises from two factors:

(a) The extra entropy of a grain boundary compared with the same amount of material in the grain interior.

(b) The change of solute concentration at a grain boundary as a function of temperature.

These aspects will be dealt with in detail in Section III.

Shockley and Read (Ref. 60) proposed that, in the case of symmetrical tilt boundaries, if the two grains are oriented such that the boundary between them consists of equally spaced edge dislocations, then the boundary energy is relatively low. From this follows the dislocation description of grain boundaries. An example of such a boundary is shown in Figure 5-3. An important deduction can be made from such a description: different atomic locations at the boundaries are associated with different stress states. For example, with reference to Figure 5-3, sites 'B' located just above the core of the edge dislocation exist in a state of hydrostatic compression, whereas sites 'A' located just below the core exist in a state of hydrostatic tension. Sites 'C' located at regions between the edge dislocations have little dilatational stress. As will be discussed later, this has a very important bearing on segregation behavior of solutes to such boundaries.

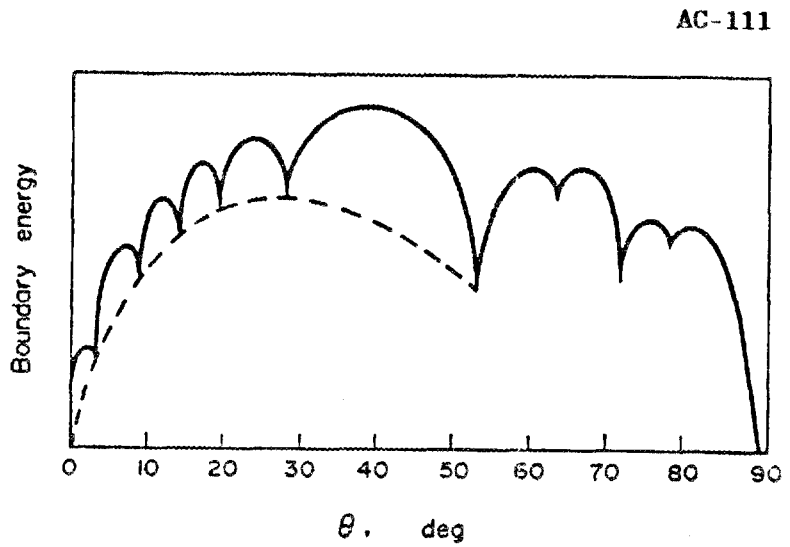

Figure 5-2. Schematic diagram of the variation of the boundary energy vs tilt angle θ. The cusps are located at orientation relationships that correspond to higher order twins (Ref. 60).

AC-112

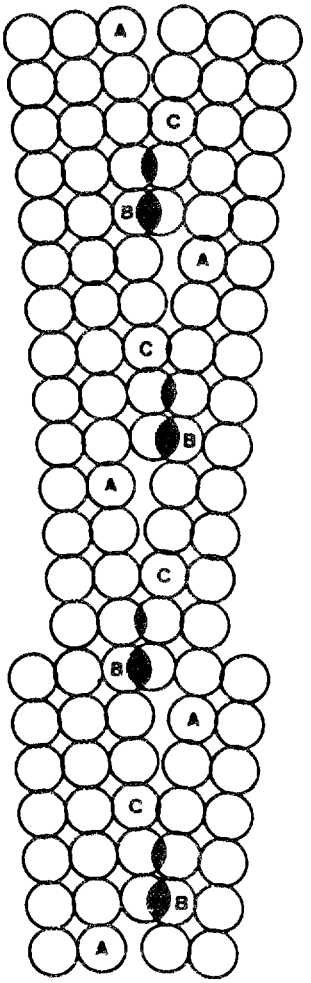

Figure 5-3. Schematic diagram of a simple tilt grain boundary (Ref. 61).

III. GRAIN BOUNDARY SOLUTE SEGREGATION

Figure 5-4 is a schematic representation of a 38° <100> tilt boundary in a simple cubic crystal. The energetics of solute segregation to grain boundaries will be discussed with reference to this figure (Ref. 62). While it is realized that the idea of "bonds" in metals is not a satisfactory representation of the true state of affairs, the concept is useful as a tool for visualizing some of the effects.

In Figure 5-4, ten atoms at the grain boundary are identified by numbers without primes, and δ_{AA} is the equilibrium spacing of solute atoms in the bulk (perfect) lattice. Some of the boundary atoms do not lie on the lattice sites of either crystal, but at intermediate positions. These intermediate positions would be determined by the fact that though individual interatomic bonds may be stretched (e.g., $\delta_{19} > \delta_{AA}$) or compressed (e.g., $\delta_{45} < \delta_{AA}$), the net force across any macroscopic region must be zero.

Figure 5-5 shows hypothetical interatomic potentials for interaction between two A atoms (solid curve), and between A and B atoms (dashed curves). Here the A-B interaction has been depicted to be weaker than A-A, and thus $\delta_{AB} > \delta_{AA}$. Let

δ_{AA} = Equilibrium A-A spacing.

ϵ_{AA} = Equilibrium binding energy between two A atoms,

i.e., energy required to separate them an infinite distance.

δ_{AB} = Equilibrium A-B spacing.

ϵ_{AB} = Equilibrium A-B binding energy.

AC-113

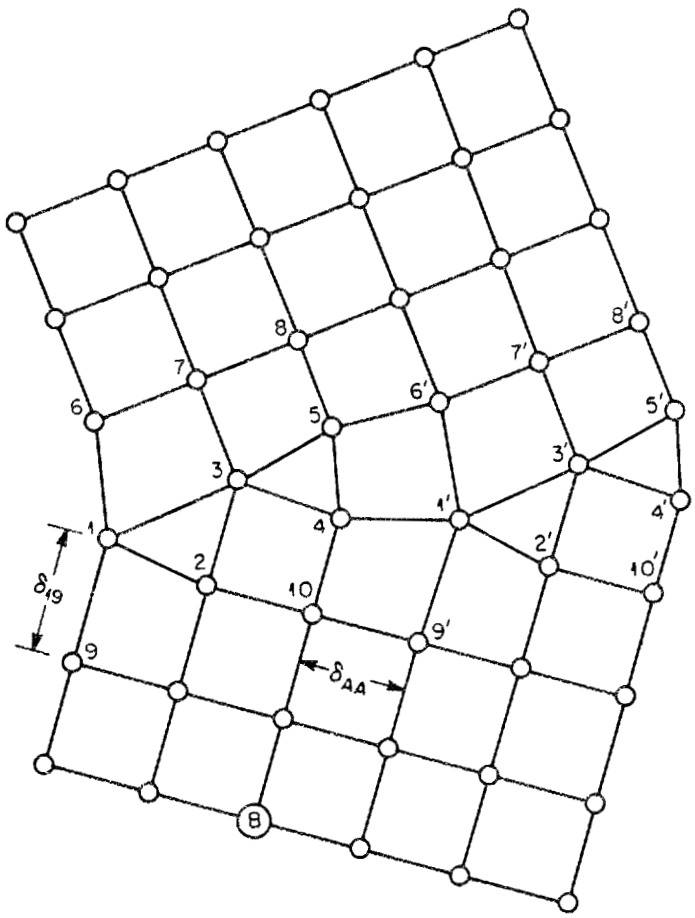

Figure 5-4. Schematic representation of a 38° <100> tilt boundary in a simple cubic crystal (Ref. 62).

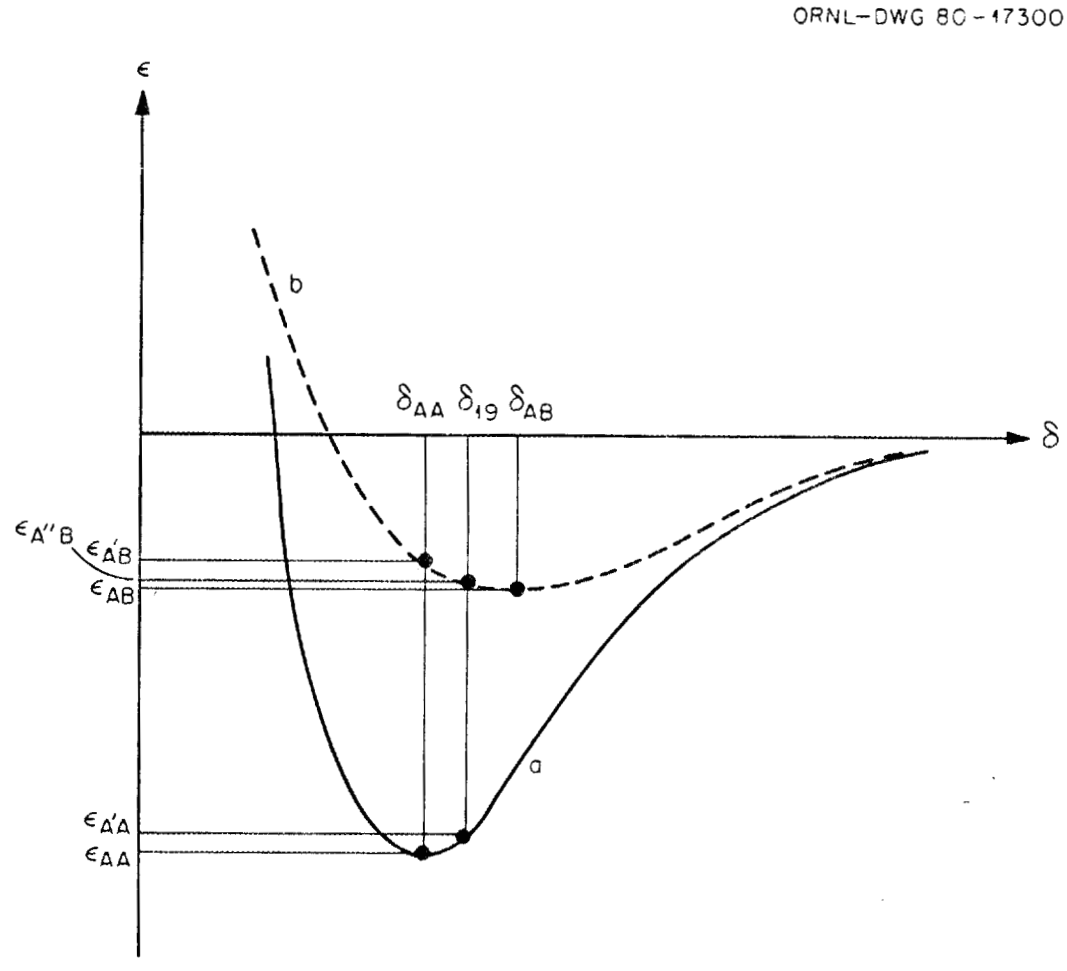

Figure 5-5. Hypothetical interatomic potential for A-A and B-B bonds (Ref. 62).

In the undistorted lattice, the spacing between B atoms and neighboring A atoms is constrained to be equal (or very close) to δ_{AA}; this leads to a lowering (in magnitude) of binding energy from ϵ_{AB} to $\epsilon_{A'B}$. In like fashion, a grain boundary A atom (e.g., at site 1 in Figure 5-4) can be displaced from its equilibrium lattice site on either adjacent grain resulting in a lower binding energy $\epsilon_{A'A}$ than A atoms in the perfect lattice (ϵ_{AA}). Hence an appropriate exchange of B atoms from the lattice for A atoms at the boundary would be energetically favorable. Such an exchange could be by an A atom at site 1 (Figure 5-4) exchanging positions with a B atom at site 9. The net energy change, $\Delta\epsilon_{19}$, in such a case would be:

$$\Delta\epsilon_{19} = (\epsilon_{AB} - \epsilon_{A''B}) + (\epsilon_{AA} - \epsilon_{A'A}) \qquad \text{Equation (5-2)}$$

In addition, other stretched bonds around site 1 and other relaxations of grain boundary structure will lead to a further lowering of effective energy. The total energy change, $\Delta\epsilon_{B1}$, associated with a fully relaxed (equilibrium) transfer of a B atom to site 1 is called the "interaction energy" between a B atom and site 1. In other words, the "interaction" or "binding" energy, $\Delta\epsilon$, is the decrease in the energy of the system when a solute atom in the bulk lattice exchanges places with a solvent atom at a grain boundary site. It is this relaxation of distorted atomic bonds and the attendant energy reduction that provides the physical basis for "positive absorption" or segregation. This will be dealt with more rigorously later.

McLean (Ref. 63) has developed a statistical thermodynamic treatment of segregation based on the assumption that all grain boundary sites have either a single valued interaction energy $\Delta\epsilon$ (i.e., $\Delta\epsilon$ is independent of

temperature and solute concentration in the lattice and the boundary) with a particular solute or they have no interaction at all. Then:

$$X^{\sigma} = \frac{X^{\alpha} \exp\ (\Delta\epsilon/_{k}T)}{1 - X^{\alpha} + X^{\alpha} \exp\ (\Delta\epsilon/_{k}T)} \qquad \text{Equation (5-3)}$$

where X^{σ} = Fraction of energetically attractive grain boundary sites occupied by solute atoms

X^{α} = Fraction of solute atoms in the lattice.

McLean suggested that approximately one third of the "grain boundary" sites might have an attractive interaction with solute atoms. Assuming a three atom layer boundary, the areal density of energetically favorable sites would then be approximately one monolayer.

McLean also has suggested that since $\Delta\epsilon = \epsilon_L - \epsilon_B$, and in cases where solute segregation is significant, $\epsilon_B << \epsilon_L$, hence $\Delta\epsilon \simeq \epsilon_L$. Now ϵ_L may be approximated by the elastic distortion energy, W, of an isotropic elastic sphere forced into a spherical cavity of a different dimension. Hence the temperature dependence of $\Delta\epsilon$ should be similar to that given for W by Pines (Ref. 64):

$$W = 24\Pi r^{3} \delta^{2} \left(\frac{KG}{3K + 4G} \right) \qquad \text{Equation (5-4)}$$

where K = Effective bulk modulus of the pure solute

G = Shear modulus of the solvent matrix

r = "in-situ" radius of the solute atom

$\delta = (r_A - r_B)/r_A$

r_A = Undistorted radius of the solvent atom

r_B = Undistorted radius of the solute atom.

Equation (5-3) predicts X^{σ} will decrease as T increases and will be roughly linearly related to X^{α} for small values of X^{σ}. While these qualitative predictions are in general agreement with experimental observations, some discrepancies in detail do exist.

Several segregation studies (Refs. 61,65) have reported a weaker temperature dependence of X^{σ} than predicted by Equation (5-3). This behavior could be due to as an increase in the (apparent) interaction energy with temperature. A better agreement is obtained by lifting the assumption that all segregating atoms have the same interaction energy, $\Delta\epsilon$, and that these interaction energies are independent of temperature.

Considering first the temperature dependence of $\Delta\epsilon$, there are three temperature dependent terms in Equation (5-4):

(a) The elastic moduli term, KG/(3K+4G):

For the case of sulphur segregation in Ni_3Al, White and Stein (Ref. 61) have found this term to decrease by about 30% as the temperature is raised from 1000 to 1500 K.

(b) The misfit parameter δ:

The change in δ (and hence δ^2) as a function of temperature may be estimated from thermal expansion coefficients of Ni_3Al. In the case of sulphur in Ni_3Al, the above authors (Ref. 61) have estimated δ^2 to increase by a factor of about 2 for a temperature increase from 1000 to 1500 K.

(c) The r^3 term:

This term is expected to increase with temperature but only by a few percent; hence its effect is negligible compared to the others.

It is worth noting that while the above arguments qualitatively rationalize the increase of $\Delta\epsilon$ with temperature, bulk material properties of the solute such as atomic radii, elastic constants and thermal expansion data have been applied for a solute atom in a dilute solid solution.

White and Stein (Ref. 61) and White and Coghlan (Ref. 66) have suggested a "spectrum of sites" approach in which the effective interaction energy between segregating solute atoms and grain boundary sites varies according to the fraction of sites already occupied. In this approach different binding energies are assumed for different types of grain boundary sites as follows. Let

$\Delta\epsilon_i$ = Binding energy of a solute atom for the "i^{th} type" of structurally distinct sites each of these being independent of temperature.

F_i^{σ} = The fraction of all grain boundary sites that are of the i^{th} type.

α = Crystalline phase.

σ = Grain boundary.

X^{α} = Fraction of lattice sites occupied by solute atoms.

X_i^{σ} = Fraction of type i grain boundary sites occupied by solute atoms.

ϵ_A^{α}, ϵ_B^{α} = The energy associated with A,B atoms on bulk lattice sites.

ϵ_{Ai}^{σ}, ϵ_{Bi}^{σ} = The energy associated with A,B atoms on type i grain boundary sites.

Assuming that the individual values of $\Delta\epsilon_i$ are unaffected by either the extent of segregation or temperature and accounting only for the configurational (not vibrational) entropy of the system, the authors (Refs. 61,66) showed that:

$$X_i^{\sigma} = \frac{X^{\alpha} \exp\ (\Delta\epsilon_i/kT)}{1 - X^{\alpha} + X^{\alpha} \exp\ (\Delta\epsilon_i/kT)} \qquad \text{Equation (5-5)}$$

Where

$$\Delta\epsilon_i = (\epsilon_B^{\alpha} - \epsilon_A^{\alpha}) + (\epsilon_{Bi}^{\sigma} - \epsilon_{Ai}^{\sigma}) \qquad \text{Equation (5-6)}$$

The overall solute concentration X^{σ} at a grain boundary of this type would be given by:

$$X^{\sigma} = \frac{\sum_i Fi\ X_i^{\sigma}}{\sum_i F_i} = \sum_i Fi\ X_i^{\sigma} \qquad \text{Equation (5-7)}$$

The values of $\Delta\epsilon_i$ for a given system are determined by the chemical interactions between the solute and solvent species as well as by the spatial relationships between atoms at various grain boundary sites. The F_i^{σ} vs $\Delta\epsilon_i^{\sigma}$ distributions were arbitrarily chosen to have the shape of a normal probability function whence these authors (Ref. 61) were able to back calculate $\Delta\epsilon_{eff}$ as a function of temperature from the following expression [which is derived from Equation (5-3)]:

$$\Delta\epsilon_{eff} = kT\ Ln\left[\frac{X^{\sigma}\ (1 - X^{\alpha})}{X^{\alpha}\ (1 - X^{\sigma})}\right] \qquad \text{Equation (5-8)}$$

Figure 5-6 shows a plot of $\Delta\epsilon_{eff}$ vs T from their paper where i_{max} and $\delta\epsilon$ were chosen so that the energy released upon saturating all energetically favorable sites with solute atoms $\sum_{i=1}^{i_L} F_i^{\sigma}\ \Delta\epsilon_i$ is one half of the grain boundary tension for a pure metal ($\gamma/2$). $\Delta\epsilon_{eff}$ approaches 0 as T approaches zero because half the sites at this hypothetical grain boundary have negative solute binding energies and hence will never be filled. Hence $X^{\sigma} < 1$ at $T = 0$ and hence $\Delta\epsilon = 0$ as per Equation (5-8). As T

AC-114

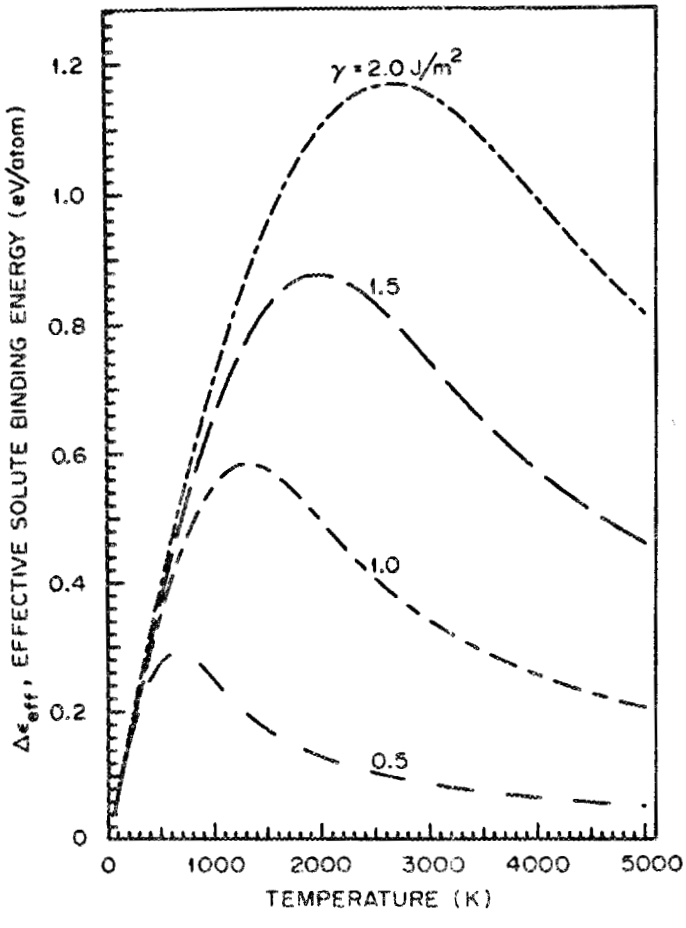

Figure 5-6. Plot of effective binding energy vs temperature for several values of grain boundary tension γ (Ref. 61).

increases, X^{σ} decreases; however, the average binding energy of the solute atoms remaining at the boundary increases. Hence X^{σ} decreases more slowly than predicted by Equation (5-3) and hence $\Delta\epsilon_{eff}$ in Figure 5-6 increases. The authors ascribe the surprising maxima shown on Figure 5-6 to unknown factors. In the above discussion $\Delta\epsilon_{eff}$ is the "effective" binding energy i.e., the binding energy that can be found from experimental measurements of X^{α} and X^{σ}.

White and Coghlan (Ref. 66) have found this approach to yield results more in accordance with experimental data. In their calculations the strain energy of the solute-grain boundary system was taken to be the sum of both size and modulus mismatch terms and both were found to cause a significant solute segregation to grain boundaries. The size mismatch term arises because the solute atom can lower the energy of the system by moving to a distorted region near the grain boundary where it can be well accommodated. The solute atom also influences the elastic constants of its immediate surroundings. The elastic energy of a strained region is directly proportional to its elastic constants, and thus solute atoms which tend to lower the elastic moduli will be attracted to highly strained regions while those that increase the moduli will be repelled. These authors point out that the modulus effect may help explain grain boundary segregation in the absence of size mismatch.

It is to be remembered that Equation (5-3) holds for equilibrium conditions only; i.e., the grain boundary must be in equilibrium with the matrix. McLean (Ref. 63) has suggested the time, $t_{\frac{1}{2}}$, necessary for the grain boundary solute concentration to reach one half its saturation value is given by:

$$t_{\frac{1}{2}} = \frac{9\alpha^2 d^2}{64\ D} \qquad \text{Equation (5-9)}$$

where $\alpha = X^{\sigma}/X^{\alpha}$

d = Grain boundary thickness

D = Diffusion coefficient of solute in the solvent matrix.

This offers an approach towards understanding the kinetics of solute segregation and will be dealt with in Chapter 10.

IV. INTERFACIAL THERMODYNAMICS

A. Basics

The following treatment follows the one presented by Lupis (Ref. 67). The comprehensive thermodynamic treatment of interfaces was first developed by Gibbs (Ref. 68).

It is to be recognized that atoms in the vicinity of an interface are in a different environment than in either adjacent bulk phase. The energy of a system containing an interface will generally be greater than the energy of equal volumes (or moles) of the constituent phases.

A real, physical interface is three dimensional - albeit often very thin (few angstroms). A planar region, σ, (shown hatched) of thickness Δt is shown separating two homogeneous bulk phases α and β in Figure 5-7. For convenience, a planar interface is considered, thereby obviating complications due to interface curvature. It is assumed that the properties of σ are uniform in a direction parallel to AA′ but not perpendicular to it (i.e., xx′).

AC-115

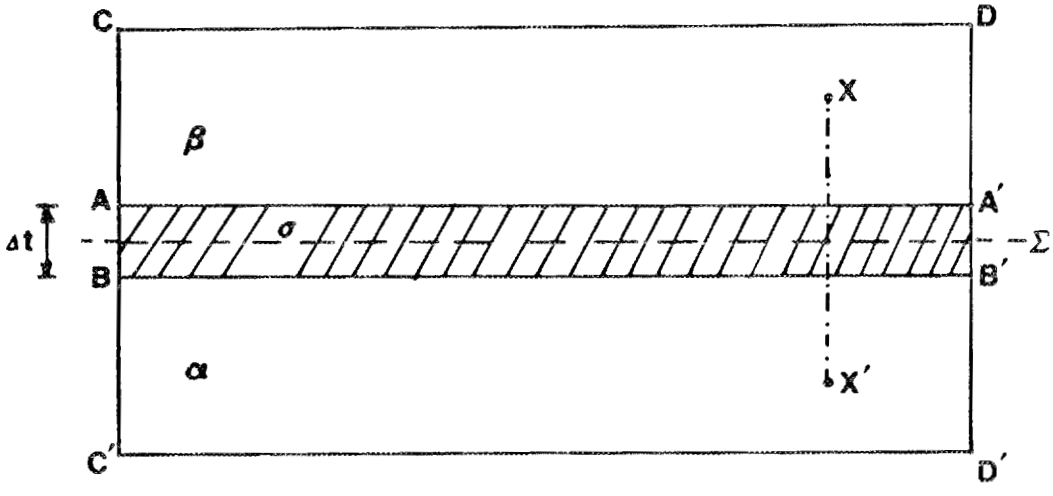

Figure 5-7. A closed system θ illustrating the concepts of a physical interface (hatched) and Gibbs dividing surface $\sum$.

The Gibbs treatment models this system as two homogeneous phases separated by the two dimensional surface $\sum$, shown dashed in Figure 5-7. The surface is chosen such that it is a plane of symmetry for the elements adjacent to it. A closed system θ is generated by surfaces CC′ and DD′ perpendicular to $\sum$. It is assumed that the only work performed by the system is done against pressure. It is possible to show (Ref. 67) that in such a system the equilibrium conditions are:

$$T^{\alpha} = T^{\beta} = T^{\sigma} \qquad \text{Equation (5-10)}$$

$$\mu_i^{\alpha} = \mu_i^{\beta} = \mu_i^{\sigma} \quad (i = 1,\text{--}m) \qquad \text{Equation (5-11)}$$

where T^{α}, T^{β} and T^{σ} are the temperatures of α, β and σ, respectively, and μ_i^{α}, μ_i^{β} and μ_i^{σ} are the chemical potentials of component i in α, β and σ, respectively. In other words, when the systems α, β and σ allow heat and mass transfer but have no moving boundaries, then the conditions for equilibrium are identical for homogeneous and heterogeneous systems (i.e., containing interfaces).

If α and β are assumed homogeneous right up to the surface $\sum$ and quantities relating to the part of the system containing α are identified by a prime while those pertaining to the part containing β by a double prime, then:

$$n_i' = c_i' V' \qquad \text{Equation (5-12)}$$

and

$$n_i'' = c_i'' V'' \qquad \text{Equation (5-13)}$$

where n_i = Number of moles of component i

c_i = Concentration of component i in moles per unit volume

V = Volume of subsystem.

The comparison between the real and model systems is shown in Figure 5-8.

For the model system to be stoichiometrically equivalent to the real system, the dividing surface $\sum$ must be assumed to contain n_i^{σ} number of moles of component i, so that the total number of moles of i in the real system n_i is:

$$n_i = n_i' + n_i'' + n_i^{\sigma} \qquad \text{Equation (5-14)}$$

The total surface EXCESS of component i is then defined as:

$$n_i^{\sigma} \equiv n_i - n_i' - n_i'' \qquad \text{Equation (5-15)}$$

In common usage the term "surface excess of component i" implies the SPECIFIC surface excess of component i given by:

$$\Gamma_i \equiv \frac{n_i^{\sigma}}{A} \qquad \text{Equation (5-16)}$$

where A = Area of surface $\sum$.

Other surface excess quantities such as energy, entropy, etc. may be similarly defined:

$$V_i^{\sigma} = V_i - V_i' - V_i'' \qquad \text{Equation (5-17)}$$

$$E_i^{\sigma} = E_i - E_i' - E_i'' \qquad \text{Equation (5-18)}$$

$$S_i^{\sigma} = S_i - S_i' - S_i'' \qquad \text{Equation (5-19)}$$

It is to be noted however that:

$$V^{\sigma} = V - V' - V'' = 0 \qquad \text{Equation (5-20)}$$

The specific surface excess of component i, Γ_i, is often called the "Adsorption of i".

AC-116

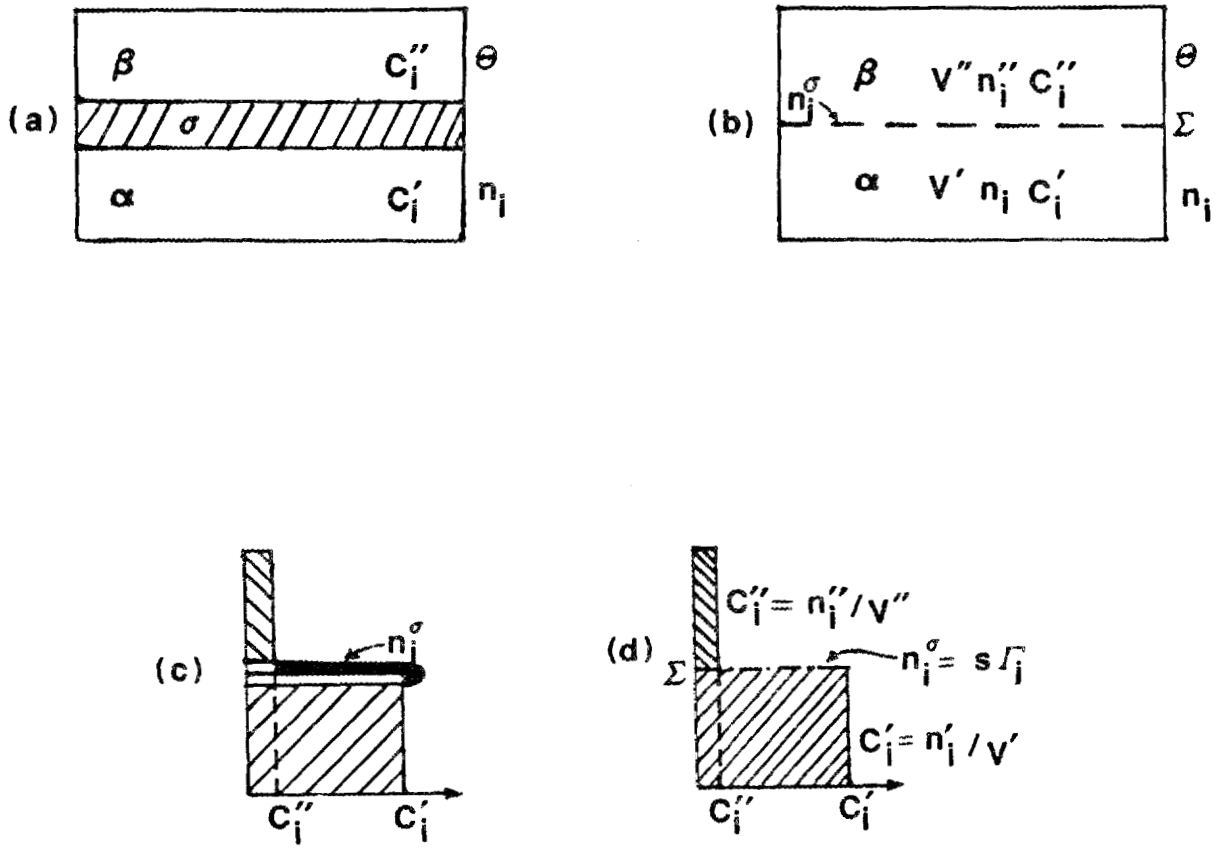

Figure 5-8. Real (*a*) and model (*b*) systems. In the model system, the phases α and β are assumed homogeneous up to the dividing surface $\sum$. The number of moles adsorbed n_i^σ is equal to the area in black (*c*) and is assumed to exist in the hypothetical surface $\sum$ (*d*).

Now for the entire closed system θ of Figure 5-8(*b*), it is possible to write:

$$E^{\theta} = TS - P'V' - P''V'' + \gamma^{\sigma}A + \sum_{i=1}^{m} \mu_i n_i \quad \text{Equation (5-21)}$$

where the only difference between E^{θ} and the expression for a homogeneous phase of the same temperature, composition, pressure and volume involves the quantities $\gamma^{\sigma}A$ and $\sum_{i=1}^{m} \mu_i n_i{}^{\sigma}$.

The properties of the individual bulk homogeneous phases lead to:

$$E' = TS' - P'V' + \sum_{i=1}^{m} \mu_i n_i' \quad \text{Equation (5-22}a\text{)}$$

$$E'' = TS'' - P''V'' + \sum_{i=1}^{m} \mu_i n_i'' \quad \text{Equation (5-22}b\text{)}$$

Subtracting Equation (5-22) from Equation (5-21), we obtain

$$E^{\sigma} = TS^{\sigma} + \gamma^{\sigma}A + \sum_{i=1}^{m} \mu_i n_i{}^{\sigma} \quad \text{Equation (5-23)}$$

Differentiation of Equation (5-23) leads to:

$$dE^{\sigma} = TdS^{\sigma} + S^{\sigma}dT + \gamma^{\sigma}dA + Ad\gamma^{\sigma} + \sum_{i=1}^{m} \mu_i dn_i{}^{\sigma} + \sum_{i=1}^{m} n_i{}^{\sigma}d\mu_i \quad \text{Equation (5-24)}$$

Using the notations used earlier for surface excess quantities:

$$dE^{\sigma} = TdS^{\sigma} + \sum_{i=1}^{m} \mu_i dn_i{}^{\sigma} + \gamma^{\sigma}dA \quad \text{Equation (5-25)}$$

Inserting Equation (5-25) in Equation (5-24) yields the Gibbs-Duhem equation for the interface (Ref. 67):

$$S^{\sigma}dT + Ad\gamma^{\sigma} + \sum_{i=1}^{m} n_i{}^{\sigma}d\mu_i = 0 \qquad \text{Equation (5-26)}$$

or

$$d\gamma^{\sigma} = -\frac{S^{\sigma}}{A}dT - \sum_{i=1}^{m} \Gamma_i d\mu_i \qquad \text{Equation (5-27)}$$

where $\frac{S^{\sigma}}{A}$ = Specific Interfacial Excess Entropy.

Equation (5-27) is the well known Gibbs Adsorption Equation, which relates surface tenion to surface composition.

The excess quantities E^{σ}, S^{σ} and $n_i{}^{\sigma}$ are determined by the state of the physical system and by the imaginary surfaces by which they are defined. In deriving Equation (5-25), it is assumed that all such surfaces are kept fixed. Then the expression of dE^{σ} for all reversible variations depends only on the position and form of the surface $\sum$. When $\sum$ is either translated or rotated, each of the quantities E^{σ}, S^{σ} and $n_i{}^{\sigma}$ will vary but Equation (5-25) will still be obeyed.

It is to be noted that Equation (5-23) provides the definition for the interfacial tension, γ^{σ} (Section II). From Equation (5-23):

$$\gamma^{\sigma}A = E^{\sigma} - TS^{\sigma} - \sum_{i=1}^{m} \mu_i n_i{}^{\sigma} \qquad \text{Equation (5-28)}$$

Since the Helmholtz free energy is:

$$F^{\sigma} = E^{\sigma} - TS^{\sigma} \qquad \text{Equation (5-29)}$$

Thus,

$$\gamma^{\sigma} = \frac{F^{\sigma}}{A} - \sum_{i=1}^{m} \Gamma_i \mu_i \qquad \text{Equation (5-30)}$$

B. Relative Adsorptions

It is important to note that, in Figure 5-8, in order for the real and model systems to be truly equivalent, the choice of $\sum$ is critical and nonarbitrary. $\sum$ is often called the "surface of tension." Most of the surface excess quantities are very sensitive to the position of the dividing surface. Hence thermodynamic functions have been developed which are invariant with respect to the position of the interface. In the special case of a grain boundary, however, most of the surface excess quantities do not depend on the exact position of $\sum$.

In a multicomponent system, the adsorption of component i is defined by Equation (5-16) as:

$$\Gamma_i \equiv \frac{n_i^{\sigma}}{A} = \frac{1}{A}\,(n_i - n_i' - n_i'') = \frac{1}{A}\,(n_i - C_i'V' - C_i''V'') \qquad \text{Equation (5-31)}$$

Since $V' = V - V''$ [Equation 5-20]

$$\Gamma_i = \frac{1}{A}\,[n_i - C_i'V - (C_i'' - C_i')V''] \qquad \text{Equation (5-32)}$$

Hence for component A:

$$\Gamma_A = \frac{1}{A}\,[n_A - C_A'V - (C_A'' - C_A')V''] \qquad \text{Equation (5-33)}$$

In Equations (5-32) and (5-33) only V'' is dependent on the position of $\sum$. Eliminating it from these two equations:

$$\Gamma_i - \Gamma_A \frac{C_i' - C_i''}{C_A' - C_A''} =$$

$$\frac{1}{A}\left[(n_i - C_i'V) - (n_A - C_A'V)\,\frac{C_i' - C_i''}{C_A' - C_A''}\right] \qquad \text{Equation (5-34)}$$

While both Γ_i and Γ_A depend on the position of $\sum$, their combination as given in the LHS of Equation (5-34) is independent of it and is called the "Relative Adsorption of i with respect to A," Γ_i^A. That is,

$$\Gamma_i^A = \Gamma_i - \Gamma_A \frac{C_i' - C_i''}{C_A' - C_A''} \qquad \text{Equation (5-35)}$$

In other words the Gibbs relative adsorption Γ_i^A is the adsorption of i at the surface when the adsorption of A is zero (i.e., $\Gamma_A = 0$).

In a similar fashion, the relative entropy with respect to A may be written as:

$$S^A = \frac{S^\sigma}{A} - \Gamma_A \frac{S' - S''}{C_A' - C_A''} \qquad \text{Equation (5-36)}$$

where S' and S'' are the entropy densities in phases α and β.

C. Binary Alloys

If A represents the solvent component and B the solute, then in the case of a binary solid solution, for each homogeneous phase on either side of $\sum$, the Gibbs-Duhem equation may be written as:

$$S'dT - dP + C_A'd\mu_A + C_B'd\mu_B = 0 \qquad \text{Equation (5-37)}$$

$$S''dT - dP + C_A''d\mu_A + C_B''d\mu_B = 0 \qquad \text{Equation (5-38)}$$

$$\text{Hence } (S' - S'')dT + (C_A' - C_A'')d\mu_A + (C_B' - C_B'')d\mu_B = 0 \qquad \text{Equation (5-39)}$$

The Gibbs adsorption equation may be written as:

$$d\gamma^\sigma = -\frac{S^\sigma}{A}dT - \Gamma_A d\mu_A - \Gamma_B d\mu_B \qquad \text{Equation (5-40)}$$

Eliminating $d\mu_A$ between Equations (5-39) and (5-40), we obtain:

$$d\gamma^\sigma = -\left[\frac{S^\sigma}{A} - \Gamma_A\left(\frac{S' - S''}{C_A' - C_A''}\right)\right]dT$$

$$-\left[\Gamma_B - \Gamma_A\left(\frac{C_B' - C_B''}{C_A' - C_A''}\right)\right]d\mu_B \qquad \text{Equation (5-41)}$$

or $$d\gamma^{\sigma} = -S^{A}dT - \Gamma_{B}^{A}d\mu_{B} \qquad \text{Equation (5-42)}$$

This is the Gibbs adsorption equation for a binary system in terms of relative adsorptions. It is to be noted that for a weakly segregating solute, the excess entropy term in Equation (5-42) would dominate. For a strongly segregating solute, however, the second term, i.e., $\Gamma_{B}^{A}d\mu_{B}$, would dominate and would cause the interfacial energy to increase with temperature.

For a binary system:

$$\Gamma_{B}^{A} = -\left(\frac{\partial\gamma^{\sigma}}{\partial\mu_{B}}\right)_{T} = -\frac{1}{RT}\left(\frac{\partial\gamma^{\sigma}}{\partial Ln^{a}{}_{B}}\right)_{T} \qquad \text{Equation (5-43)}$$

Hence Γ_{B}^{A} may be obtained from the dependence of the surface tension on the activity of solute B at any given temperature.

From Equation (5-42) the Gibbs adsorption isotherm would be given by:

$$(d\gamma^{\sigma})_{T,P} = -\Gamma_{B}^{A}d\mu_{B} \qquad \text{Equation (5-44)}$$

The following may then be defined with respect to Equation (5-44):

(i) Positive adsorption implies a case where the interfacial tension γ^{σ} decreases with an increase in solute B; for this to be true Γ_{B}^{A} must be positive; i.e.:

$$\Gamma_{B} - \Gamma_{A}\left(\frac{C_{B}' - C_{B}''}{C_{A}' - C_{A}''}\right) > 0$$

or

$$\Gamma_{B}/\Gamma_{A} > \left(\frac{C_{B}' - C_{B}''}{C_{A}' - C_{A}''}\right)$$

(ii) Negative adsorption implies a case where the interfacial tension γ^{σ} increases with an increase in solute B; hence:

$$\Gamma_B/\Gamma_A < \frac{C_B' - C_B''}{C_A' - C_A''}$$

Figure 5-9 schematically depicts three cases: no excess, positive and negative absorption.

V. EXPERIMENTAL METHODS FOR DETERMINATION OF INTERFACIAL AND SURFACE FREE ENERGIES

This section gives a brief account of the different methods for obtaining free energies of interfaces and surfaces. Much more detailed accounts are available in the works of Adamson (Ref. 70) and McLean (Ref. 63).

If a polycrystalline metal is heated to a temperature high enough to ensure atomic mobility, there will be an equilibrium between the interfacial energies of adjoining interfaces. Using virtual work arguments, Smith (Ref. 71) showed that in the case of triple junctions, as in Figure 5-10(*a*), the equilibrium may be represented as:

$$\frac{\lambda_1}{\mathrm{Sin}_{\alpha_1}} = \frac{\lambda_2}{\mathrm{Sin}_{\alpha_2}} = \frac{\lambda_3}{\mathrm{Sin}_{\alpha_3}} \qquad \text{Equation (5-45)}$$

where λ_1, λ_2, and λ_3 are the interfacial free energies (here assumed equal to interfacial tension) and the α's are the dihedral angles between the grain boundaries. This simple situation would prevail for a single phase material.

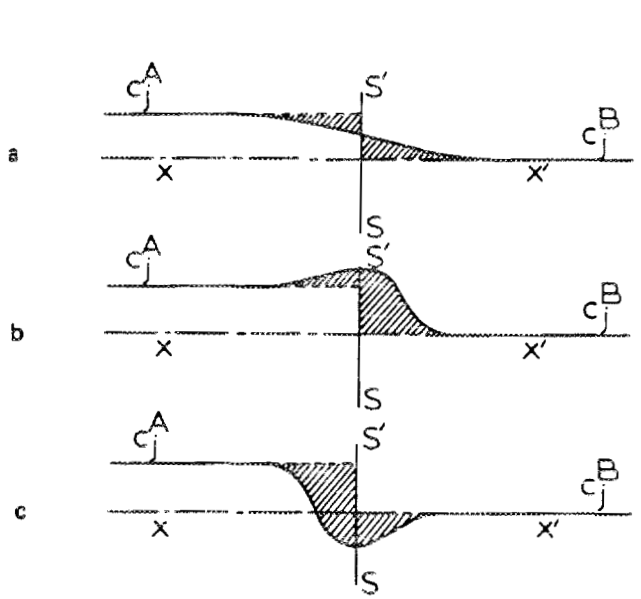

Figure 5-9. Idealized variations in volume concentration, c_j, of the j^{th} component in the general two phase (multicomponent) system for $c_j^A \neq c_j^B$. (*a*) No excess for a symmetric distribution about the dividing surface. (*b*) Effective positive adsorption. (*c*) Effective negative adsorption (Ref. 69).

If a section is made normal to the junction line of the three grains, then the ratios of λ's for the boundaries are obtainable by measurement of the angles (α). Several investigators have used this approach to find the relation between grain boundary tension and the orientation difference between the two grains separated by a boundary (Refs. 71,72,73,74,75,76). By performing a series of experiments where the orientations of two of the grains were held constant while that of the third was varied, the tensions of each grain boundary were extracted.

In the case of a polyphase material, e.g., at a triple junction where two grains of the same phase (α) meet one of another phase (β) as in Figure 5-10(*b*) [a special case of Figure 5-10(*a*)], Smith (Ref. 71) found the following relation:

$$\lambda_1 = 2\lambda_2 \text{ Cos } (^{b}/_{2}) \qquad \text{Equation (5-46)}$$

If a polycrystalline metal sample is heated in a vacuum or suitable atmosphere, the grain boundary and surface free energies are adjusted to equilibrium to produce grooves on the surface as shown in Figure 5-11. In such a case Equation (5-46) becomes:

$$\lambda_{GB} = 2\lambda_S \text{ Cos } (^{\alpha}/_{2}) \qquad \text{Equation (5-47)}$$

Hence this method of "thermal etching" may be employed to find the ratio of grain boundary to surface free energy by measurement of the groove angle α.

The above mentioned methods can be used to find relative boundary tensions. Absolute values of grain boundary tensions have been determined for very specific cases. Thompson (Ref. 77) measured the electrical resistance of steel specimens heat treated to contain very large and very

AC-118

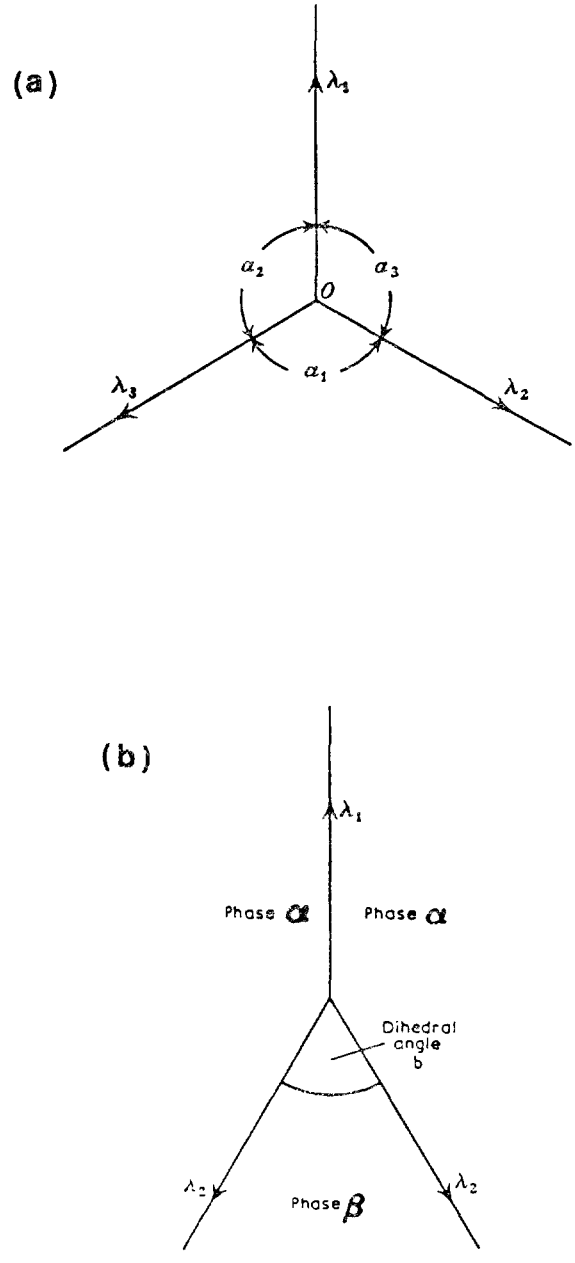

Figure 5-10. (*a*) Junction of three grain boundaries. The junction line is perpendicular to the plane of the paper. (*b*) Junction between grain of phase β and two grains of phase α. The junction line is perpendicular to the plane of the paper (Ref. 63).

AC-119

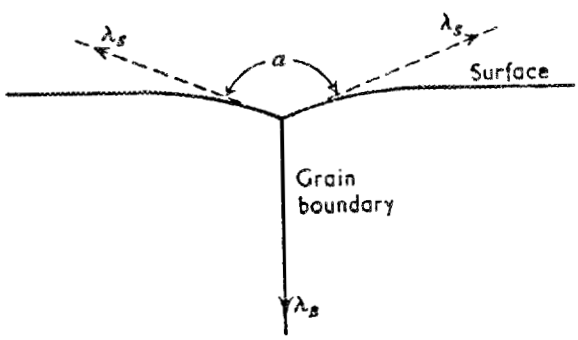

Figure 5-11. Equilibrium between grain boundary and surface free energies (Ref. 63).

small carbide (Fe_3C) particles. The difference in their resistance was used to deduce the difference in carbon solubility between Fe and Fe_3C. This solubility difference was introduced into a thermodynamic formula relating solubility, particle size and interfacial energy to arrive at the value of 1350 ergs/cm^2 for the interfacial energy between Fe and Fe_3C. Fisher, Holloman and Turnbull (Ref. 78) estimated the austenite-martensite interfacial energy (24 ergs/cm^2) from principles of nucleation theory. Hess (Ref. 79) has suggested that grain boundary energy might be determined by measuring the small quantities of energy released during grain growth.

For interfaces other than grain boundaries, several methods have been developed:

(a) The Droplet Method: This can be used in the case of imperfect wetting where Equation (5-45) can be used for the equilibrium of a liquid droplet on a solid surface. This method measures the interfacial energy at the melting point.

(b) The Zero Creep Method: This absolute measurement method applies a virtual work argument to a case where the contraction of a heated foil or thin wire is prevented by the action of weights attached to the sample. Since the experiments are carried out at extremely slow deformation rates there is negligible volume resistance to plastic deformation and only the following four terms need be considered:

(i) Work done by the weight in slightly extending the wire.

(ii) Work done longitudinally against surface tension.

(iii) Work done against surface tension in laterally contracting the specimen.

(iv) Work done by grain boundary tension if the grain boundary area changes.

(c) The Heat of Solution of a Powder: In this method, either the extra heat of solution of a powder over and above that of the same mass of nonporous metal or the difference between the heats of solution of equal masses of powders of different particle sizes is used to find the total surface energy. If the total area of powder surface is known, then the specific surface energy can be easily found.

(d) The EMF of a Powder: This method relies on the fact that surface free energy leads to higher electrode potential for a powder than for the same material in bulk form. Hence an experimentally determined difference in emf P can be used to find the surface free energy γ_s (Ref. 63):

$$\gamma_s = \frac{Pvfr}{2V} \qquad \text{Equation (5-48)}$$

where

r = Radius of particles

f = Faraday constant

v = Valency

V = Volume per mole.

Most of these experiments are difficult to perform and are very specific in application.

CHAPTER 6

INTERGRANULAR FRACTURE

I. EFFECT OF SEGREGATION ON GRAIN BOUNDARY COHESION

The cohesive energy of grain boundary, ϕ_c, is defined as the energy required to reversibly separate the two adjacent grains to form free surfaces (Ref. 62). Since two free surfaces are created due to the destruction of a single boundary, as depicted in Figure 6-1, it follows that:

$$\phi_c = 2 F_s - F_b \qquad \text{Equation (6-1)}$$

where

F_s = Specific surface energy

F_b = Specific grain boundary energy.

Note that here interfacial tension and specific energies are assumed equal. As indicated by Equation (5-44) both F_s and F_b depend on Γ_B^A; hence the cohesive energy of grain boundaries is related to solute segregation.

Consider a bicrystal with a planar grain boundary normal to the tensile axis, with the atoms in the two crystals initially at a mean equilibrium separation δ_o. Let the two crystals be isothermally and reversibly extended at constant pressure and with no change in the number of atoms. Then the mean free energy change as a function of separation from δ_o to δ_∞ is as shown in Figure 6-2(*a*) (Ref. 80). The cohesive energy of a grain boundary, ϕ_c, is then the net work per unit area or $\Delta G/A$ with reference to Figure 6-2(*a*). The slope of the G vs δ curve is the normal

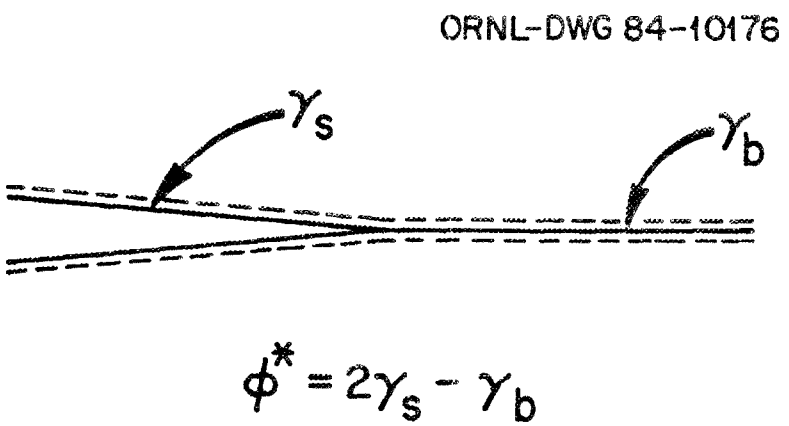

Figure 6-1. Grain boundary cohesive energy, ϕ_c, required for propagation of a crack along a solute segregated boundary (Ref. 41).

AC-120

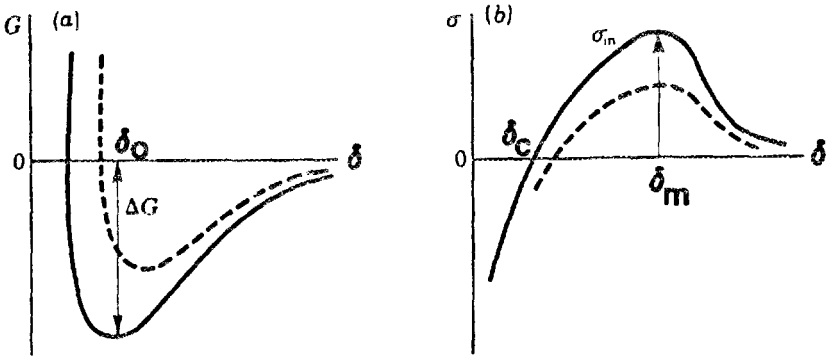

Figure 6-2. (*a*) Free energy-separation diagram for a grain boundary uniformly separating along its boundary plane. (*b*) Corresponding normal stress-separation diagram. Broken lines represent changes with solute adsorption (Ref. 80).

force required for extension and gives the stress vs displacement curve of Figure 6-2(*b*) when normalized to unit area.

Hence

$$\phi_c = \int_{\delta_o}^{\delta_\infty} \sigma \, d\delta = 2F_s - F_b \qquad \text{Equation (6-2)}$$

The cohesive stress, σ_c, of a grain boundary is the maximum force per unit area required to uniformly separate two adjacent grains along their common boundary (Ref. 62). It would seem that measurement of σ_c would then be a simple matter, for Equation (6-2) would be valid for a uniformly separating grain boundary. This measurement is rendered impossible because such a separation is impossible in reality. Orowan (Ref. 81) assumed:

(a) Sinusoidal σ vs δ curve, and

(b) Identical grain boundary and bulk elastic moduli to arrive at a cohesive σ_{co}:

$$\sigma_{co} = \frac{[E \, \phi_c^*]^{1/2}}{2 \, \delta_o} \qquad \text{Equation (6-3)}$$

In Equation (6-3), ϕ_c^* is the cohesive energy modified to reflect the fact that during brittle intergranular fracture the specific surface energy of the rapidly created free surfaces (F_s^*) is not equal to the equilibrium value of F_s. The limitations of Orowan's expression (Equation 6-3) have been noted (Ref. 62); however, a superior expression has yet to arrive.

As has been discussed by Rice (Ref. 82), the normal stress can be expressed as a function either of:

(a) Boundary displacement (δ) and boundary composition (in terms of interfacial concentration excess, Γ); i.e.:

$$\sigma = \bar{\sigma}\ (\delta, \Gamma) \qquad \text{Equation (6-4)}$$

or

(b) Boundary displacement (δ) and boundary potential (μ); i.e.:

$$\sigma = \hat{\sigma}\ (\delta, \mu) \qquad \text{Equation (6-5)}$$

Since both Γ and μ vary with δ there will be two limiting cases (Ref. 82):

(a) Separation at constant Γ – the two crystals separate at a rate such that further matter transport to the interface is precluded (i.e., a "fast" separation).

(b) Separation at constant μ – the two crystals separate at a rate that allows complete compositional equilibrium between the interface and a matter source at constant potential (i.e., a "slow" separation).

Our interest here is in the problem of brittle intergranular fracture, and several authors (Refs. 62,80,83,84) have pointed out that under this condition the crack propagates along the boundary so rapidly that there is no time for compositional equilibration and case (a) is the applicable limiting case. Hence in the following discussion it will be assumed that σ can be treated as a function of interface composition Γ and displacement (δ), i.e.:

$$\sigma = \bar{\sigma}\ (\delta, \Gamma) \qquad \text{Equation (6-4)}$$

Figure 6-3 (Ref. 58) shows concentration profiles across a grain boundary in a binary A-B system. The grain boundary solute adsorption Γ_B^A is the shaded area under the C_B vs Z curve of Figure 6-3(*a*). In our case of a very rapid grain boundary crack growth, the fracture surface created "inherits" an adsorption level that is one half that for the grain

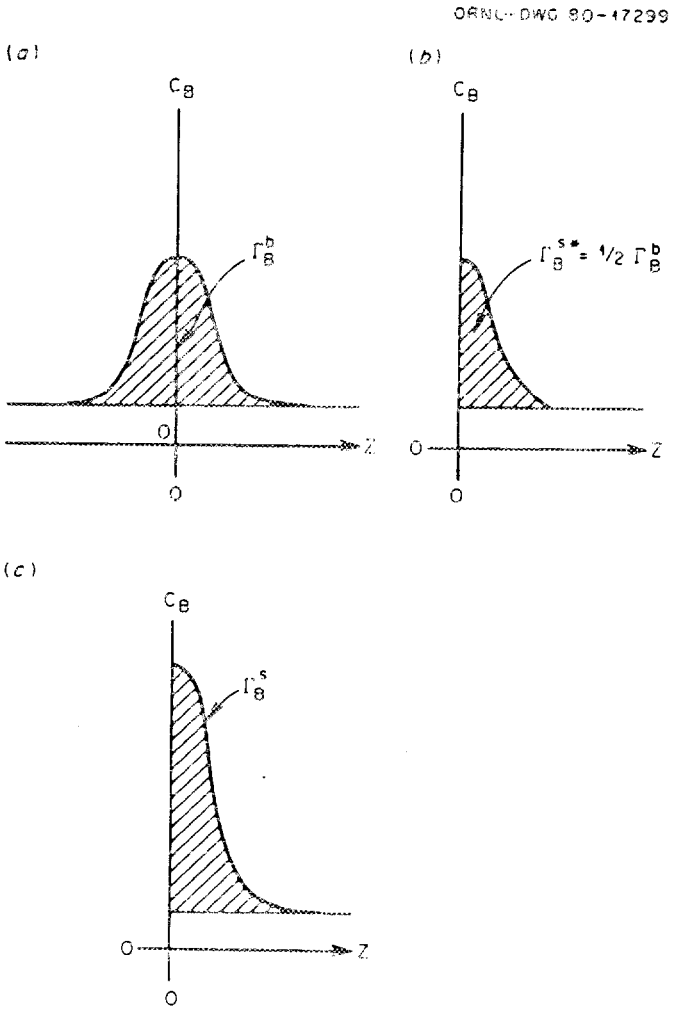

Figure 6-3. Composition, C_B, vs distance, Z, profiles across (*a*) a grain boundary, (*b*) a free surface created by rapid fracture of the grain boundary in (*a*), and (*c*) a free surface created by equilibrium separation of the bulk concentration, C_B, such that $\Gamma_B^S = (1/2)\Gamma_B^b$ (Ref. 62).

boundary, i.e., $\Gamma_B^{S^*} = \frac{1}{2}\Gamma_B^b$ as shown in Figure 6-3(*b*), a nonequilibrium level.

If the crack were in equilibrium, the effect of segregation on the surface energy F would be given by the Gibbs adsorption isotherm (Equation 5-44).

$$dF_s = -\left[\Gamma_B^s - \frac{X_B}{X_A}\Gamma_A^s\right]d\mu_B \qquad \text{Equation (6-5)}$$

However, the crack is NOT under equilibrium and hence the surface energy F_s^* and ϕ^* will be given by an expression originally formulated by Rice (Ref. 82) and later clarified by others (Refs. 80,83,84). This expression is (Equation 10 in Ref. 82):

$$\frac{d\phi^*}{d\Gamma_B^b} = \mu_B^S\left(\Gamma_{\frac{B}{2}}^b\right) - \mu_B^b\left(\Gamma_B^b\right) \qquad \text{Equation (6-6)}$$

where μ_B^b = Solute chemical potential as a function of equilibrium grain boundary excess Γ_B^b - shown as solid curves in Figure 6-4.

μ_B^S = Solute chemical potential as a function of equilibrium surface excess Γ_B^S – this is evaluated at $\Gamma_B^S = 1/2\ \Gamma_B^b$ – shown as dashed curves in Figure 6-4.

Hence $\mu_B^S\left(\Gamma_B^b/_2\right)$ is the solute chemical potential that would result in an equilibrium surface excess equal to half the grain boundary excess for the grain boundary that is actually undergoing fracture.

It follows from Equation (6-6) that if the right-hand side of the equation is negative then the solute segregation will decrease ϕ^*, i.e., the solute will promote intergranular cracking. This can happen as shown

in Figure 6-4(*a*) where the solute segregates more strongly to free surfaces than to grain boundaries. Here the grain boundary concentration of solute at equilibrium is $\Gamma^{b'}$; corresponding to this the chemical potential is $\mu_B{}^b\left(\Gamma^{b'}\right)$. The rapidly formed crack surface inherits a composition of $\Gamma^{s'} = \Gamma^{b'}/_2$ whence the chemical potential is $\mu_B{}^S\left(\Gamma^{b'}/_2\right)$ as shown. Hence Equation (6-6) yields a negative $d\phi^*/_d\Gamma_B{}^b$ in this case. This has been observed for sulphur in Ni_3Al with the qualitative observations agreeing with the predictions (Ref. 41).

In his original paper, Rice (Ref. 82) allowed for the possibility of the reverse effect, i.e., the case where a solute segregates more strongly to a grain boundary than to a free surface. Such a situation is depicted in Figure 6-4(*b*). Following a reasoning as given above it is easy to see that a fast crack propagation approximation leads to a POSITIVE $d\phi^*/_d\Gamma^b$ value, i.e., the segregation of solute enhances grain boundary cohesiveness. Indeed, boron has been observed to show this effect in Ni_3Al (Ref. 41).

Two points need to be clarified. The first is that $\Gamma^b > \Gamma^S$ is a necessary but not sufficient criterion for a positive $d\phi^*/_d\Gamma^b$; for if Γ^S is only slightly below Γ^b in Figure 6-4(*b*) there is still the possibility of a negative $d\phi^*/_d\Gamma^b$. Using the simplifying assumptions of Γ^b and Γ^S being linearly proportional to solute atom fraction and the solute obeying Henry's law, it can be shown that the condition for positive $d\phi^*/_d\Gamma^b$ is $\Gamma^b > \Gamma^S$.

The second, which is of general interest but does not bear directly on the present discussion, is that had the crack opened up and propagated

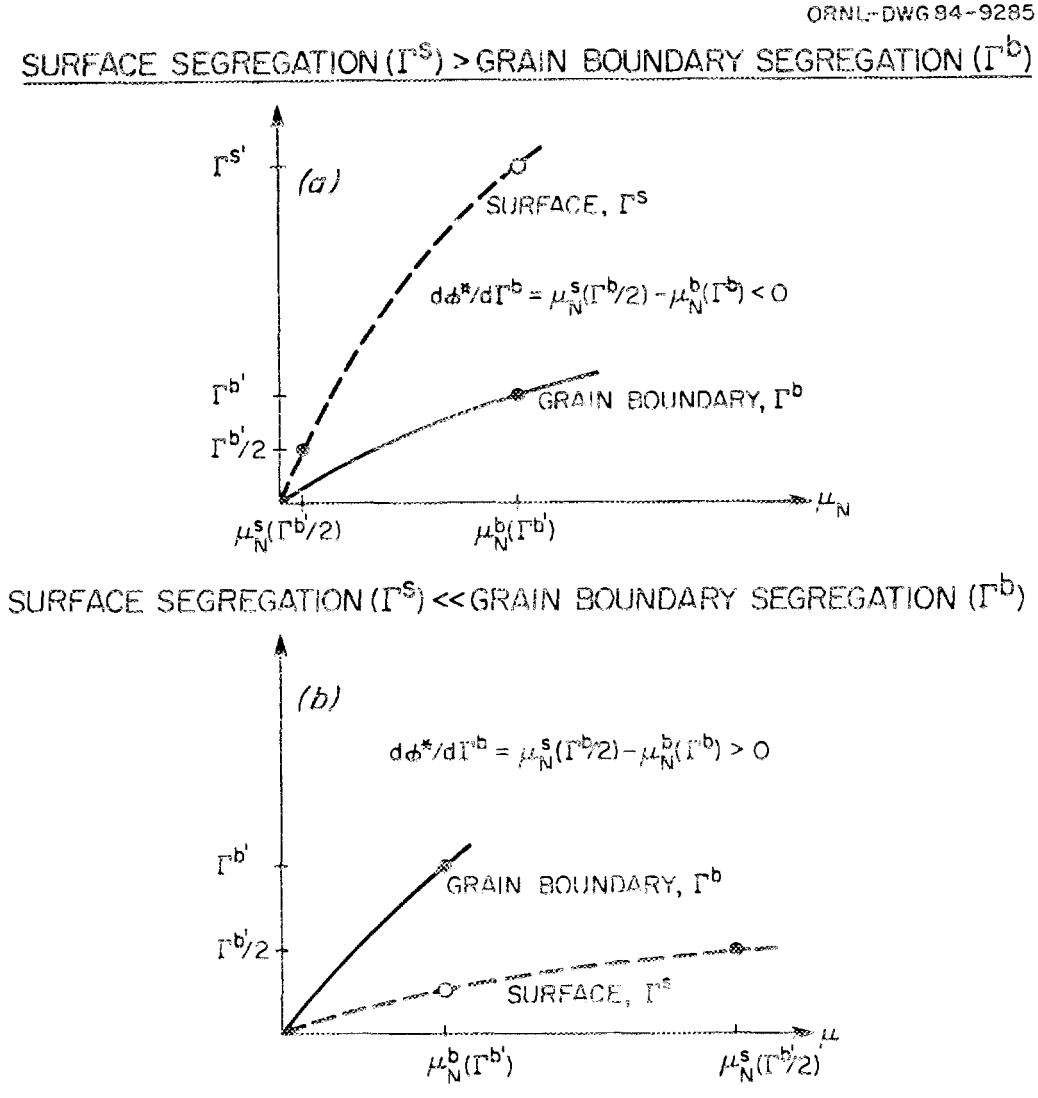

Figure 6-4. A schematic diagram showing the effect of solute segregation on the solute chemical potential of free (cavity) surfaces, μ_N^S, and grain boundaries, μ_N^b, for two types of solutes. (*a*) The the solute has a strong tendency to segregate to grain boundaries but not to free surfaces, and (*b*) the solute tends to segregate more strongly to free surfaces than to grain boundaries (Ref. 41).

under equilibrium conditions, then the C_B vs Z curve would have been that depicted in Figure 6-3(c). In such a case Figure 6-4(a) shows:

$$\mu_B = \mu_B{}^b\left(\int^{b'}\right) = \mu_B{}^S\left(\int^{S'}\right) \qquad \text{Equation (6-7)}$$

II. BRITTLE FRACTURE AND THE GRIFFITH CRITERION

Using any energy balance, Griffith (Ref. 85) derived a necessary condition for the propagation of an unstable crack in an isotropic, homogeneous, linearly elastic continuum having a sharp elliptical crack of half length, a, and a normal uniformly applied stress, σ_A, as shown in Figure 6-5. According to Griffith, the crack will propagate for an applied stress $\sigma_A > \sigma_{AG}{}^*$ where:

$$\sigma_{AG}{}^* = \left[\frac{2\ \Phi_C{}^*\ E}{\pi a\ (1-\nu^2)}\right]^{1/2} \qquad \text{Equation (6-8)}$$

where

ν = Poisson's ratio

$\sigma_{AG}{}^*$ = Critical stress derived by Griffith (Ref. 85).

In principle, Equation (6-8) yields an expression for $\phi_C{}^*$; as per some reports discussed in Ref. 62, some experimental results bear out such an expression. The Griffith criterion, however, is not a sufficient criterion since it neglects the detailed mechanisms of interatomic separations at the cracktip; such separations require local crack tip stresses in excess of σ_C (Section I). With reference to Figure 6-5, Inglis (Ref. 86) estimated the local tensile stress $\sigma_{yy}(\rho)$ at the tip of an elliptical crack of tip radius ρ as:

$$\sigma_{yy}(\rho) = \sigma_A\ (a/\rho)^{1/2} \qquad \text{Equation (6-9)}$$

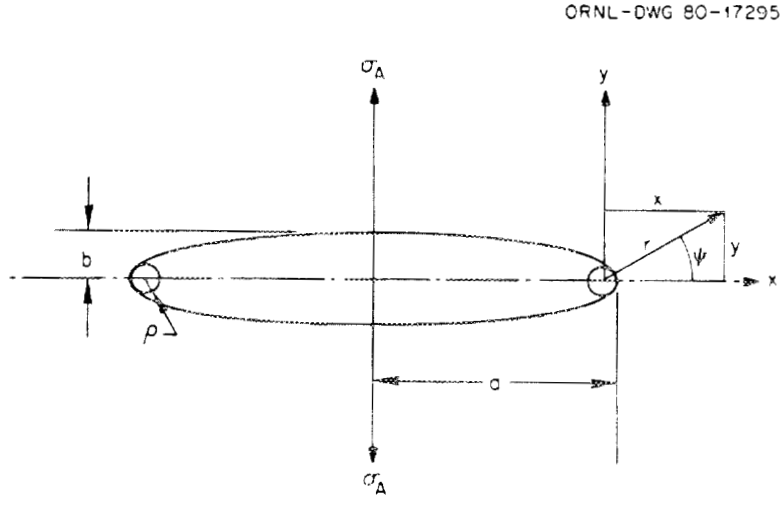

Figure 6-5. Schematic of an elliptical, Griffith type crack (Ref. 62).

Hence the critical applied stress σ_{AC}^* at which $\sigma_{yy}(\rho) = \sigma_C$ is

$$\sigma_{AC}^* = (\rho/a)^{1/2} \qquad \text{Equation (6-10)}$$

Substituting the Orowan expression of Equation (6-3) one gets:

$$\sigma_{AC}^* = \left[\left(\frac{E\phi_C^*}{a}\right)\left(\rho/_{2\delta_o}\right)\right]^{1/2} \qquad \text{Equation (6-11)}$$

Comparison of Equations (6-8) and (6-11) shows that $\sigma_{AG}^* \simeq \sigma_{AC}^*$ when $\rho \cong \delta_o$, i.e., the crack must be atomically sharp.

An implicit assumption in the previous discussions is linear elastic behavior of the material surrounding the crack tip; as shown in Figure 6-2(*b*) the material behaves nonlinearly at stresses on the order of σ_C. Such nonlinearity of interatomic forces has been treated by Barenblatt (Ref. 87) who considered the crack plane to be divided into three regions as shown in Figure 6-6:

(a) A linearly elastic region away from the crack tip.

(b) A "cohesive" region where interatomic forces are large and nonlinear.

(c) The free surface region where the crack is completely separated into noninteracting free surfaces.

His conclusion was that the nonlinearity of interatomic attractions does not severely detract from the Griffith criterion when the cohesive region is small compared to the total crack length.

The Griffith theory and Barenblatt's extension of it are the result of continuum considerations and predict that the crack is stable at a single stress value above which it propagates catastrophically and below which the crack heals. In contrast to this, the treatment of Thomson et al. (Refs. 84,85) regards the discrete nature of the lattice through which the crack propagates. Such a treatment yields the phenomena

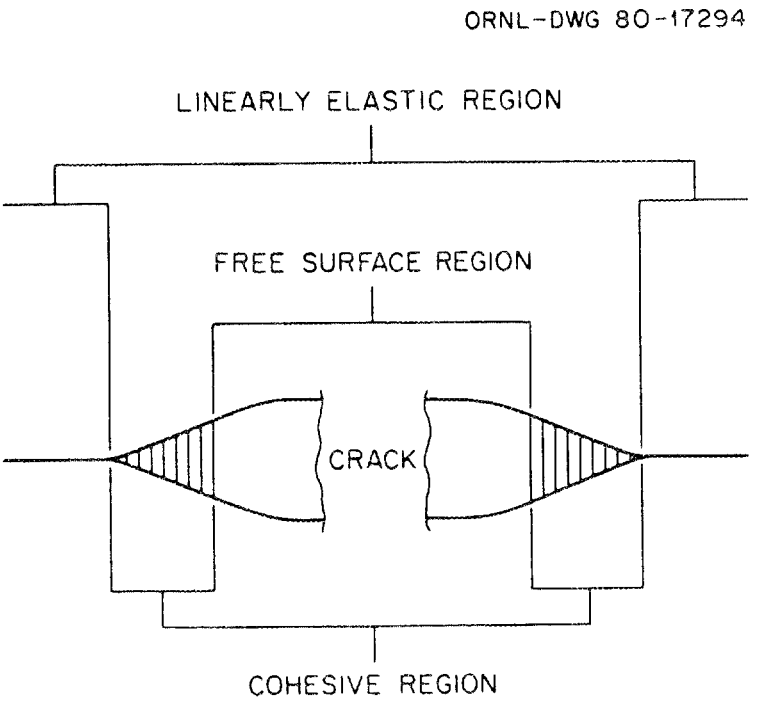

Figure 6-6. Schematic of a Barenblatt type crack (Ref. 62).

of "lattice trapping," the terminology accruing from the fact that the crack is trapped at a single lattice position over a range of stresses comparable to the Griffith critical stress given by Equation (6-8). This leads to the conclusion that in a discrete lattice the propagation of a brittle crack might require stresses significantly in excess of σ_{AG}^* of Equation (6-8). Without delving into the mathematical details of the approach, the following major points are of interest here:

(a) As in the Griffith approach, the equilibrium critical stresses are inversely proportional to the square root of the crack half length.

(b) The surface energy term in the Griffith expression ϕ_c^*, Equation (6-8), is a thermodynamic surface energy team as shown in Equation (6-1).

(c) It is to be noted that in Thomson et al.'s formulation both the surface energy term and the degree of lattice trapping are a strong function (both are complicated analytical functions) of the width of the "cohesive region" of Barenblatt's formulation.

(d) From Thomson et al.'s approach, unlike Griffith's, two discrete values of critical stress can be extracted: one is a "crack opening" function while the other is a "healing" function. Both of these are monotonically increasing functions of crack length. Corresponding to these notions, there are two values of the surface energy term, one for crack opening (γ_+) and the other for healing (γ_-), their ratio being $\gamma_+/\gamma_- \simeq 5.76$. These authors point out that these surface energy terms bear no simple relation to

the thermodynamic surface energy although the latter is intermediate between γ_+ and γ_-.

It may then be concluded that segregation can affect brittle crack propagation in three ways:

(a) A decrease in ϕ_c^* leading to enhanced brittleness; however this is not the sole explanation.

(b) Changes in σ_c influencing σ_{AC}^*.

(c) Lattice trapping effects.

III. NEARLY BRITTLE GRAIN BOUNDARY CRACKS

At temperatures significantly above absolute zero, fracture always involves some degree of plastic deformation, the extent depending on temperature, strain rate and material. Figure 6-7 shows the main features associated with crack tip plasticity. This kind of plasticity has three effects:

(a) The mechanical work expended in plastic work lowers the elastic strain energy available for bond breakage.

(b) The stress intensity is lowered, which raises the stress required for $\sigma_{AG}^* > \sigma_c$. This is referred to as crack blunting.

(c) The possibility of spontaneous crack healing is completely obviated.

Orowan (Refs. 81,90) and Irwin (Ref. 91) postulated a fracture energy, ϕ_f, related to the fracture stress σ_{AO}^* (for nearly brittle crack propagation):

$$\sigma_{AO}^* = \left[\frac{2\phi_f^* E}{\pi a (1-\nu^2)}\right]^{1/2} \qquad \text{Equation (6-12)}$$

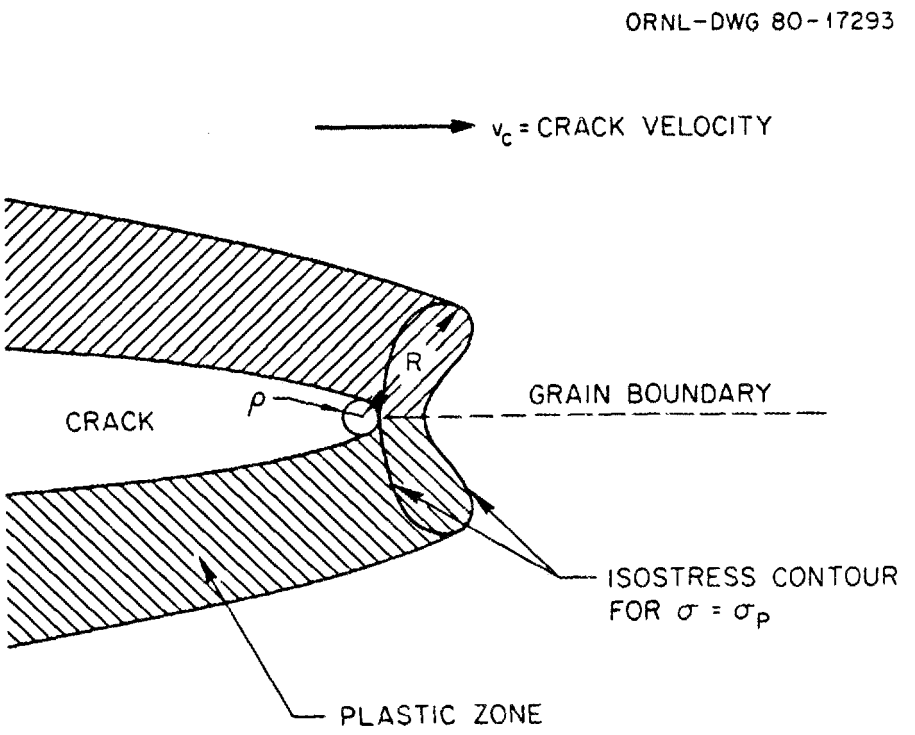

Figure 6-7. Schematic of the plastic deformation associated with a propagating grain boundary crack (Ref. 62).

or $$\phi_f = \frac{(\sigma_{AO}^*)^2 \pi a (1-\nu^2)}{2E}$$ Equation (6-13)

where $\phi_f = \phi_c^* + \phi_p$

and ϕ_p = plastic work per unit area.

It has been suggested by McLean (Ref. 92) that ϕ_c^* acts as a kind of "valve" controlling ϕ_p, i.e., segregation affects ϕ_c^* and hence ϕ_p because $\phi_f = \phi_c^* + \phi_p$.

The blunting effect of dislocation emission or adsorption from the crack tip results in an increase of the crack tip radius and hence lowering of the stress intensity. It is unlikely that the extremely thin segregated regions at grain boundaries can affect the internal sources of dislocations, i.e., sources within the grain but close enough to the boundary to be activated as the crack tip stress field passes by. Per contra, segregation might affect dislocation generation AT the crack tip.

IV. ATOMIC BONDING

Whereas most of the previous discussions have dealt with a classical thermodynamical approach to the intergranular brittleness problem, a rather recent development has been the introduction of quantum mechanical approaches.

Losch (Ref. 93) suggested that since the grain boundary represents a strong perturbation of the lattice periodicity, the nature of the interatomic bonding at the interface ought to be significantly altered by the presence of segregants at the grain boundary. He assumed that impurity segregated grain boundary surfaces are adequately represented by a free

surface model with localized electron states and hence surface chemisorption models can be utilized for similar grain boundary problems. As an example, the theoretical model for sulphur chemisorbed on nickel indicates a predominance of S(3p) - Ni(4s) type covalent unidirectional bonds as opposed to Ni(4s) - Ni(4s) type metallic bonds. Since covalency implies very rigid localized directional orbitals, such bonding shows unexpectedly high inelasticity against deformation and such a bonding normally fractures by cleavage. Indeed such a covalently bonded, two-dimensional phase can be formed at the grain boundary due to the presence of less than a monolayer of impurities (Ref. 94). Although the S(3p) - Ni(4s) bonds are very strong there is a concomitant weakening of the neighboring Ni(4s) - Ni(4s) bonds, and this further contributes to the enhanced probability of intergranular fracture.

A series of papers by Briant and Messmer (Refs. 95,96,97,98) have addressed the question of details of electronic effects in bond strength reduction due to segregation. In their approach, they use a cluster of atoms representation of the local environment at the grain boundary. Depending on the situation, the cluster could either be a simple Bernal Tetrahedra or a tetragonal dodecahedron. Molecular orbital theory is used to solve for the electronic structure of the cluster of atoms.

These authors make the following observations:

(a) Embrittling elements are often from groups IV to VI of the periodic table.

(b) Impurities which are more electronegative with respect to their transition metal hosts (i.e., as one moves from group IV to VI there are more potent embrittlers).

(c) For a given electronegativity, a larger atom is a more potent embrittler than a smaller one.

In accordance with these observations, they reach conclusions similar to Losch (Ref. 93) in that the formation of Ni-S bonds weakens the Ni-Ni bonds; hence the stress required for fracture is lowered. A similar argument holds for S in Fe. In contrast, B in Ni forms a covalent bond and there is no drawing out of charge from Ni; this enhances cohesion at the boundary. They suggest that C and P are "benign" elements in Fe; the observation that C improves brittleness follows from the fact that C most probably displaces S from the grain boundary. These authors have also extended their work to include ternary systems and to explain the effects of Sb on Fe, Ni and Cr.

One of the limitations of Briant and Messmer's approach is that they have not allowed for relaxation of the clusters in their calculations.

CHAPTER 7

AUGER ELECTRON SPECTROSCOPY

I. BACKGROUND

In 1923, Auger (Ref. 99) experimentally observed that upon photoexcitation an atom emits not only the expected photoelectrons but also electrons emitted due to a radiationless transition inside the atom. It was also realized that such transitions were characterized by energies dependent upon the element. However, Auger's experiments were conducted in a cloud chamber and an "Auger spectrum" was not obtained.

While the existence of Auger transitions was known for a number of years, the application of these as a viable research tool had to await the development of two important ancilliary fields: ultrahigh vacuum technology and electron spectrometers of sufficient sensitivity and reliability to detect these transitions.

When a primary electron beam of energy E_p impinges on a surface, the resultant distribution of emitted electrons is shown schematically in Figure 7-1. Such a distribution curve has three regions:

Region 1: At the very low energy range are the "true secondary electrons" ejected due to inelastic collisions between primary and bound electrons. Since the energy transferred in such collisions is very small, there is copious evolution of such electrons.

Region 2: At the medium energy range is a smooth background on which are small peaks caused by Auger electron emissions and the characteristic

AC-121

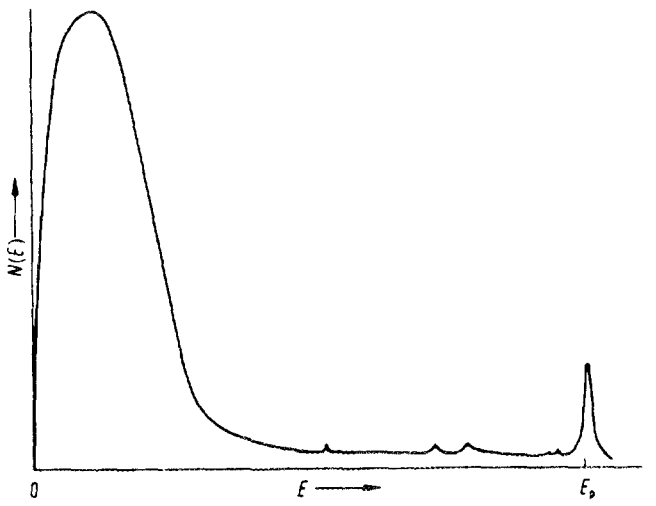

Figure 7-1. Energy distribution N(E) of back-scattered slow electrons as a function of their energy. E_p is the energy of the primary electrons (Ref. 100).

energy losses which are utilized for Electron Energy Loss Spectroscopy (EELS).

Region 3: A small fraction of primary electrons are elastically back scattered. In detecting this peak, its width is determined by the energy spread of the primary beam and the limited resolution of the energy analyser. These electrons can be used for Low Energy Electron Diffraction (LEED) if E_p is small and the specimen is a single crystal.

As can be seen, it is difficult to characterize Auger energies from the N(E) vs E curves because the Auger transitions are such small peaks on the broad background. Discussions in Section III will show the development of electron spectrometers to detect these transitions.

Whereas a primary beam of electrons of several KeV can penetrate a surface to a considerable depth, most elements exhibit principal Auger transition energies between 50 and 2000 eV. Electrons of such energies can travel only a few atomic distances in a solid before undergoing inelastic scattering. Hence, although Auger electrons may be generated quite deep under the surface (typically 1 μm), only those from within a few atomic layers of the sample surface escape with the characteristic Auger energy. The precise escape depth depends upon the energy of the electron and the matrix through which the electron must pass to escape from the surface, and thus varies between elements and between the various Auger transitions associated with each element. The depth of analysis (or electron escape depth) is given by λ_M (E) is the Inelastic Mean Free Path (IMFP) of electrons with energy E, in the sample matrix M, and θ is the angle between the surface normal and the escaping electron (i.e., between the surface normal and the axis of the entrance aperture of the electron

detection system) (Ref. 101). The IMFP is a parameter defined by the statistical process of electron scattering, being the characteristic length of an exponential decay; only 37% of the unscattered Auger electrons therefore derive from depths greater than $\lambda_M(E)$.

It is the shortness of the IMFP that makes AES such a surface sensitive technique. Seah and Dench (Ref. 102) have given an empirical relation obtained from a best fit curve of all available data (shown on Figure 7-2):

$$\lambda_M(E) \approx \frac{538}{E^2} + 0.42\sqrt{aE} \text{ atomic layers} \qquad \text{Equation (7-1)}$$

where E is the electron energy in eV and a (nm) is the atomic size calculated from tabulated bulk densities ρ (kg/m^3), Avogadro's number N_A and the atomic weight A by:

$$\rho N_A a^3 = 10^{24} A \qquad \text{Equation (7-2)}$$

Within the energy range appropriate to Auger electrons, the IMFP and hence the "depth of analysis" lies between 2 and 10 atomic layers.

Figure 7-3 schematically shows the depths of backscattered and Auger electron emission while Figure 7-4 schematically shows the regimes of surface, thin film and bulk analyses.

Since AES is a surface sensitive technique, it is imperative to ensure that the surface being analysed remains unaltered in the course of the analysis – which often takes a few hours. Using the kinetic theory of gases, Ertl and Kuppers (Ref. 100) have shown that the number of particles, $\dot{n}_S$, striking a surface of 1 cm^2 in 1 second is given by:

$$\dot{n}_S \approx 3.5 \times 10^{22} \frac{P}{\sqrt{MT}} \text{ (Cm}^{-2}\text{ S}^{-1}\text{)} \qquad \text{Equation (7-3)}$$

AC-122

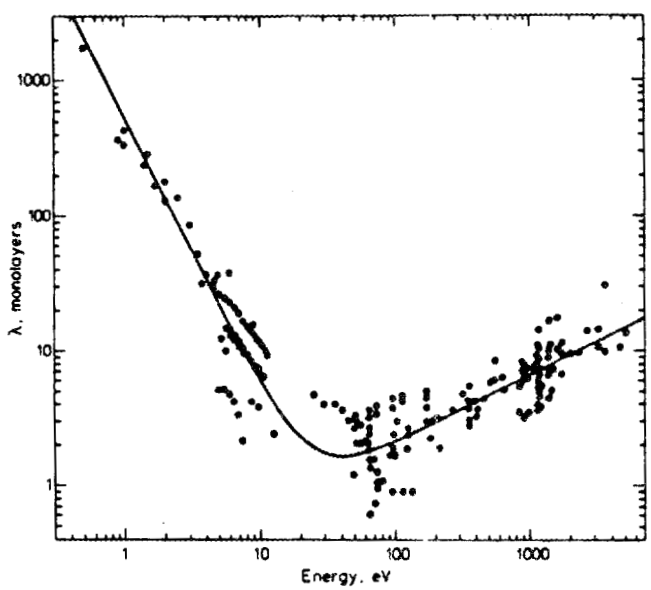

Figure 7-2. Experimental measurements of inelastic mean free path $\gamma(E)$ for pure elements (Ref. 102).

AC-123

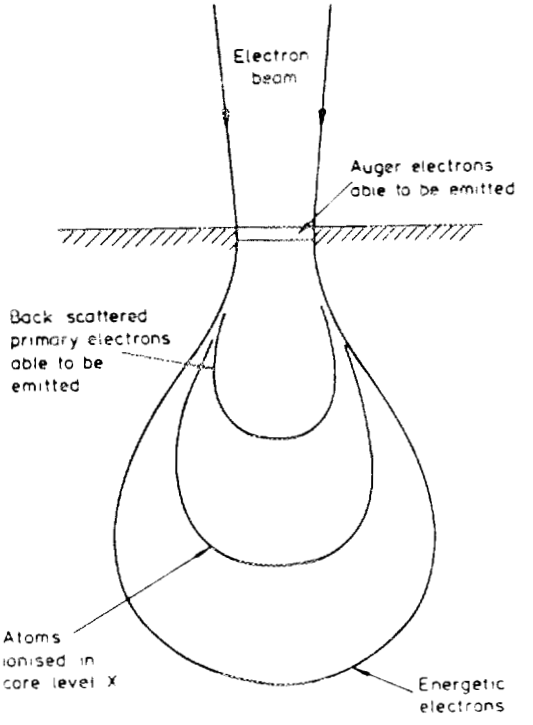

Figure 7-3. Schematic representation of electron scattering in AES (Ref. 102).

AC-124

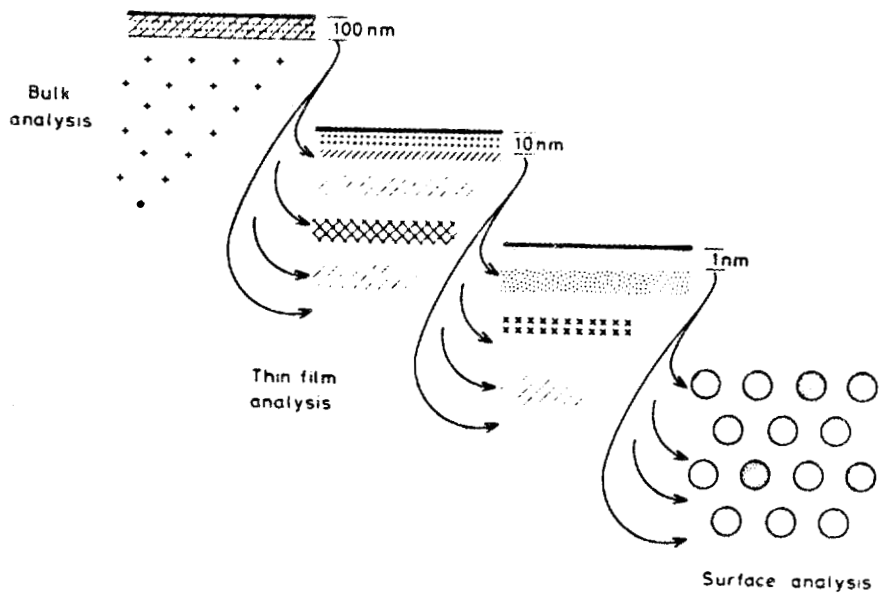

Figure 7-4. The regions of surface analysis, thin film analysis and bulk analysis (Ref. 103).

where T = Absolute temperature (K)

P = Gas pressure in Torr

M = Molecular Weight.

If it is assumed (as an example) that the number of particles required for a monolayer of coverage of the surface is $\sim 3 \times 10^{14}$ particles/cm^2, then at T = 300 K (room temperature), assuming an average M = 28, Equation (7-3) yields:

$$\dot{n}_S \simeq 10^6 . P \text{ [monolayers } S^{-1}\text{]} \qquad \text{Equation (7-4)}$$

Hence at a pressure of 10^{-6} Torr, the number of particles which are necessary for the buildup of a monolayer is offered to a surface every second.

The time of coverage, τ, is given by:

$$\tau = \frac{1}{\dot{n}_S . S} \simeq \frac{10^{-6}}{S . P} \text{ (S/monolayer)} \qquad \text{Equation (7-5)}$$

where S = the probability that an impinging particle becomes absorbed; frequently this is unity.

It can be seen from Equation (7-5) that, in order to get at least one hour before the "clean" surface gets covered by a monolayer of species from the surrounding atmosphere, it is necessary to reduce the pressure to the range of 10^{-10} Torr. This necessitates the use of Ultra High Vacuum (UHV) techniques in AES.

It is because of the above mentioned point that the development of AES as a surface analysis tool was delayed. The inception of UHV can be dated back to 1950 (Ref. 105). Prior to that, methods had been continually improved to a state where about 10^{-8} Torr could be attained by

about the mid 1940's. However, it appeared that further refinements in vacuum technique were unable to achieve any lower pressure. In 1947 Wayne B. Nottingham of MIT suggested that the "10^{-8} barrier" was one of measurement rather than pumping. The standard ion gauge in use during the 1940's (Figure 7-5) consisted of a hot wire cathode surrounded by a positively charged grid which in turn was enclosed in an ion collecting shell. Electrons emitted by the cathode were accelerated towards the grid. Such accelerated electrons ionized the gas in the gauge. These positive ions moved to the negatively charged collector generating a collector current. Since the number of ions generated depends on the pressure, so did the collector current. Nottingham realized that electrons bombarding the grid produced low energy X rays. These X rays led to photoemission of electrons from the collector and thus a current in it. His calculations showed this irreducible current corresponded to a pressure of about 10^{-8} Torr.

A couple of years later, Robert T. Bayard and Daniel Alpert (Ref. 106) hit on a simple modification of the ion gauge that not only extended the lower pressure limits of operation on ion gauges but also proved the correctness of Nottingham's analysis. In this modification (Ref. 106) they switched the positions of the cathode and the ion collector. In the Bayard-Alpert gauge as shown in Figure 7-6, the cathode consists of a heated wire outside the grid, and the collector is a thin wire running down the axis of the instrument. While it still picks up most of the positive ions, very little X-radiation is intercepted by the collector by virtue of its greatly reduced surface area. Bayard and Alpert were able to show that the residual current is equivalent to a pressure of

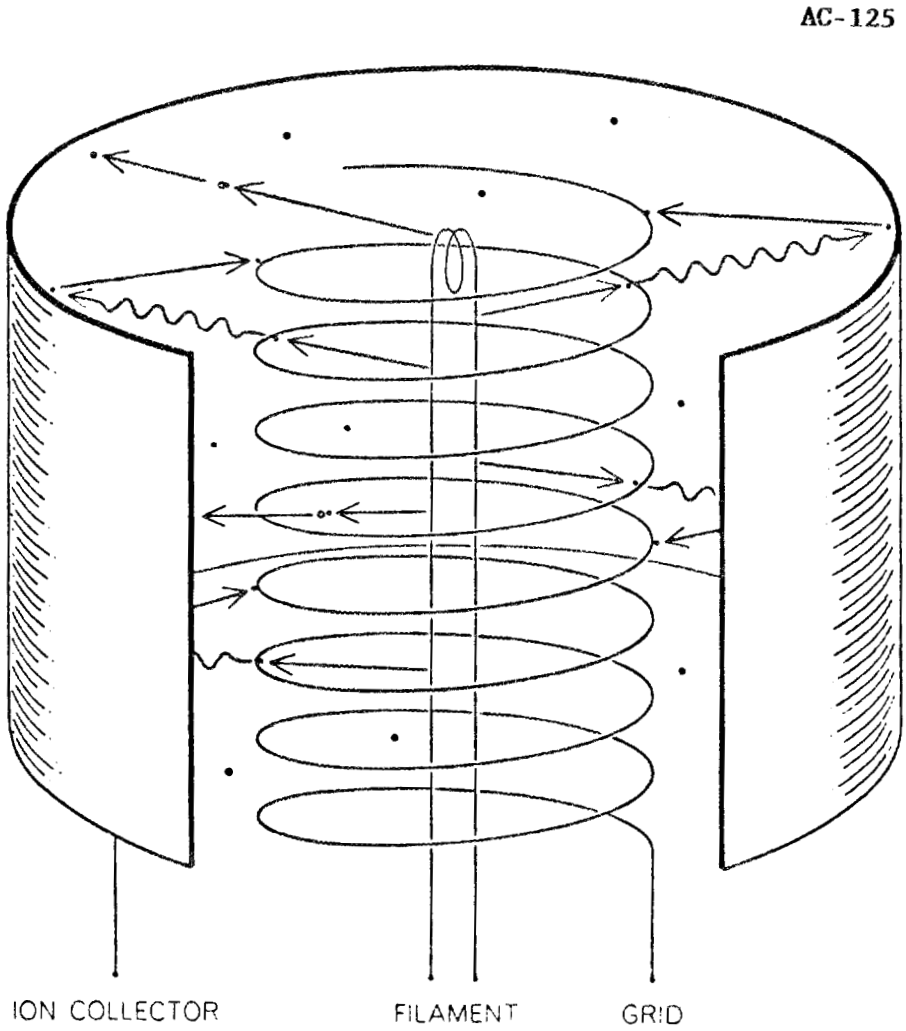

Figure 7-5. X ray problem made it impossible for early ion gauges to register below 10^{-8} Torr. Electrons from the filament created positive ions (dark dots) that struck the collector and were counted. But electrons reaching the grid produced X rays (wavy arrows). When the X rays struck the large-area collector, they liberated electrons, causing a photoelectric current that could not be distinguished from the current resulting from ion impact (Ref. 105).

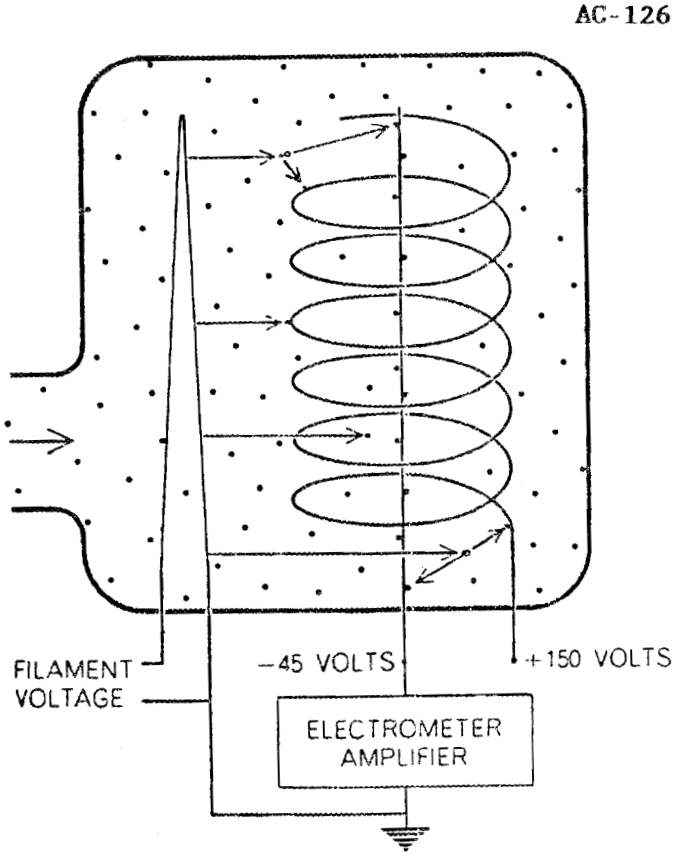

Figure 7-6. Bayard-Alpert gauge avoided the X ray problem by putting the heated filament cathode outside the grid and making the collector a thin axial wire. The negatively charged collector still gathers positive ions, but because of its small area it intercepts fewer X rays and therefore emits a smaller photoelectric current (Ref. 105).

about 10^{-11} Torr. It is also notable that this gauge also has a pumping action since the ions reaching the collector are trapped and removed from the vacuum chamber.

While this breakthrough was the single most important event which brought UHV into its own, it certainly was not the only one. Significant progress in UHV technology has been made in both pumping systems and in monitoring the low pressures attained. A brief account of some UHV pumps is given in Section VII.

In addition to being an effective tool for a number of varied types of studies, AES has been used remarkably successfully in studies of grain boundary segregation. The reasons are:

(a) the ability to sample very thin surface layers.

(b) the ability to detect very light elements, Hydrogen and helium are exceptions since they do not have sufficient electrons for the process.

(c) when combined with inert-ion sputtering, the concentration of impurities as a function of distance from the grain boundary can be measured.

II. THE AUGER PROCESS

When an atom has been ionized (excited) in one of its inner shells (states), it can return to its electronic ground state by an electron from an energetically higher level being transferred to the core hole. The excess energy from this process can be released in two ways:

(a) as a quantum of characteristic X-radiation, or

(b) in a radiationless manner to a second electron which is ejected from the atom with a characteristic energy.

These two processes are schematically depicted in Figure 7-7.

The electrons emitted by the second process are called Auger electrons. These are commonly denoted by a three-letter symbol, e.g., $X_p\ Y_q\ Z_r$

where X_p = Initially ionized core level

Y_q = Outer level from which an electron travels to fill the core hole

Z_y = Outer level from which the Auger electron is emitted.

Sometimes the electron transfer is between two subshells having the same principal quantum number, e.g., $W_p\ W_q\ Z_r$. Such transitions are called Coster-Kronig transitions.

In the case of free atoms, the energy of an $X_p\ Y_q\ Z_r$ electron is given by:

$$E(X_pY_qZ_r) = E(X_p) - E(Y_q) - E(Z_r,Y_q) \qquad \text{Equation (7-6)}$$

where $E(X_p)$ = Binding energy of an electron in state X_p

$E(Y_q)$ = Binding energy of an electron in state Y_q

$E(Z_r,Y_q)$ = The energy of an electron in state Z_r but moving in a potential of increased positive charge since another electron in the state Y_q is missing.

However, the measured energy of Auger electrons is given by:

$$E(X_p,Y_q,Z_r) = E(X_p) - E(Y_q) - E(Z_r,Y_q) - \phi_A \qquad \text{Equation (7-7)}$$

where ϕ_A = Work function of the electron analyzer.

It is to be noted that the above is true only if the sample and the analyzer are electrically connected so that both have identical Fermi levels.

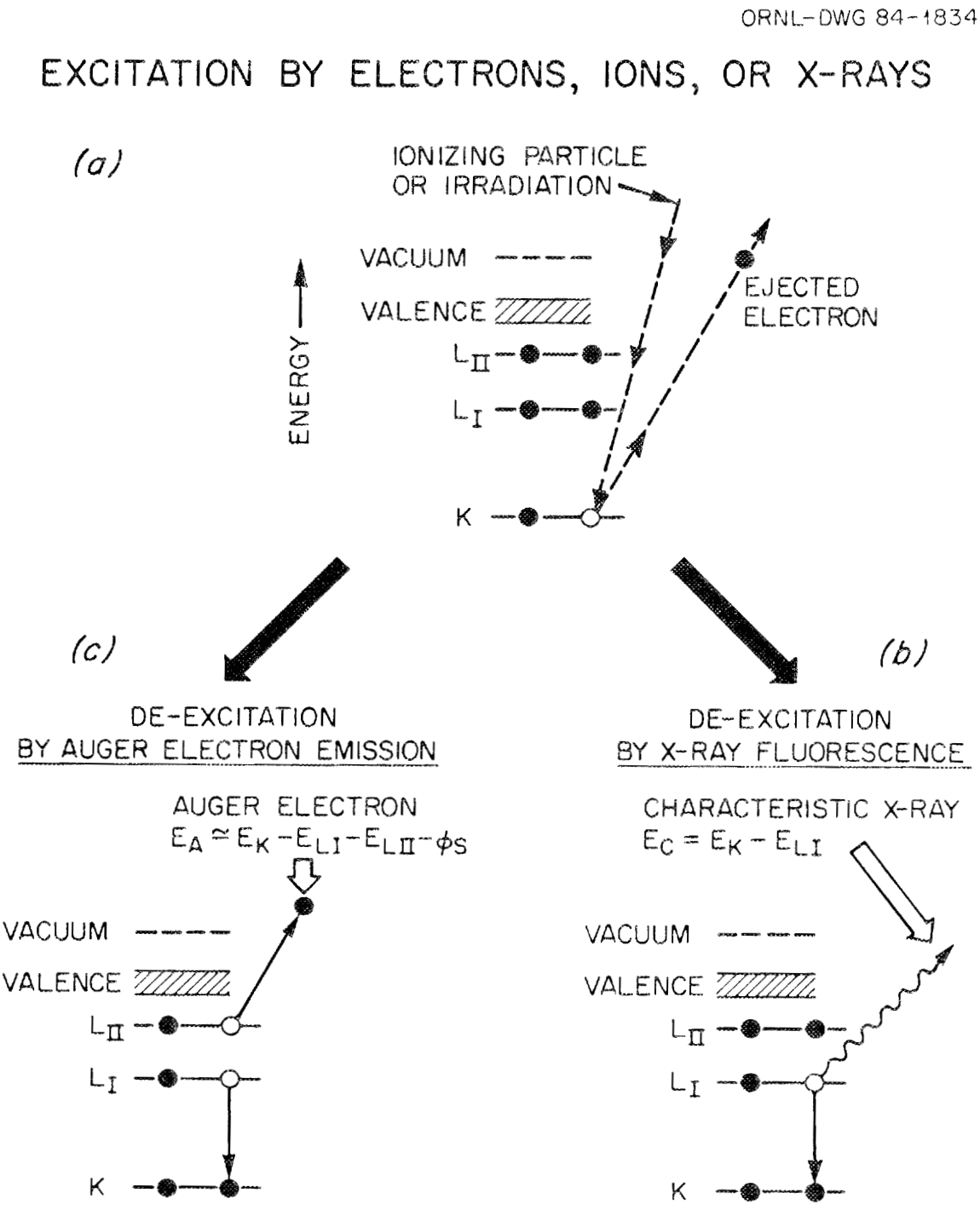

Figure 7-7. Comparison of the Auger transition with the more familiar process of X-ray fluorescence (Ref. 58).

In general, most elements display a number of peaks. Hence although there may be an overlap in the peak energy values for different elements, they can usually be identified by referring to different peaks unique to the individual elements.

It is to be noted that chemical effects can lead to a shift in the energy levels of any of the electrons participating in the transition which in turn can lead to a shift in the energy level of an Auger peak.

If an Auger electron is emitted with a probability of P_a subsequent to a core filling event, then the probability for the emission of X rays is:

$$P_x = 1 - P_a \qquad \text{Equation (7-8)}$$

In other words, Auger electron emission and X-ray emission are competitive processes. It is thus that Siegbahn et al. (Ref. 107) found the Auger electron and X-ray yields for transitions of the K type (X-ray emission K_α, K_β and Auger emission KLL) to vary with the atomic number Z as shown in Figure 7-8. While the K emission Auger yields are low for $Z > 13$ it must be borne in mind that for elements with $Z > 13$ it is convenient to look at L and M transitions. In general, the production of X rays is negligible, especially for lighter elements and energies below 500 eV, and becomes comparable to the Auger yield only in the energy range of ~2000 eV (Refs. 108,109). This is one of the major reasons that Auger spectroscopy is such a sensitive tool for surface studies.

III. EXPERIMENTAL METHOD FOR OBTAINING AUGER SPECTRA

The following are the essential components for obtaining Auger spectra:

AC-127

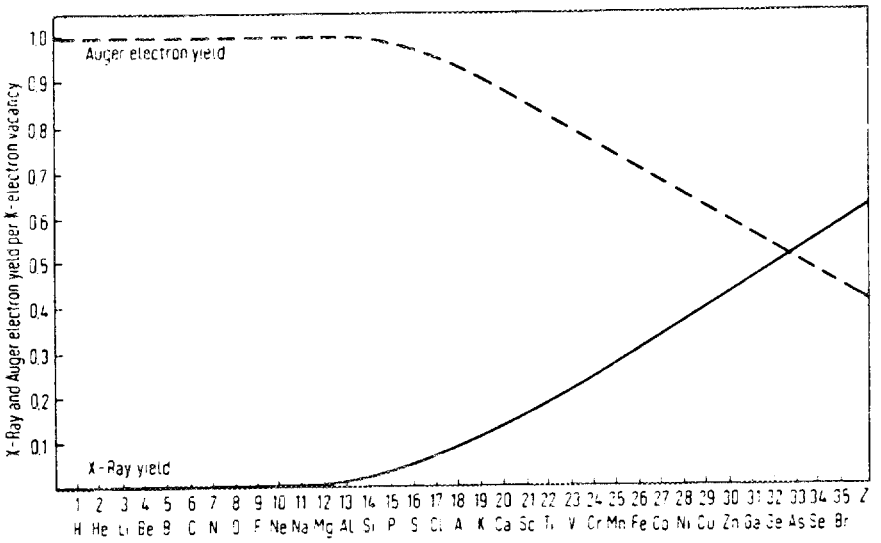

Figure 7-8. Auger electron and X-ray yields per K - electron vacancy as a function of the atomic number Z (Ref. 107).

(a) a source of primary excitation,

(b) the sample, and

(c) an analyzer and detector system,

(a) The Primary Excitation Source

Although any type of radiation capable of ionizing the inner shells of atoms may be used as the primary excitation source, it is more or less standard practice to use an electron beam. This is readily provided by a common electron gun with focusing and deflection electrodes. Recent designs permit true microanalysis by providing extremely small spot sizes. The sensitivity of AES is very high since the atomic ionization cross sections for electron impact are in the range of 10^{-20} cm^2 and are fairly independent of the primary energy. The best Auger emission is obtained when the primary beam impinges at 10 to 15° to the surface.

(b) The Sample

Any solid is in principle a suitable Auger sample. Surface smoothness of the sample does affect the quality of the spectra; and, in nonconducting solids, charge buildup often impairs the applicability of AES.

(c) Analyzer and Detector System

As shown in Figure 7-1, electron excited Auger transitions generally appear as small "humps" on a large varying background of the secondary emission spectrum. Hence the electron analyzer for Auger spectroscopy is required to have not only a high energy resolution but also a high sensitivity to detect the small Auger signals. Various analyzer design have been used in the past and these will be discussed very briefly here.

Retarding Field Analyzers (RFAs) were used for LEED long before being used for AES. Originally they consisted of two grids concentric with a

phosphor-coated collector or screen. The inner grid was grounded while the second grid was held at a negative potential close to that of the primary energy and the screen was held at a high positive potential. Once the potential for using this arrangement in AES was realized (Refs. 110,111), the number of grids used was increased to four. One of the methods used to detect an Auger signal is to superimpose a small modulating ac voltage (generally sinusoidal) on the retarding potential and comparing the modulated collector current with the reference signal from the signal source. This is generally carried out in a phase sensitive detector, also known as a lock-in amplifier.

Two of the major disadvantages of RFAs are the borderline energy resolution for AES work and more importantly the very poor signal-to-noise ratio.

Some of the other types of analyzers are the 127° analyzer and the Concentric Hemisphere Analyzer (CHA) (Ref. 100). A major breakthrough that was responsible for enhancing the status of AES greatly was the introduction of the Cylindrical Mirror Analyzer (CMA) by Palmberg et al. (Ref. 112). Due to its importance, the following section gives a detailed description of the CMA.

IV. THE CYLINDRICAL MIRROR ANALYZER

The CMA is a dispersion type analyzer where the electrons are focused electrostatically such that only those having energies within the pass band of the analyzer form an image of the source or entrance slit on the collector; hence only these electrons constitute the collector current.

The electron source is often mounted coaxially inside the CMA in which case the primary beam is normal to the sample surface. Figure 7-9 shows a typical arrangement of sample, gun and analyzer. The geometry of the CMA and the electron trajectory through it is depicted schematically in Figure 7-10.

A cylindrically symmetrical electrical field is created between the two coaxial cylindrical electrical electrodes of radii r_1 (inner) and r_2 (outer) by the application of a potential V between them, the outer cylinder being negative with respect to the inner one. Electrons entering the analyzer through the annular entrance are deflected towards the inner cylinder by an amount depending on their initial kinetic energy.

Only the electrons entering at an angle α to the axis and possessing a particular energy E_o are deflected so as to pass through another aperture to a focus on the axis. The general relation between V and E_o is (Ref. 114):

$$\frac{Eo}{eV} = \frac{K}{Ln(r_2/r_1)} \qquad \text{Equation (7-9)}$$

where K is an instrument constant which depends on the entrance angle α. For the special case where $\alpha = 42°18'$, the CMA becomes a second order focussing instrument (Ref. 115) and K = 1.31.

Since apertures have a finite width (leading to an enhancement of the sensitivity), there is a spread of angles, $\Delta\alpha$, about α over which electrons are accepted. For the common case of $\Delta\alpha < 6°$, the resulting minimum trace width W_M is given by (Ref. 115):

$$\frac{W_M}{r_1} = 7.76\ (\Delta\alpha)^3 \qquad \text{Equation (7-10)}$$

AC-128

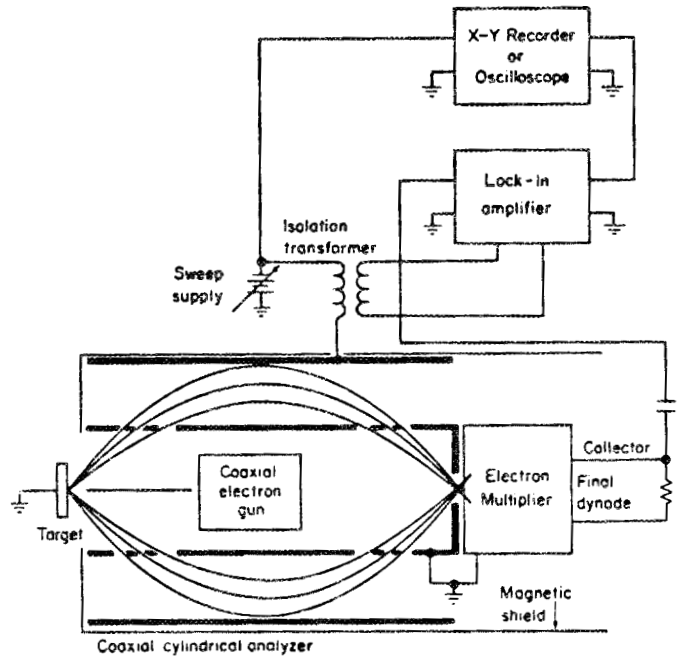

Figure 7-9. Schematic diagram of a cylindrical mirror analyzer and associated electronics (Ref. 113).

AC-129

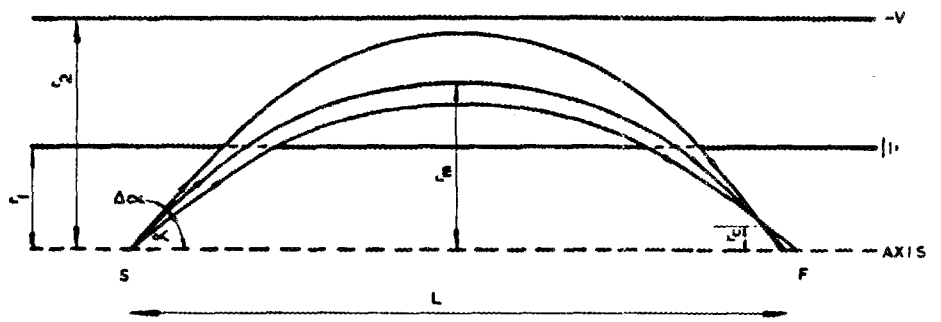

Figure 7-10. Diagrammatic depiction of the arrangement of a CMA (Ref. 114).

It is important to note that the position of the minimum trace width (Figure 7-10) is off axis and slightly ahead of the focal position. Its distance r_c off the axis is given by (Ref. 110):

$$r_c = (r_1) \times (5.28)\ (\Delta\alpha)^2 \qquad \text{Equation (7-11)}$$

It is apparent that an improvement in energy resolution without any attendant loss in sensitivity may be achieved by placing an additional aperture at the position of the minimum trace width and making both equal in size.

The energy resolution of a CMA at the half width of the energy spread is given by (Ref. 114):

$$\frac{\Delta E}{E_o} = \frac{0.18W}{r_1} + 1.39\ (\Delta\alpha)^3 \qquad \text{Equation (7-12)}$$

where w = slit width.

Hence for a given CMA, the energy resolution $\Delta E/E_o$ is constant. The collector current is given by:

$$i \propto N(E_o).\Delta E \qquad \text{Equation (7-13)}$$

where $N(E_o)$ is the energy distribution function of secondary electrons emitted from the surface of a sample.

Since $\Delta E \propto E_o$, the collector current i may be given by:

$$i \propto N(E_o).E_o \qquad \text{Equation (7-14)}$$

This illustrates an important feature of the CMA - the pass band width (the spread of energy levels admitted at any given energy level) is energy dependent.

Differentiation of Equation (7-14) leads to:

$$\frac{di}{dE_o} \propto \frac{d[N(E_o).E_o]}{dE_o} \qquad \text{Equation (7-15)}$$

Figure 7-11 shows a typical undifferentiated and a differentiated curve for comparison (Ref. 58). It is immediately evident how much the detectability of "Auger peaks" is enhanced due to differentiation. In most of the modern systems, $N(E_o).E_o$ data are gathered by a suitable software system which then differentiates the data and displays them.

The energy of an Auger transition is defined by convention as the minimum in the high energy wing of the differentiated peak.

V. QUANTIFICATION OF AES DATA

The intensity of the signal I_A from element A in a solid is proportional to its molar fraction X_A in the analysis depth (Ref. 103). Thus:

$$X_A = Ia/I_A^{\infty} \qquad \text{Equation (7-16)}$$

where I_A^{∞} = Intensity from pure A.

Generally I_A^{∞} is not known, but $I_A^{\infty}/I_B^{\infty}$ may be, where B is another constituent of the solid. Hence Equation (7-16) may be written as:

$$X_A = \left[I_A/I_A^{\infty}\right] \Big/ \left[\sum_{i = A,B} I_i/ I_i^{\infty}\right] \qquad \text{Equation (7-17)}$$

where the summation is over all the constituents of the solid.

The peak-to-peak values of the Auger signal in the derivative energy spectrum are valid for I_A and I_A^{∞} with three restrictions:

(a) the peak shapes are the same in the analysis and a reference spectra.

(b) the analysers used for both spectra have the same resoluton $\Delta E/E$.

(c) the same modulation is used, if the spectra are obtained by a lock-in amplifier (Section III).

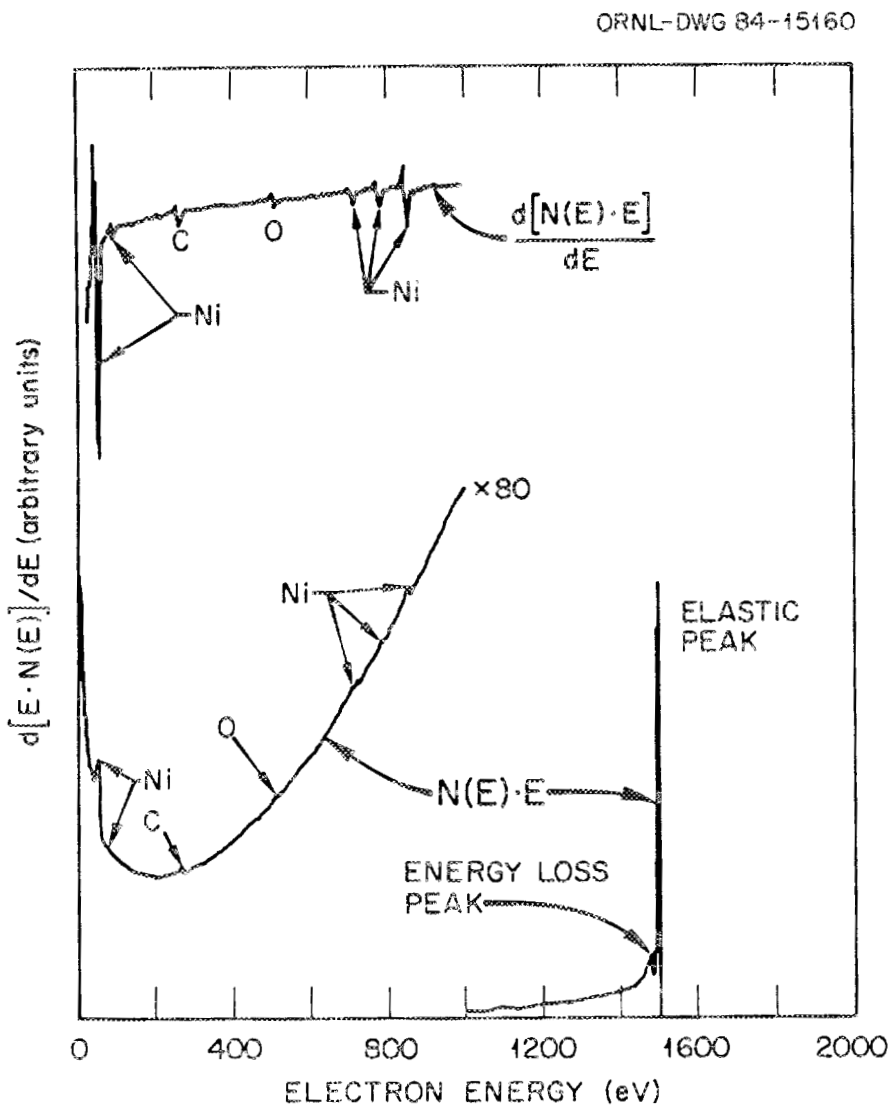

Figure 7-11. Secondary electron spectra from a nickel alloy, obtained using a CMA (Ref. 58).

In the case of a binary A - B system, it is possible to write Equation (7-17) as:

$$X_A = I_A \times \frac{I_B^{\infty}}{I_A I_B^{\infty} + I_B I_A^{\infty}} \qquad \text{Equation (7-18)}$$

If a standard set of spectra for the pure components is available, then I_A^{∞} and I_B^{∞} are easily found. However, different elements have different Auger sensitivities due to various reasons. It is, however, possible to correlate all Auger signals with the standard spectrum for a single pure element (usually Ag). Then Equation (7-18) may be multiplied and divided by the signal for pure silver, I_{Ag}^{∞}, to yield:

$$X_A = I_A I_{Ag}^{\infty} \times \frac{I_B^{\infty}}{I_A I_B^{\infty} I_{Ag}^{\infty} + I_B I_A^{\infty} I_{Ag}^{\infty}} \qquad \text{Equation (7-19)}$$

or,

$$X_A = \frac{I_A/(I_A^{\infty}/I_{Ag}^{\infty})}{\left(\frac{I_A}{I_A^{\infty}/I_{Ag}^{\infty}}\right) + \left(\frac{I_B}{I_B^{\infty}/I_{Ag}^{\infty}}\right)} \qquad \text{Equation (7-20)}$$

In Equation (7-20) the quantities $I_A^{\infty}/I_{Ag}^{\infty}$ and $I_B^{\infty}/I_{Ag}^{\infty}$ are denoted in Auger spectroscopy parlance as "Elemental Sensitivity Factors." If these are called S_A and S_B for the elements A and B, respectively, then Equation (7-20) can be written as:

$$X_A = \frac{(I_A/S_A)}{(I_A/S_A) + (I_B/S_B)} \qquad \text{Equation (7-21)}$$

Spectra obtained under standardized conditions have been published (Ref. 116) and these are used to compute the sensitivity factors for the elements.

The above development shows the method most commonly employed to compute atom fractions of elements from Auger data. A much more detailed, theoretical development for binary alloys and samples with thin overlayers is given in Appendix A.

While the theoretical developments shown in Appendix A are valid, it is to be remembered that very often the various theoretical terms are unknown. Of particular importance to this work is the fact that in the case of grain boundaries not only the level of segregation but also the intensities of the Auger signals are a function of boundary orientation, structure, etc. In particular, the orientation of the boundary relative to the analyzer is of concern; however, exact relationships are not known for all orientations. Hence, for this study, this problem is circumvented by analyzing a large number of grain boundaries in each sample so as to obtain statistically valid, mean values for the level of segregation.

Another cause for concern is the fact that, while it is not too difficult to obtain relative quantities for the level of segregation of a particular species in a particular alloy, it is extremely difficult to extrapolate such values to obtain absolute concentrations. Such an exercise would involve an extensive calibration and standardization procedure. This is not only very time consuming but also prohibitively expensive.

VI. COMPOSITION DEPTH PROFILING

A. Basics

Depth profiling is a special case of distribution analysis of chemical composition where the third dimension (perpendicular to the surface) is of primary interest. One of the most common methods of exposing successively underlying atomic layers for the purpose of analysis using AES is surface erosion by inert ion sputtering. Sputtering is a destructive method: the sample is bombarded with ions accelerated in an ion gun to an energy above 100 eV (typically 0.5 to 5 KeV). A small fraction of the energy is transferred to surface atoms and causes them to leave the sample; they are sputtered away. Thus, successive layers under the surface are exposed; the ions sputtered away can be analyzed, e.g., by secondary ion mass spectroscopy (SIMS), and the residual surface can be analyzed by AES and/or X-ray photoelectron spectroscopy (XPS). The principal advantages of depth profiling by AES and XPS combined with ion sputtering are (Ref. 117):

(a) the information depth is of the order of 1 nm.

(b) the influence of the matrix on the elemental detection sensitivity is small.

(c) the analyzed area is small compared to the sputtered area, thus minimizing crater edge effects.

Figure 7-12 shows a schematic diagram of an inert ion sputtering apparatus. Electrons (typically of 100 eV energy) produced by a heated tungsten filament are drawn towards a positively biased anode. The atoms

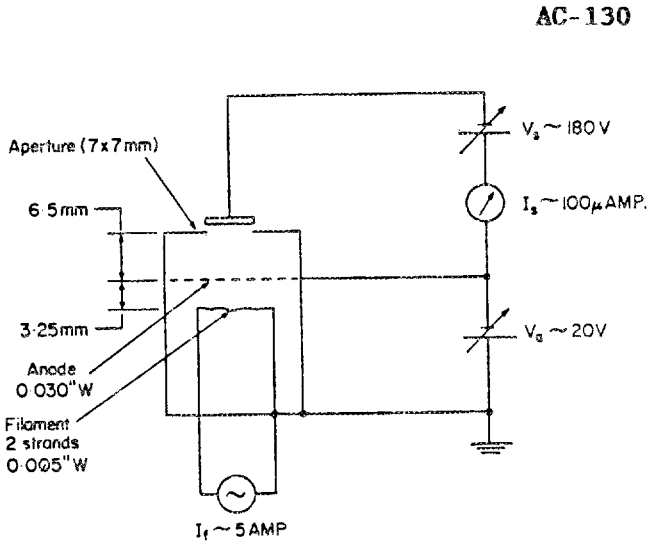

Figure 7-12. Schematic diagram of a sputter chamber and associated circuits diagram (Ref. 113).

of the inert gas in the chamber are thus ionized by collisional excitation. The filament and anode are surrounded by a tantalum container run at a positive potential with respect to the sample (target). The positive ions are thus accelerated to between 0.5 and 5 KeV and focussed on the sample electrostatically, creating a sputtered spot of about 1 to 5 mm in diameter.

To achieve an ion current density of the order of 100 $\mu A/cm^2$, the pressure in the ion formation section should be about 5×10^{-5} Torr. One mode of operation in ion pumped systems is to backfill the whole chamber with argon with the ion pumps off. The ratio of the partial pressures of impurities to that of the sputtering gas should not exceed $10^{-10}/5 \times 10^{-5} = 2 \times 10^{-6}$.

The above description is for "static" systems, e.g., normal incidence guns. It is to be remembered that, having raised the chamber pressure to 5×10^{-5} Torr, Auger analysis has to be interrupted during sputtering with such systems. Hence sputtering and analysis must be carried out sequentially. Also, very often the sample has to be swung around from a position aligned with the electron gun/analyzer assembly to a position aligned with the ion gun.

In contrast to this, the more modern "dynamic" systems such as the differentially pumped guns allow the specimen to remain aligned with the electron gun/analyzer assembly while being sputtered. Further, such systems operate under a pressure differential across a small orifice (about 1 mm diam) between the ion gun and analysis chamber. Hence the analysis can be carried out simultaneously with the sputtering action since the chamber is at about $10^{-2} \times$ ion gun gas pressure. This is a

major advantage in surface segregation kinetics studies. Further, the sputter damage of the electron gun cathode filament caused by accelerated positive ions is reduced.

For precise depth profiling, an ion gun with x/y beam deflection capability should be used, thus enabling precise matching of analyzed and sputtered areas. Rastering of the well focused ion beam over a larger area (up to 10 × 10 mm) improves the uniformity of the ion beam intensity leading to a flat bottom of the sputtering crater which is necessary for optimum depth resolution. Furthermore, at constant beam current the raster area is inversely proportional to the total primary ion density so that the sputtering rate is easily controlled.

The orientation of the ion gun with respect to the sample surface is an important consideration. The gun may be directed normal to the surface – a normal incidence gun – or it may be positioned so that the ion beam strikes the surface at a very shallow angle – a grazing incidence gun.

To prevent shadowing effects in working with rough surfaces, the angles between the ion beam, the electron beam and the electron take-off should be as small as possible. Thus for depth profiling of fracture surfaces, it is desirable to use normal incidence ion guns in preference to grazing incidence ion guns.

B. Quantification of Sputtering Profiles

It is necessary to obtain the original distribution of concentration C with depth Z, $C = f(Z)$, from the measured sputtering profile, which is usually the signal intensity I of the detected elements (e.g., peak-to-peak height) as a function of sputtering time, t [i.e., $I = f(t)$].

Figure 7-13 shows the steps needed for such a conversion. The sputtering time scale must be calibrated in terms of the main eroded depth $Z = f(t)$ and the intensity of the Auger signal must be calibrated in terms of the local elemental concentration, $C = f(I)$. From such information it would be possible to establish a "real" concentration profile if sputtering proceeded homogeneously in an ideal atom layer-wise manner. However, profile distortions due to sputter induced topographical and compositional changes of the instantaneous sample surface must be taken into account; herein lies the concept of "depth resolution."

Since the mean escape depth of Auger electrons is finite, the measured concentration profile is broadened with respect to the true profile. This can be illustrated by a case where the true concentration profile is a step function. In such a case, the expected sputtering profile (Refs. 117,118) is that of an error function as shown in Figure 7-14. The depth resolution ΔZ can be defined by:

$$\Delta Z = 2\sigma \qquad \text{Equation (7-22)}$$

where σ = the standard deviation.

Once the depth resolution is known, the measured profile may be mathematically deconvoluted to obtain the true concentration profile.

C. Calibration of the Depth Scale [$Z = f(t)$]

The instantaneous sputtering rate $\dot{Z} = dZ/dt$ describes the velocity of surface erosion. Hence the mean eroded depth Z as a function of sputtering time t is given by:

$$Z(t) = \int_0^t \dot{Z}\, dt \qquad \text{Equation (7-23).}$$

AC-131

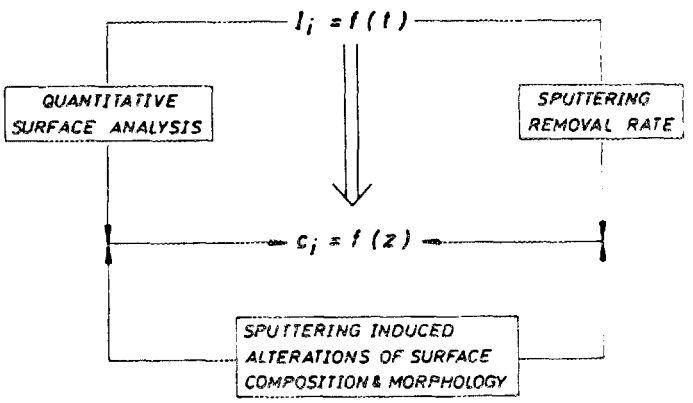

Figure 7-13. Principles of sputtering profile evaluation: conversion of a measured sputtering profile I = f(t) to a true concentration profile c = F(z) (Ref. 117).

AC-132

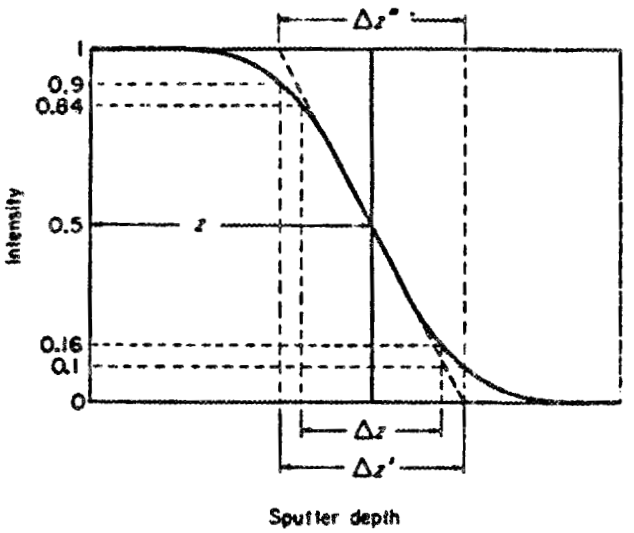

Figure 7-14. Definition of depth resolution ΔZ. For an error function profile, $\Delta Z = 2\sigma$ where σ is the standard deviation (Ref. 118).

The sputtering rate $\dot{Z}$ (m/s) is given by:

$$\dot{Z} = \frac{M}{\rho N e} S j_p \qquad \text{Equation (7-24)}$$

where M = Atomic mass number

ρ = Density (kg/m^3)

N = Avogadro's number

e = Electron charge (1.6×10^{-19} As)

S = Sputtering yield (atom/ion)

j_p = Primary ion current density (A/m^2).

For a constant sputtering rate:

$$Z = \dot{Z}t \qquad \text{Equation (7-25)}$$

Hence only one point is necessary (besides 0,0) to calibrate in terms of $\dot{Z}$.

In Equation (7-24), $\dot{Z}$ can be calculated by taking literature values of S and values of j_p measured with a Faraday cup. The yield S is a function of energy, mass, angle of the incident ions and surface composition.

A better method of obtaining $\dot{Z}$ is to measure the time required to sputter through a layer of known thickness, e.g., anodized tantalum pentoxide foils. The thickness of oxide on tantalum is easily controlled by the formation voltage and in addition, the sharp metal-oxide interface provides a quick test method for the instrumental depth resolution. Hence Z is determined with the knowledge of the Ta_2O_5 sputtering rate.

In general, however, $\dot{Z}$ varies with composition because M and S in Equation (7-24) are a function of composition. This leads to non-linearity

in the depth vs sputtering time for a binary A/B system, if the total sputtering rate $\dot{Z}$ is assumed to be:

$$\dot{Z} = X_A\dot{Z}_A + X_B\dot{Z}_B \qquad \text{Equation (7-26)}$$

is

$$Z_1\ (t_1) = \int_0^{t_1} [X_A(t)\dot{Z}_A + X_B(t)\dot{Z}_B]\ dt \qquad \text{Equation (7-27)}$$

where the mole fractions X_A and X_B can be found from the normalized Auger signals I_{A/I_A^∞}, I_{B/I_B^∞}, and $\dot{Z}_A$ and $\dot{Z}_B$ are the sputtering rates of the pure components.

D. Calibration of the Concentrations Scale [C = f(I)]

The relationship between Auger signal intensity I_i and concentration C_i of element i can be described in terms of effective electron escape depth and electron backscattering factor as shown in Appendix A. In AES, the electron backscattering is only a second-order effect compared to the escape depth influence. A detailed mathematical description of these phenomena is given in Ref. 117.

E. Factors Limiting Depth Resolution

As has been noted before, the problem in depth profiling is translation of the Auger peak intensity vs sputtering time data to concentration vs distance (below surface) information. It is a problem because various factors can distort the original composition profile as it appears on an intensity profile. A discussion of some of these factors follows, but this is by no means comprehensive. A detailed discussion of these factors and the deconvolution techniques adopted to correct for them can be found in Ref. 117.

(a) Instrumental Factors:

If the residual atmosphere in the analysis chamber is impure, absorption of certain species during sputtering can lead to problems. There may also be impurities in the ion beam itself. Nonuniformity of the ion beam intensity can also distort the profile.

(b) Sample Characteristics:

For fracture studies, this is the least controllable variable. Sample surface topology can lead to shadowing and other effects. In the case of alloys, preferential sputtering of certain species can severely distort sputtering profiles. Sometimes the presence of a second phase on the sample surface will lead to redeposition of a certain species leading to a "smearing" of the concentration after sputtering. In the case of insulators, charging of the sample is an inherent problem.

(c) Radiation Induced Effects:

The impingement of ions on the sample surface causes changes in the microtopography; this leads to changes in the concentration profile. Depth profiles can also be broadened by surface atoms being displaced to deeper layers ("knock-on" effect) and by random mixing of target atoms ("atomic mixing"). The sputtering yield (Y) being different for different components, the surface composition in a multicomponent system is generally changed during sputtering. If the sputtering yield of components is independent of their bulk concentration C_b, the surface

composition C_S is inversely proportional to the respective sputtering yields (Ref. 113):

$$\frac{C_{SA}}{C_{SB}} = \frac{Y_B}{Y_A} \times \frac{C_b(A)}{C_b(B)} \qquad \text{Equation (7-27)}$$

VII. VACUUM PUMPS - A SHORT NOTE

In conjunction with the ability to measure very low pressures, pumps have also been continuously developed to attain progressively lower pressures. Oil diffusion pumps are generally not used in UHV applications due to the difficulties involved in avoiding backstreaming of oil vapor and subsequent cleanup should this occur. A very brief discussion of some of the important pumps follows.

(a) The Cryogenic Pump: This pump has no moving parts and operates simply by condensation of gas molecules on a very cold surface (typically at the temperature of liquid nitrogen or liquid helium).

(b) The Ion Pump: In this pump, gas molecules are ionized by accelerated electrons. An electric field drives the ions to a collector surface, typically titanium, where they are absorbed. The impingement of ions exposes fresh layers of collector surface. One of the principal disadvantages of this pump is that it pumps chemically reactive gases much faster than inert gases.

(c) The Turbomolecular Pump: The principle of operation of this pump is that a molecule can be given momentum in a desired direction by repeated collisions with a rapidly moving solid surface. In this pump this is offered by the vanes of a high rpm turbine. It

is not very effective in pumping very low atomic weight gases like hydrogen.

(d) Getter Pumps: In a getter pump, chemically active gases are pumped at an evaporated getter film by a combination of chemisorption, formation of chemical compounds and solution. Although Zr, Mo and Mb are occasionally used as getter materials in UHV applications, Ti is the most widely used. The getter material may be sublimed either continuously or flashed by either resistance heating or electron beam bombardment. Since rare gases are not pumped by getter pumps, such pumps are usually used in conjunction with other pumps.

One of the major problems in attaining UHV is the slow desorption of gases from the surfaces in the vacuum chamber. This factor has obviated the use of most nonmetallic sealants for UHV. Developments like using soft, oxygen-free copper gaskets, low desorption materials like borosilicate glass for viewing ports, use of Viton, etc., have been instrumental in advancing UHV technology. These have permitted the entire UHV system to be baked at a high temperature (~200°C) to desorb gases which are then pumped out of the system.

CHAPTER 8

EXPERIMENTAL PROCEDURE

I. INTRODUCTION

This chapter deals with the details of the experimental procedures used in the course of this research. In general, the sequence of steps followed has been:

(a) Alloy Preparation

(b) Heat Treatment

(c) Cathodic Hydrogen Charging and Copper Plating

(d) Fracture in Tension under UHV

(e) Auger Analysis

(f) SEM Fractography

In addition to work carried out directly towards understanding segregation, several ancilliary experiments were carried out and these are also discussed in this chapter.

II. ALLOY PREPARATION

Ni_3Al alloys doped with boron were prepared at Oak Ridge National Laboratory by arc melting and drop casting. The cast ingots were fabricated into 0.7 mm (0.030 inch) thick sheets by repeated rolling at room temperature, with intermediate anneals at 1323 K. The ingots did not show appreciable weight loss during arc melting and thus the aluminum and nickel concentrations attained were assumed to be very close to the

appreciable weight loss during arc melting and thus the aluminum and nickel concentrations attained were assumed to be very close to the nominal values. Rectangular specimens 12.7 × 3.2 mm (~1/2 × 1/8 inches) were cut out from the sheets and heat treated.

In all, four alloys have been studied in the course of this research. Each of these contained 24 at. % Al while the boron levels were 100, 300, 500 and 1000 wppm nominally. The alloys were designated 860019, 850014, 860013 and 860018, respectively, as shown in Table 8-1. Subsequent to alloy preparation, the chemical composition of each alloy was determined (minor elements only) by spark source mass spectroscopy (SSMS) and the results are shown in Table 8-2. As can be seen, the interstitial content of these alloys, especially of harmful elements such as sulphur, was very low. It is worth pointing out that; in the course of alloy preparation, one heat of material containing about 30 wppm sulphur had been received. It was not possible to ductilize this alloy with about 500 wppm boron and subsequent Auger analysis revealed considerable amounts of sulphur on its grain boundaries, as shown in Figure 8-1. This reinforces the contention that in order to successfully use this class of alloys, careful attention must be paid to tramp element - especially sulphur - control.

In the rest of this dissertation individual samples will be designated according to their bulk boron contents. For example, a sample designated 19A2 refers to sample A2 from heat 860019 containing 100 wppm boron, while 18A2 refers to sample A2 from heat 860018 containing 1000 wppm boron.

Table 8-1. Designation of alloys used in this study

Alloy Designation	Bulk Boron Level (wppm)
860019	100
850014	300
860013	500
860018	1000

Table 8-2. Chemical analysis of alloys used in this study as determined by SSMS

Alloy Element	860019	850014	860013	860018
Mo		<1		
Zr		<1		
Zn		<0.3		
Cu	<1	3	10	<1
Co		3		
Fe	2	5	20	50
Mn		2		
Cr	20	1	600	250
V		<0.1		
Ti		0.5		
Ca	<1	<0.1	2	<1
K		<0.1		
Cl		0.5		
S	<1	<1	<1	<1
Si		5		
Mg		<0.1		
Na		5		
B	50	300	400	800
P	2		<1	<1
Rb	3		3	5
W	<10		1500	80

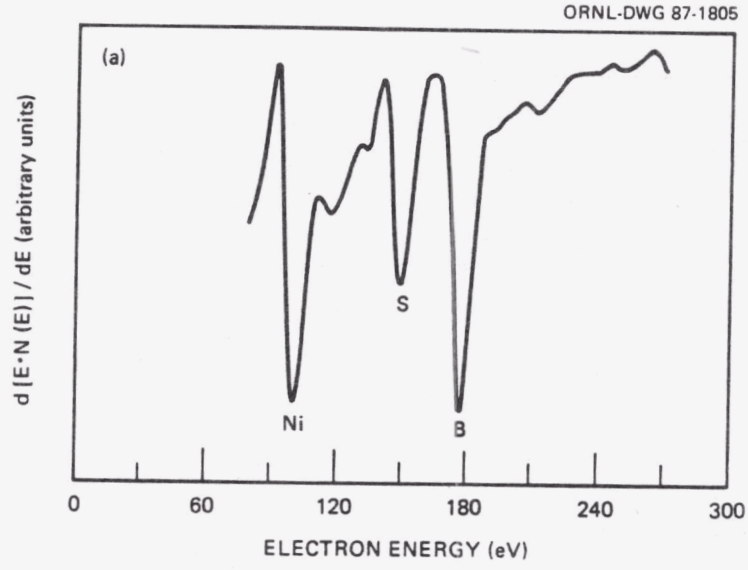

ORNL-PHOTO YP3265

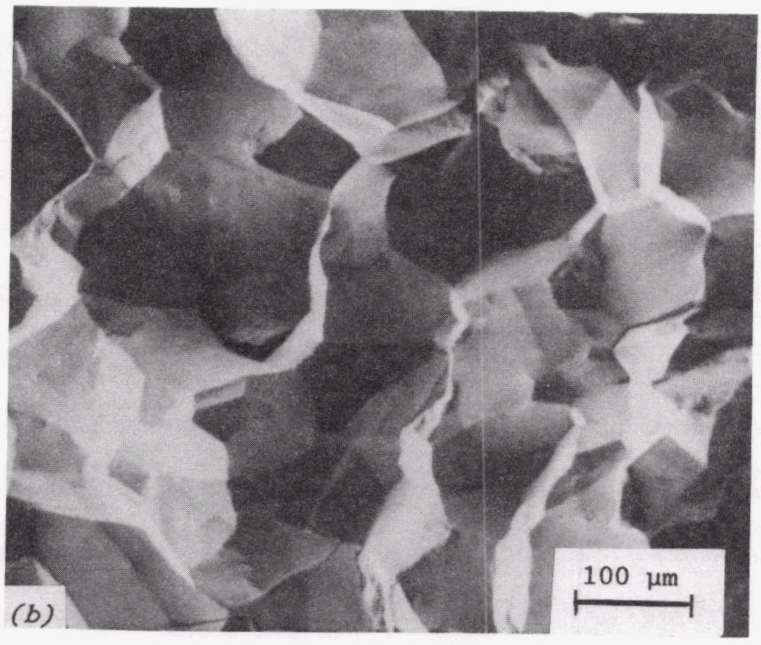

Figure 8-1. Figure illustrating the deleterious effect of sulphur even in the presence of boron (Ni + 24 at. % Al + 500 wppm B + 30 wppm S); (*a*) typical Auger spectrum from grain boundary, (*b*) typical fractograph.

III. HEAT TREATMENTS

Cold rolled samples (as-received) were recrystallized for 30 minutes at 1323 K in an evacuated (1.3×10^{-4} Pa) tube furnace, followed by a slow cool (~0.1 K/s) in the cold zone of the furnace. All samples used in this research were subjected to this treatment, henceforth referred to as base annealing (BA).

In the initial part of this research, the effects of thermal history on the level of intergranular boron segregation were investigated; to this end two basic thermal treatments were implemented. In the first treatment, samples wrapped in platinum gauze were heated to 1323 K in a vertical furnace under flowing (tank) helium, held at temperature for 30 minutes and then quenched in water (Figure 8-2); this condition will henceforth be referred to as water quenched (WQ). The flowing helium gas was used in an effort to minimize the extent of surface oxidation on the samples.

For the second treatment, samples were heated to 1323 K in an evacuated (1.3×10^{-4} Pa) tube furnace, then slowly cooled to room temperature. They were then reheated in vacuum in sequence at 1273, 1223, 1173, 1123, 1073, 1023 and 973 K, using 30 minutes holding time at each temperature followed by intermediate cooling (~0.1 K/s) to room temperature. This treatment is depicted schematically in Figure 8-2. These samples will henceforth be referred to as step annealed (SA). The initial intention had been to slowly cool to 973 K after a 30-minute hold at 1323 K without intermediate room temperature cooling, but the instructions had been misconstrued.

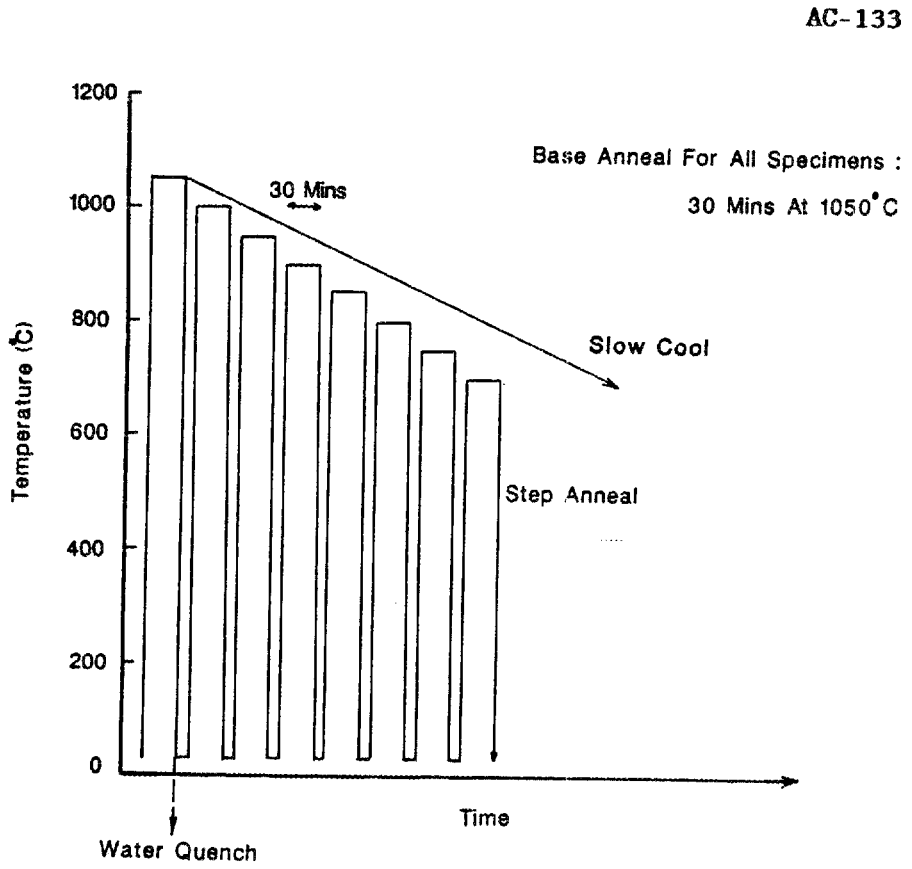

Figure 8-2. Schematic representation of thermal treatment used in this study.

In addition to the treatments mentioned above, samples from the 300 wppm B heat (850014 series) were also subjected to reversibility treatments, i.e., one set of samples was water quenched and then step annealed (WQ + SA) while another set was first step annealed and then water quenched (SA + WQ).

Samples from heats containing 100, 500 and 1000 wppm B were subjected to a treatment called slow cooling (SC) instead of SA given to samples from the heat containing 300 wppm B (850014 series). In this treatment (Figure 8-2), samples were heated to 1323 K in an evacuated tube furnace, held at temperature for 30 minutes and then cooled slowly in the furnace to 973 K. The heat treatment schemes followed on all samples used for the thermal history studies are summarized in Table 8-3.

In order to study the kinetics of segregation, a series of isothermal and isochronal annealing treatments were carried out on alloys with 100 and 1000 wppm boron (860019 and 860018 series, respectively). Table 8-4 summarizes the heat treatment schemes followed for samples used in the kinetic study. All samples used in this study were WQ following the isothermal and isochronal annealing treatments in order to arrest the segregation level attained just prior to quenching. For the 1-, 10-, and 100-minute annealings, samples were wrapped in platinum gauze, held for the appropriate time at temperature in a vertical tube furnace in an atmosphere of flowing helium gas and then drop quenched in water. Samples to be annealed for longer times (1000 and 10,000 minutes) were wrapped in 1.27 mm (0.050 in.) thick nickel foil and placed in quartz tubes. The quartz tubes were then sealed under a vacuum (10^{-4} Pa range) and the

Table 8-3. Summary of samples used in thermal history studies

Sample Number	Bulk Boron	Heat Treatment	H_2 Charged?
19A	100	SC	No
19B	100	SC	Yes
19C	100	SC	Yes
19D	100	WQ	No
19E	100	WQ	No
14V	300	SA	No
14T	300	SA	No
14X2	300	SA	Yes
14Y2	300	SA	Yes
14V	300	WQ	No
14W	300	WQ	No
14G3	300	WQ	No
14E3	300	WQ+SA	Yes
14F3	300	WQ+SA	Yes
14V2	300	SA+WQ	No
14V2	300	SA+WQ	No
14W2	300	SA+WQ	No
13A	500	SC	No
13B	500	SC	Yes
13C	500	SC	Yes
13D	500	WQ	No
13E	500	WQ	Yes
13H	500	WQ	Yes
18A	1000	SC	No
18B	1000	SC	Yes
18C	1000	SC	Yes
18D	1000	WQ	No
18E	1000	WQ	Yes
18F	1000	WQ	Yes

Table 8-4. Summary of samples and heat treatments used for the kinetics studies

Sample Number	Bulk Boron Level (wppm)	Heat Treatment	
		Temp. (C)	Time (min)
19A2	100	700	1
19B2	100	700	1
19E2	100	700	1,000
19F2	100	700	1,000
19M2	100	700	10,000
19N2	100	700	10,000
19I	100	900	1
19J	100	900	1
19M	100	900	1,000
19O	100	900	1,000
19W2	100	500	1,000
19X2	100	500	1,000
19V2	100	600	1,000
19T2	100	600	1,000
18K	1,000	700	1
18L	1,000	700	1
18M	1,000	700	1,000
18N	1,000	700	1,000
18R	1,000	700	10,000
18S	1,000	700	10,000
18V	1,000	500	1,000
18W	1,000	500	1,000
18Y	1,000	600	1,000
18Z	1,000	600	1,000
18B2	1,000	500	1
18D2	1,000	500	1
18F2	1,000	500	10
18G2	1,000	500	10
18J2	1,000	500	100
18K2	1,000	500	100
18N2	1,000	500	10,000

capsule so formed was heat treated in a tube furnace. Following the annealing for the requisite time, the samples (wrapped in nickel foil) were WQ by rapidly impacting the quartz tube to break it.

IV. MEASUREMENT OF COOLING RATE OBTAINED IN WATER QUENCHING

The cooling rate obtained during water quenching of samples from the vertical tube furnace mentioned earlier was measured. This parameter is important since an inadequate quench rate could lead to dynamic segregation in the course of quenching. Thus the segregation level observed in such samples would not be representative of the segregation level attained just prior to quenching. To this end the fixture shown schematically in Figure 8-3 was constructed, and the following is a description of it.

Two 213 cm (7 ft) lengths of 0.5 mm (0.020 in.) diam Pt/Pt-10% Rh thermocouple wire were threaded through alumina sheathing. Straight pieces of sheathing were used for the first 91 cm (3 ft) while the rest was enclosed in beads; the latter portion was thus flexible. One of the ends of the thermocouple wires was spot welded to 1.27 mm (0.050 in.) diam Pt/Pt-10% Rh thermocouple wires, which in turn was spot welded onto the surface of a rectangular specimen similar in dimension to the samples used in the course of this research (Section II). The straight sections of the sheathing were tied to a stiff wire, the top end of which was hooked so that it could be hung from the furnace's glass hook (rotatable about a horizontal axis). The lower end of the stiff wire was attached to a weight.

During heating for this experiment, the wire hook was hung from the furnace's glass hook. The beaded portion of the thermocouple was formed

AC-134

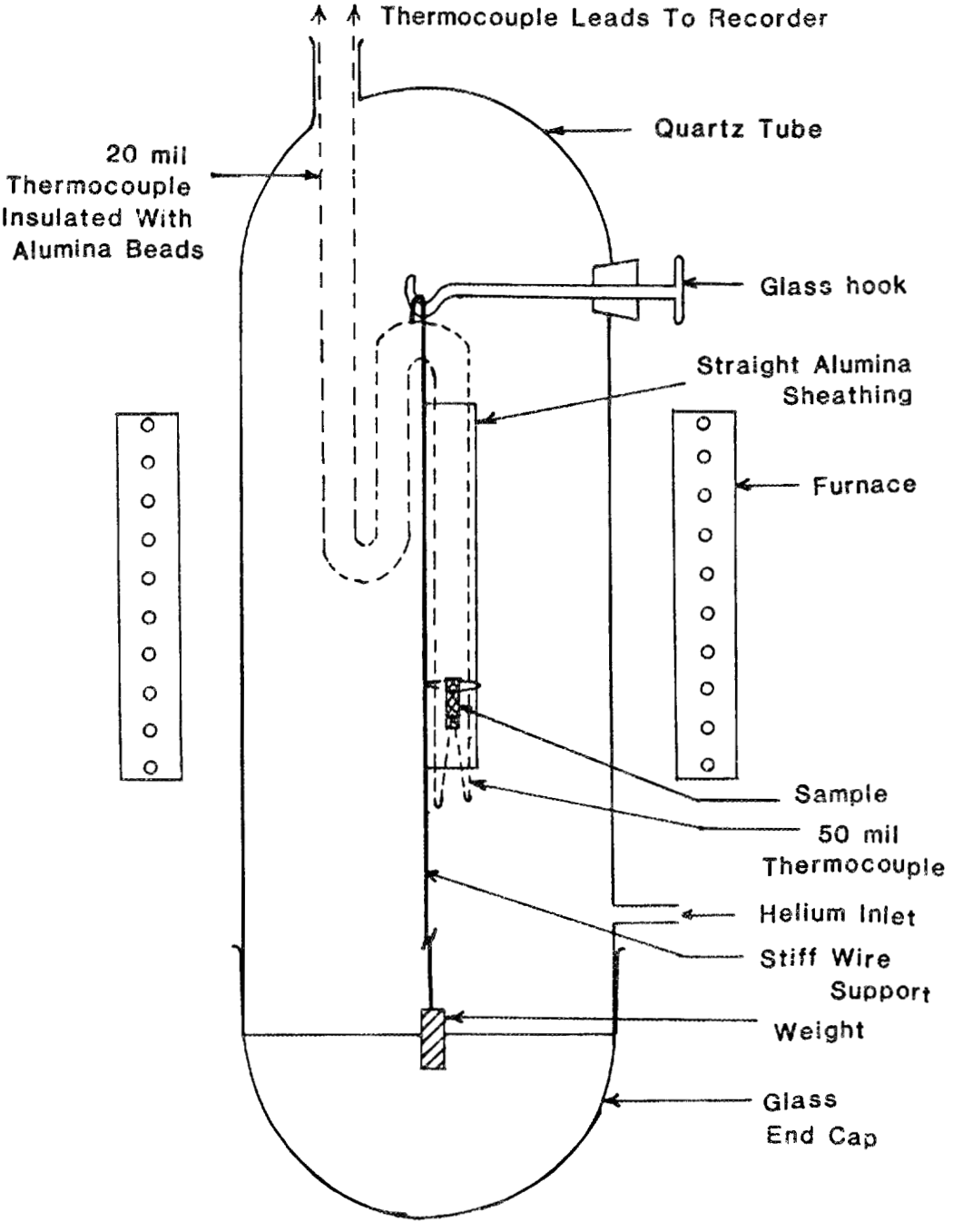

Figure 8-3. Schematic diagram of setup for water quenching.

into a vertical loop above the straight portion and exited the furnace through the gas vent at the top of the furnace. The thermocouple leads coming out of the top vent were connected to a temperature and time recording device. The heating was carried out under a steady flow of helium gas in order to better duplicate actual heat treating conditions. A second prior to quenching, the furnace power was switched off to avoid interference of stray signals with the thermocouple output. Quenching was carried out after holding the sample at 1323 K for 30 minutes. This was activated by rotating the glass hook such that the wire hook was freed and the sample dropped into the water container placed below the furnace. In so doing, the flexible portion of the thermocouple was pulled straight. During quenching the temperature at the surface of the sample was monitored by the thermocouple output.

In all, three runs were made in order to obtain the quench rate:

(a) In the first run a strip chart recorder as used to obtain the cooling rate. The chart speed was set at 40 cm/min and the full scale was set to 15 mV. The output from this run is reproduced in Figure 8-4. Using standard mV-temperature conversion charts, these data yield an average cooling rate of 1683 C/s. However, it was felt that the recorder response was not fast enough to acquire the true quench rate.

(b) In this run, a Nicolet digital storage oscilloscope was used. It was triggered manually and the frequency of data acquisition was one data point per millisecond. The data obtained from this run are shown on Figure 8-5. This plot was obtained by first converting the thermocouple

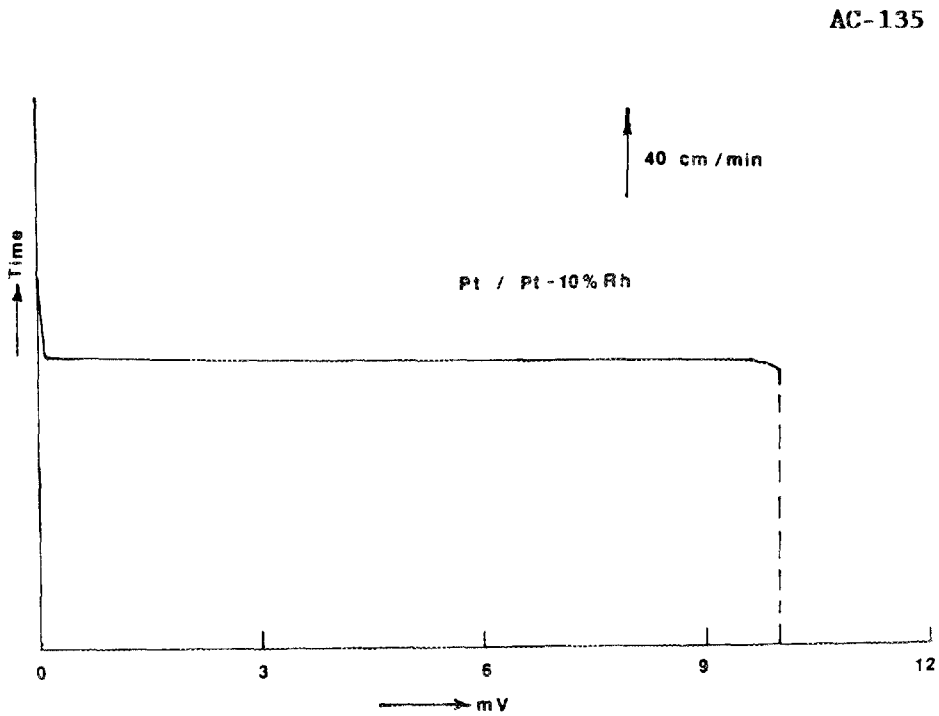

Figure 8-4. Time-temperature profile from strip chart recorder; first run for determination of cooling rate in water quenching.

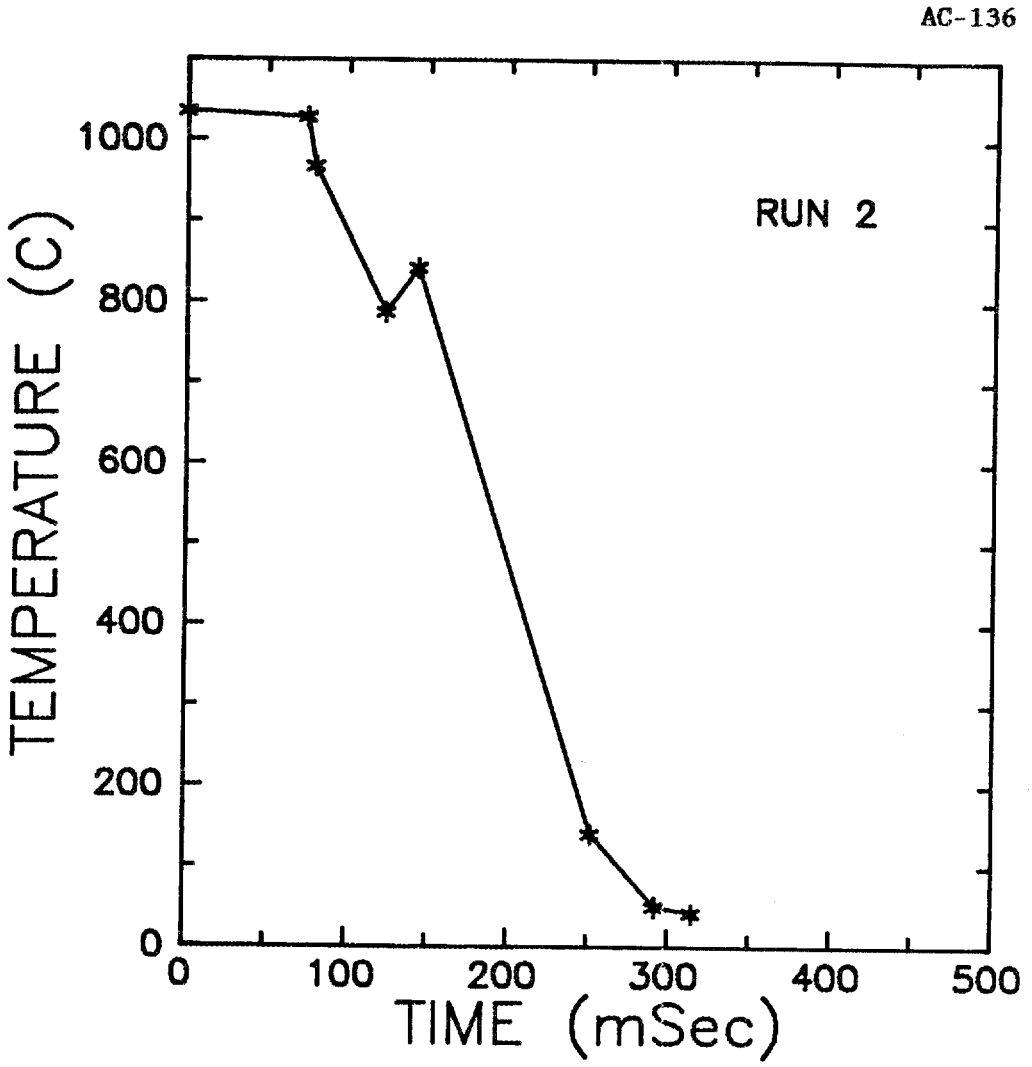

Figure 8-5. Time-temperature profile obtained from storage oscilloscope; second run for determination of cooling rate in water quenching.

output for selected points (asterisks) to temperature and plotting the same as a function of time. It is to be noted that there is a reheating of about 55 K at around 1073 K. It is felt that this is due to an impediment in the heat extraction by the quenchant (water) due to the formation of a vapor blanket around the specimen. Since the specimen was tied to a relatively massive heat source, viz, the alumina thermocouple sheathing, the heat from it may have been enough to cause the temperature rise before the vapor blanket could be removed. To verify that this was not a chance occurrence, the experiment was repeated. From the run the following cooling rates were calculated:

Average cooling rate before reheating = 4.9×10^3 C/s.

Average cooling rate after reheating = 6.4×10^3 C/s.

Overall average cooling rate (start to finish) = 5.0×10^3 C/s.

(c) This run was made using the same equipment and parameters as in the second run. The data obtained from this run are shown in Figure 8-6. It is to be noted that a temperature rise (40 K) similar to that in the second run occurred in this case. From the data in this run, the following cooling rates have been calculated:

Average cooling rate before reheating = 7.4×10^3 C/s.

Average cooling rate after reheating = 4.3×10^3 C/s.

Overall average cooling rate (start to finish) = 3.7×10^3 C/s.

From the results presented above it is surmised that the cooling rate obtained using the quenching fixture used in this study is of the order of $3.5 - 5.0 \times 10^3$ C/s.

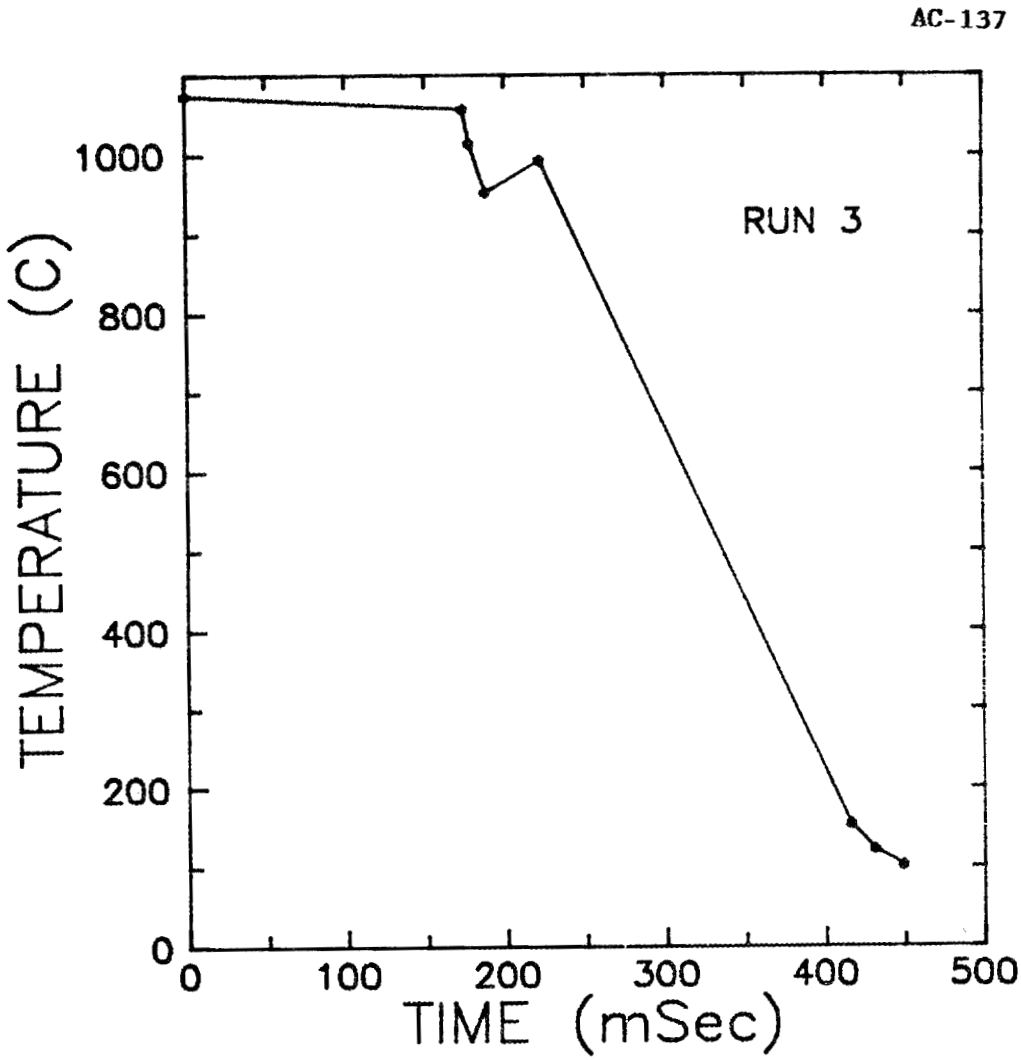

Figure 8-6. Time-temperature profile obtained from storage oscilloscope; third run for determination of cooling rate in water quenching.

V. CATHODIC HYDROGEN CHARGING AND COPPER PLATING

In order to obtain statistically valid results on the the level of intergranularly segregated solute in a polycrystalline specimen, it is necessary to expose a large number of grain boundaries for analysis. In the case of boron-doped Ni_3Al alloys, this poses a problem since the fracture surfaces are primarily transgranular and the incidental grain boundary facets one observes are in all probability not representative (in terms of segregant level) of the state of affairs in the majority of grain boundaries in the sample. In such samples then, a method is required to open up normally cohesive boundaries to expose them for analysis. Based on the work of Kuruvilla and Stoloff (Ref. 119), we decided to test the feasibility of cathodic hydrogen charging in exposing otherwise cohesive boundaries for analysis.

The initial efforts at charging were unsuccessful in opening up significant numbers of grain boundaries. We then systematically varied a number of parameters in the charging and plating sequence until a point was reached where we obtained a significant degree of intergranular fracture along the periphery of the sample but very little at locations a few grains below the surface. Further manipulation of the parameters finally yielded a set of conditions whereby virtually 100% intergranular fracture could be obtained through the cross section of the samples. The relevant values of the parameters are listed below for cathodic hydrogen charging of Ni_3Al:

Current density: 50 miliamperes/cm^2

Solution used: 1 N H_2So_4 with 50 milligrams/liter of sodium arsenite (Na_2AsO_4)

Solution temperature: ~298 K (room temperature)

Charging time: 24 hours

Extension rate used for tensile fracture: 0.13 mm/min (0.005 in./min)

For the sample dimensions used and the geometry of the charging setup, the potential between the anode and the cathode was usually about 2 V. In the charging solution, the sodium arsenite acts as a hydrogen recombination poison (retardant) so that nascent hydrogen is available at the sample surface for inward diffusion into the sample.

Two important variables found to be critical to the success of charging were notching prior to charging and sample surface preparation. Initial trials with sharp notches, made by a triangular file on two edges of the sample, met with failure. We realized that in order to obtain intergranular fracture, sufficient time must be afforded for hydrogen diffusion ahead of the propagating crack and hence a slow strain rate was desirable. For the same extension rate, a rounded notch should provide a slower strain rate than a sharp notch. To this end the samples were notched with a round file and this went a long way in improving the degree of intergranular fracture obtained.

With regard to the surface preparation prior to charging, the following was found to be essential to the success of charging. The samples were first notched as shown in Figure 8-7. All surfaces were then ground on 600 grit emery paper. The electrodes were then quickly spot

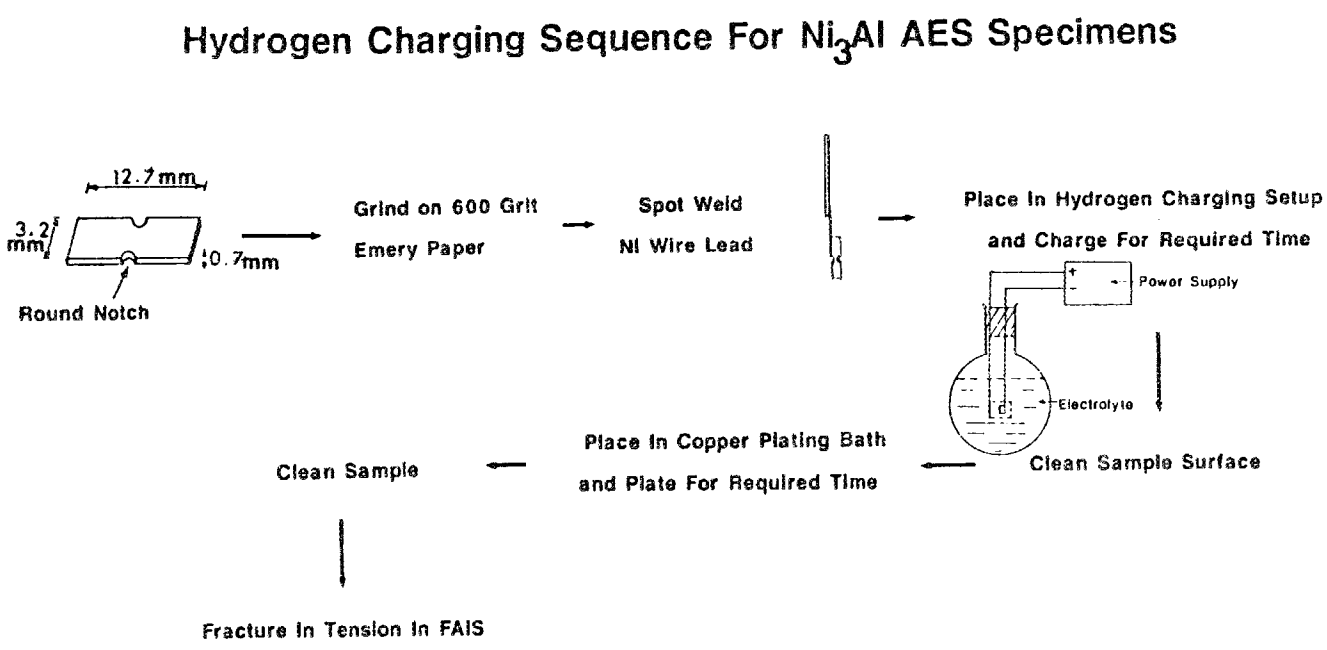

Figure 8-7. Schematic representation of sequence of steps used to hydrogen charge, copper plate and fracture samples prior to Auger analysis.

welded on. The sample was then dip etched for about 20 seconds in a solution containing:

HCl: 50 cc

HNO_3: 40 cc

Acetic acid: 20 cc

HF: 15 cc

It was important to transfer the sample as quickly as possible into the charging solution after it had been cleaned following the dipetching.

The physical setup used in shown schematically in Figure 8-8. It consisted of a round bottomed flask for containment of the charging solution; the solution was stirred using a magnetic stirrer. The anode consisted of a cylindrical platinum mesh basket which was connected to a straight stainless steel rod; the latter exited the teflon stopper through a closely fitting, drilled hole. The sample (cathode) was spot welded along one thin edge to a 0.76 mm (0.030 in.) diam nickel wire which in turn was spot welded to a short length (~10 cm) of stainless steel rod. Another piece of stainless steel rod was kept attached to the stopper with a slip-on connector inside the flask. The sample assembly was simply slipped onto the connector just prior to commencement of charging. An adjustable power supply was connected to the electrodes above the teflon stopper to supply the charging power.

The initial tensile-fracture trials on the charged specimens were carried out in air. When modest success was met in terms of degree of intergranular fracture obtained, we decided to try fracturing charged specimens under UHV, since this would be required if Auger analysis was to be performed on the fracture surfaces. Samples which had undergone

AC-139

Hydrogen Charging Setup

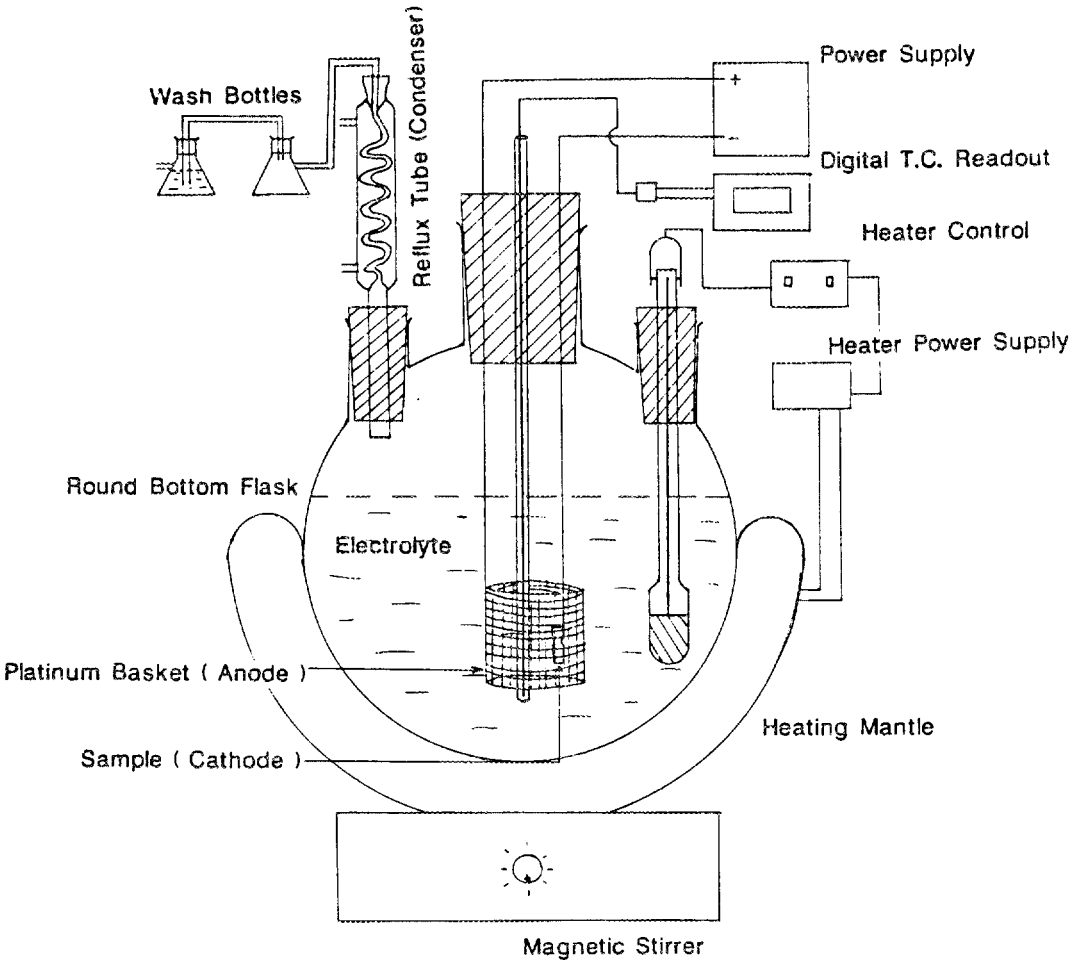

Figure 8-8. Schematic representation of experimental setup used for cathodic hydrogen charging of samples.

exactly the same treatments in terms of thermal history and hydrogen charging showed very little intergranular fracture. We realized that the hydrogen in the charged samples was being literally pulled out of the samples by the vacuum, leaving very little in the samples to effect intergranular cracking. The next challenge was thus to prevent hydrogen escape from the samples under vacuum conditions. Based on the experience of others, we decided to electrolytically plate copper onto the sample surface after hydrogen charging. Both cadmium (Refs. 120,121,122) and copper (Ref. 123) have been used by others to prevent the escape of hydrogen; the former is a potent recombination poison for hydrogen and thus prevents its escape as molecular hydrogen, while the latter is mostly a physical diffusion barrier to the outward diffusion of hydrogen into the vacuum. The presence of cadmium in UHV chambers can be disastrous because of its high vapor pressure. We thus decided to use copper plating. This involved determining another set of parameters, and the following parameters were found optimal in terms of obtaining a smooth adherent plating which was effective in preventing hydrogen escape:

Plating current density: 200 milliamperes/cm^2

Plating time: 5 min

Plating temperature: 298 K (room temperature)

Plating solution: copper sulphate: 210 g/liter

sulphuric acid: 52 g/liter

The physical setup used for the plating is shown schematically in Figure 8-9. It consists of a conical flask to hold the solution in which is an anode of copper tubing and a cathode electrode made from stainless steel rod. At the end of this rod (inside the flask) is a connector into

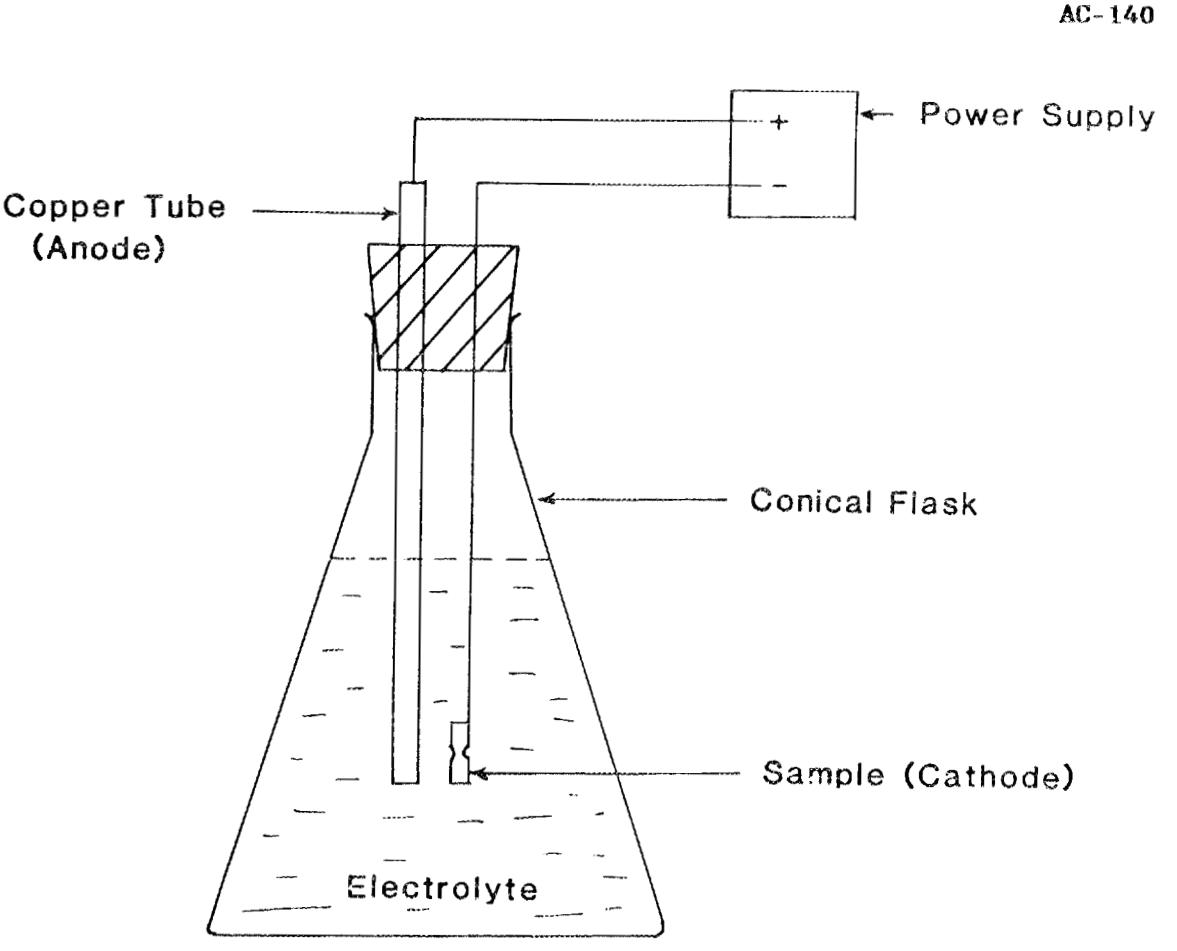

Figure 8-9. Schematic representation of experimental setup used for copper plating of samples.

which the rod to which the sample is connected can be slipped. An adjustable power supply provides the necessary power for plating.

It is necessary to transfer the sample from the charging setup to the plating setup with the least possible delay. Very often a black deposit formed on the sample surface in the course of the charging. It was necessary to clean this deposit prior to plating in order to obtain a smooth adherent plating. This was done by simply wiping the surfaces carefully with a paper towel and then rinsing in water. When this was not done, the plating obtained was found to be globular and not very adherent. While the deposit was not analyzed, it is speculated that it might be some hydride. In addition, trials at higher plating current densities were found to yield globular nonadherent platings.

VI. TENSILE FRACTURE AND AUGER ANALYSIS

The Auger analysis was carried out in a Physical Electronics Model 590 Scanning Auger Microprobe (SAM). Attached to this is an in-house fabricated Fracture And Introduction System (FAIS). A schematic representation of the entire setup is shown in Figure 8-10. FAIS has an independent vacuum system and can be isolated from the Auger analysis chamber by a valve. Thus, samples can be introduced into FAIS by letting up to air without interrupting the vacuum in the analysis chamber.

In the case of samples that did not require hydrogen charging, they were loaded onto stainless steel grips with the round notch between grips. Figure 8-11(*a*) schematically shows the grip assembly used. After a few runs the stainless steel gripping surfaces of the grips were deformed and

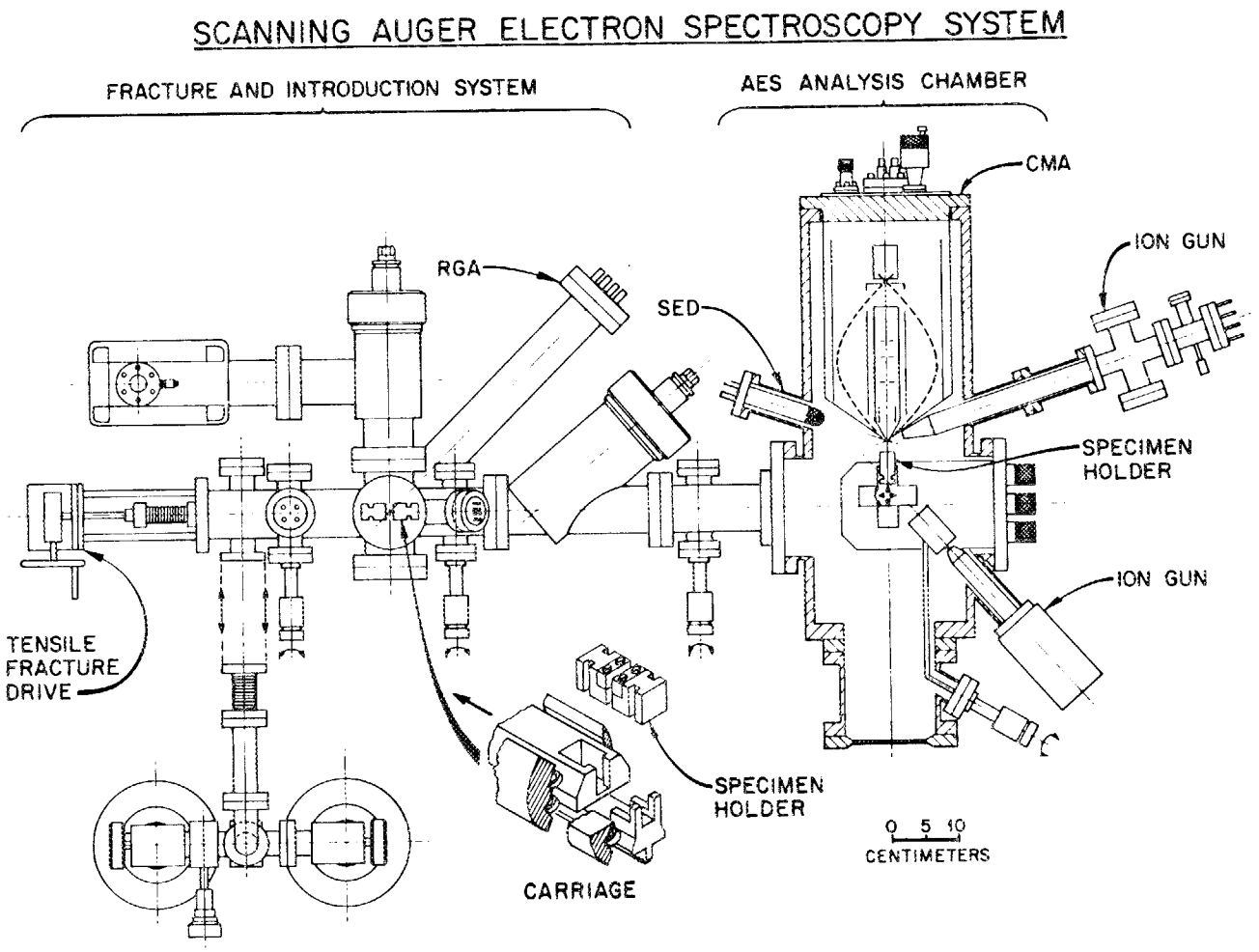

Figure 8-10. Schematic diagram of PHI 590 Scanning Auger Microprobe (SAM) and the Fracture and Introduction System (FAIS).

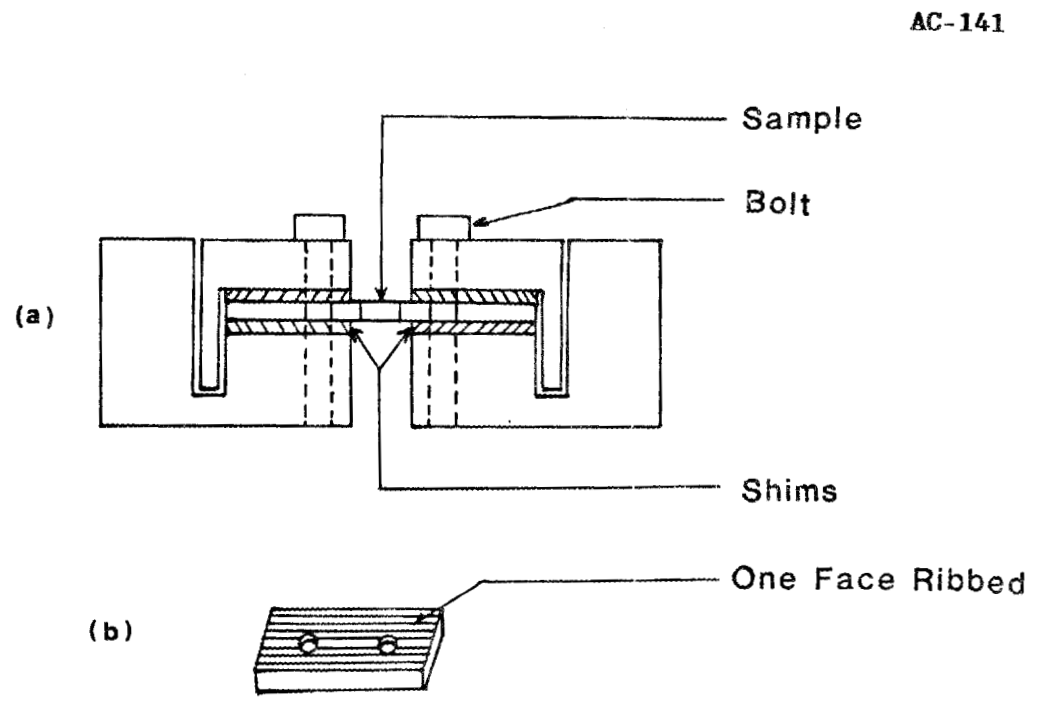

Figure 8-11. (*a*) Side view of grips and sample assembly used for tensile fracture of samples in FAIS. (*b*) Schematic diagram showing ribbed face of tungsten shim.

thus samples started to slip out during tensile loading. A set of tungsten shims (grooved on one face) were then fabricated to grip the sample better; this is shown in Figure 8-11(*b*). The grip assembly with the sample was then loaded into FAIS. FAIS was then pumped down to the low 10^{-4} Pa range. Subsequent to this, FAIS was baked-out, usually for 8 hours at 473 K.

In the case of hydrogen charged samples, bake-out had to be foregone in the interest of retaining hydrogen. As a consequence, the pressure in FAIS (during fracture) was usually higher (low 10^{-5} to high 10^{-6} Pa range) for the charged samples than for the uncharged ones where bake-out was possible. A bake-out was tried on a charged and copper plated sample. The fracture surface obtained did not show the desired level of intergranular fracture. Thus, it is surmised that while the copper plating is effective in retarding the outward diffusion of hydrogen at room temperature, it is not effective in retarding this at a higher temperature.

As shown in Figure 8-10, the grip assembly is held between the two carriages in the FAIS. During tensile loading the bottom carriage is held fixed while the top carriage travels. The sample is loaded in tension by exerting a tensile force on the top carriage; this is done from outside the vacuum system. In the initial trials, a hand cranked actuator was used to exert this force. The control on extension rate (and thus strain rate) achieved by this method was very crude, nonuniform and nonreproducible. A motorized reduction gearbox-actuator assembly was thus developed. It was possible to achieve two extension rates with this system: 0.64 mm/min (0.025 in./min) and 0.13 mm/min (0.005 in./min). The degree of intergranular fracture obtained in the hydrogen charged

samples was found to be significantly improved upon use of the slower extension rate; thus, this was adopted for fracturing all samples.

Upon fracturing the samples, the bottom carriage (with half of the sample) was moved into the analysis chamber where it was loaded onto a carousel. The carousel was then swung around so that the fracture surface faced the electron gun-CMA analyzer assembly.

For the Auger analysis, the sample was first correctly positioned by obtaining a crossover in the elastic peak at 2 KeV. The primary beam voltage used for the Auger analysis was 5 KeV and the beam current was of the order of 3 nanoamperes. During analysis the background pressure in the analysis chamber was in the very low 10^{-7} Pa to high 10^{-8} Pa range for the uncharged samples, and in the mid-range of 10^{-7} Pa for the charged samples.

The first analysis obtained on each sample was that of a rastered area on the freshly fractured surface. A secondary electron image was then obtained of the entire fracture surface and from this, individual features, such as grain boundary facets, were identified. Usually 25 grain boundary facets were analyzed, primarily for boron content, with a partial spectrum of 0 to 300 eV. For this analysis a single point on each grain boundary was analyzed for a total of 10 minutes of data acquisition time using 0.5 eV steps and with 50 milliseconds for each step. In addition, at least one grain boundary point and one transgranular point were analyzed using the full 0.2 KeV spectrum for a total of 20 minutes of data acquisition time using 1 eV per step and 50 millisecond per step.

Subsequent to the analysis on the fresh fracture surface the carousel was swung around so that the fracture surface faced a normal incidence sputter ion gun. The sample was then sputtered for 2 minutes with argon ions energized at 5 KeV at a chamber pressure of 6.7×10^{-3} Pa. The emission current of the ion beam was 25 milliamperes and it was rastered to obtain a current density of 12 microamperes/cm^2.

After sputtering, the sample was swung back to face the electron gun and CMA analyzer assembly and an area analysis was carried out on the same area analyzed prior to sputtering. The points from which the 0-2 KeV spectra had been obtained prior to sputtering were reanalyzed along with a few other selected intergranular points.

A detailed description of conversion of raw Auger data to actual grain boundary concentrations is given in Appendix B.

VII. HYDROGEN RELEASE DURING FRACTURE

In order to ascertain whether hydrogen was being released during tensile fracture of the hydrogen charged samples, a quadrupole mass analyzer was utilized. FAIS has such a Residual Gas Analyzer (UTI Model 100C) attached to it.

After the charged samples were introduced in FAIS, a vacuum was pulled on it. When the pressure in FAIS was in the low 10^{-4} Pa range, the valve connecting FAIS to the RGA was opened. The output from the RGA was simultaneously monitored on an oscilloscope and plotted on a X-Y recorder. The scanning system on the RGA was set to monitor the hydrogen level (2 AMU).

Since some hydrogen is continuously desorbed from the sample surface in spite of the copper plating, the output showed a steady background level of hydrogen. Upon loading the sample no hydrogen was observed for a short while. Subsequent to this there was a series of bursts of hydrogen release. Presumably as the grain boundaries are opened up, the hydrogen trapped between them is released. Figure 8-12 shows a reproduction of a typical trace on the X-Y recorder. The X axis corresponds to time while the Y axis is a current level corresponding to the amount of hydrogen. This experiment was not done very systematically in that no effort was made towards rigorous quantification of the hydrogen release.

An indirect outcome of this set of experiments was that I was able to determine that the optimum time interval between the end of hydrogen charging and the start of specimen tensile loading (inside FAIS) is about 1 1/2 hours. For much longer loading times, enough hydrogen escapes so that the degree of intergranular fracture obtained is not very satisfactory for analysis. A much shorter time does not allow the pressure in FAIS to drop sufficiently and the fracture surface is contaminated by intolerable levels of carbon and oxygen.

VIII. SEM FRACTOGRAPHY

Subsequent to the Auger analysis, the fracture surface topology was carefully examined in an AMR 900 Scanning Electron Microscope. This was done since the limited spatial resolution of the Auger system (~3000 Angstroms) often led to confusion as to whether an examined surface was indeed intergranular. The SEM fractography proved a means of

AC-142

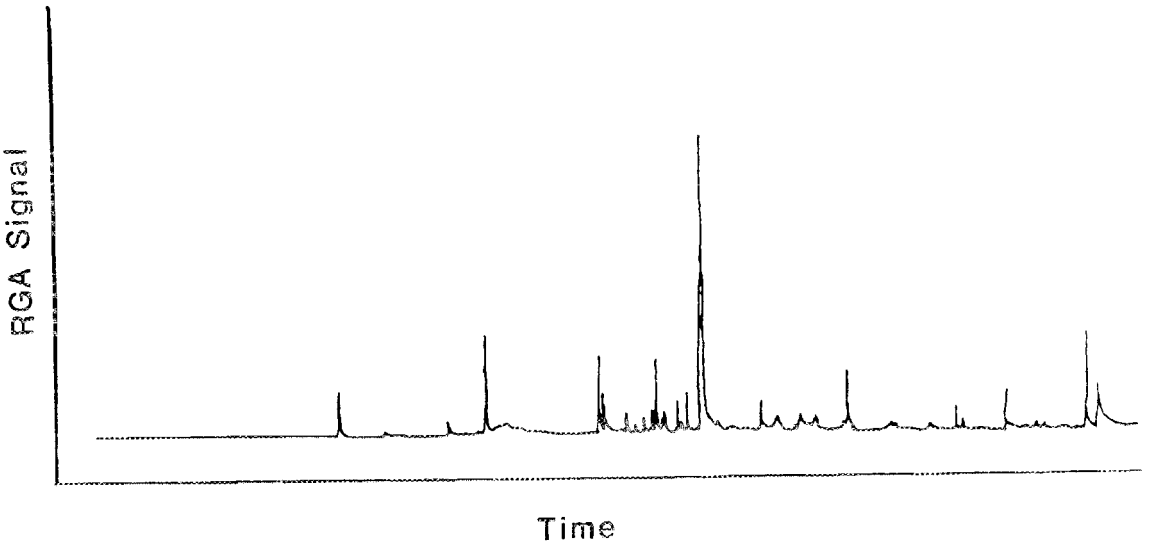

Figure 8-12. RGA trace obtained during tensile fracture of hydrogen charged sample showing "bursts" of hydrogen release.

ascertaining this. For most of the samples, each analyzed point was imaged and photographed to unequivocally determine whether it lay on an intergranular facet or a transgranular region.

CHAPTER 9

EXPERIMENTAL RESULTS

I. INTRODUCTION

As experimental work progressed in this research, questions surfaced regarding the accuracy and adequacy of the experimental approach. This chapter presents not only the results of the main thrust of the investigation but also some of the experiments carried out to address these questions. A detailed analysis of the pertinent results is presented in Chapter 10.

As mentioned in Chapter 8, Appendix B shows the method used to calculate the concentration of boron at the grain boundaries and also the enrichment ratio of boron between the boundaries and the bulk. Since only qualitative comparisons between samples are to be made in this chapter, only one of the concentrations defined in Appendix B (viz, B1) will be used for such comparisons. In Chapter 10 a rationale will be discussed for choosing this value to calculate other quantities such as binding energy.

II. IN-HOUSE STANDARDS

While the bulk of reported Auger data rely on available standard spectra (Ref. 116) for deriving sensitivity factors, it was felt essential to develop our own standard spectra to obviate questions regarding spectrometer-to-spectrometer variations.

All spectra were obtained on a PHI model 590 scanning Auger microprobe (Super Sam) using a primary electron beam energy of 5 KeV. In view of the focus on nickel-base alloys, the Ni 848 eV peak was used as the standardizing peak for obtaining elemental sensitivity factors. It is to be remembered that the manufacturer of the instrument (PHI) used a silver standard for the sensitivity factors reported in the handbook. Since all the experimental spectra were obtained at a CMA energy resolution setting of 0.6%, the standard spectra were also obtained at this energy resolution. The elements analyzed were: nickel, boron, carbon, aluminum, magnesium, oxygen (aluminum oxide sample) and molybdenum. Only in the case of molybdenum was a chemical analysis available, and this is shown on Table 9-1; all other samples were of purity greater than 99%.

Table 9-2 shows the results for the elements mentioned above and also compares them with values reported by PHI. The asterisks indicate elements for which PHI supplies only 3 KeV spectra and hence a comparison seems to be unfounded. Henceforth all values of elemental peak heights will be reported after corrections by the in-house sensitivity factors reported in Table 9-2.

III. REPRODUCIBILITY

The study of grain boundary segregation is often complicated by the fact that the amount of segregation measured by Auger electron spectroscopy can be quite variable both with respect to boundary-to-boundary variations in a given sample was well as variations within a single grain boundary facet. Briant (Ref. 124) has reviewed this aspect of segregation studies and some of the following discussion is based on his work.

Table 9-1. Chemical analysis of molybdenum sample used in obtaining standard spectra

By Qualitative Spectrographic Analysis	
Molybedenum	Major
Iron	0.00X
Silicon	0.00X

Elements checked but not found: manganese, copper, silver, nickel, chromium, cobalt, vanadium, tungsten, bismuth, antimony, arsenic, zinc, cadmium, indium, lead and tin.

Table 9-2. Elemental sensitivity factors obtained in this study and comparison with values from PHI

Element	Peak Energy (eV), PHI	Peak Energy (eV), In-house	Sensitivity Factor, PHI	Sensitivity Factor, In-house
Boron	179	176	*	2.667
Carbon	272	268	0.560	1.961
Aluminum	68	62	0.814	0.974
	1396	1398	0.248	0.226
Nickel	61	58	0.970	1.377
	102	100	0.089	0.105
	716	716	0.267	0.272
	783	782	0.406	0.404
	848	850	1	1
Magnesium	32	26	*	0.853
	1174	1180	*	1.421
Oxygen	503	502	*	2.211
Molybdenum	120	121	0.197	0.178
	148	145	0.162	0.035
	161	160	0.377	0.178
	186	186	0.969	0.480
	221	221	0.870	0.378

In this research some of these questions were addressed by carrying out a series of experiments on the fracture surface of one specimen: 850014G3. The sample had undergone a water quenching treatment as described in Section III of Chapter 8.

The first aspect to be addressed is that of variations in segregation level on a single grain boundary. To this end, ten nonoverlapping points were analyzed on a single grain boundary. Figure 9-1 shows a secondary electron micrograph of this boundary, and the individual points analyzed are identified by letters. Table 9-3 shows the atom fraction of boron (B1) for these points and the average and standard deviation for all ten points. As can be seen, the standard deviation of B1 is almost 30% of the average value, and thus it would seem that there are large variations of segregant level on a single grain boundary.

Figure 9-2 shows the spatial distribution of boron (B1) on this grain boundary. The concentration of boron on points O, S, R and M is much lower than on the other points; i.e., there appears to be two regions on this grain boundary with different segregant levels. If only points J, K, L, N, P and Q are considered (one region), then the average value of B1 is 1.82 and the standard deviation is 0.14; i.e., the standard deviation is ~8% of the average value. Briant (Ref. 124) has reported values of 10% and 4% for phosphorus and antimony segregation, respectively, in steel. From the above stated values it might be concluded that variations in segregant level on a single grain boundary do occur but that these variations are small.

The second question to be addressed in this experiment was that of variations in signal level with time. To this end, one intergranular

AC-143

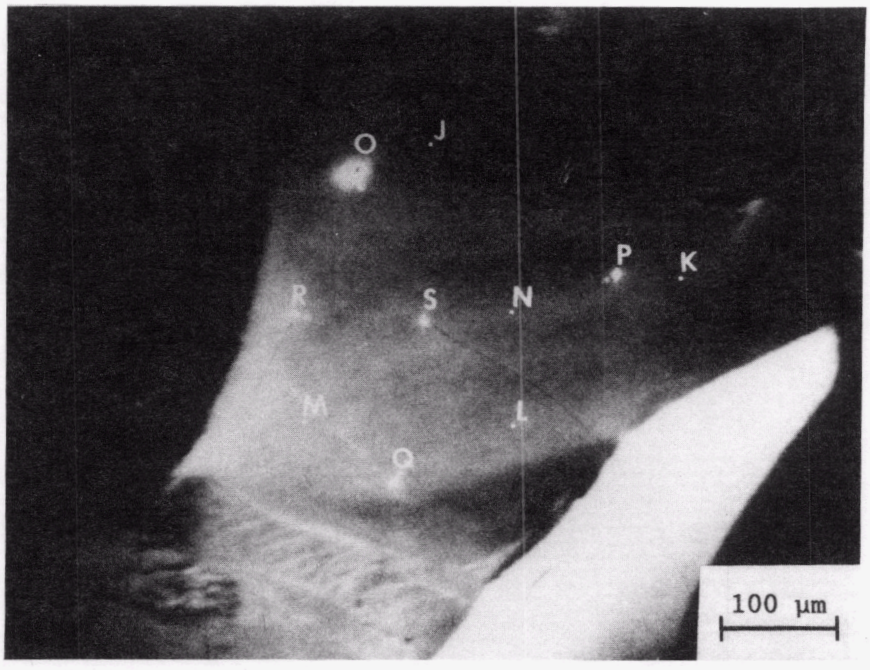

Figure 9-1. Secondary electron image of grain boundary on which ten points (identified by letters) were analyzed.

Table 9-3. Results of Auger analysis on 10 points lying on the same grain boundary

Point Name	B1
J	1.67
K	1.87
L	1.79
M	0.69
N	1.86
O	1.22
P	2.07
Q	1.64
R	1.06
S	1.04
Number	10
Average	1.49
Standard Deviation	0.45

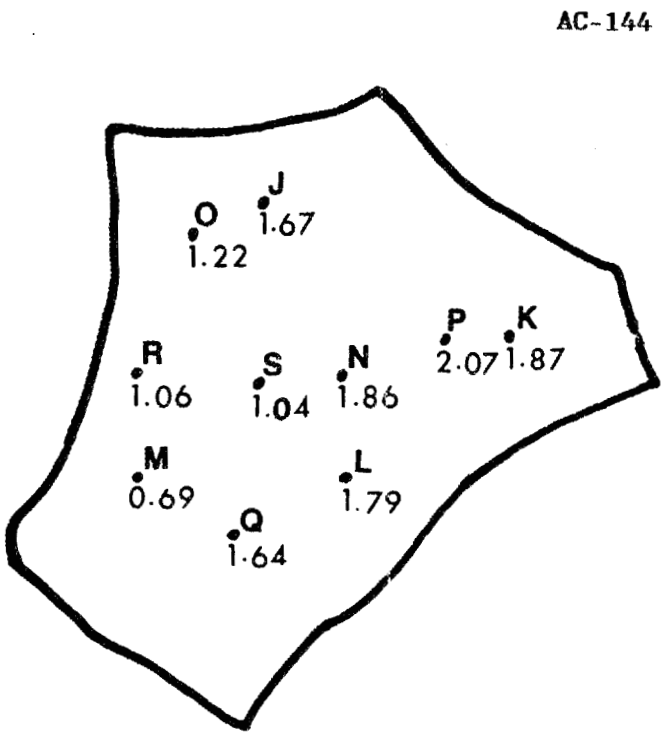

Figure 9-2. Schematic diagram showing spatial distribution of boron (B1) on the grain boundary shown in Figure 9-1.

point (T) was analyzed three times using a one hour time lapse between the start of each data acquisition sequence. Spectra of 0 to 2000 eV were obtained for each case using a data acquisition time of 20 minutes per point. Table 9-4 shows the data obtained in this fashion in terms of B1; in this table, T1, T2 and T3 denote the sequence of data acquisition; i.e., data for T3 was obtained about three hours after data for T1 had been obtained. As can be seen, there is no detectable trend in the values of B1 as a function of time. Also, the standard deviation of B1 for T is only 14% of the average value. Thus, in all the following analyses, at least 14% uncertainty in the measured segregation level should be expected.

Variations of segregant level among grain boundaries was also studied in this experiment. Twenty-five grain boundaries on this sample were analyzed for boron content, and the results are shown in Table 9-5. It is to be noted that in this case the standard deviation is 31% of the average value (of B1); this is much larger than the 8% found for points on a single boundary. Such variations in the segregant level among boundaries can be primarily attributed to the different structures existing at different boundaries. Figure 9-3 shows the distribution of points having B1 values as shown. This figure was obtained using the range definition shown in Table 9-6. As can be seen from Figure 9-3, more than 70% of the points have B1 values within ±30% of the average value.

The next question addressed was whether the analysis of 25 grain boundary points was indeed enough to yield a fair representation of the segregant level in a given sample. A second piece from the same sample (the unused half from the previous set of measurements) as fractured

Table 9-4. Results of repeated Auger analyses on the same point on a grain boundary

Point Name	B1
T1	1.74
T2	1.46
T3	2.01
Number	3
Average	1.74
Standard Deviation	0.28

Table 9-5. Results of Auger analyses on 25 grain boundary points on one fracture surface

Point Name	B1
V	.55
AA	.59
Y	.63
SS	.69
FF	.71
HH	.72
CC	.81
X	.87
PP	.88
Z	.90
OO	.99
JJ	1.04
KK	1.07
BB	1.09
MM	1.09
W	1.12
NN	1.21
DD	1.24
QQ	1.25
LL	1.30
GG	1.31
RR	1.36
EE	1.40
II	1.78
T	1.79
Number	25
Average	1.06
Standard Deviation	0.33

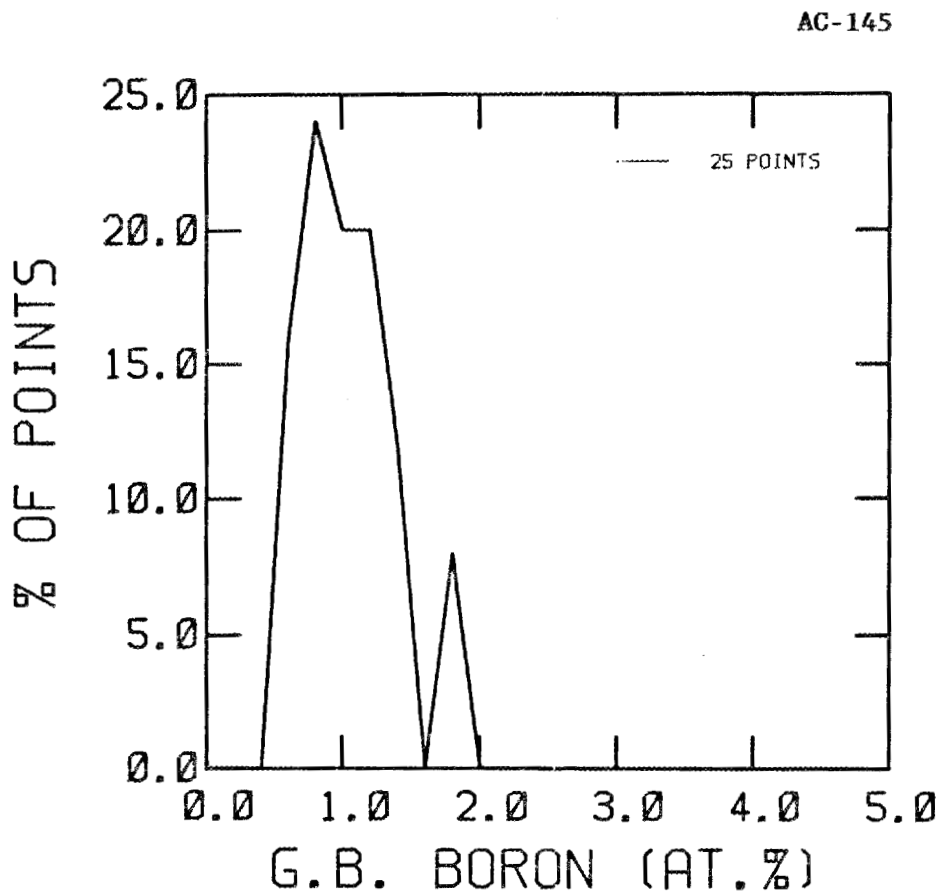

Figure 9-3. Distribution of boron levels on one fracture surface (25 points analyzed).

Table 9-6. Range of boron levels (B1) used to generate the distribution shown in Figure 9-3

Low Value	High Value	Average Value
0.00	0.10	0.00
0.11	0.30	0.20
0.31	0.50	0.40
0.51	0.70	0.60
0.71	0.90	0.80
0.91	1.10	1.00
1.11	1.30	1.20
1.31	1.50	1.40
1.51	1.70	1.60
1.71	1.90	1.80
1.91	2.10	2.00
2.11	2.30	2.20
2.31	2.50	2.40
2.51	2.70	2.60
2.71	2.90	2.80
2.91	3.10	3.00
3.11	3.30	3.20
3.31	3.50	3.40
3.51	3.70	3.60
3.71	3.90	3.80
3.91	4.10	4.00
4.11	4.30	4.20
4.31	4.50	4.40
4.51	4.70	4.60
4.71	4.90	4.80
4.91	5.10	5.00

under UHV and 50 grain boundary points were analyzed. Table 9-7 shows the results of this analysis. As can be easily seen, the average value of B1 obtained in this case is 1.16 as compared to a value of 1.06 for the case when 25 grain boundaries were analyzed (Table 9-5). The difference between these two values is 9%, which is well within the expected scatter. Also, for the two cases the ratios of standard deviation to average are 0.35 and 0.31; i.e., the difference between these two cases is insignificant. In addition, 66% of the points have segregant levels within ±30% of the average value. It thus appears that a sampling of 25 grain boundaries on a given sample is adequate for our purposes; this is the number of grain boundaries analyzed for most of the samples in this research. Figure 9-4 is a distribution plot for the segregant level in the case where 50 points where analyzed; the general features are similar to those of Figure 9-3.

Briant (Ref. 124) has pointed out, however, that other factors can contribute to the variation in the analyses. One such factor is the variation in relative orientation of the analyzed boundaries with respect to the CMA. In a series of experiments where a flat specimen was pivoted to provide different angles with respect to the CMA, Briant (Ref. 124) has shown that variations in the elemental peak height ratios with angle were minimal and could not account for the observed variations in segregant level. While such an experiment was not conducted in the course of this research, it is felt that a similar conclusion would hold for the problem at hand and hence the effect of this factor can be neglected. A second factor to be considered is that, upon fracturing, each half of the fracture surface is assumed to inherit half the level of segregant existing at the

Table 9-7. Results of Auger analyses on 50 grain boundary points on one fracture surface

Point Name	B1	Point Name	B1
KK	0.27	A	1.12
CC	0.59	MM	1.18
FF	0.63	T	1.21
R	0.69	NN	1.22
SS	0.70	J	1.24
W	0.70	WW	1.25
M	0.71	VV	1.26
P	0.71	EE	1.29
RR	0.74	DD	1.31
Q	0.77	LL	1.31
AA	0.84	QQ	1.33
XX	0.84	E	1.37
UU	0.85	V	1.41
BB	0.88	OO	1.42
TT	0.89	PP	1.43
B	0.94	X	1.47
G	0.99	Z	1.48
JJ	0.99	HH	1.50
F	1.01	D	1.57
YY	1.01	Y	1.60
I	1.03	S	1.69
N	1.04	K	1.80
L	1.05	H	2.05
U	1.05	GG	2.10
C	1.10	II	2.38

Number	50
Average	1.16
Standard Deviation	0.41

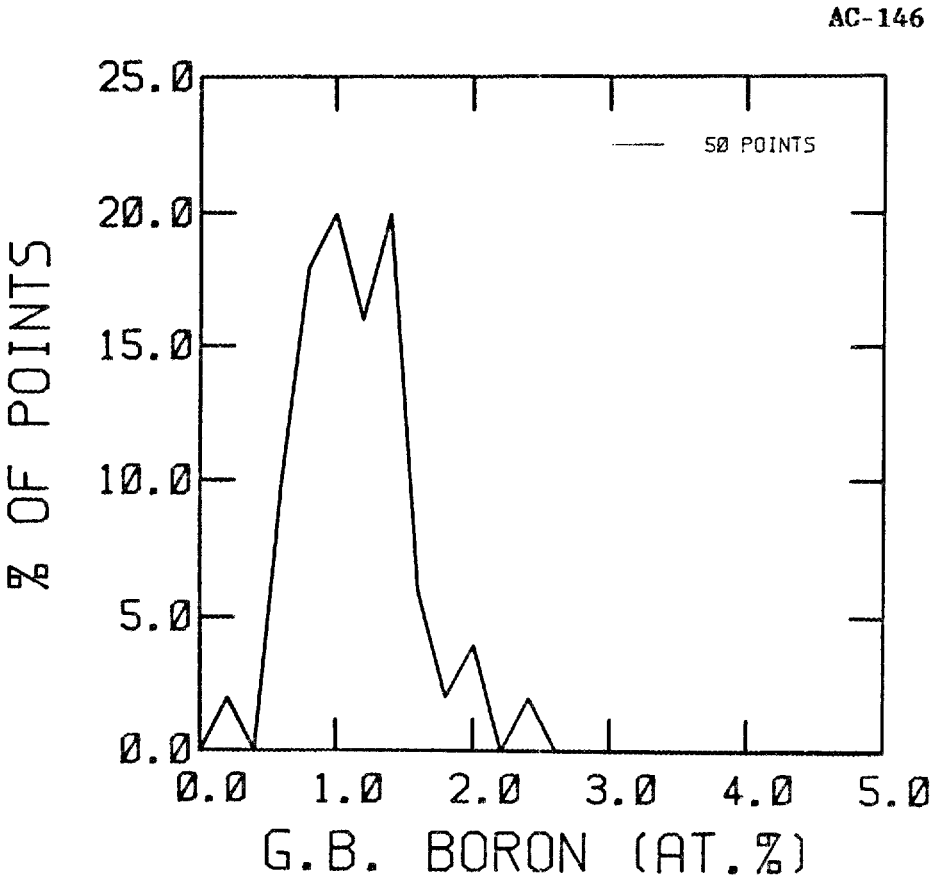

Figure 9-4. Distribution of boron levels on one fracture surface (50 points analyzed).

grain boundary. Briant (Ref. 124) has conducted analyses on both halves of a fracture surface and has concluded that while the apportioning of segregant may not be exactly 50% - 50%, it is between 45 and 55%. Such an experiment was not conducted in the present research and Briant's results will be accepted to arrive at the conclusion that the measured segregant level should be multiplied by two to arrive at the segregant level at the boundaries. It is also worth noting that such an apportioning is in keeping with Briant and Messmer's contention of breaking of only metal-metal bonds in the course of fracture (Ref. 125).

Another important factor to be considered is that of sample-to-sample variations in segregant level. In all the data reported here, at least two samples were analyzed for each heat treatment condition. In the absence of evidence to the contrary, it is felt that this was adequate to obviate questions regarding sample-to-sample variations. Briant (Ref. 124) points out the fact that variations in homogeneity of the samples could contribute to scatter of the measured segregant levels; no significant evidence of such inhomogeneity were found in this study and hence this factor will be ignored. In addition, the fact that some grain boundaries may reach equilibrium earlier than others and thus would exhibit non-equilibrium segregant levels will be ignored in this study.

A discussion of Briant's (Ref. 124) arguments relating to the question of why some grain boundaries exhibit segregant levels well beyond (say 30%) the average value is warranted at this point. In addition to grain boundary structure being responsible for such as effect, it is claimed that the variations in the chemical bonding at the boundaries also contribute significantly to this effect. Different types of chemical

bonding lead to different types of atomic configurations (clusters) at the boundaries. Figure 9-5 is a schematic representation of the kinds of atomic clusters that may comprise a grain boundary and their energy spectra (these are purely hypothetical). As the energy minima for the clusters decreases below that for the bulk, the clusters become traps for interstitials; the strength of the trapping effect is reflected in the depth of the energy minima. Thus there is a wide distribution in the strength of the traps. The sequence in which a solute occupies such traps will be dictated by the relative magnitude of the energy minima. A wide variation in the level of segregated solute is thus to be expected from grain boundary to grain boundary depending on the structure and chemical bonding existing in the boundaries.

IV. EFFECT OF THERMAL HISTORY ON EXTENT OF SEGREGATION

McLean's theory of grain boundary segregation (Ref. 63) predicts that the level of equilibrium segregation of a solute should depend on the temperature and time. In metallurgical terms, the level of segregation should vary with the thermal history imposed on a sample. As indicated in Section I of Chapter 6, such variations in the level of segregation should effect the fracture morphology. In order to verify this in the case of boron segregation in Ni_3Al, samples of substoichiometric (24 at. % Al) containing 300 wppm boron in the bulk were given widely varying thermal treatments. The tensile fracture morphology and level of grain boundary boron were then correlated with these treatments.

AC-147

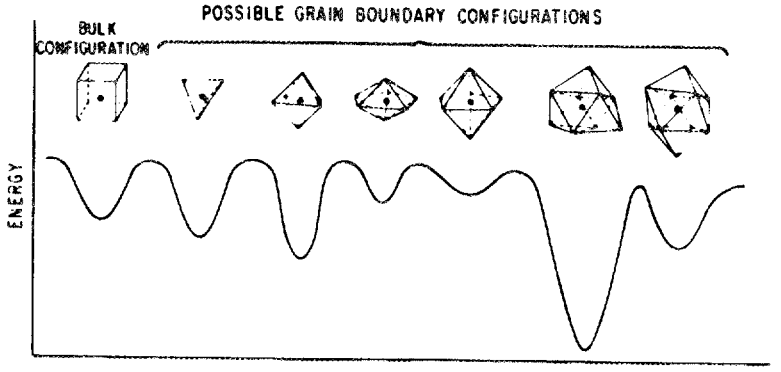

Figure 9-5. Schematic representation of the types of clusters (at grain boundaries) and their energy levels (Ref. 124).

Table 8-3 shows the sample numbers (850014 series) and their heat treatments for the initial studies. Details concerning heat treatments, hydrogen charging, tensile fracture under UHV and the subsequent Auger analysis can be found in Chapter 8.

Figure 9-6(*a*) and (*b*) compares the typical fracture morphology of uncharged samples in the SA and WQ conditions. The first two rows of Table 9-8 show the boron level (B1) at the boundaries in each case. It is immediately obvious that variations in thermal history have a dramatic effect on the fracture morphology; specifically, the level of intergranular fracture in the WQ sample is much larger than in the SA sample. The boron level, however, does not reflect this; i.e., the boron level does not appear to be very different in the two cases, although the average values in the SA case show more scatter than in the WQ case.

Cathodic hydrogen charging was used to enhance the degree of intergranular fracture in the SA samples. Figure 9-6(*c*) shows a typical fracture surface of a hydrogen charged SA sample. Comparison of the boron level between the uncharged WQ samples and the charged SA samples (third row in Table 9-8) shows that the average level of intergranular boron in the SA samples is about twice that in the WQ samples.

By quenching from 1323 K, and thereby "freezing-in" the lower level of segregation associated with that temperature, the characteristic intergranular fracture morphology shown in Figure 9-6(*b*) is obtained. Since the SA samples have experienced lower temperature annealing in the course of the heat treatment, the intergranular boron level in these samples is expected to be higher than in the WQ samples. If boron is indeed a cohesiveness improver in this system, then the grain boundaries

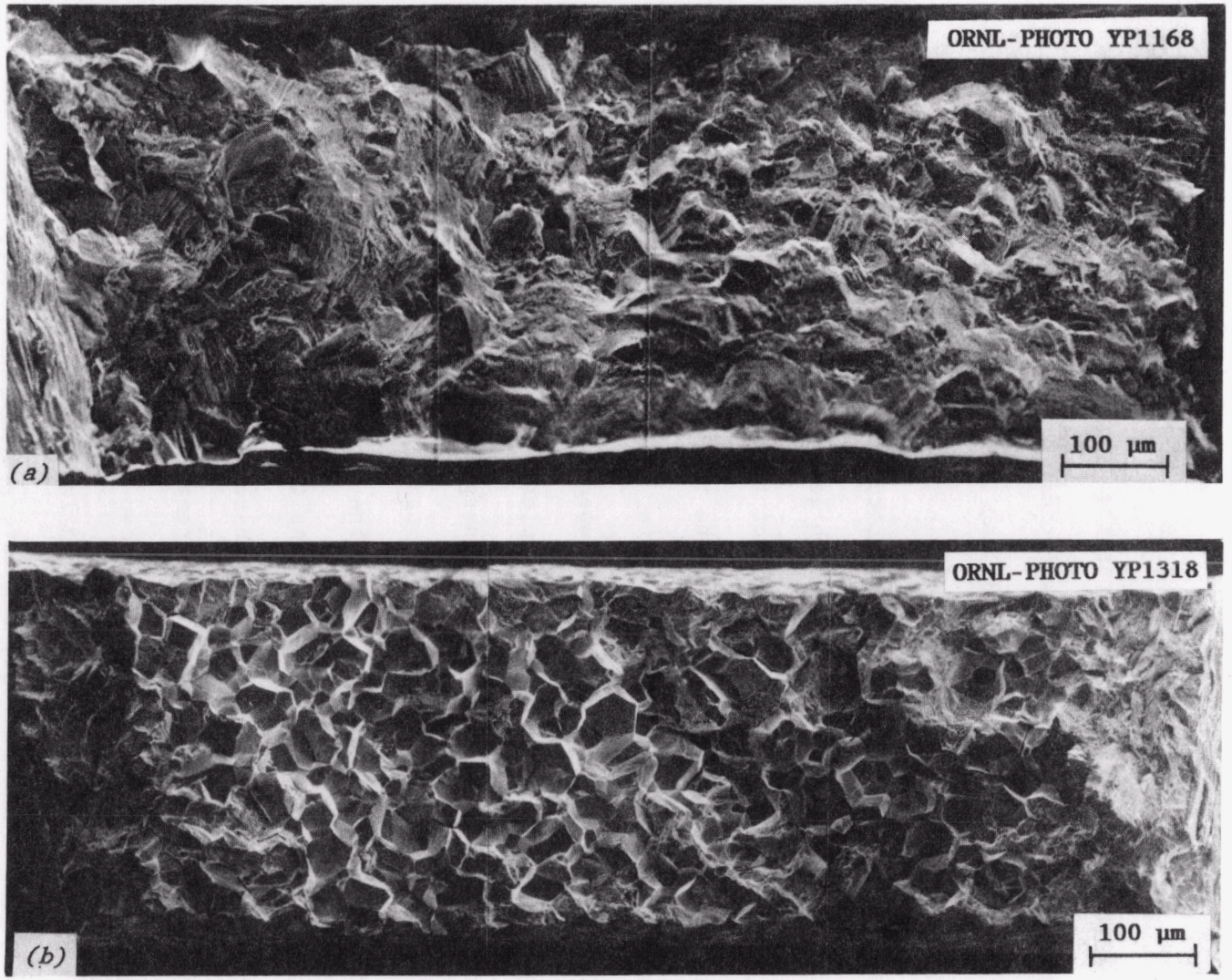

Figure 9-6. Scanning electron fractographs of samples given different thermal histories. (*a*) Step annealed, uncharged. (*b*) Water quenched, uncharged. (*c*) Step annealed, hydrogen charged (p. 199).

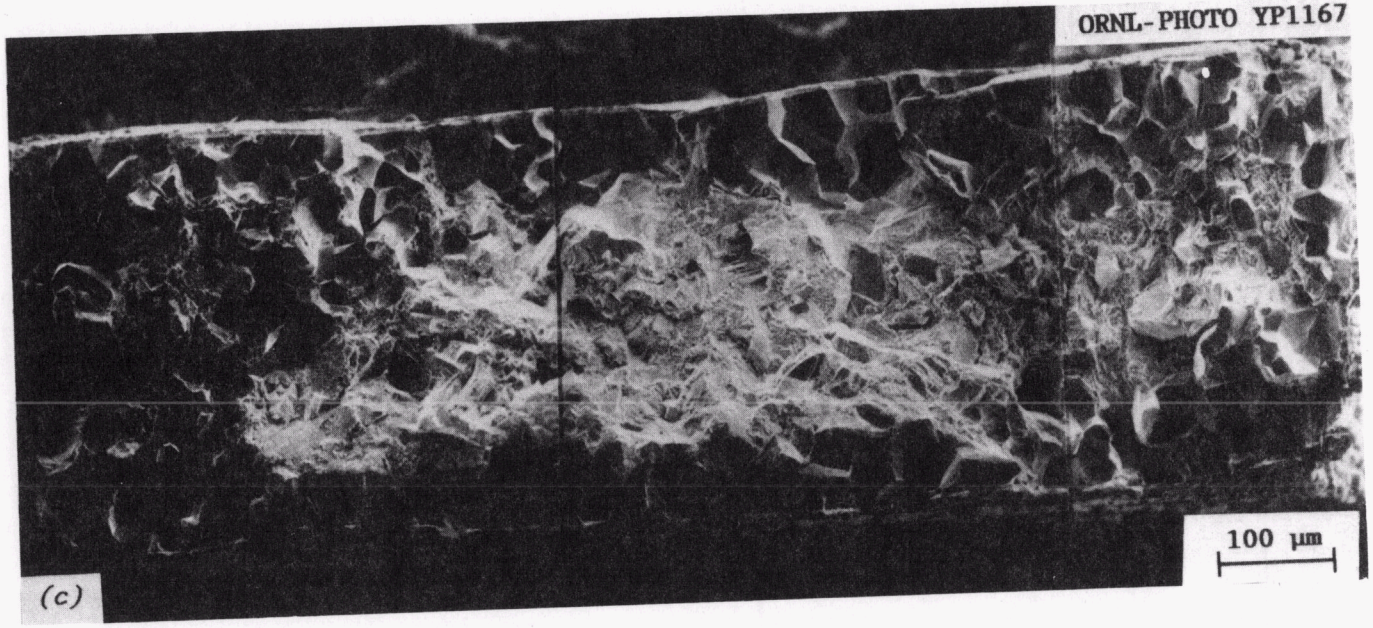

Figure 9-6. (*c*) continued.

Table 9-8. Results of Auger analysis on samples with different thermal histories

Sample Number	Heat Treatment	H_2	Number	Average	B1 Standard Deviation
850014U	SA	No	10	0.27	0.50
850014T	SA	No	10	0.87	0.70
850014V	WQ	No	6	1.02	0.44
850014W	WQ	No	15	0.78	0.33
850014X2	SA	Yes	19	1.63	0.43
850014Y2	SA	Yes	23	1.54	0.41
850014E3	WQ + SA	Yes	11	1.60	0.59
850014F3	WQ + SA	Yes	24	1.64	0.56
850014U2	SA + WQ	No	14	1.07	0.30
850014V2	SA + WQ	No	13	1.03	0.33
850014W2	SA + WQ	No	6	0.95	0.20

in the SA samples should be more cohesive. This effect is reflected in the fracture morphology. The few grain boundaries exposed in the uncharged SA samples show a much lower boron level than the average level on grain boundaries in the charged samples where a much higher percentage of grain boundaries were exposed for analysis. This comparison suggests that those few grain boundaries that do fail in uncharged SA samples tend to be those with lower levels of boron enrichment, which further supports the correlation between boron segregation and enhanced grain boundary cohesion. Also, this observation experimentally shows the expected boundary-to-boundary variation of segregation level (mentioned in Section III).

In addition to the above experiments, a set of reversibility studies was conducted. In these experiments, a set of WQ samples was subjected to the SA treatment following water quenching and a set of SA samples was water quenched following the SA treatment. These thermal histories are also indicated in Table 8-3. Figure 9-7(*a*) and (*b*) compares the fracture morphology obtained in each case. It is to be noted that the WQ + SA samples had to be hydrogen charged in order to expose enough grain boundaries for a representative analysis. The last two rows of Table 9-8 show the results obtained from the Auger analysis on these samples. Noteworthy is the fact that the segregated boron level in the WQ + SA samples is almost identical to that in the SA samples (third row) while the SA + WQ samples exhibit levels comparable to the WQ samples. A similar effect of reversibility is noted in the fracture morphology.

These observations lead to the conclusion that the effects of thermal history on intergranular boron enrichment (and its subsequent

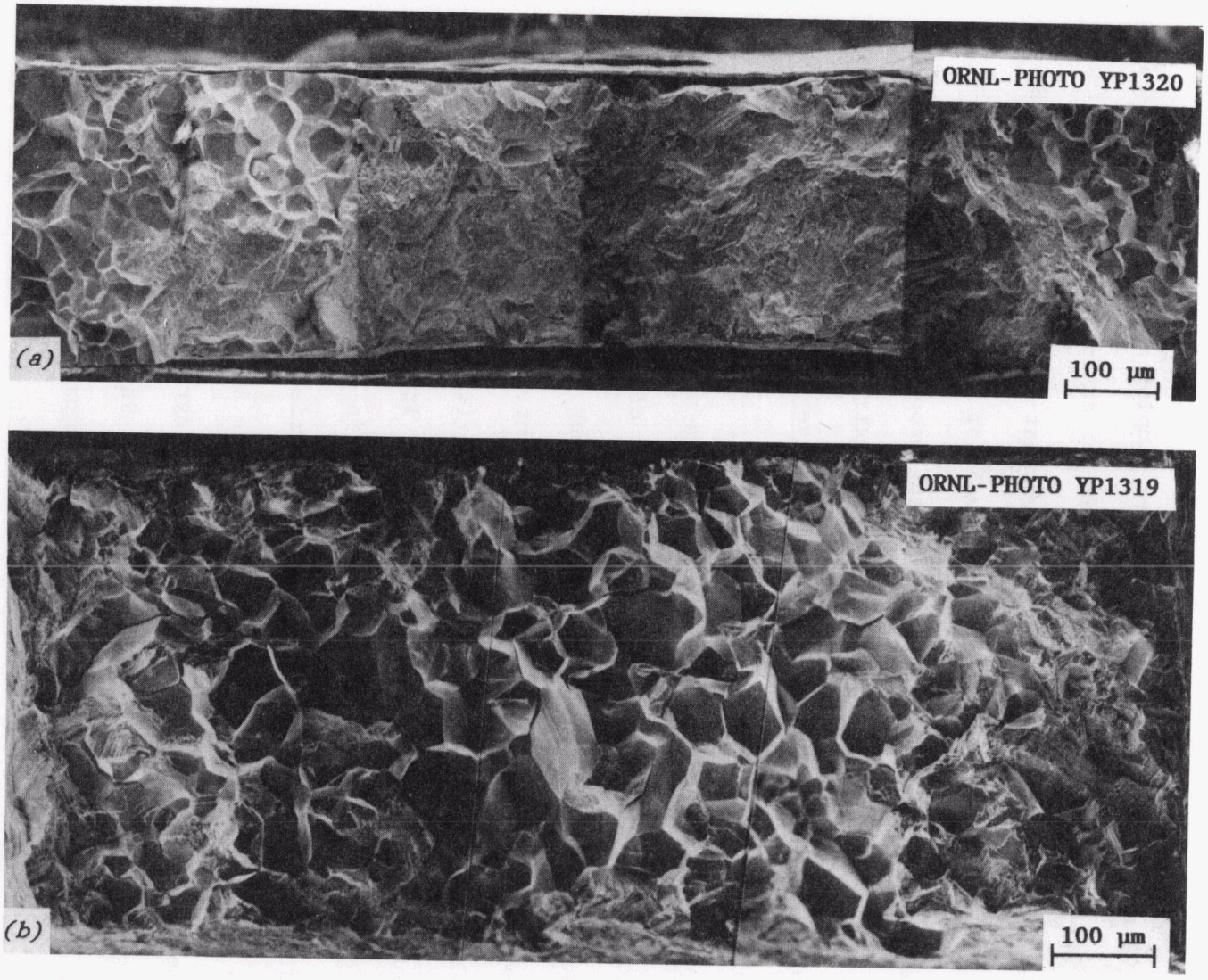

Figure 9-7. Scanning electron fractographs of samples used in reversibility studies. (*a*) Water quenched then step annealed, hydrogen charged. (*b*) Step annealed then water quenched, uncharged.

effect on fracture morphology) are entirely reversible. This further indicates that the driving force for intergranular segregation of boron in Ni_3Al is equilibrium in nature and not (for example) the result of a vacancy flux to the grain boundaries during cooling, or any other transient phenomena that would permit desegregation to occur after long times at service temperatures.

V. EFFECT OF HYDROGEN CHARGING ON LEVEL OF SEGREGATION

As mentioned in Chapter 8 and Section IV of this chapter, cathodic hydrogen charging has been used extensively in this research to open up cohesive grain boundaries for Auger analysis. Since the charging was carried out at room temperature, it was not expected to effect the level of segregant. However, this was verified experimentally in the following manner.

One way to verify this would be to compare the analyses from an uncharged and a charged specimen with the same thermal history. It was shown in Section IV of this chapter that the fracture morphology of WQ samples containing 300 wppm boron was primarily intergranular. Hence the level of segregant (boron) in a charged, WQ sample (sample 850014Y) was compared to that in uncharged, WQ samples (samples 850014V and 850014W). Table 9-9 shows the Auger results for three samples and identifies the charged and uncharged samples. As can be seen, there is no difference between the charged and the uncharged cases and thus it is concluded that cathodic hydrogen charging does not alter the level of segregation at a grain boundary.

Table 9-9. Results of Auger analysis of uncharged and hydrogen charged samples with similar thermal histories

Sample Number	Hydrogen Charged?	AES Results		
		N	Average B1	Standard Deviation
850014Y	Yes	11	0.87	0.35
850014V	No	6	1.02	0.44
850014W	No	15	0.78	0.33

VI. ADEQUACY OF COOLING RATE OBTAINED IN WATER QUENCHING

An important variable in the study of the effects of thermal history is the cooling rate obtained in water quenching. The uneven cooling through the cross section of the samples could yield a cooling rate at the center slow enough to permit dynamic redistribution of boron in the course of quenching. Hence the level of boron measured at the grain boundaries of such water quenched samples would not be representative of the equilibrium level at the quenching temperature.

The cooling rate at the centerline of the samples should be somewhat lower than the 3.5 to 5 $\times 10^3$ C/s measured (Section IV, Chapter 8) at the surface of the samples. If the level of boron at the grain boundaries close to the centerline does not show any significant difference from that at the grain boundaries close to the surface, then it is reasonable to assume that direct water quenching is adequate to arrest the equilibrium boron level achieved at the quenching temperature.

To this end, data from one water quenched sample from each of the heats containing 100, 500 and 1000 wppm boron were analyzed as follows. The boron level (B1) for each intergranular point analyzed was plotted as a function of distance of such points from the centerline of the sample. Figure 9-8(*a*), (*b*) and (*c*) shows these plots for the three samples.

As is clearly evident from this figure, there is no distinct trend in the level of boron as a function of distance from the sample centerline. Hence, it is concluded that the cooling rate experienced by the samples during water quenching is quite adequate to arrest the equilibrium boron level achieved at the quenching temperature.

AC-148

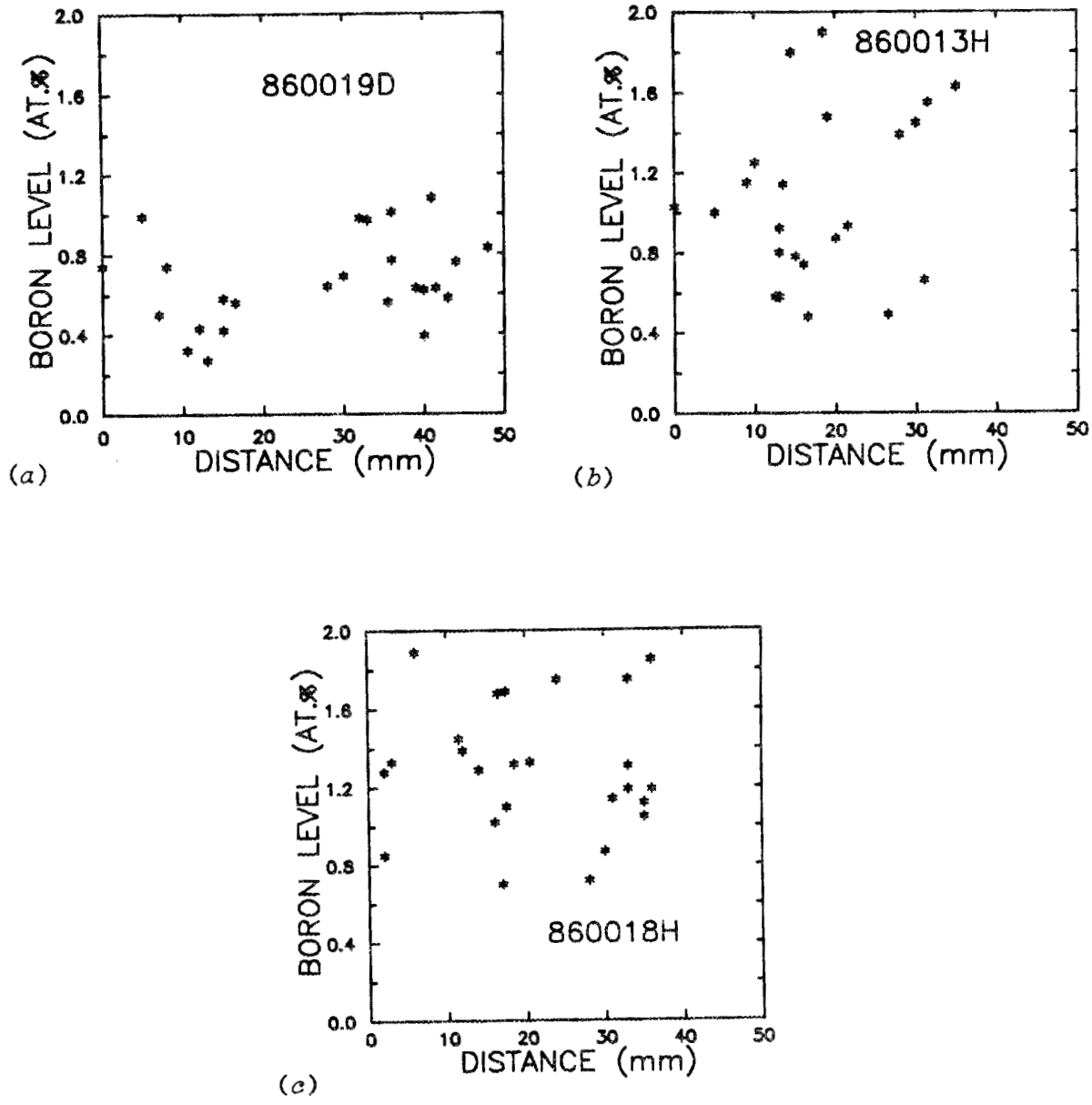

Figure 9-8. Distribution of intergranular boron as a function of distance from the centerline of the sample. (*a*) 100 wppm boron, sample 860019D. (*b*) 500 wppm boron, sample 860013H. (*c*) 1000 wppm boron, sample 860018H.

VII. EFFECT OF BULK BORON LEVEL

In addition to thermal history, the concentration of solute in the bulk lattice should also effect the level of segregated solute (Ref. 63). In order to verify this in the case of boron segregation in Ni_3Al, three alloys were tested. The aluminum content of each alloy was the same (nominally 24 at. %) whereas the boron levels were 100, 500 and 1000 wppm. Samples from each of these alloys were given two widely different thermal treatments: one set was WQ while another set was slowly cooled (SC). These heat treatments are described in Section III of Chapter 8. The samples and their heat treatments are identified in Table 8-3.

Figure 9-9 shows a collage of the fracture morphology of the WQ samples while Figure 9-10 shows a collage for the SC samples. It is evident from Figure 9-9 that the degree of intergranular fracture obtained in the WQ samples decreases as the bulk level of boron is increased; the 500 and 1000 wppm boron samples required hydrogen charging in order to expose enough grain boundaries for analysis. Also, the strong effect of thermal history (mentioned in Section IV) can be seen by comparing the uncharged fracture surfaces of the 100 ppm boron alloy in the two heat treatment conditions. Even this alloy required hydrogen charging in the SC condition to expose enough grain boundaries for analysis.

Table 9-10 summarized the results from the Auger analysis of this group of samples. Figure 9-11 graphically depicts the weighted averages of B1 as a function of bulk boron content for the WQ samples (uncharged and charged) while Figure 9-12 shows a similar effect for the SC samples. In both of these figures the results from the 300 wppm alloy have been

AC-149

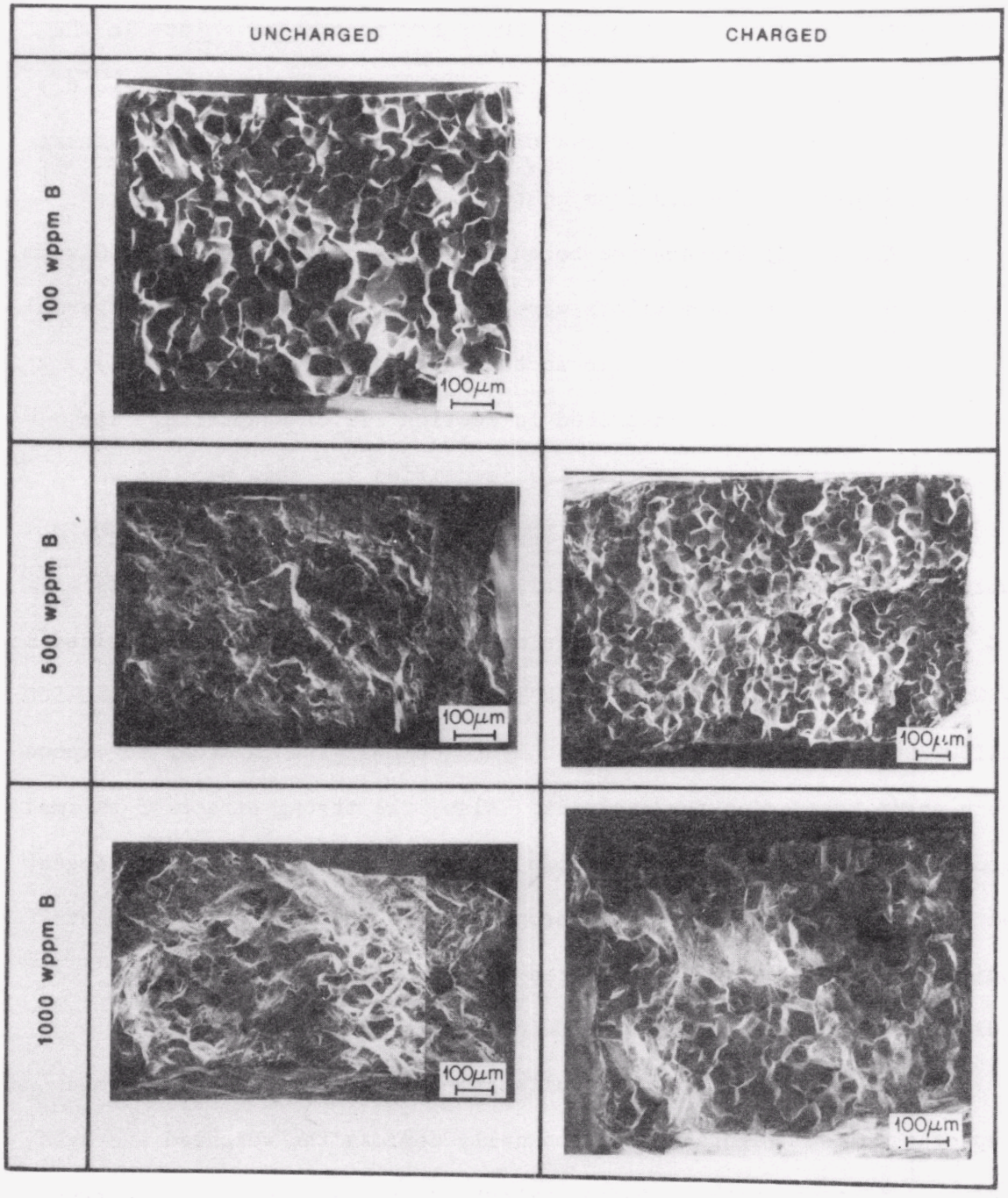

Figure 9-9. Scanning electron fractographs of WQ samples containing different levels of boron in the bulk.

AC-150

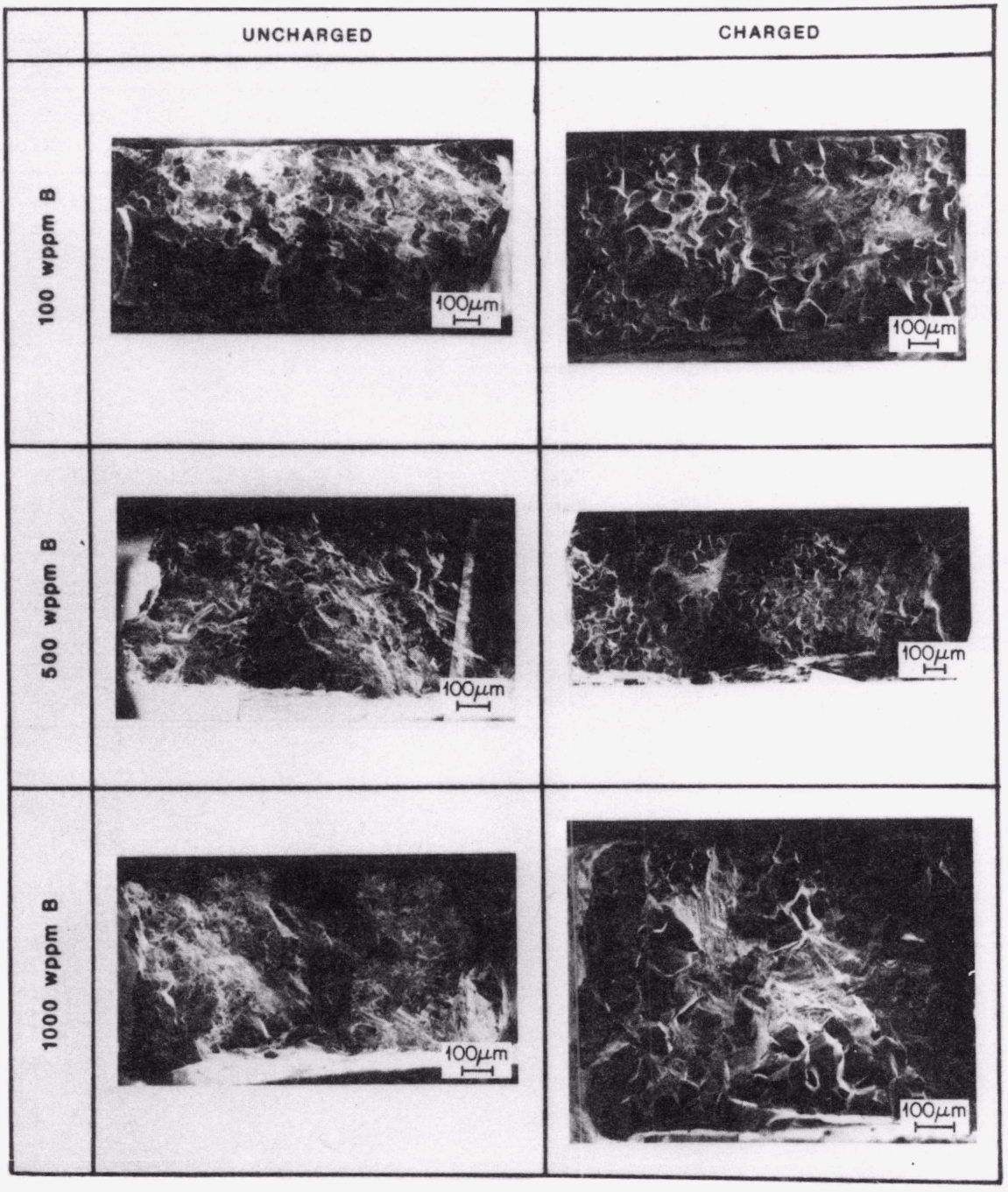

Figure 9-10. Scanning electron fractographs of SC samples containing different levels of boron in the bulk.

Table 9-10. Results of Auger analysis on samples containing different levels of boron in the bulk and subjected to different thermal treatments

Sample Number	Boron Level	Heat Treatment	H_2?	AES Results		
				Number	Average B1	Standard Deviation
860019A	100	SC	No	15	0.74	0.49
860019B	100	SC	Yes	26	1.10	0.26
860019C	100	SC	Yes	28	1.36	0.74
860019D	100	WQ	No	25	0.67	0.22
860019E	100	WQ	No	25	0.52	0.19
860013A	500	SC	No	14	0.23	0.17
860013B	500	SC	Yes	24	2.03	1.56
860013C	500	SC	Yes	28	1.50	0.51
860013D	500	WQ	No	18	0.97	0.27
860013E	500	WQ	Yes	27	0.82	0.18
860013H	500	WQ	Yes	25	1.18	0.56
860018A	1000	SC	No	3	0.47	0.11
860018B	1000	SC	Yes	22	2.35	0.53
860018C	1000	SC	Yes	20	2.02	0.35
860018D	1000	WQ	No	24	1.09	0.41
860018E	1000	WQ	Yes	25	1.44	0.37
860018H	1000	WQ	Yes	25	1.29	0.34

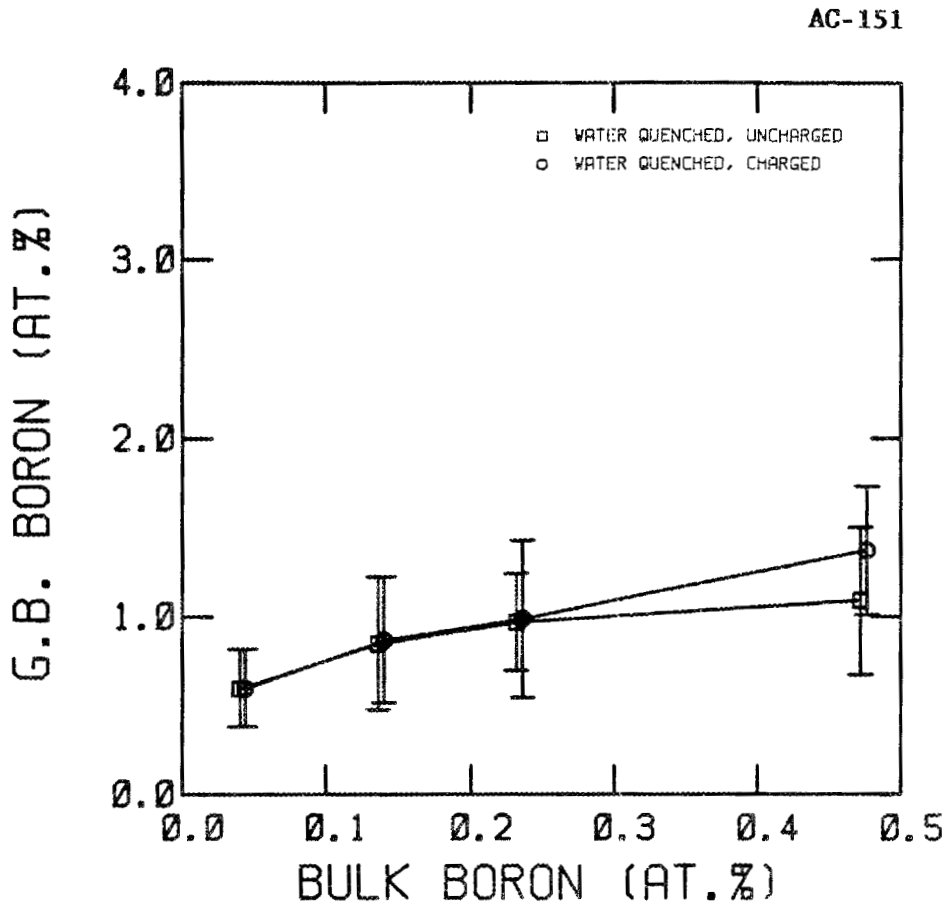

Figure 9-11. Level of segregated boron (B1) as a function of bulk boron level; WQ samples.

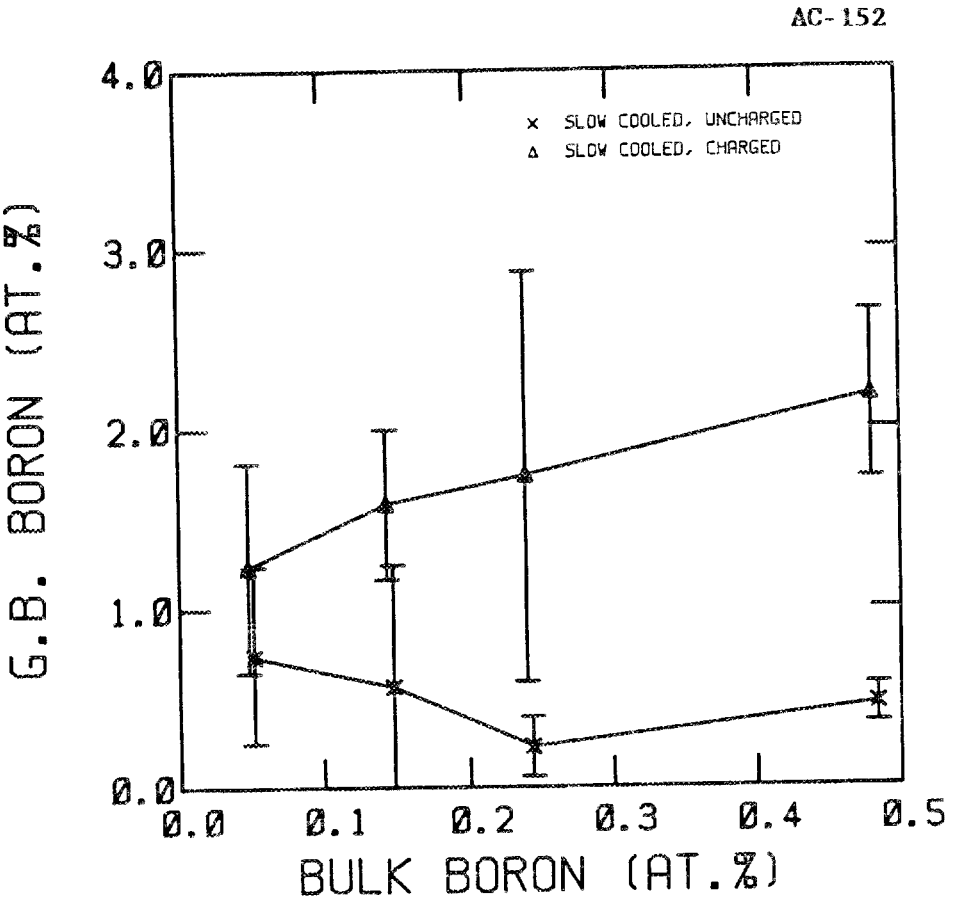

Figure 9-12. Level of segregated boron (B1) as a function of bulk boron level; SC and SA samples.

incorporated with the assumption that the step annealing and the slow cooling are equivalent thermal treatments. In each case, the level of measured boron at the grain boundaries is higher for the charged samples than the uncharged ones; this reiterates the importance of hydrogen charging in exposing a representative set of grain boundaries for analysis. Figure 9-13 shows the weighted averages of B1 for the two heat treatment conditions as a function of bulk boron level (except for the 100 and 300 wppm boron WQ samples, all others are in the charged condition). This figure shows the potent effect of thermal history on the level of segregation and also shows that the level of segregation increases with the bulk solute level. It is to be noted, however, that a tenfold increase in the bulk solute level (100 to 1000 wppm boron) does not lead to a tenfold increase in the level of segregated solute. This hints strongly to a saturation phenomena at the grain boundaries; this will be discussed in greater detail in Chapter 10.

Figures 9-14 through 9-16 show the distribution of segregated solute in terms of the percentage of analyzed points exhibiting the levels of boron indicated. These figures were obtained using the range allocation scheme shown in Table 9-6; also, in cases where multiple samples with similar thermal histories and charging condition were analyzed, their cumulative effect is shown. These figures are informative in that they show that while there is indeed a wide boundary-to-boundary variation in the segregation level, the trends predicted by McLean (Ref. 63) still hold true. Specifically, for the same thermal history, the distributions move towards higher boron levels with increasing bulk boron level. Also, for the same bulk boron level, the distributions move towards higher

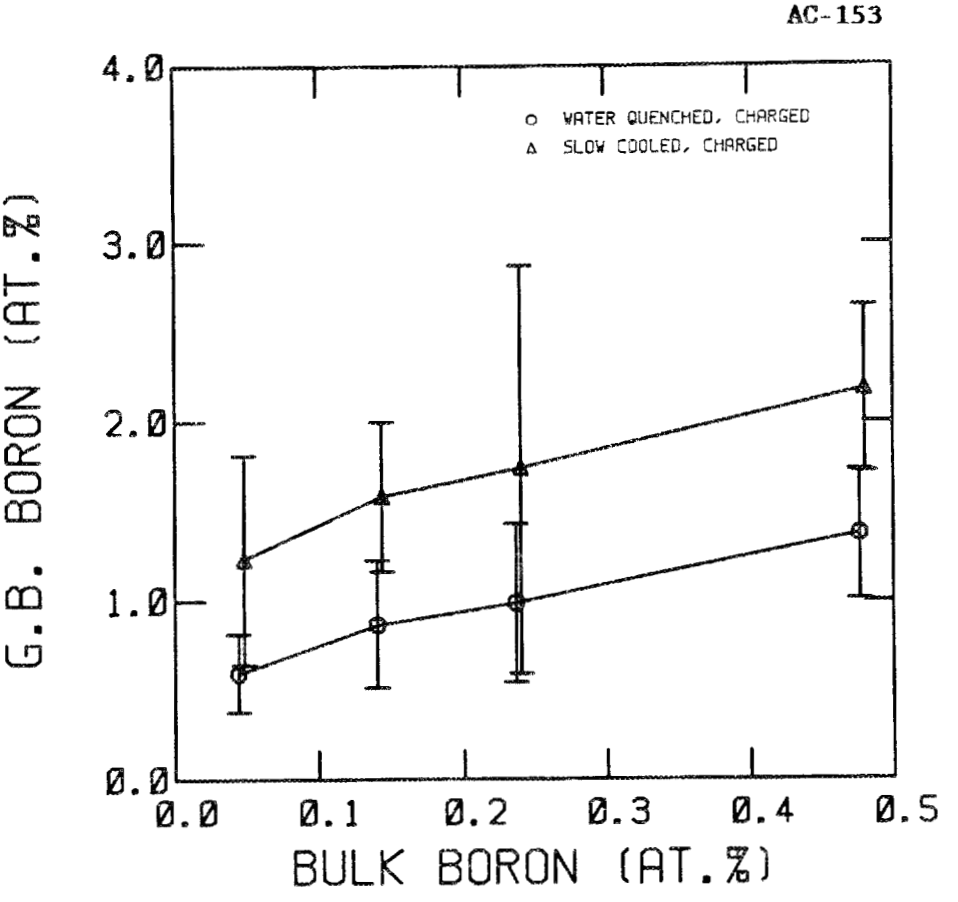

Figure 9-13. Level of segregated boron (B1) as a function of bulk boron level and thermal history.

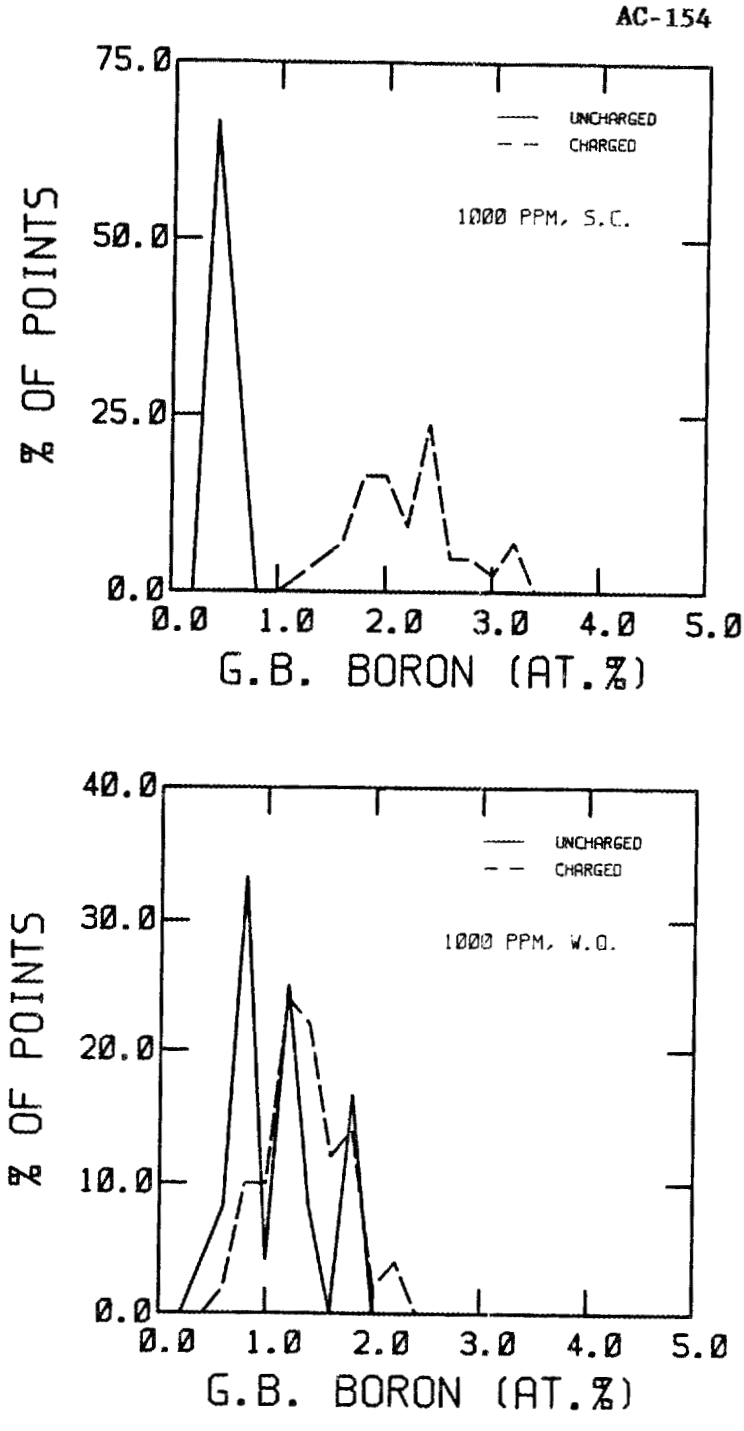

Figure 9-14. Distribution of segregated boron - effect of hydrogen charging: (*a*) SC samples, (*b*) WQ samples.

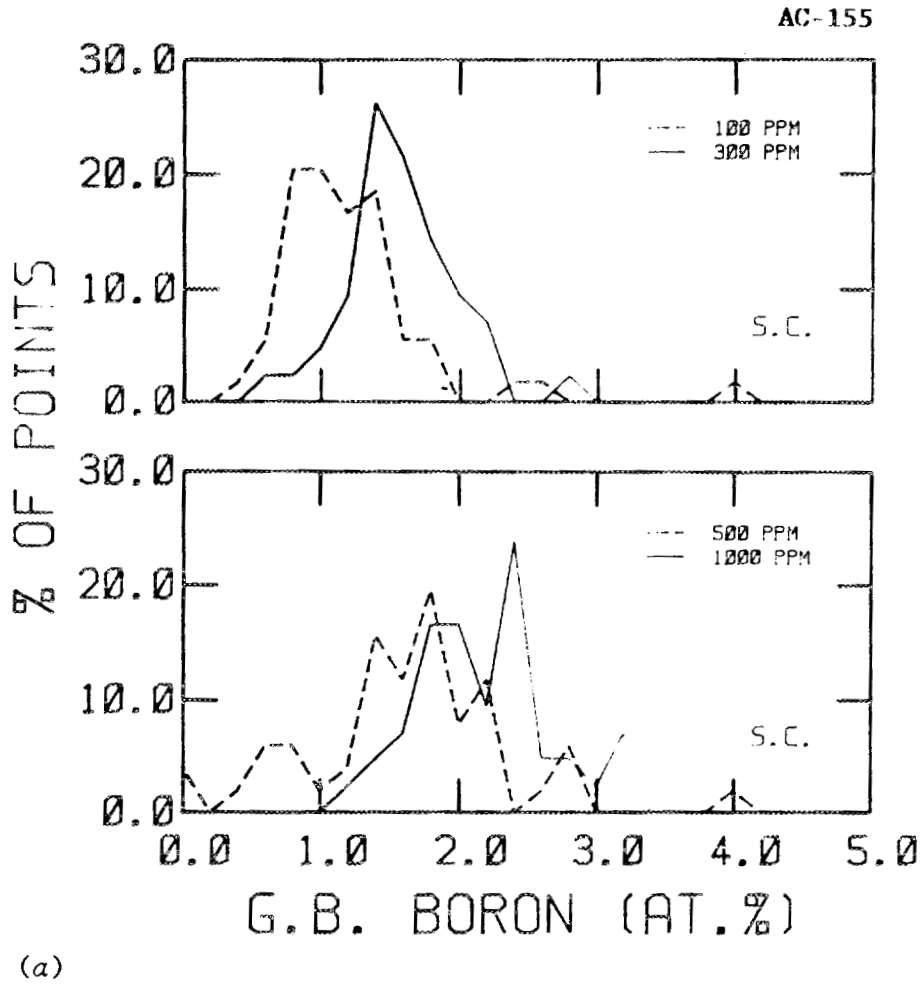

(*a*)

Figure 9-15. Distribution of segregated boron - effect of bulk boron level: (*a*) SC or SA samples, (*b*) WQ samples (p. 217).

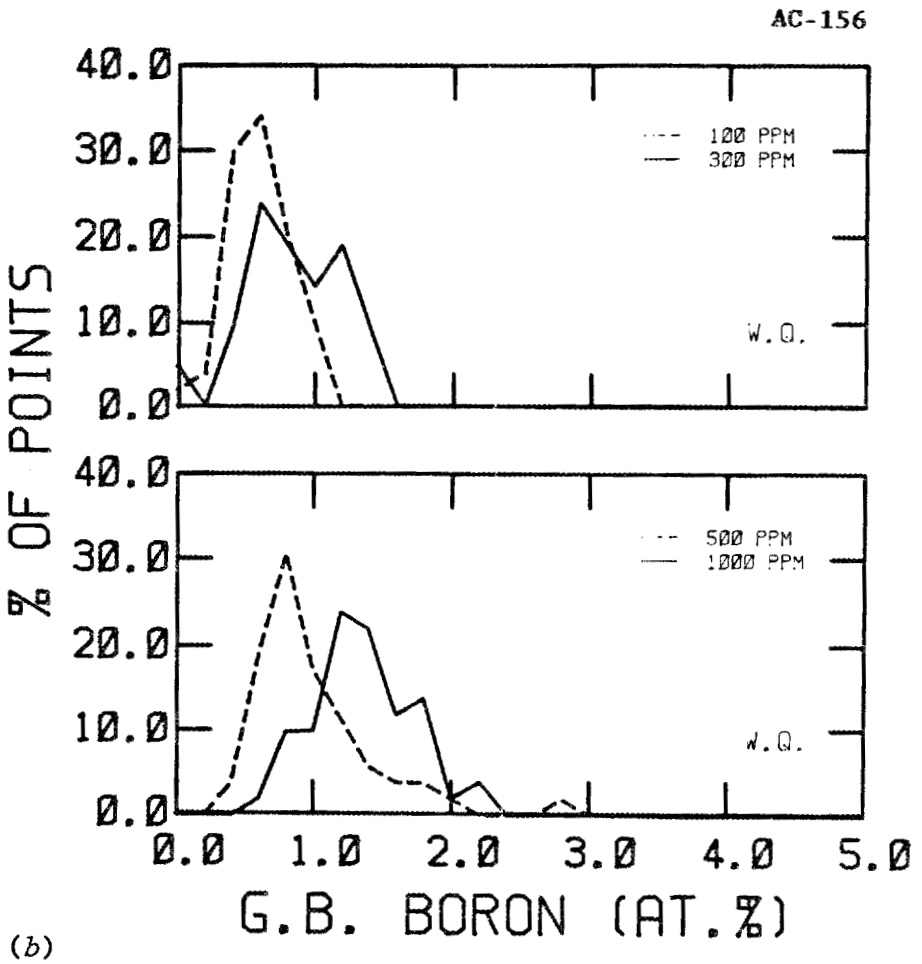

(*b*)

Fig. 9-15. (*b*) continued.

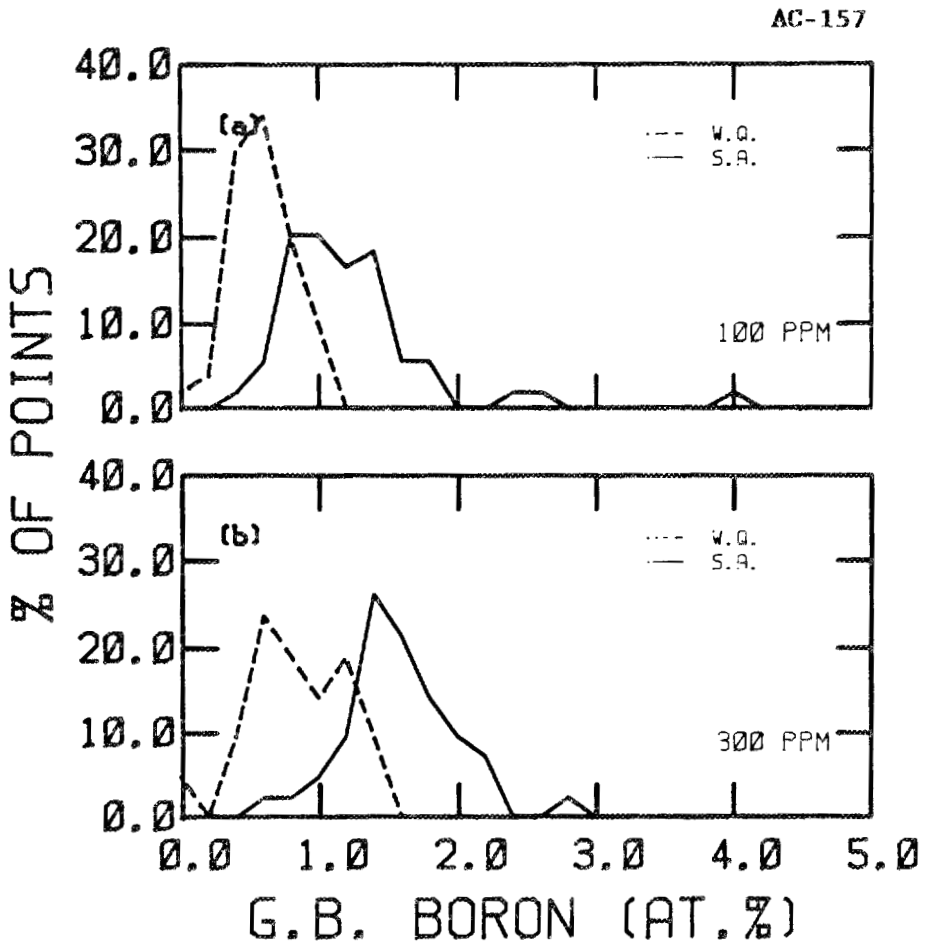

Figure 9-16. Distribution of segregated boron - effect of thermal history: (*a*) 100 wppm boron in the bulk, (*b*) 300 wppm boron in the bulk, (*c*) 500 wppm boron in the bulk, and (*d*) 1000 wppm boron in the bulk (p. 219).

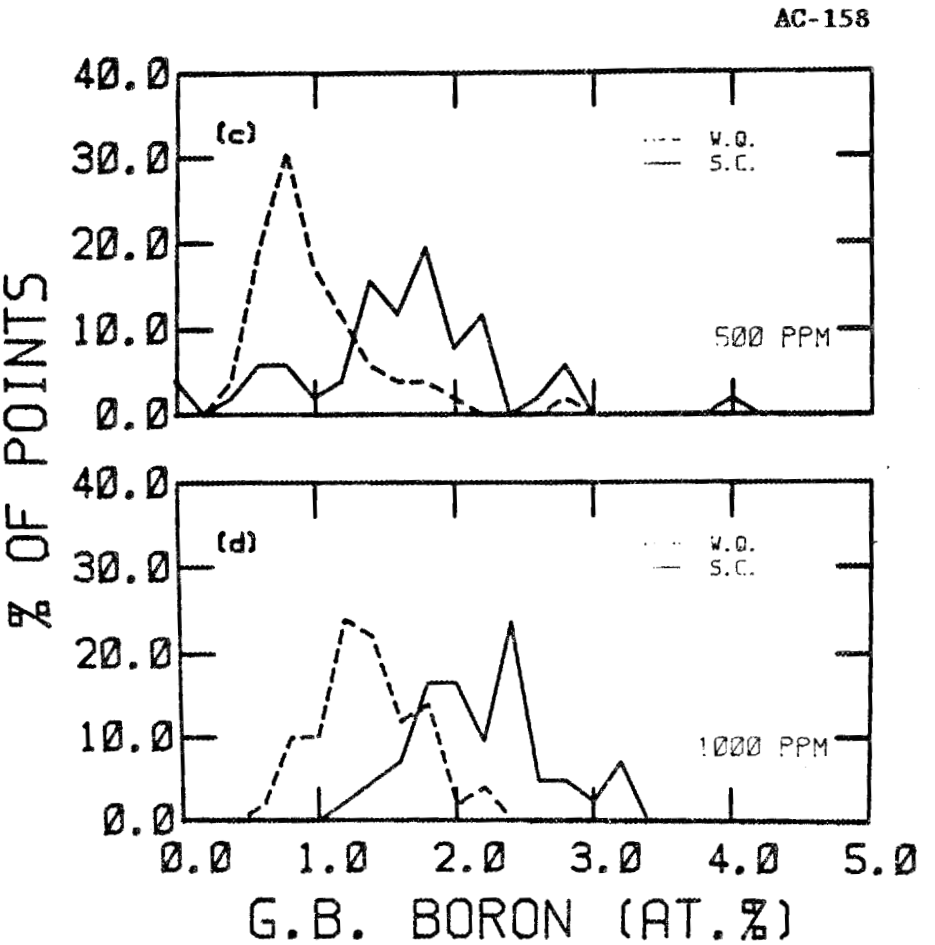

Fig. 9-16. (*c*) and (*d*) continued.

segregation levels as the thermal history is changed for WQ to SC or SA. The effect of hydrogen charging on enhancing the measured level of segregation is also seen.

VIII. KINETIC ASPECTS

The kinetic aspects of boron segregation in Ni_3Al were addressed in this study and to this end two of the alloys (100 and 1000 wppm boron) were given the thermal treatments shown in Table 8-4. As can be seen, there were two main classes of experiments: isothermal annealing and isochronal annealing.

Table 9-11 shows the results of Auger analysis (in terms of B1) for all the samples analyzed in this set. While a detailed discussion of the rate of segregation will be postponed until Chapter 10, the general trends can be discussed here.

In order to evaluate the effect of time at a given temperature, two limiting values were selected. Since all the samples in this phase of the study were water quenched prior to the isothermal or isochronal annealing, the grain boundary boron level at the start of these treatments can be assumed to be that obtained for the WQ samples mentioned in Section VII. The effect of time at various temperatures is shown for the two alloys in Figures 9-17 through 9-19 where the WQ values are located at 0 time. At the other end are plotted the SC values since these can be assumed to be the maximum values attainable at these temperatures. These values are arbitrarily assigned a time of 100,000 minutes; in all these figures, assigning times longer than 10,000 minutes to these SC values does not alter the analysis very much since the segregation levels have saturated at these

Table 9-11. Results of Auger analysis on samples used in the kinetics studies

Sample Number	Boron Level	Heat Treatment		Auger Analysis Results		
		Temperature	Time	Number	Average B1	Standard Deviation
860019A2	100	700	1	25	0.77	0.29
860019B2	100	700	1	26	0.89	0.28
860019E2	100	700	1,000	25	0.87	0.39
860019F2	100	700	1,000	25	0.80	0.24
860019M2	100	700	10,000	27	0.72	0.24
860019N2	100	700	10,000	25	1.06	0.43
860019I	100	900	1	24	0.71	0.27
860019J	100	900	1	25	0.66	0.22
866019M	100	900	1,000	25	0.82	0.24
8600190	100	900	1,000	26	0.48	0.22
860019W2	100	500	1,000	25	1.09	0.48
860019X2	100	500	1,000	26	1.08	0.34
860019U2	100	600	1,000	23	0.95	0.27
860019T2	100	600	1,000	25	1.13	0.61
860018K	1,000	700	1	27	1.21	0.35
860018L	1,000	700	1	27	1.16	0.58
860018M	1,000	700	1,000	33	1.81	1.15
860018N	1,000	700	1,000	25	1.59	0.36
860018R	1,000	700	10,000	25	1.89	0.77
860018S	1,000	700	10,000	27	1.78	0.89
860018V	1,000	500	1,000	27	1.97	0.67
860018W	1,000	500	1,000	25	2.39	0.65
860018Y	1,000	600	1,000	28	2.26	0.77
860018Z	1,000	600	1,000	27	2.02	0.79
860018B2	1,000	500	1	26	1.81	0.40
860018D2	1,000	500	1	26	1.63	0.38
860018F2	1,000	500	10	27	1.64	0.50
860018G2	1,000	500	10	26	2.08	0.40
860018J2	1,000	500	100	30	2.37	1.12
860018K2	1,000	500	100	27	1.92	0.44
860018N2	1,000	500	10,000	26	1.92	0.41
860018O2	1,000	500	10,000	28	2.12	0.82

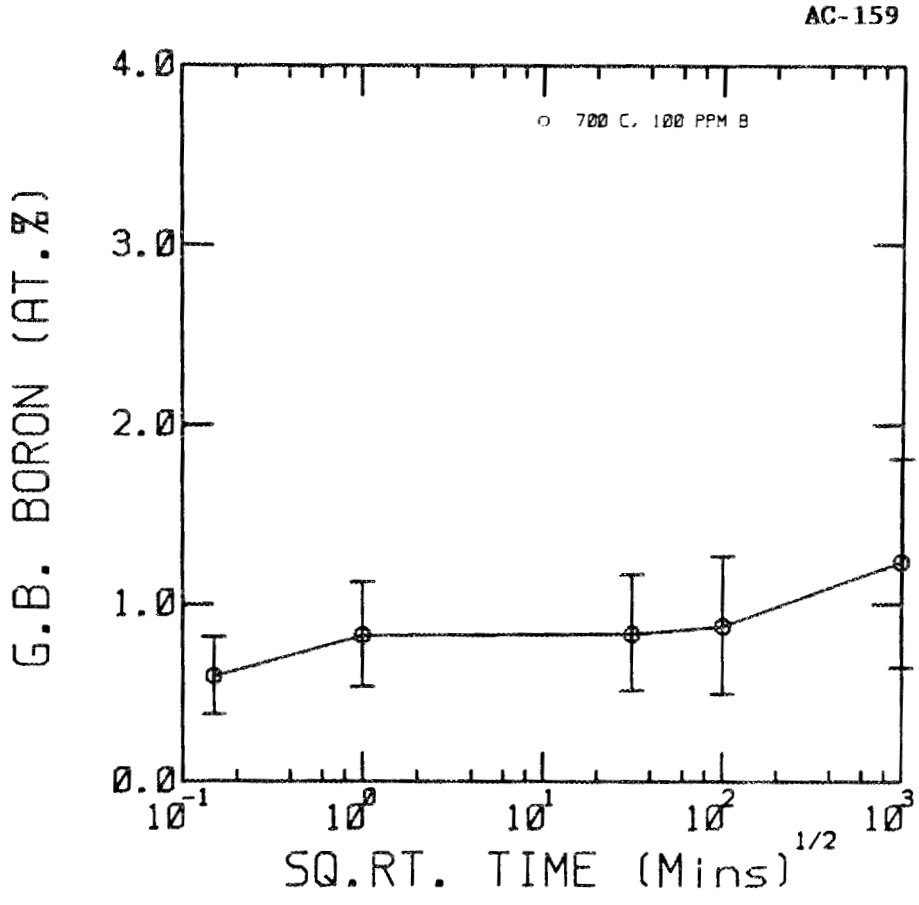

Figure 9-17. Grain boundary boron level (B1) as a function of time at 700°C for the alloy containing 100 wppm boron in the bulk.

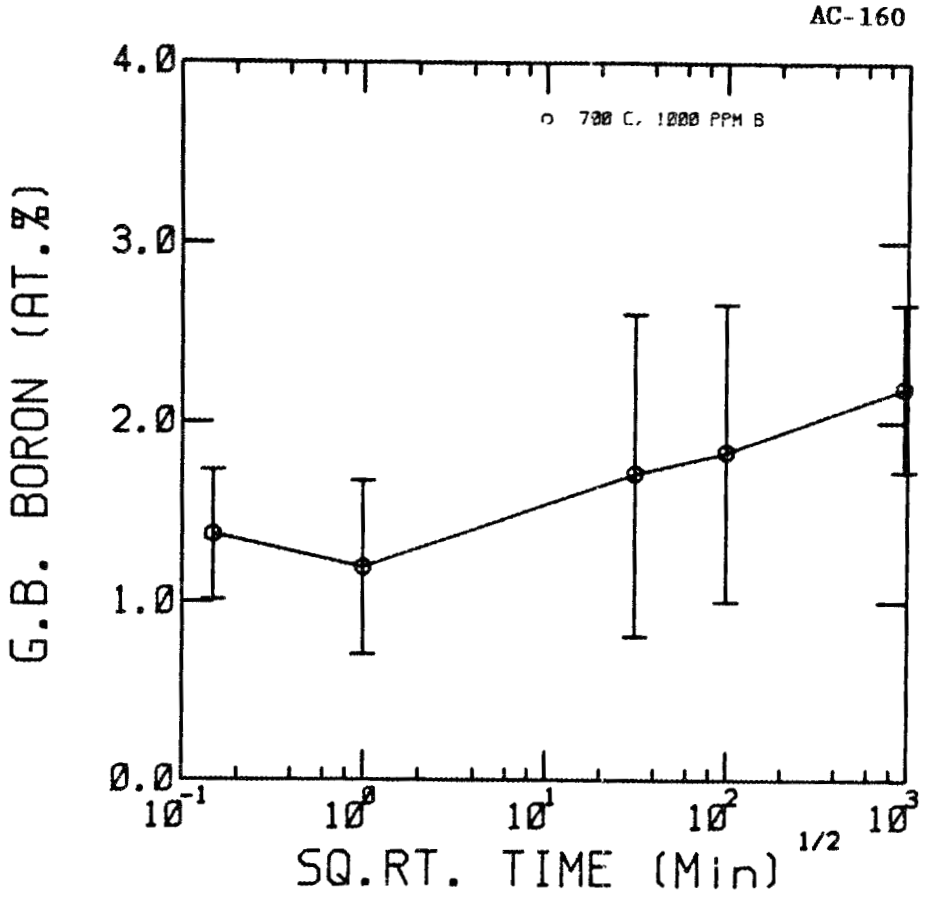

Figure 9-18. Grain boundary boron level (B1) as a function of time at 700°C for the alloy containing 1000 wppm boron in the bulk.

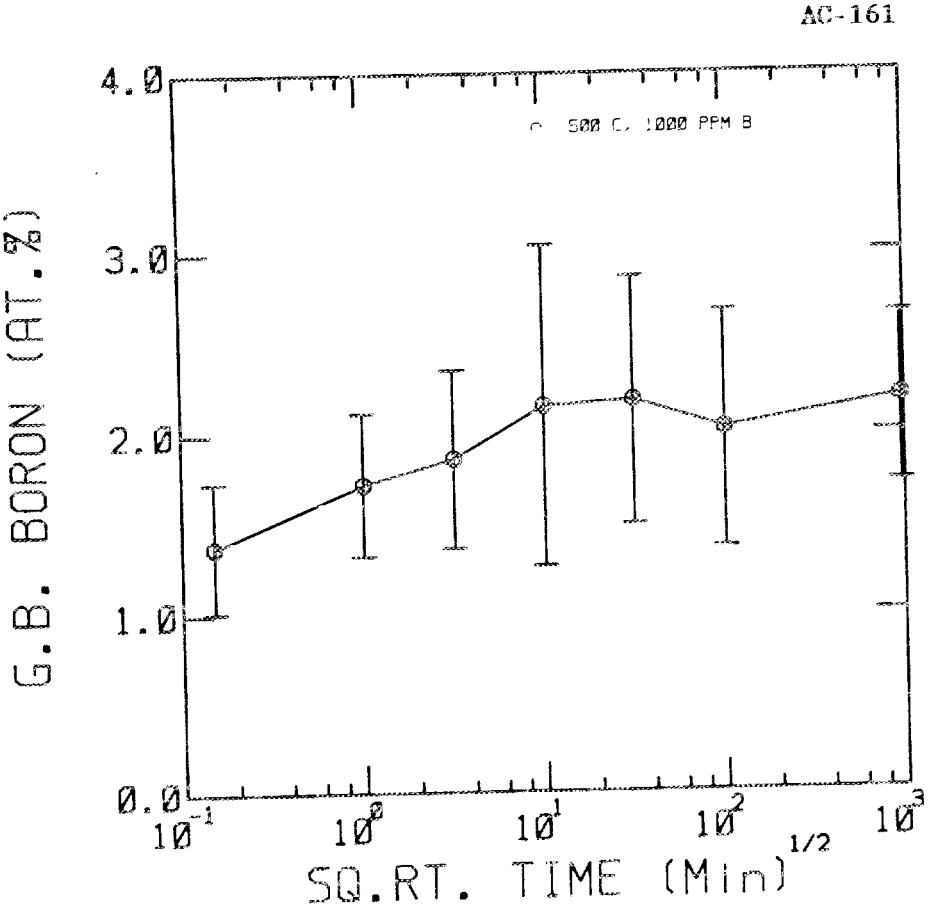

Figure 9-19. Grain boundary boron level (B1) as a function of time at 500°C for the alloy containing 1000 wppm boron in the bulk.

values. The important conclusion to be drawn from these figures is that, even at low temperatures, equilibrium is attained at a fast rate; quantification of this rate will be done in Chapter 10.

Figures 9-20 and 9-21 show the effect of temperature on the equilibrium level of segregation for the two alloys. These were obtained from samples isochronally annealed for 1000 minutes. A distinct trend of decreasing segregant level with increasing temperature is easily seen; this is in keeping with the predictions from McLean's theory (Ref. 63). Similar plots for 1 minute and 10,000 minutes are shown in Figures 9-22 through 9-24. In these cases, only two temperatures were investigated for each time and thus the exact nature of the trend is in doubt, i.e., straight line vs other types of trends. Drawing from the conclusion of 1000-minute results (Figures 9-20 and 9-21), however, a straight line trend can be safely assumed.

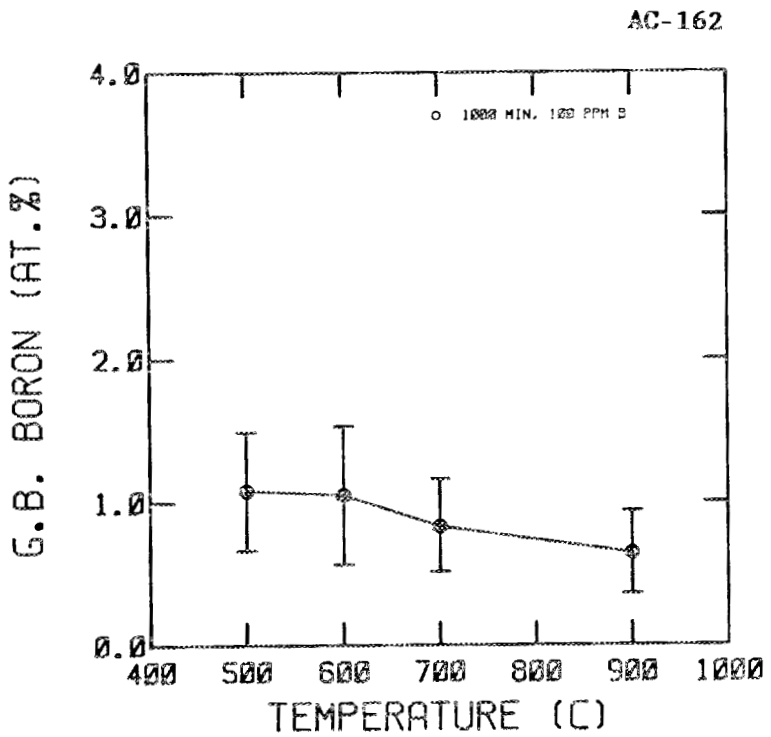

Figure 9-20. Grain boundary boron level (B1) as a function of temperature for an annealing time of 1000 minutes in the alloy containing 100 wppm boron in the bulk.

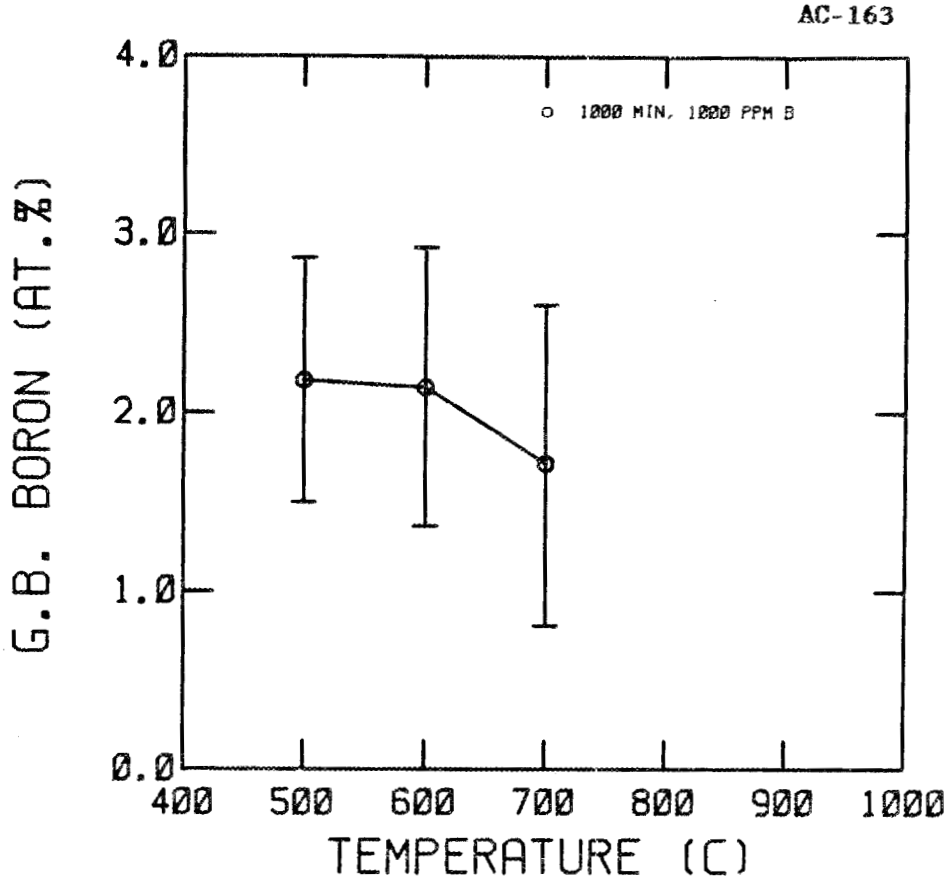

Figure 9-21. Grain boundary boron level (B_i) as a function of temperature for an annealing time of 1000 minutes in the alloy containing 1000 wppm boron in the bulk.

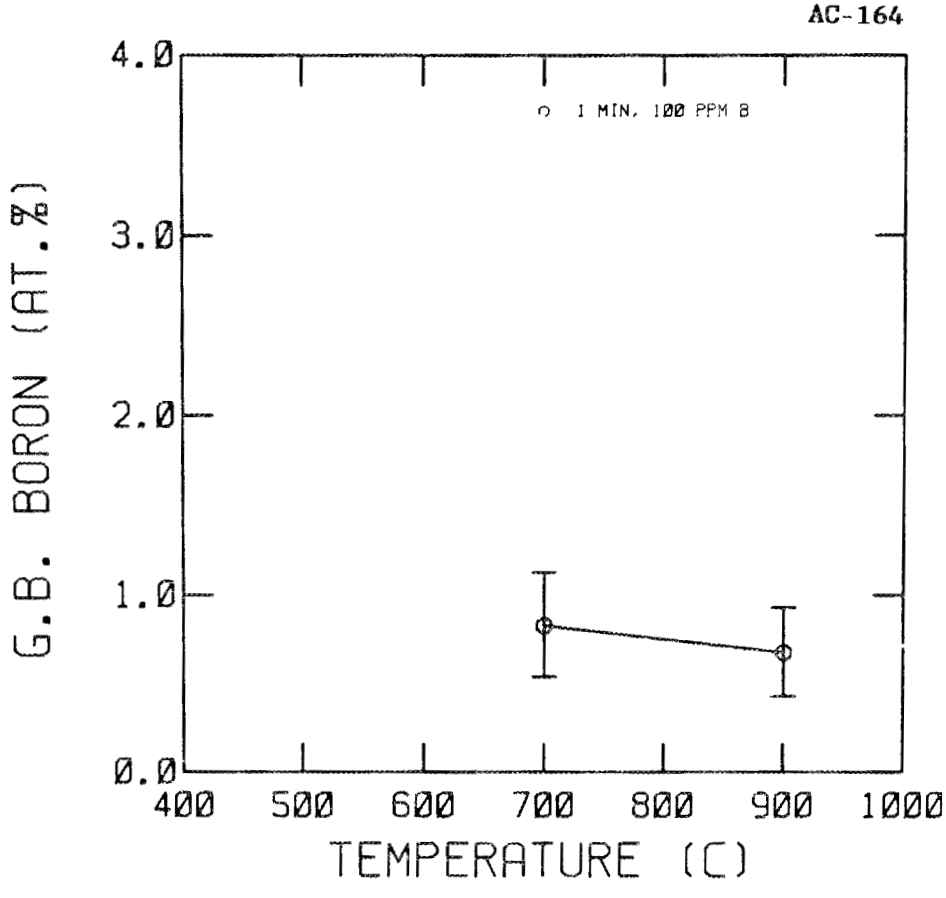

Figure 9-22. Grain boundary boron level (B1) as a function of temperature for an annealing time of 1 minute in the alloy containing 100 wppm boron in bulk.

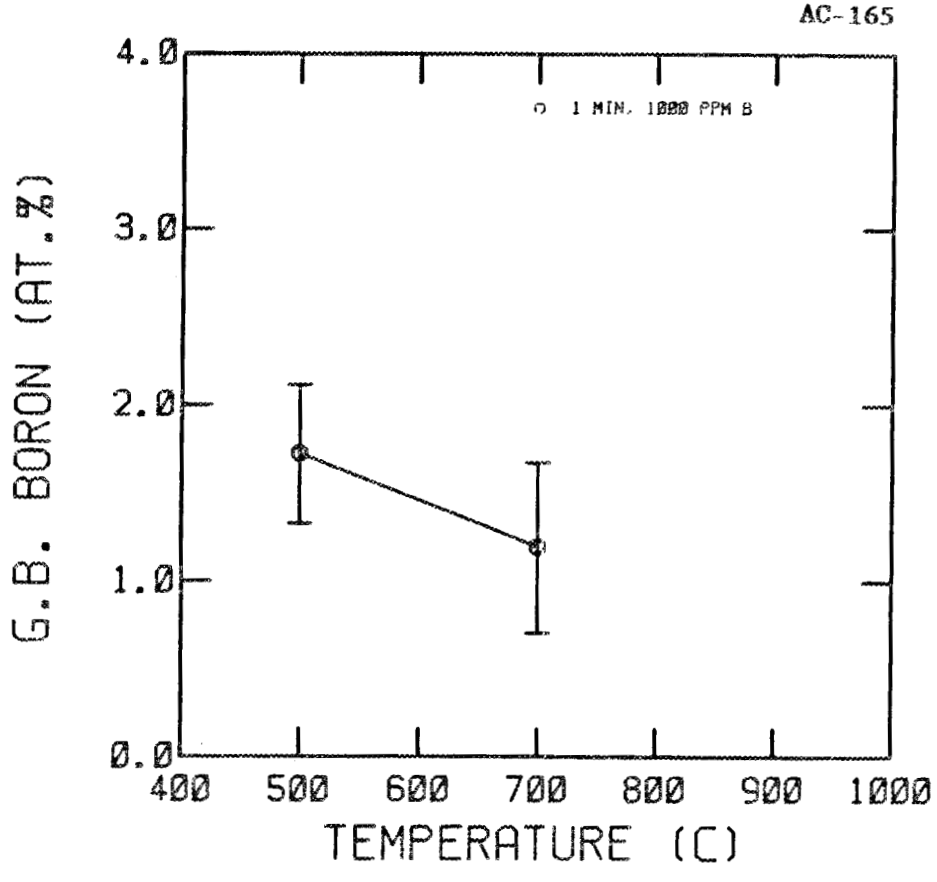

Figure 9-23. Grain boundary boron level (B1) as a function of temperature for an annealing time of 1 minute in the alloy containing 1000 wppm boron in the bulk.

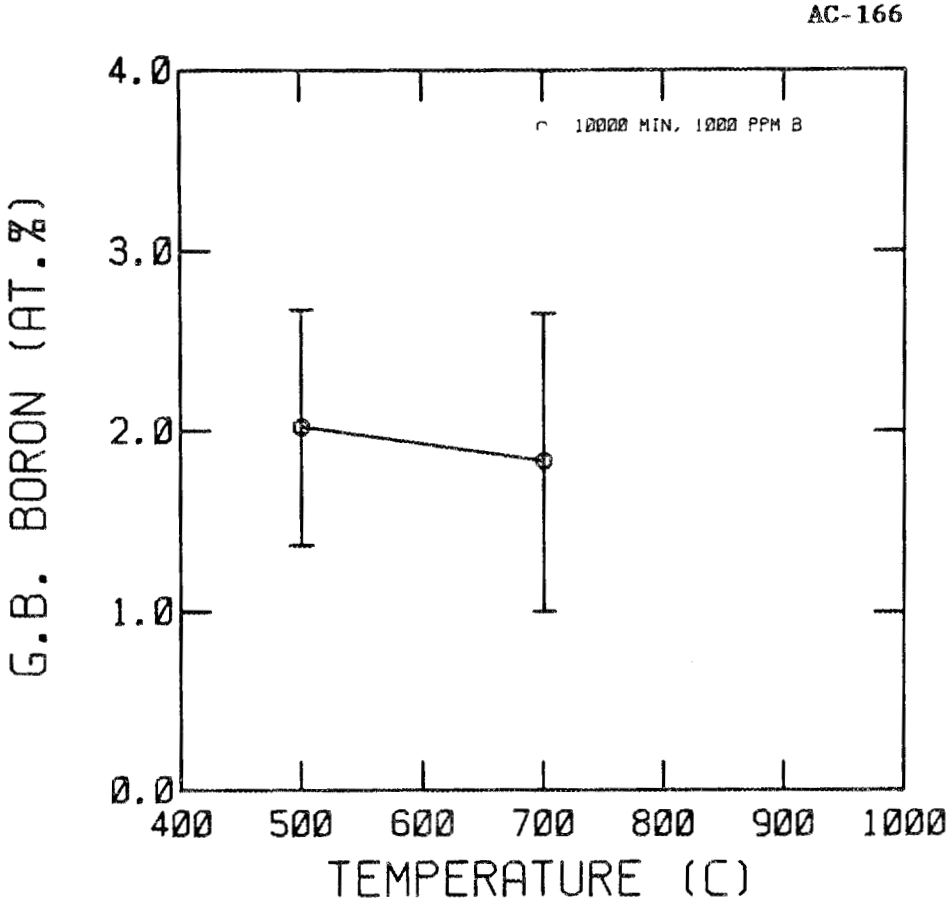

Figure 9-24. Grain boundary boron level (B1) as a function of temperature for an annealing time of 10,000 minutes in the alloy containing 1000 wppm boron in the bulk.

CHAPTER 10

DISCUSSIONS

I. INTRODUCTION

This chapter deals with the analysis of the data presented in Chapter 9. The detectability of boron in Auger analysis is shown to be adequate and the use of B1 (Appendix B) as the correct measure of the grain boundary boron content is rationalized. The binding energy for boron at the grain boundaries of Ni_3Al is calculated as a function of both bulk boron level and temperature. The kinetics of segregation are explicitly addressed and from this a value is found for the diffusion coefficient of boron in Ni_3Al. The problems associated with this calculation are addressed and a rationale presented for the very low value found in this work.

II. DETECTABILITY OF BORON IN AUGER ANALYSIS

The difficulty associated with quantifying the detectability limits (for elements) in AES is often circumvented by assuming that it is about 0.1% of the first monolayer of the surface. In certain cases where high spatial resolution or electron beam charging or damage limit the total primary electron beam current, however, the detectability may not be as low as 0.1%. Since boron is a low atomic number element, there is concern as to the detectability of boron in AES. The detectability limit for boron is thus calculated here to address this issue.

The quality (or usefulness) of Auger data is often related to the signal-to-noise (S/N) ratio of the data. If the S/N = 1, the signal is of the same intensity as the noise and is thus undetectable. The S/N required for unequivocal elemental identification is often arbitrary (operator determined). In this research, S/N = $\sqrt{2}$ was used as the required condition.

Reference 126 deals with a method used to determine the detectability limit of AES and the following is based on this approach. Figure 10-1 shows a nomogram relating a factor H to the primary beam current (I_B) and the analysis time per data channel (τ). The factor H is defined by:

$$H = (S/N) \; / \; [(a_x) \times (s_x)] \qquad \text{Equation (10-1)}$$

where a_x = The atom fraction for the element x within the analysed volume

s_x = Relative sensitivity factor for the element x from Ref. 116.

In the case of this research, the primary beam current used was about 3 nanoamperes (Section VI, Chapter 8). Also in most of the analyses, a 10-minute data acquisition time was used to collect 0 to 300 eV data using 0.5 eV per step. Hence the analysis time per data channel is:

$$\tau = [10 \times 60] \; / \; [(300) \; / \; (0.5)]$$

$$\text{or } \tau = 1 \text{ s}$$

The value of H corresponding to this combination of I_B and τ (from Figure 10-1) is about 600.

From Equation (10-1), the atom fraction of x is calculated as:

$$a_x = (1.41) \; / \; (600 \times 0.138)$$

hence $a_x = 0.02$.

Thus it would appear that about 2 at. % of boron should be present in the first atom layer in order for it to be detected.

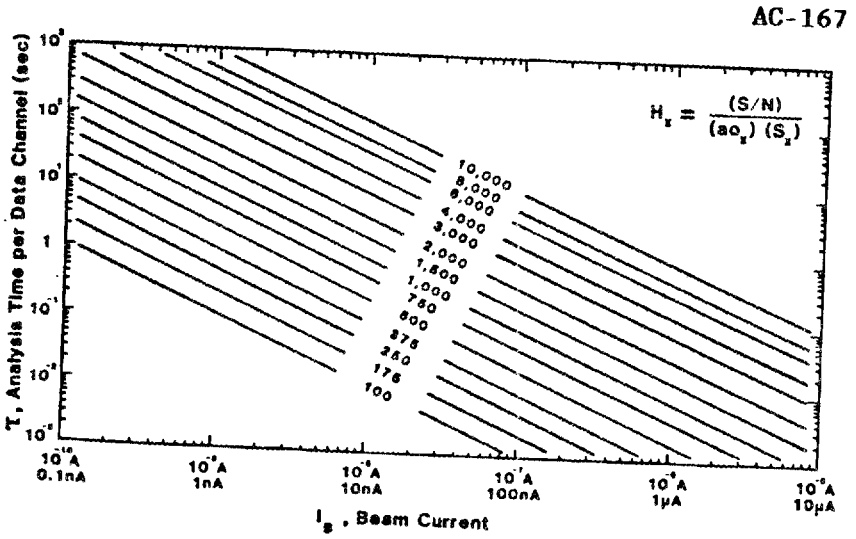

Figure 10-1. Nomogram relating the beam current (I_B), analysis time (τ) and the factor H (Ref. 126).

It was mentioned in Section II of Chapter 9 that Ref. 116 did not contain a standard spectrum for boron using a 5 KeV beam; it was reported for a 3 KeV beam. Using this spectrum to obtain the sensitivity factor calculated as in Section II of Chapter 9, the value reported by PHI (for boron) is about four times smaller than was found in this research. Hence the detectability limit for boron in this research is about 0.5 at. %. The majority of the analyses in this research revealed boron levels at the grain boundaries in excess of this and hence it is concluded that boron is eminently detectable in the equipment used for this research.

III. CHEMICAL ANALYSIS

As mentioned in Section II of Chapter 8, four alloys were studied in this research. In all the alloys the aluminum content aimed for during alloy preparation was 24 at. %. Subsequent to alloy preparation, however, aluminum analysis was not carried out. Since the weight loss during melting was negligible, it was presumed that the attained composition was the same as that aimed for. While this has not been explicitly verified, it is certain that all the alloys were substoichiometric (in Al) since they could all be ductilized by boron additions (Ref. 41). In view of the extreme sensitivity of this system to alloy stoichiometry, however, it is recommended that chemical analysis of melts be done on a routine basis in future research.

Of much more importance in this research is the actual boron content of the alloys. Table 10-1 shows the nominal compositions and the compositions as analyzed using spark source mass spectroscopy (SSMS); clearly

Table 10-1. Nominal and analyzed boron level in the four alloys studied here

Heat Number	Nominal B (wppm)	Analyzed B (wppm)	B (at. %)
860019	100	50	0.048
850014	300	300	0.144
860013	500	400	0.240
860018	1000	800	0.480

they are not identical for the three heats melted expressly for this research, i.e., 860019, 860013 and 860018. It is noteworthy that many of the conventional microanalytical techniques (SSMS included) for boron analysis, especially in the composition range considered here, are known to be unsatisfactory in terms of reproducibilty and thus reliability (Refs. 127,128). It has been reported in the medical literature (Ref. 127) that neutron activation techniques that utilize the $^{10}B(n,\alpha)^{7}Li$ reaction are by far the most reliable in this case. It is suggested that this technique be investigated for use in future research. SSMS can be as unreliable as 50% of the measured value (Ref. 129). Thus, in this research, the nominal values of boron content will be used in the analysis of the data.

Using 58.71, 26.98 and 10.81 as the atomic weights of Ni, Al and B, respectively, and assuming the alloy compositions to be based on $(Ni_{0.76}\ Al_{0.24})_{1-x}\ B_x$, the nominal boron content was converted to atomic percent and the values are shown in Table 10-1. These values were used in Chapter 9 to show the effects of bulk boron concentration.

IV. QUANTIFICATION OF GRAIN BOUNDARY BORON LEVEL

As discussed in Appendix B, the conversion of Auger results to grain boundary boron concentrations in this research is based on the assumption that only Ni, Al and B are present at the boundaries. It is to be recognized that in a number of cases, especially in the hydrogen charged samples, some carbon was often found on the grain boundaries; for the present analysis this was ignored.

It is also mentioned in Appendix B that there are two alternative ways to calculate the atomic percent of boron at the grain boundaries: one based on the Ni 102 eV peak, the other on the Ni 848 eV peak. These have been termed B1 and B2, respectively; corresponding to these, two enrichment ratios, ENRAT1 and ENRAT2 have been calculated. Table B-4 shows calculated values of B1, B2 ENRAT1 and ENRAT2 for sample 860019D.

It is seen from Table B-4 that the values of B2 and ENRAT2 are consistently about 7% lower than B1 and ENRAT1, respectively. This was the case for all analyzed samples. It is to be remembered that the IMFP (Ref. 102) for 800 eV electrons is about three times larger than that for 100 eV electrons. This implies a greater sampling depth when 800 eV electrons are used for analysis than when 100 eV electrons are used. Since the majority of the segregated boron is expected to reside in the first few atom layers from the boundary, the 800 eV electrons are averaging this boron over a larger sampling volume than the 100 eV electrons, and hence the concentration of boron obtained in the former case is lower. It is thus felt that the 102 eV analyses (and hence B1 values) are more representative of the true grain boundary concentration. Also, the majority of the grain boundaries were analysed in the 0 to 300 eV range while only one grain boundary from each sample was analyzed in the full 0 to 2000 eV range. Thus, greater reliability can be placed in the former analyses. It is for these reasons that B1 is chosen in this dissertation as the valid measure of grain boundary boron concentration.

V. ENRICHMENT RATIOS AND THE SATURATION EFFECT

In the previous section, a rationale was presented to select B1 as the measure of grain boundary boron level. It follows that the appropriate measure of the enrichment factor between the grain boundaries and the bulk is ENRAT1 (appendix B).

Figure 10-2 shows the effect of bulk boron level on both the average boron level at the grain boundaries (B1) and the enrichment ratio (ENRAT1). The results from the slowly cooled, hydrogen charged samples were chosen for this figure. As can be seen from this figure, while the absolute level of sergregant (boron) increases with the level of solute in the bulk, the level of enrichment progressively decreases.

It has been pointed out by McLean (Ref. 63) that at low solute concentration ($X^{\alpha} << 1$), the level of segregated solute is approximated by:

$$X^{\sigma} = \frac{X^{\alpha} \exp(\Delta\epsilon/kT)}{1 + X^{\alpha} \exp(\Delta\epsilon/kT)}$$

or

$$X^{\sigma}/X^{\alpha} = [\exp(\Delta\epsilon/kT)]/[1 + X^{\alpha} \exp(\Delta\epsilon/kT)] \quad \text{Equation (10-2)}$$

Hence for a given binding energy, the enrichment ratio should show a decrease with increasing bulk solute level; the experimental results in Figure 10-2 reflect this trend.

It has been mentioned before (Section III in Chapter 5) that the concept of a spectrum of binding energies is physically more realistic than that of a single binding energy. During the process of segregation,

AC-168

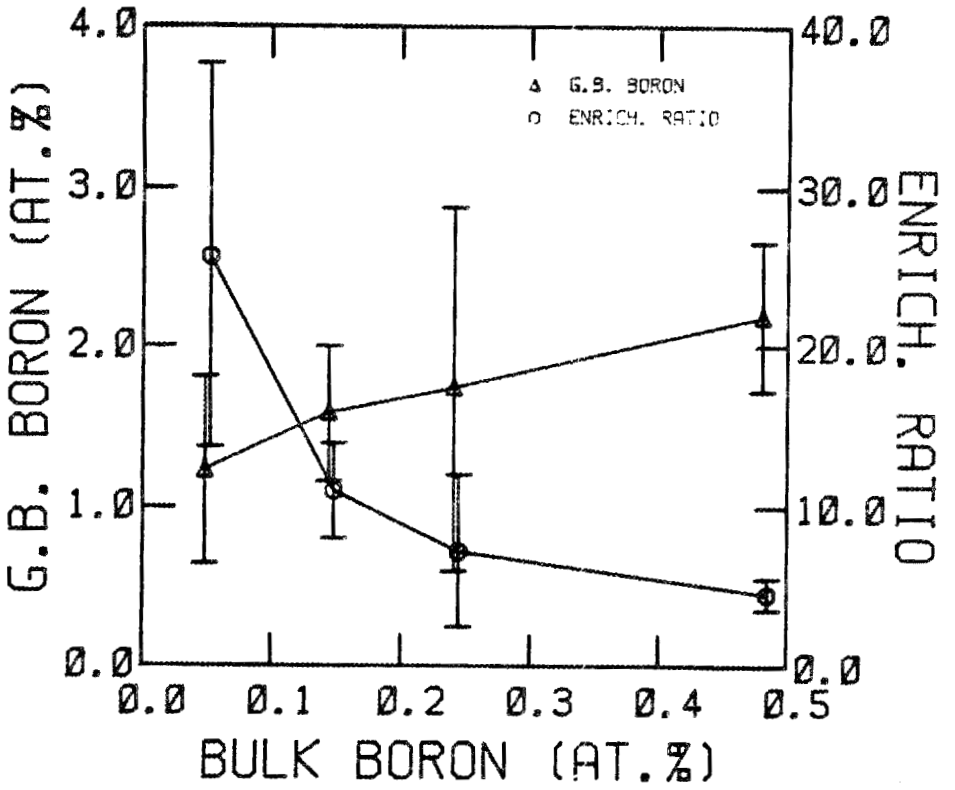

Figure 10-2. Comparison of grain boundary boron level and enrichment ratio as a function of bulk boron level.

solute atoms will occupy grain boundary sites in a sequence dictated by the sites' binding energies, the sites with the highest $\Delta\epsilon$ being filled first. A stage will be reached when most of the remaining unoccupied sites have low binding energies and the boundaries are thus effectively saturated with solute. This saturation effect has been reported before (Refs. 59,66). While only the results from the hydrogen charged, slowly cooled samples have been presented for this discussion, a similar trend was also observed in this research for other heat treatment conditions.

VI. BINDING ENERGY CONCEPTS

McLean's formulation for the concentration of solute at a "distorted region" (in this case a grain boundary) is given by:

$$X^{\sigma} = \frac{X^{\alpha} \exp(\Delta\epsilon/kT)}{1 - X^{\alpha} + X^{\alpha} \exp(\Delta\epsilon/kT)}$$

Thus the binding energy, $\Delta\epsilon$, can be expressed as:

$$\Delta\epsilon = kT \, \mathrm{Ln} \left[\frac{X^{\sigma}(1 - X^{\alpha})}{X^{\alpha}(1 - X^{\sigma})} \right] \qquad \text{Equation (10-3)}$$

In order to calculate $\Delta\epsilon$, it is necessary to understand each of the terms in Equation (10-3).

A. The Binding Energy

In his original formulation, McLean considered the distortion energy caused by a solute atom in an undistorted site (in this case in the bulk lattice) to be E while that caused by a solute atom in an initially distorted site (in this case a grain boundary) to be e. He then defined the binding energy $\Delta\epsilon$ as:

$$\Delta\epsilon = (E - e) \qquad \text{Equation (10-4)}$$

The binding energy is thus the difference in energy when a solute atom moves from a bulk site to a grain boundary site. In the case of a substitutional solute, such a movement would involve an EXCHANGE of solute atom between the boundary and the bulk. In the case of boron in Ni_3Al, i.e., an interstitial solute, this difference would be the difference in energy when a boron atom in the bulk moves to a site at the grain boundary; an exchange is not imperative in this case. It is to be noted that in the preceding discussion, $\Delta\epsilon$ was referred to as a "difference." If this difference is negative, it is obvious that the solute will not move to the grain boundary site; i.e., a negative $\Delta\epsilon$ will preclude segregation. It is thus necessary to have a positive $\Delta\epsilon$ for segregation to occur.

It has been instructive to examine McLean's formulation in detail and recognize some of its limitations. These are mentioned here in the interest of clarity. In formulating his expression, McLean assumed a single value for e; by his own admission, this cannot be true in practice. Furthermore, the derivation involved the minimization of the free energy of the entire system. His expression for the free energy, however, involved ONLY the configurational entropy; the vibrational entropy was ignored. Subsequent refinements of McLean's approach (Ref. 61) also involve only the configurational term. It is obvious that McLean distinguished grain boundary sites and bulk sites in terms of "distortion." The factors contributing to this distortion, however, need to be addressed. The ones that come to mind are a size effect, a modulus effect and a chemical (or bonding) effect.

B. X^{α} and X^{σ}

In the bulk lattice, X^{α} is the fraction of sites available for occupancy by solute that are actually occupied by solute. It is known that boron occupies the octahedral interstices in the Ni_3Al lattice (Ref. 130). In the FCC lattice there is one such site for every lattice atom present; for the present discussion it is immaterial whether it is a nickel or an aluminum atom. If the atomic percent of boron in the lattice is analyzed (chemical analysis) to be Y^{α}, then in a lattice containing a total of 100 atoms, Y^{α} atoms are boron atoms while $(100 - Y^{\alpha})$ are Ni + Al atoms. Hence the number of sites available for occupancy by boron is also $(100 - Y^{\alpha})$. Thus:

$$X^{\alpha} = \frac{Y^{\alpha}}{100 - Y^{\alpha}} \qquad \text{Equation (10-5)}$$

At the grain boundaries, X^{σ} is the fraction of sites available for occupancy by solute that are actually occupied by solute. Suppose Y^{σ} is the MEASURED (say by AES) atomic percent of boron at the grain boundaries. If there are 100 atoms in the analyzed volume, then Y^{σ} is the number of boron atoms while $(100 - Y^{\sigma})$ are Ni + Al atoms. All the atoms in the analyzed volume, however, are not grain boundary atoms. For the present, it will be assumed that a certain fraction of these, say M, are grain boundary atoms. Then the number of Ni + Al grain boundary atoms are $(100 - Y^{\sigma}) \times M$. Another simplifying assumption needs to be made here: as the case in the bulk, there is one octahedral site available for occupancy for each Ni or Al atom at the grain boundary. In such a case, the number of available sites at the grain boundary (for occupancy by boron) is $(100 - Y^{\sigma}) \times M$.

It follows from the above that $(100 - Y^{\sigma}) \times (1 - M)$ are the number of atoms in the analyzed volume that belong to the bulk lattice. Of these, some are boron and some are Ni + Al. It was shown previously that in the bulk, there are Y^{α} boron atoms for every $(100 - Y^{\alpha})$ Ni + Al atoms. Hence the number of boron atoms in the analyzed volume that can be apportioned to the lattice are:

$$Z = \{(100 - Y^{\sigma})\ (1 - M)\} \times \left(\frac{Y^{\alpha}}{100 - Y^{\alpha}}\right) \qquad \text{Equation (10-6)}$$

Hence of the analyzed boron atoms (Y^{σ} in number) only $(Y^{\sigma} - Z)$ are grain boundary boron atoms. Thus X^{σ} may be written as:

$$X^{\sigma} = \frac{(Y^{\sigma} - Z)}{(100 - Y^{\sigma})M} \qquad \text{Equation (10-7)}$$

Substituting Equation (10-6) in Equation (10-7):

$$X^{\sigma} = \left(Y^{\sigma} - \frac{(100 - Y^{\sigma})\ (1 - M)Y^{\alpha}}{(100 - Y^{\alpha})}\right)\frac{1}{(100 - Y^{\sigma})M}$$

or

$$X^{\sigma} = \left[\frac{Y^{\sigma}}{(100 - Y^{\sigma})M}\right] - \left[\frac{(Y^{\alpha} - MY^{\alpha})}{(100 - Y^{\alpha})M}\right] \qquad \text{Equation (10-8)}$$

VII. BINDING ENERGY CALCULATIONS

A. Effect of Bulk Solute Level

In the initial calculations, it will be assumed that 30 minutes at 1323 K is sufficient to attain equilibrium at that temperature. It will be further assumed that the equilibrium segregant level at the end of this period is effectively "frozen in" by water quenching to room temperature. In other words, the water quenched samples (uncharged in the 100 and

300 wppm alloys and charged in the 500 and 1000 wppm alloys) were used to determine the equilibrium grain boundary level of segregant (boron). Substituting Equations (10-5) and (10-8) into Equations (10-3) yields:

$$\Delta\epsilon = kT \, Ln \left[\frac{\{100Y^{\sigma} - 100Y^{\alpha} + 100MY^{\alpha} - MY^{\alpha}Y^{\sigma}\}\{100 - 2Y^{\alpha}\}}{\{100M\,(100 - Y^{\sigma} - Y^{\alpha}) + Y^{\sigma}\,(MY^{\alpha} - 100 + Y^{\alpha}) + Y^{\alpha}\,(1-M)\}\,Y^{\alpha}} \right]$$

Equation 10-9

Table 10-2 shows the values of Y^{α} and Y^{σ} for the four alloys studied. For $k = 0.862 \times 10^{-4}$ eV.K^{-1} and T = 1323 K, Table 10-3 shows the values of $\Delta\epsilon_{eff}$ for values of M ranging from 0.2 to 1.0 at increments of 0.2. It also shows the values of $\Delta\epsilon$ for the four alloys for the special case of M = 0.33. Figure 10-3 shows a plot of the calculated effective binding energies at 1323 K as a function of M for the four alloys.

From Table 10-3 and Figure 10-3, two trends are easily deduced. First, for a given bulk boron level, the calculated $\Delta\epsilon_{eff}$ decreases as the value of M increases. M is the fraction of analyzed atoms (AES) that are grain boundary atoms. It is seen that a threefold increase in M (say from 0.2 to 0.6) leads to a lowering of $\Delta\epsilon_{eff}$ by only about 30% (for the 100 wppm alloy) to 50% (for the 1000 wppm alloy). Considering the uncertainties in the quantification procedure this is not a very dramatic effect. The escape depth for 1000 eV electrons is about 6 monolayers. If the segregated boron atoms are assumed to reside within the first 2 layers, then M = 0.33; for the sake of discussion the values of $\Delta\epsilon_{eff}$ corresponding to this value of M will be considered.

The second obvious trend is that, for a given M (say M = 0.33), the effective binding energy decreases with increasing bulk boron level. A tenfold increase in the bulk level (from 100 to 1000 wpm) causes a 60%

Table 10-2. Y^{α} and Y^{σ} (WQ) for the four alloys

Heat Number	Bulk Boron (wppm)	Y^{α}	Y^{σ}
860019	100	0.048	0.60
850014	300	0.144	0.85
860013	500	0.240	0.99
860018	1000	0.480	1.37

Table 10-3. Calculated effective binding energy of boron for the four alloys as a function of M

M	$\Delta\epsilon_{eff}$ (eV/atom) 100 wppm B	$\Delta\epsilon_{eff}$ (eV/atom) 300 wppm B	$\Delta\epsilon_{eff}$ (eV/atom) 500 wppm B	$\Delta\epsilon_{eff}$ (eV/atom) 1000 wppm B
0.200	0.468	0.374	0.326	0.272
0.330	0.411	0.318	0.271	0.220
0.400	0.389	0.298	0.251	0.201
0.600	0.344	0.255	0.211	0.164
0.800	0.313	0.226	0.183	0.139
1	0.289	0.204	0.163	0.122

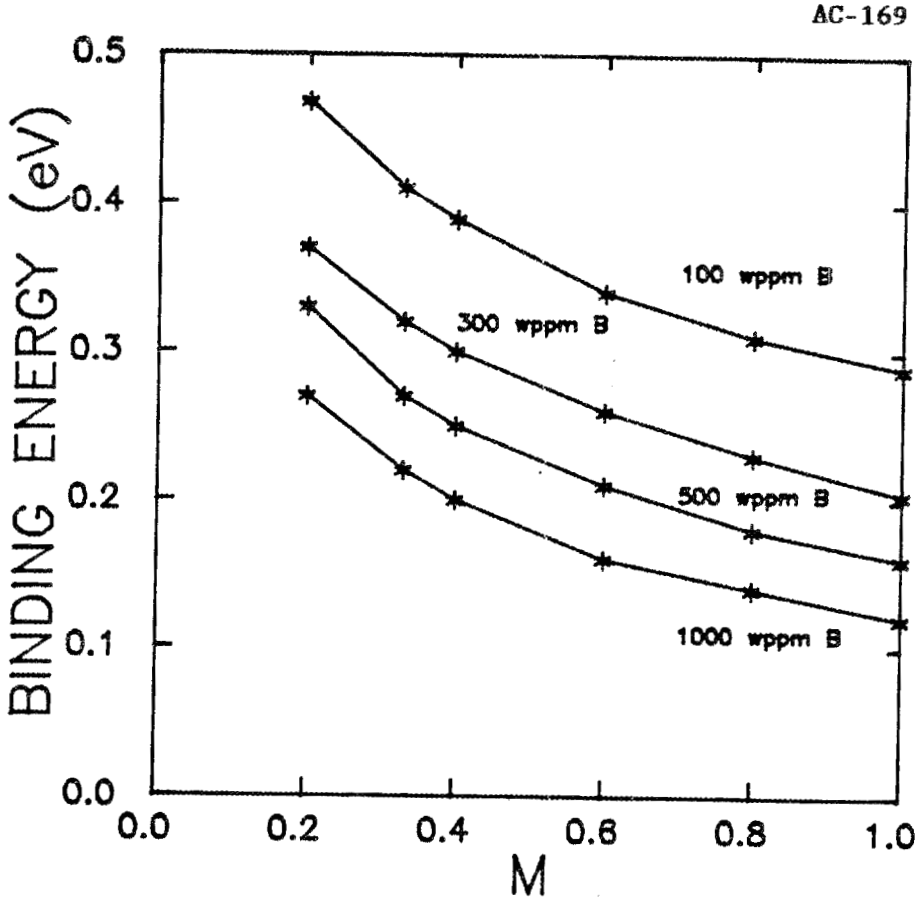

Figure 10-3. The effective binding energy of boron at the grain boundaries for the four alloys as a function of M.

decrease in the effective binding energy. This is perceived as experimental proof of the fact that McLean's assumption of an unique binding energy for a particular solute-solvent combination is not valid. The lowering of the calculated effective binding energy may be rationalized as follows. Two initial assumptions will be made. First, prior to the occurrence of segregation, a grain boundary is assumed to possess the same level of solute as the bulk. Second, the distribution of sites as a function of binding energy is assumed to be either unaffected by the bulk solute level or at best very weakly affected.

Figure 10-4 shows hypothetical distributions of sites for two cases. Case A [Figure 10-4(*a*)] contains a lower level of solute in the bulk than Case B [Figure 10-4(*b*)]. It is to be noted that the distributions are identical in the two cases. As per the first assumption, prior to segregation, the distributions are filled (with solute) to levels E_1 (Case A) and E_2 (Case B). After equilibrium segregation has occurred, the distributions are filled to levels E_1' and E_2', respectively. It is seen from this schematic that the observed effective binding energies in the two cases are E_A and E_B, respectively; it can be seen that E_B is lower than E_A.

B. Effect of Temperature

In order to calculate the effective binding energy as a function of temperature, it is necessary to ensure that the level of segregant at the boundaries represents the equilibrium level. Figures 9-17 and 9-18 show that, for the alloys containing 100 and 1000 wppm boron, the grain boundary boron level is at or very close to the equilibrium value upon annealing at 700°C for 1000 minutes. If it is assumed that 1000 minutes is sufficient

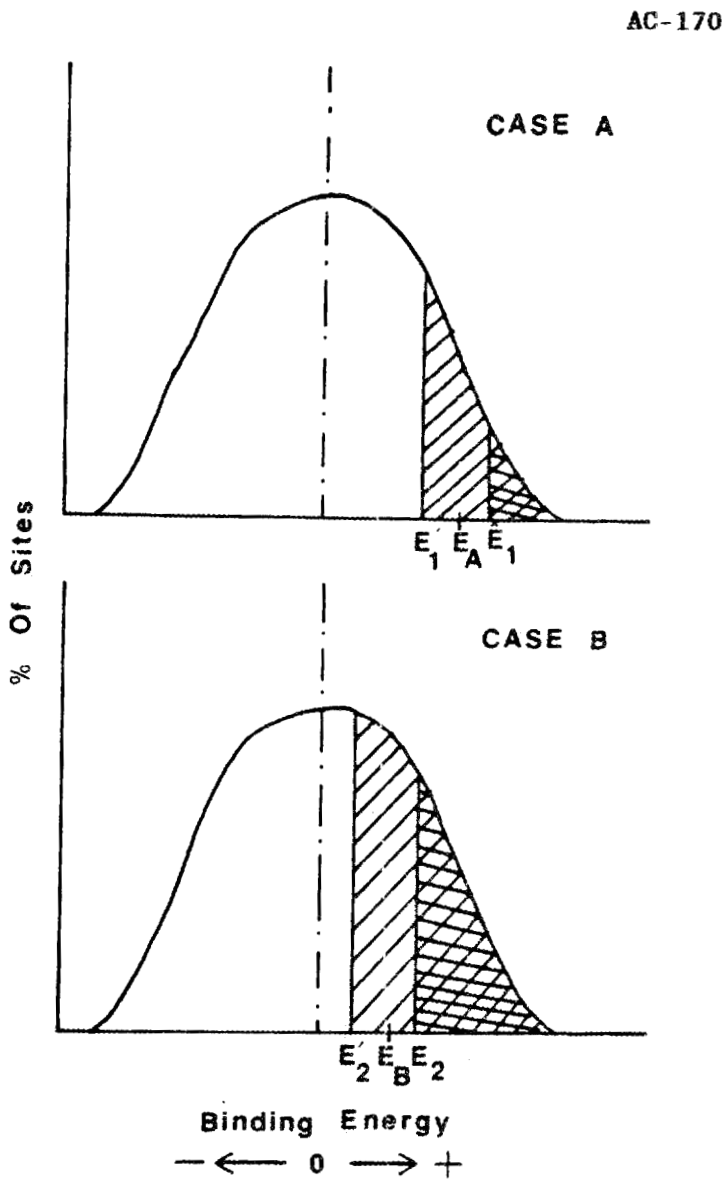

Figure 10-4. Schematic illustration for the decrease in effective binding energy as a function of increasing bulk boron level.

to attain equilibrium at 500, 600 and 900°C too, then the data presented in Figures 9-20 and 9-21 can be used to calculate $\Delta\varepsilon_{eff}$ in the same manner as calculated in the previous subsection. The discussions in the next section (kinetics) of this chapter show that this is a valid assumption.

Table 10-4 shows the values of Y^{α} and Y^{σ} for both the alloys at the temperatures considered here: 773, 873, 973 and 1173 K (only 100 wppm boron alloy). Table 10-5 shows the values of $\Delta\varepsilon_{eff}$ calculated for each case assuming M = 0.33. The calculated values of $\Delta\varepsilon_{eff}$ have been plotted as a function of temperature for the two alloys in Figure 10-5. The effective binding energy is seen to increase with increasing temperature. This figure also illustrates the decrease of effective binding energy with increasing bulk solute level at any given temperature.

A similar effect of increasing effective binding energy with temperature has been reported for sulphur in Ni-23 at. % Al and Ni-21.6 at. % Al-2.7 at. % Ti alloys (Ref. 61) and for sulphur in Fe-Sn-S alloys (Ref. 65). In a Ni-23 at. % Al alloy containing 64 at. ppm sulphur in the bulk, White and Stein (Ref. 61) found an increase (on the average) of 3.6×10^{-4} eV/K for the effective binding energy of sulphur. In the present research, the 100 wppm boron alloy shows an average increase of 2.3×10^{-4} eV/K while the 1000 wppm boron alloy shows an average increase of 9×10^{-5} eV/K. A curious fact was noticed in White and Stein's results. In the case of the Ni-Al-Ti alloys, the effective binding energies at any given temperature decrease with increasing bulk solute level (similar trend to that observed here) while in the Ni-Al alloys, the opposite trend is seen.

Table 10-4. Y^{α} and Y^{σ} for the two alloys as a function of temperature for 1000 minutes isochronal annealing

Heat Number	Bulk Boron (wppm)	Temp. (K)	Y^{α}	Y^{σ}
860019	100	773	0.048	1.08
860019	100	873	0.048	1.05
860019	100	973	0.048	0.84
860019	100	1173	0.048	0.65
860018	1000	773	0.480	2.18
860018	1000	873	0.480	2.14
860018	1000	973	0.480	1.71

Table 10-5. The calculated effective binding energy of boron in two alloys as a function of temperature

Heat Number	Bulk Boron (wppm)	Temp. (K)	$\Delta\epsilon_{eff}$ (eV)
860019	100	773	0.282
860019	100	873	0.316
860019	100	973	0.333
860019	100	1173	0.373
860018	1000	773	0.169
860018	1000	873	0.189
860018	1000	973	0.187

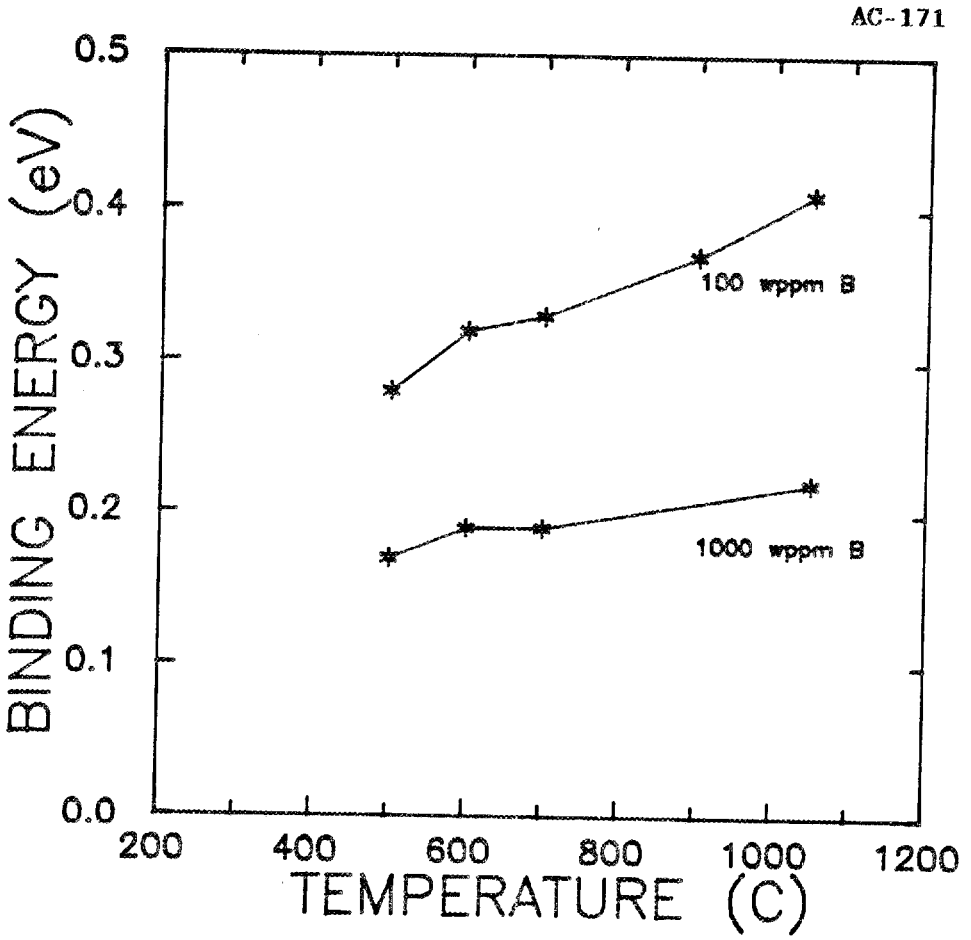

Figure 10-5. The effective binding energy of boron as a function of temperature in alloys containing 100 and 1000 wppm boron in the bulk.

VIII. KINETICS

McLean (Ref. 63) derived an expression for the rate at which the grain boundary concentration builds up after a specimen has been suddenly cooled from a high to a low temperature. This is given by:

$$\frac{X_t^\sigma - X_o^\sigma}{X_\infty^\sigma - X_o^\sigma} = 1 - \exp\left(4Dt/\alpha_2^2 d^2\right) \operatorname{erfc}\left\{2(\sqrt{Dt})/\alpha_2 d\right\} \quad \text{Equation (10-10)}$$

Where X_t^σ = The grain boundary concentration after time t at the low temperature

X_o^σ = The initial grain boundary concentration, i.e., the "quenched-in" concentration

X_∞^σ = The equilibrium grain boundary concentration attained after infinite time at the low temperature

D = Diffusion coefficient at the low temperature

t = Time

d = Thickness of the grain boundary

α_2 = The ratio X_∞^σ/X^α

X^α = Grain interior (i.e., bulk) concentration.

Figure 10-6 shows the schematic variation of the reduced grain boundary concentration [LHS of Equation (10-10)] as a function of the dimensionless term $N = 2\sqrt{Dt}/\alpha_2 d$.

Equation (10-10) was derived assuming that the cooling is too rapid for any change in concentration to occur before the lower temperature is reached. It was also assumed that the grain boundary thickness is small

AC-172

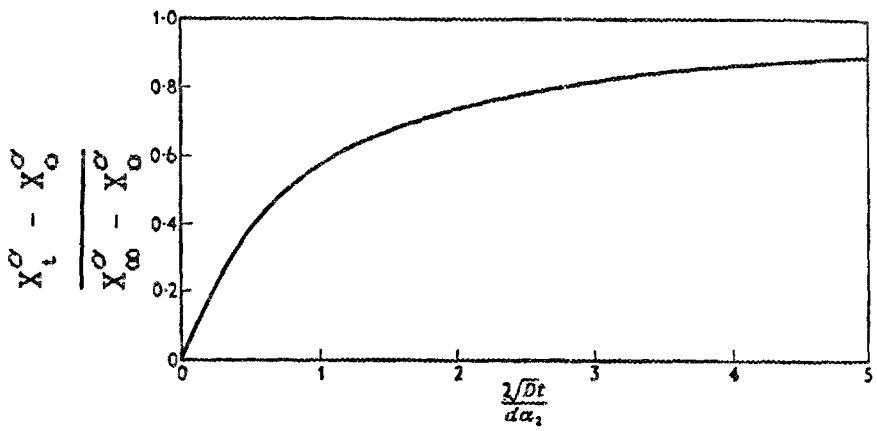

Figure 10-6. Change of grain boundary concentration with time for initial concentration X^σ_o to final equilibrium concentration X^σ_∞ (Ref. 63).

compared to the grain diameter and hence the diffusion to the boundary is entirely from a narrow region at the edge of the crystal. The boundary conditions used were those for linear flow in a semi-infinite mass feeding the boundary.

Equation (10-10) can be used to predict the variation of grain boundary concentration with time. In the case at hand, however, the problem is that the diffusion coefficient of boron in Ni_3Al is not known. It was thus decided to use the kinetic data obtained in this research to calculate a "first-cut" value of the diffusion coefficient.

It is seen from Figure 10-6 the LHS of Equation (10-10) reaches a value of 0.5 when N = 0.75. If the time required to get to this point is designated as $t_{\frac{1}{2}}$ then:

$$\frac{2\sqrt{Dt_{\frac{1}{2}}}}{\alpha_2 d} = 0.75 \qquad \text{Equation (10-11)}$$

or

$$D = \frac{9\alpha_2^2 d^2}{64 t_{\frac{1}{2}}} \qquad \text{Equation (10-12)}$$

The data of Figures 9-17, 9-18 and 9-19 can be used to calculate values of D. The first question to be addressed is the value to be used for the grain boundary thickness (d). The grain boundary was assumed to be four interplanar spacings thick. An average value for the interplanar spacings of the (100), (110) and (111) planes of Ni_3Al was used. The lattice parameter (a) of Ni_3Al has been reported (Ref. 131) to be 3.5677×10^{-8} cm.

The three interplanar spacings mentioned above are thus:

$$d(100) = a/2 = 1.7839 \times 10^{-8}\text{cm},$$

$$d(110) = a/\sqrt{2} = 2.5228 \times 10^{-8}\text{cm},$$

$$d(111) = 2a/\sqrt{3} = 4.1196 \times 10^{-8}\text{cm}.$$

The d value is thus given by:

$$d = \frac{4\,[d(100) + d(110) + d(111)]}{3} = 11.2352 \times 10^{-8}\text{cm}.$$

The next question is that of α_2. The data of Figure 9-17 are for the 100 wppm boron alloy at 700°C; this is called case A. Case B refers to Figure 9-18, i.e., the 1000 wppm boron alloy at 700°C and case C refers to Figure 9-19, i.e., the 1000 wppm boron alloy at 500°C. It is possible to ascribe two values to X_∞^σ in each case. One corresponds to the value for 10,000 minutes annealing (the longest time studied) in each case. The uncertainty involved in this assumption is whether or not 10,000 minutes is long enough to attain equilibrium. A second approach would be to ascribe X_∞^σ to the slowly cooled values for each alloy. This is a rather drastic assumption since the slowly cooled segregant level may correspond to annealing for infinite time at temperatures lower than the temperatures considered here, i.e., 700°C and 500°C. Also, for cases B and C, this assumption implies the same X_∞^σ; it was shown in the previous section that this cannot be true. It is seen in Figures 9-17, 9-18 and 9-19 that while there is not a large difference in segregant level between 1000 min annealing and 10,000 minutes annealing, the difference is quite appreciable between 10,000 minutes and the slowly cooled value. This is interpreted here to mean that the slowly cooled value does indeed correspond to the

equilibrium value at a temperature below those considered here. Hence α_2 has been calculated in Table 10-6 for the three cases assuming the 10,000 minutes segregant levels to represent equilibrium at the respective temperatures. It is to be remembered that X^{α} and X^{σ}_{∞} in this table were calculated in the same manner as in Section VI of this chapter using a value of M = 0.33.

Now $t_{\frac{1}{2}}$ refers to the time required for the solute concentration to be raised to half the difference between the quenched-in value and the equilibrium value. It is difficult to extract this time from semilog plots such as Figures 9-17, 9-18 and 9-19, since the exact shape of the curves are in doubt.

As shown in Figure 10-6, the grain boundary solute concentration shows an initial rapid rise. If the half concentration (designated here as $Y_{\frac{1}{2}}$) lies between the water quenched value and the first data point available (1 minute in these three cases), then it is reasonable to assume a straight line between the water quenched value and the first data point and to read the time ($t_{\frac{1}{2}}$) corresponding to $Y_{\frac{1}{2}}$. The $Y_{\frac{1}{2}}$ values for the three cases are shown on Table 10-7. It is seen that the $Y_{\frac{1}{2}}$ values do indeed lie between the water quenched and the 1 minute annealing values for cases A and C but not for case B. In case B, the value for $Y_{\frac{1}{2}}$ lies between the 1 minute and the 1000 minutes annealing values. Hence a straight line was assumed between the 1 minute and the 1000 minutes value to arrive at the $t_{\frac{1}{2}}$ value shown on Table 10-7; it also shows the $t_{\frac{1}{2}}$ values for cases A and C. Upon examination of Figure 9-18 (case B), it is seen that the 1 minute value is lower than the water quenched value. It is for

Table 10-6. α_2 and the values required to calculate it for the three cases considered

Case	Bulk Boron (wppm)	Temp. (K)	Y^{α} (at. %)	Y^{σ} (at. %)	X^{α} (at. %)	X^{σ}_{∞} (at. %)	α_2
A	100	973	0.048	0.88	4.80×10^{-4}	0.03	56.02
B	1000	973	0.48	1.83	4.82×10^{-3}	0.06	11.49
C	1000	773	0.48	2.02	4.82×10^{-3}	0.06	12.94

Table 10-7. $t_{\frac{1}{2}}$ and the values used to find it for the three cases considered

Case	Bulk Boron (wppm)	Temp. (K)	Y_o^σ (at. %)	Y_∞^σ (at. %)	$Y_{\frac{1}{2}}$ (at. %)	$t_{\frac{1}{2}}$ (at. %)
A	100	973	0.60	0.88	0.74	37.50
B	1000	973	1.37	1.83	1.60	47322
C	1000	773	1.37	2.02	1.70	56.60

this reason that $Y_{\frac{1}{2}}$ for this case is higher than the 1 minute value. This leads to the very large $t_{\frac{1}{2}}$ value. It is thus felt that there is some experimental error in this 1 minute (case B) measurement. It is for this reason that the results of case B are neglected for the present calculation.

Table 10-8 summarizes α_2, d and $t_{\frac{1}{2}}$ for the two valid cases: A and C. It also shows the values of D calculated using Equation (10-12). If the diffusion coefficient is assumed to be a function only of temperature, i.e., $D = D_o \exp(-Q/RT)$, then the temperature independent diffusion coefficient, D_o, and the activation energy for diffusion, Q, can be calculated from the two values of D shown on Table 10-8. These values are:

$$Q = 105.3 \text{ KJ/mole} = 1.09 \text{ eV}$$

$$D_o = 6.13 \times 10^{-8} \text{ cm}^2/\text{s}$$

It is instructive to compare the values of D_o and Q obtained in this research with values for other interstitial solute-FCC solvent combinations. Table 10-9 shows such a comparison. While the value obtained here for Q seems reasonable, the value of D_o seems to be very low.

The diffusion rate of carbon in Ni can be used here as a comparative case. At 973 and 773 K, the diffusion coefficient (of C in Ni) is 1.01×10^{-9} and 8.4×10^{-12} cm^2/s, respectively. Hence the values of D calculated here are three to four orders of magnitude lower than this. It is felt that boron does indeed diffuse very rapidly in Ni_3Al. The anomaly in the present results can be understood as follows.

The present calculations are based on the assumption that 1 minute annealing yielded a segregant level lying between the $Y_{\frac{1}{2}}$ value and the

Table 10-8. D and the values used to calculate it for the two valid cases

Case	Bulk Boron (wppm)	Temp. (K)	d (cm)	α_2	$t_{\frac{1}{2}}$ (s)	D (cm^2/s)
A	100	973	11.24×10^{-8}	56.02	37.50	1.49×10^{-13}
C	1000	773	11.24×10^{-8}	12.94	56.60	5.25×10^{-15}

Table 10-9. Comparison of D_o and Q as calculated in this work with comparative cases reported in the literature

Solvent	Solute	D_o (cm^2/s)	Q (KJ/mole)	Reference
Ni_3Al	B	6.13×10^{-8}	105.30	PRESENT WORK
Ni	C	.11	149.70	132
Ni	S	.20	192.50	133
Ni	F	2.13×10^{-3}	118.60	134
Ni	Be	.02	193.30	135
Ni	N	6.6×10^{-2}	27.50	136
Fe	Be	.10	241	135
Fe	C	.15	142.30	137
Fe	S	1.70	221.80	138
Cu	S	23	205.90	138
Cu	H	10^{-2}	41.80	139
Cu	O	10^{-3}	192.50	139

equilibrium level at the temperatures considered. The calculated diffusion coefficients, however, are very low. The data for carbon in nickel (shown above) indicate a value of ~ 10^{-9} cm^2/s would be expected at 973 K. An approximate calculation based on Equation (10-12) shows that the $t_{\frac{1}{2}}$ required to yield a diffusion coefficient of ~ 10^{-9} cm^2/s at 973 K (case A) would be in the range of 5×10^{-5} s. This implies that upon 1 minute annealing, the segregant level should be a significant fraction of the equilibrium value. In fact, closer examinations of Figures 9-17, 9-18 and 9-19 shows that if the error bars are taken into account, there is not an appreciable difference between the segregant levels obtained between 1 minute annealing and the longer times. In other words, the apparent trend of increasing levels with time (beyond 1 minute) seen from the averages is not a reflection of the true state of affairs; i.e., the profile has virtually "flattened out." Thus the 1 minute value should not be used for calculation of diffusion coefficients based on the $t_{\frac{1}{2}}$ approach.

There would be two possible ways to overcome this effect: annealing for much shorter times or annealing at much lower temperatures. Experimentally, the former would be very difficult to carry out. The latter approach provided a means to lower the diffusion coefficient to a value such that the time required to reach equilibrium would be appreciable. Hence annealing for shorter times than this would provide data pertaining to the approach to equilibrium. The usual methods adopted to measure diffusion coefficients are very costly and laborious. It is felt that the suggested method provides a relatively simple experimental approach to estimating diffusion coefficients. It is strongly urged that future work in this system should be directed at addressing this issue.

CHAPTER 11

CONCLUSIONS AND FUTURE WORK

I. CONCLUSIONS

The following conclusions have been reached regarding the intergranular segregation behavior of boron in Ni_3Al:

(1) The level of segregation can be controlled by variations in the thermal history imposed on the alloy and the bulk level of boron in the alloy. Specifically, slow cooling from a high temperature leads to a high level of segregation, while fast cooling from a high temperature arrests a low level of segregated boron. The level of segregated boron increases with increasing levels of boron in the bulk.

(2) These variations in segregation level profoundly effect the tensile fracture morphology of the alloys. The degree of grain boundary cohesiveness increases with the level of segregated boron. Hence, as the level of segregated boron increases, the fracture morphology becomes increasingly transgranular.

(3) The effective binding energy of boron to the grain boundaries of Ni_3Al decreases with an increase in the bulk boron level and with decreasing temperature. The effective binding energy varies between about 0.2 and 0.45 eV.

(4) Attempts at estimating the diffusion coefficient of boron in Ni_3Al from the kinetic data yielded questionable results. Model

calculations done later showed that, even at the lowest temperatures studied in this research (500°C), the time involved in attaining a segregant level close to the equilibrium level was much shorter than the shortest time studied here (1 minute).

(5) Within a given sample, the segregation level does vary from boundary to boundary, probably due to differences in boundary structure resulting from differences in relative grain orientation.

(6) Cathodic hydrogen charging can be used to advantage in exposing grain boundaries for analysis.

II. FUTURE WORK

(1) The variation of segregation level with relative grain orientation needs to be addressed.

(2) The chemical state of intergranularly segregated boron needs to be investigated in order to verify the reasons for boron induced grain boundary cohesion.

(3) Kinetic studies need to be carried out at temperatures lower than those investigated in this research. From such investigations, the diffusion coefficient of boron in Ni_3Al can be found.

(4) The cosegregation of boron with species such as sulphur and carbon should prove to be very interesting.

(5) Two sets of experiments can be carried out with slight modifications on the existing setup. The first would be to investigate the segregation level on both halves of a fracture surface. The

second would be to carry out kinetic studies by heating fracture surfaces in the analysis chamber (in-situ heating).

(6) It would be instructive to obtain a direct correlation between the segregant level and the tensile properties by carrying out these measurements on the same specimen. In fact, it is possible to carry out a tensile test under UHV and then analyze the resulting fracture surface using AES.

REFERENCES

1. S. Takeuchi and E. Kuramoto, *Acta Met.* 21, 415–425 (1973).
2. P. H. Thornton, R. G. Davies and T. L. Johnston, *Met. Trans.* 1, 207–218 (1970).
3. S. M. Copely and B. H. Kear, *Trans. TMS-AIME* 239, 977–984 (1967).
4. D. P. Pope, *Phil. Mag.* 25, 917–927 (1972).
5. C. T. Liu, W. Jemian, H. Inouye, J. V. Cathcart, S. A. David, J. A. Horton and M. L. Santella, ORNL-6067, 1–60 (1984).
6. *Metals Handbook*, Eighth Edition, Metals Park, OH, ASM.
7. C. T. Liu and J. O. Stiegler, *Science* 226, 636–642 (1984).
8. E. M. Grala, in: *Mechanical Properties of Intermetallic Compounds*, (New York, 1960) pp. 358–402.
9. K. Aoki and O. Izumi, *Trans. JIM* 19, 203–210 (1978).
10. K. Aoki and O. Izumi, *Nippon Kinzoku Gakkaishi* 43 (12), 1190–1195 (1979).
11. T. Ogura, S. Hanada, T. Masumoto and O. Izumi, *Met. Trans. A* 16A, 441–443 (1985).
12. E. M. Schulson, D. L. Davidson and D. Viens, *Met. Trans. A* 14A, 1523–1524 (1983).
13. C. T. Liu and H. Inouye, *Met. Trans. A* 10A, 1515 (1979).
14. C. T. Liu, *Int. Met. Rev.* 29(3), 168–194 (1984).
15. P. A. Flinn, *Trans. TMS-AIME* 218, 145–154 (1960).
16. S. J. Liang and D. P. Pope, *Acta Met.* 25, 485–493 (1977).

17. J. H. Westbrook, *Trans. TMS-AIME* 209, 898–904 (1957).

18. R. G. Davies and N. S. Stoloff, *Trans. TMS-AIME* 233, 714–719 (1965).

19. D. P. Pope and S. S. Ezz, *International Metals Review* 29(3), 133–166 (1984).

20. B. H. Kear and H. G. F. Wilsdorf, *Trans. TMS-AIME* 224, 382–386 (1962).

21. A. E. Staton-Bevan and R. D. Rawlings, *Phys. Stat. Sol. (A)* 29, 613–622 (1975).

22. A. E. Staton-Bevan and R. D. Rawlings, *Phil. Mag.* 32, 787–800 (1975).

23. C. Lall, S. Chin and D. P. Pope, *Met. Trans. A* 10A, 1323–1332 (1979).

24. M. J. Marcinkowski, N. Brown and R. M. Fisher, *Acta Met.* 9, 129–137 (1961).

25. B. H. Kear, A. F. Giamei, J. M. Gilcock and R. K. Ham, *Scripta Met.* 2, 287–293 (1968).

26. B. H. Kear, A. F. Giamei, G. R. Leverant and J. M. Oblak, *Scripta Met.* 3, 123–129 (1969).

27. J. A. Lopez and G. F. Hancock, *Phys. Stat. Sol. (A)* 2, 469–474 (1970).

28. O. Noguchi, Y. Oya and T. Suzuki, *Met. Trans. A* 12A, 1647–1653 (1981).

29. R. W. Guard and J. H. Westbrook, *Trans. TMS-AIME* 215, 807–814 (1959).

30. L. R. Curwick, Ph. D. Dissertation, University of Minnesota (1972).

31. R. D. Rawlings and A. E. Staton-Bevan, *J. Mater. Sci.* **10**, 505–514 (1975).

32. K. Aoki and O. Izumi, *Phys. Stat. Sol. (A)* **38**, 587–594 (1976).

33. D. M. Wee, O. Noguchi, Y. Oya and T. Suzuki, *JIM* **21**, 237–247 (1980).

34. D. M. Wee and T. Suzuki, *JIM* **20**, 634–646 (1979).

35. T. Takasugi and O. Izumi, *Acta Met.* **33**(7), 1247–1258 (1985).

36. T. Takasugi, O. Izumi and N. Masahashi, *Acta Met.* **33**(7), 1259–1269 (1985).

37. T. Takasugi, N. Masahashi and O. Izumi, *Acta Met.* **35**(2), 381–391 (1987).

38. C. T. Liu, C. L. White, C. C. Koch and E. H. Lee, *Proc. Symp. High Temp. Materials Chemistry II - The Electrochemical Society*, (Pennington, NJ, 1983) pp. 32–41.

39. C. L. White, R. A., Padgett, C. T. Liu and S. M. Yalisove, *Scripta Met.* **18**(12), 1417–1420 (1984).

40. C. T. Liu, C. L. White, H. Inouye, J. V. Cathcart, R. K. Williams, J. A. Horton, A. DasGupta and N. S. Stoloff, ECUT Workshop - Ordered Intermetallic Alloys (1984).

41. C. T. Liu, C. L. White and J. A. Horton, *Acta Met.* **33**(2), 213–229 (1985).

42. H. H. Stadelmaier and A. C. Fraker, *Metall.* **16**(3), 212–214 (1962).

43. J. D. Schobel and H. H. Stadelmaier, *Z. Metall.* 53(5), 326–328 (1962).

44. E. O. Hall, *Proc. Phys. Soc.*, Sect. B. 64, 747–753 (1951).

45. N. J. Petch, *JISI* 174, 25–28 (1953).

46. E. M. Schulson, T. P. Weihs, D. V. Viens and I. Baker, *Acta Met.* 33(9), 1587–1591 (1985).

47. E. M. Schulson, T. P. Weihs, I. Baker, H. J. Frost and J. A. Horton, *Acta Met.* 34(7), 1395–1399 (1986).

48. T. Takasugi, N. Masahashi and O. Izumi, *Scripta Met.* 20(10), 1317–1321 (1986).

49. J. W. Cahn, *J. Phys. Colloque* C6 43(12), C6-199 (1982).

50. R. W. Balluffi, *Interfacial Segregation - ASM Meeting - 1977*, (1979) pp. 193–237.

51. W. Bollmann, *Crystal Defects and Crystalline Interfaces.* (New York, 1970).

52. H. Gleiter, *Atomistics of Fracture*, (New York, 1981) pp. 433–464.

53. R. W. Balluffi and G. B. Olson, *Met. Trans. A* 16A, 529–541 (1985).

54. T. Takasugi and O. Izumi, *Acta Met.* 31(8), 1187–1202 (1983).

55. D. Farkas, *Scripta Met.* 19, 467–470 (1985).

56. D. Farkas, in: *High Temperature Ordered Intermetallic Alloys - MRS Symp.*, Proc. Symp. Date 1984, (Pittsburgh, PA, 1985) pp. 133–140.

57. A. P. Sutton and V. Vitek, *Acta Met.* 30, 2011–2033 (1982).

58. C. L. White, *American Ceramic Society Bulletin* 64(122), 1571–1580 (1985).

59. H. Gleiter and B. Chalmers, *High Angle Grain Boundaries Progress in Materials Science*, Vol. 16, (New York, Pergamon Press 1972).

60. W. T. Read and W. Shockley, *Phys. Rev.* 78(3), 275–289 (1950).

61. C. L. White and D. F. Stein, *Met. Trans. A* 9A, 13–21 (1978).

62. C. L. White, in: *Proc. First Intl. Aluminum - Lithium Conf.*, (Stone Mountain, GA, 1980) pp. 141–170.

63. D. McLean, *Grain Boundaries in Metals*, Oxford (1957).

64. B. J. Pines, *J. Phys.* 3, Moscow, 309 (1940).

65. M. P. Seah and E. D. Hondros, *Proc. Roy. Soc. Lond.* A335, 191–212 (1973).

66. C. L. White and W. A. Coghlan, *Met. Trans. A* 8A, 1403–1412 (1977).

67. C. H. P. Lupis, *Chemical Thermodynamics of Materials*, (New York, 1983).

68. J. W. Gibbs, *J. W. Gibbs - Collected Works*, (Yale University Press, 1948).

69. L. E. Murr, *Interfacial Phenomena in Metals and Alloys*, Reading, MA, Addison-Wesley Publishing Co. (1975).

70. A. W. Adamson, in: *Physical Chemistry of Surfaces, Fourth Eddition*, Chapter VII, (New York, 1982) pp. 260–293.

71. C. S. Smith, *Trans. AIME* 175, 15 (1948).

72. B. Chalmers, *Proc. Roy. Soc.* A196, 64 (1949).

73. K. T. Aust and B. Chalmers, *Proc. Roy. Soc.* A201, 210 (1950).

74. K. T. Aust and B. Chalmers, *Proc. Roy. Soc.* A204, 359 (1950).

75. C. G. Dunn, F. W. Daniels and M. J. Bolton, *J. Metals* 2, 368 (1950).

76. C. G. Dunn, F. W. Daniels and M. J. Bolton, *J. Metals* 2, 1245 (1950).

77. F. C. Thompson, *Trans. Faraday Soc.* **17**, 391 (1922).

78. J. C. Fisher, J. H. Holloman and D. Turnbull, *J. Metals* 1, 691 (1949).

79. J. B. Hess, *Metal Interfaces*, ASM (1951).

80. J. P. Hirth, *Phil. Trans. R. Soc. Lond.* **A295**, 139–149 (1980).

81. E. Orowan, *Rep. Prog. Phys.* **12**, 185–232 (1948–9).

82. J. R. Rice, in: *The Effect of Hydrogen on the Behavior of Metals*, (New York, 1976), pp. 455–466.

83. R. J. Asaro, *Phil. Trans. R. Soc. Lond.* **A295**, 151–163 (1980).

84. J. P. Hirth and J. R. Rice, *Met. Trans. A* **11A**, 1501–15 (1980).

85. A. G. Griffith, *Phil. Trans. Roy. Soc.* **221**, 163–198 (1920).

86. C. Inglis, *Inst. Nav. Architecture* **50**, 219–230 (1931).

87. G. I. Barenblatt, *Advances in Applied Mechanics*, Dryden and Von Karman, New York (1962).

88. R. M. Thomson, C. Hsieh and V. Rana, *J. Appl. Phys.* 42(8), 3154–3160 (1971).

89. C. Hsieh and R. Thomson, *J. Appl. Phys.* 44(5), 2051–2063 (1973).

90. E. A. Orowan, *Fatigue and Fracture of Metals*, Wiley, New York (1950).

91. G. Irwin, *Trans.* ASM **147** (1947).

92. D. McLean, *Mechanical Properties of Metals*, Wiley, New York (1962).

93. W. Losch, *Acta Met.* 27, 1885-1892 (1979).

94. M. Hashimoto, Y. Ishida, R. Yamamoto and M. Doyama, *Acta Met.* 32, 1-11 (1982).

95. C. L. Briant and R. P. Messmer, *Phil. Mag.* B42(4), 569-576 (1980).

96. R. P. Messmer and C. L. Briant, *Acta Met.* 30, 457-467 (1982).

97. C. L. Briant and R. P. Messmer, *Acta Met.* 30, 1811-1818 (1982).

98. C. L. Briant and R. P. Messmer, *Acta Met.* 32(11), 2043-2052 (1984).

99. P. Auger, *J. Phys. Rad.* 6, 205-211 (1925).

100. G. Ertl and J. Kuppers, *Low Energy Electrons and Surface Chemistry*, Weinheium, Verlag Chemie (1974).

101. C. Lea, *Met. Sci.* 17, 357-367 (1983).

102. M. P. Seah and W. A. Dench, *Sur. Interface Anal* 1, 2-11 (1979).

103. M. P. Seah, in: *Practical Surface Analysis by Auger and X-Ray Photoelectron Spectroscopy*, (New York, 1983) pp. 181-216.

104. M. P. Seah and D. Briggs, in: *Practical Surface Analysis by Auger and X-Ray Photoelectron Spectroscopy*, (New York, 1983) pp. 1-15.

105. H. A. Steinherz and P. A. Redhead, *Sci. Amer.*, March, 2-13 (1962).

106. R. T. Bayard and D. Alpert, *Rev. Sci. Instr.* 21, 571-572 (1950).

107. K. Siegbahn, *ESCA Applied to Free Molecules*, Amsterdam, North Holland (1969).

108. E. H. S. Burhop, *The Auger Effect and Other Radiationless Transitions*, London, Cambridge Univ. Press (1952).

109. I. Bergstrom and C. Nordling, *Alpha-, Beta-, and Gamma*-Ray Spectroscopy, Amsterdam, North Holland, (1965).

110. L. N. Tharp and E. J. Scheibner, *J. Appl. Phys.* 38, 3320-3330 (1967).

111. P. W. Palmberg and T. N. Rhodin, *J. Appl. Phys.* 39, 2425-2432 (1968).

112. P. W. Palmberg, G. K. Bohn and J. C. Tracy, *Appl. Phys. Lett.* **15**, 254-255 (1969).

113. D. F. Stein, W. C. Johnson and C. L. White, in: *Grain Boundary Structure and Properties*, (New York, 1976) pp. 301-351.

114. J. C. Riviere, in: *Practical Surface Analysis by Auger and X-Ray Photoelectron Spectroscopy,* (New York, 1983) pp. 17-85.

115. V. V. Zashkvara, M. I. Korsunskii and O. S. Kosmachev, *Soviet Physics - Technical Physics* 11(1), 96-99 (1966).

116. L. E. Davis, N. C. McDonald, P. W. Palmberg, G. E. Riach and R. E. Weber, *Handbook of Auger Electron Spectroscopy*, Physical Electronics Industries (1976).

117. S. Hofmann, in: *Practical Surface Analysis By Auger and X-Ray Photoelectron Spectroscopy,* (New York, 1983) pp. 141-179.

118. S. Hofmann, *Sur. Interface Anal.* 2(4), 148-160 (1980).

119. A. K. Kuruvilla and N. S. Stoloff, in: *High Temperature Ordered Intermetallic Alloys: MRS Symp. Proc. 1984*, (Pittsburgh, 1985) pp. 229-238.

120. W. W. Gerberich and Y. T. Chen, *Met. Trans.* A 6A, 271-278 (1975).

121. R. A. Mulford, *Met. Trans.* A 14A, 865-870 (1983).

122. R. Gibala and D. S. DeMiglio, in: *Hydrogen Effects In Metals; Third International Conference on the Effect of Hydrogen on the Behavior of Materials*, (1981) pp. 113-122.

123. J. M. Hyzak and W. M. Garrison, *ADIP Semiannual Progress Report - Sept. 30, 1981*, DOE/ER-0045-7, 186-203 (1981).

124. C. L. Briant, *Acta Met.* 31(2), 257-266 (1983).

125. C. L. Briant and R. P. Messmer, in: *Embrittlement By Liquid and Solid Metals Proc. Symp. Oct. 24-28, 1982*, (1984) pp. 79-103.

126. Detectability Limits for Auger Analysis, *PHI Technical Bulletin* #T8401, (1984).

127. R. G. Fairchild, D. Gabel, B. H. Laster, D. Greenberg, W. Kiszenick and P. L. Micca, *Med. Phys.* 13(1), 50-56 (1986).

128. A. I. Taub, Private Communication, (1987).

129. C. T. Liu, Private Communication, (1987).

130. H. Bohn, J. M. Williams and C. T. Liu, *High Temperature Ordered Intermetallic Alloys - MRS Symp. Proc.*, Mtg. date 1986, (1987).

131. F. X. Kayser and C. Stassis, *Phys. Stat. Sol.* 64, 335-342 (1981).

132. T. A. Massaro and E. E. Petersen, *J. Appl. Phys.* 42(13), 5534-5539 (1971).

133. S. Wang and H. Grabke, *Z. Met.* Bd61,H8 597 (1970).

134. S. N. S. Reddy and R. A. Rapp, *Met. Trans. B*, 11B, 99–106 (1980).

135. G. P. Tiwary and B. D. Sharma, *Trans. Indian Inst. Met.* 20, 83 (1967).

136. V. P. Chesnokov B. V. Linchevskii, *Izv. Akad. Nauk.*, SSSR, 5 75–77 (1977).

137. V. M. Ananyn, V. P. Gladkov, V. P. Zotov and D. M. Skorov, *At. Energy* 29(3), 220 (1970).

138. C. T. Tomizuka, *Sol. State Phys.* **10**, (1960).

139. *Metals Handbook*, Desk Edition, ed. (Metals Park, Ohio, 1985) p. 28, 66.

140. H. E. Bishop and J. E. Reviere, *J. Appl. Phys.* 40(4), 1740–1744 (1969).

141. C. R. Worthington and S. G. Tomlin, *Proc. Phys. Soc.* A69, 401–412 (1956).

APPENDIXES

APPENDIX A

THEORETICAL QUANTIFICATION OF AES DATA

A. Homogeneous Binary Solids

Bishop and Riviere (Ref. 140) used the Worthington and Tomlin (Ref. 141) cross section to calculate the ionization cross section $\sigma_x(E)$ by electrons of energy E in AES as:

$$\sigma_{ax}(E) = 1.3 \times 10^{-13}\ b\ \ C/E_{AX}^2 \quad cm^2 \qquad \text{Equation (A-1)}$$

where b = 0.35 for the K shell

= 0.25 for the L shell.

The function C depends on the primary electron beam energy E_p; it varies from zero at $E_p = E_{AX}$ to 0.6 at (2 to 3)E_{AX} and then declines slowly at higher energies.

The core level X of atoms in the surface zone is ionized not only due to the energy of the primary beam (E_p) but also due to back-scattered (elastically scattered) energetic electrons. If the true back-scattered electron spectrum is n(E) per unit incident electron, the total ionization of level X is given by:

$$\sigma_T = \sigma_{AX}\ (E_p) + \int_{E_{AX}}^{E_P} \alpha_{AX}(E)\ n(E)dE \qquad \text{Equation (A-2)}$$

which is often written as:

$$\sigma_T \approx \sigma_{AX}(E_p)[1 + r_M(E_{AX}, E_p, \alpha)] \qquad \text{Equation (A-3)}$$

where the back-scattering term r_M depends on the matrix M in which the A atoms are embedded and the angle α to the surface normal of the incident electron beam. Generally, r_M increases with atomic number Z and reduces with the depth of the core level E_{AX} or a given E_p.

Another source of additional ionization of the core level X arises from Coster-Kronig transitions. Due to these, the more weakly bound levels have added ionization and give stronger Auger electron peaks.

To find the total Auger electron signal, it is necessary to consider two points:

(a) the probability of Auger electron emission, and

(b) the probability that such an emitted electron will indeed travel outside the material without undergoing inelastic scattering.

The ionized core level X decays with a probability, γ_{XYZ}, of Auger electron emission through the XYZ transition. The flux of Auger electrons decays as $\exp(-1/\lambda)$ as a function of the distance 1 from the point of origin. The characteristic depth from which Auger electrons can be emitted is $\lambda_m \cos\theta$; this is often called the Escape Depth, λ. The created Auger electron then has a probability e^{-1} of traveling a distance characterized by the IMFP (λ_M) before being inelastically scattered. The emitted Auger electron is then detected by an electron spectrometer with transmission efficiency, $T(E_{AXYZ})$, and an electron detector of efficiency, $D(E_{AXYZ})$. Hence the Auger electron current I_{AXYZ} may be written as (subscripts XYZ have been dropped for clarity):

$$I_A = I_o \sigma_A(E_p)[1+r_m(E_A,\alpha)]T(E_A)D(E_A)\int_o^\infty N_A(Z)\exp -Z/\lambda_M(E_A)\cos\theta \, dz$$

Equation (A-4)

where I_o = Primary electron beam current

N_A (Z) = A atom distribution with depth Z into the sample surface.

If the electron spectrometer has a large angular aperture, the current should be integrated over the appropriate solid angle.

For homogeneous binary systems, A/B, the integral in Equation (A-4) is evaluated to be $N_A\lambda_M$ $(E_A)\cos\theta$. The ratio of intensities I_A/I_B is related to the ratio of the intensities from the pure elements I_A^∞/I_B^∞ recorded by the same instrument by:

$$\frac{I_A/I_A^\infty}{I_B/I_B^\infty} = \frac{[1 + r_{AB}(E_A)]N_A\lambda_{AB}(E_A)[1+r_B(E_B)]N_B^\infty\lambda_B(E_B)R_B^\infty}{[1 + r_{AB}(E_B)]N_B\lambda_{AB}(E_B)[1+r_A(E_A)]N_A^\infty\lambda_A(E_A)R_A^\infty} \qquad \text{Equation (A-5)}$$

where R_A^∞ and R_B^∞ are the roughnesses of the pure element standards and N_A^∞ and N_B^∞ their atom densities. The ratio R_A^∞/R_B^∞ can be ignored if the ratio I_A^∞/I_B^∞ is established for many samples or from an in-situ fracture surface of a homogeneous A/B alloy. Further,

$$N_A^\infty = a_A^{-3} \text{ and } N_A = a_{AB}^{-3}X_A \qquad \text{Equation (A-6)}$$

hence

$$\frac{N_A N_B^\infty}{N_B N_a^\infty} = \frac{X_A}{X_B}\left(\frac{a_A}{a_{AB}}\right)^3 \qquad \text{Equation (A-7)}$$

where X_A = Required molar fraction of solid

a_M = Atom size of A (in nanometers) from: $\rho_M N a_M^3 = A_M$

ρ_M = Density

N = Avogadro's number

A_M = Mean atomic weight of the matrix atom.

Seah and Dench (Ref. 102) have given IMFP as:

$$\lambda_M = 0.41\ a_M^{1.5}\ E_M^{0.5} \qquad \text{Equation (A-8)}$$

where λ_M and a_M are in nanometers and E_M in eV. Hence Equation (11-5) gets reduced to:

$$\frac{X_A}{X_B} = F_{AB}^{A}\ \frac{I_A/I_A^{\infty}}{I_B/I_B^{\infty}} \qquad \text{Equation (A-9)}$$

where the Auger electron matrix factor F_{AB}^{A} is given by:

$$F_{AB}^{A}\ (X_A \to 0) = \left(\frac{1 + r_A(E_A)}{1 + r_B(E_B)}\right)\ (a_B/a_A)^{1.5} \qquad \text{Equation (A-10)}$$

$$F_{AB}^{A}\ (X_A \to 1) = \left(\frac{1 + r_A(E_A)}{1 + r_B(E_B)}\right)\ (a_B/a_A)^{1.5} \qquad \text{Equation (A-11)}$$

F_{AB}^{A} varies very little across the composition range from A to B and hence may be considered to be a constant for the A/B system.

B. Samples With Thin Overlayers

The thin layers under consideration may be adsorbates requiring analysis or a thin C contamination whose effect needs to be allowed for in quantifying the surface under the contamination.

The signal of the substrate B covered by a fractional monolayer ϕ_A of A is given by the sum of the unattenuated emmission from $(1 - \phi_A)$ of the surface and an attenuated part from ϕ_A:

$$I_B = I_B^{\infty} \{1-\phi_A + \phi_A \exp [-a_A/\lambda_A(E_B)\cos\theta]\} \quad \text{Equation (A-12)}$$

If covered by a thickness d_A of the overlayer of A:

$$I_B = I_B^{\infty} \exp [-d_A/\lambda_A (E_B) \cos \theta] \quad \text{Equation (A-13)}$$

From the two cases given above, the signal from the overlayer is given by:

$$I_A = \phi_A I_A^{\infty} \left(\frac{1+r_B(E_A)}{1+r_A(E_A)}\right)\{1-\exp [-a_A/\lambda_A(E_A)\cos\theta]\} \quad \text{Equation (A-14)}$$

$$I_A = I_A^{\infty} \left(\frac{1+r_B(E_A)}{1+r_A(E_A)}\right)\{1-\exp [-d_A/\lambda_A(E_A)\cos\theta]\} \quad \text{Equation (A-15)}$$

Conversely the fractional monolayer coverage ϕ_A is given by:

$$\frac{\phi_A \{1-\exp[-a_A/\lambda_A(E_A)\cos\theta]\}}{1-\phi_A \{1-\exp[-a_A/\lambda_A(E_B)\cos\theta]\}} = \left(\frac{1+r_A(E_A)}{1+r_B(E_A)}\right) \frac{I_A/I_A^{\infty}}{I_B/I_B^{\infty}} \quad \text{Equation (A-16)}$$

If the Auger peaks are at high energy and if ϕ_A is small:

$$\phi_A = Q_{AB} \frac{I_A/I_A^{\infty}}{I_B/I_B^{\infty}} \quad \text{Equation (A-17)}$$

where

$$Q_{AB} = \left(\frac{\lambda_A(E_A)\cos\theta}{a_A}\right) \left(\frac{1+r_A(E_A)}{1+r_B(E_A)}\right) \quad \text{Equation (A-18)}$$

APPENDIX B

CONVERSION OF AUGER DATA TO CONCENTRATIONS (ATOMIC PERCENT)

IN THIS DISSERTATION

I. INTRODUCTION

The procedure for obtaining elemental concentrations from the Auger analyses is discussed in this appendix. This is done by referring to the entire sequence of steps followed for the analysis of one sample: 860019D.

II. PEAK HEIGHTS

On this sample, 0 to 300 eV Auger spectra were obtained from 24 intergranular points (Points A through X). In addition, 0 to 2000 eV spectra were obtained from one intergranular (Point AA) and one transgranular (Point Y) point. A typical 0 to 300 eV spectrum (Point A) is shown in Figure B-1. Figure B-2(*a*) shows the 0 to 2000 eV spectrum from Point AA (intergranular) and Figure B-2(*b*) shows a partial (0 to 300 eV) reproduction from the same analysis.

From the partial reproduction of the spectrum for Point AA [(Figure B-2(*b*)], the peak-to-peak heights for the Ni 102 eV (PHNi102) peak and the B 179 eV (PHBB179) peak are obtained as shown. The vertical expansion factor of the printed spectrum is denoted as MAG1 (in this case it is 25.0). Similarly the peak-to-peak heights of the Ni 848 eV (PHNi848) peak and the Al 1396 eV (PHAl1396) peak are measured as shown

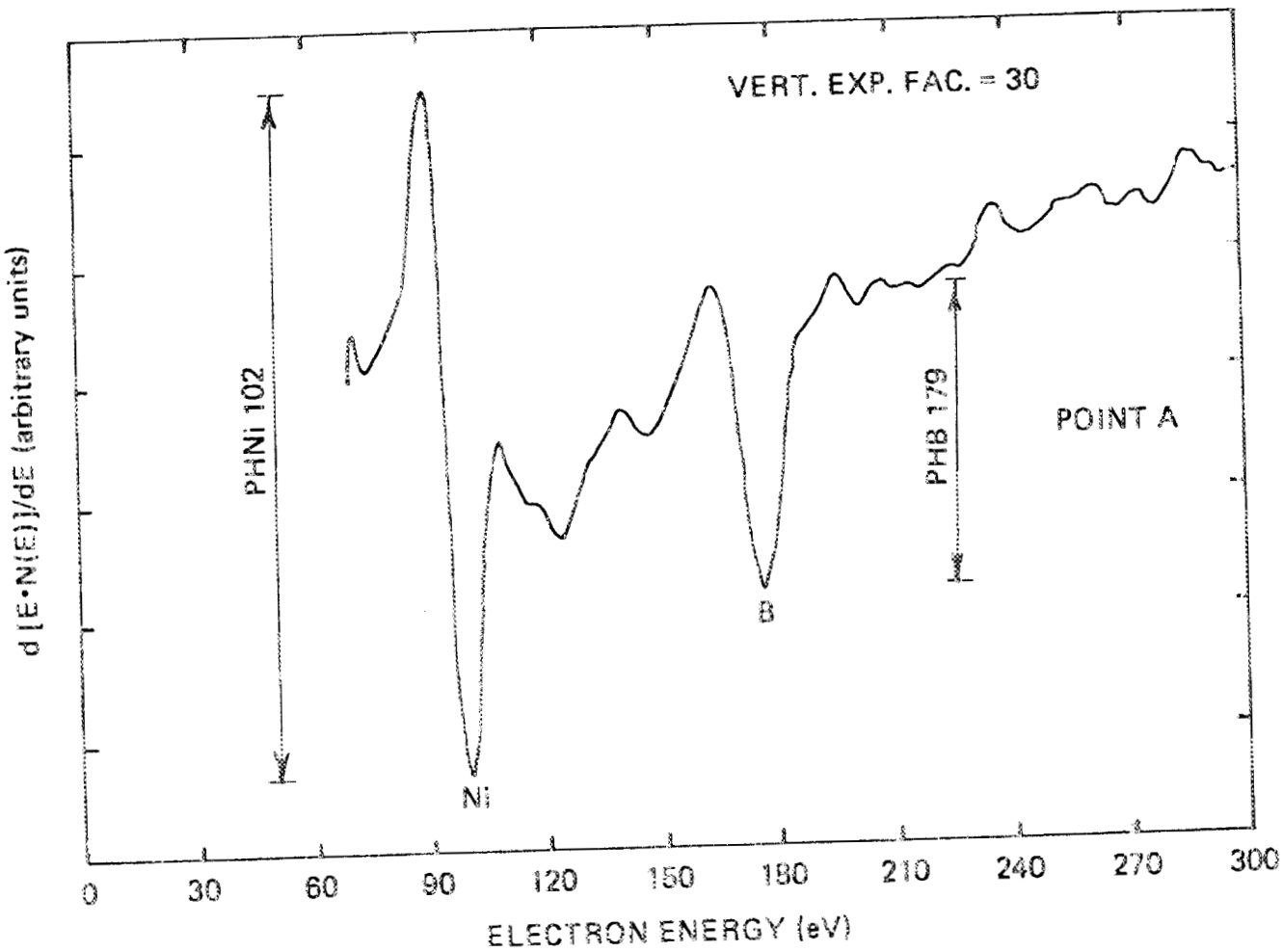

Figure B-1. Typical 0 to 300 eV differentiated Auger spectrum obtained from an intergranular point. Peak heights for elemental peaks are measured as shown.

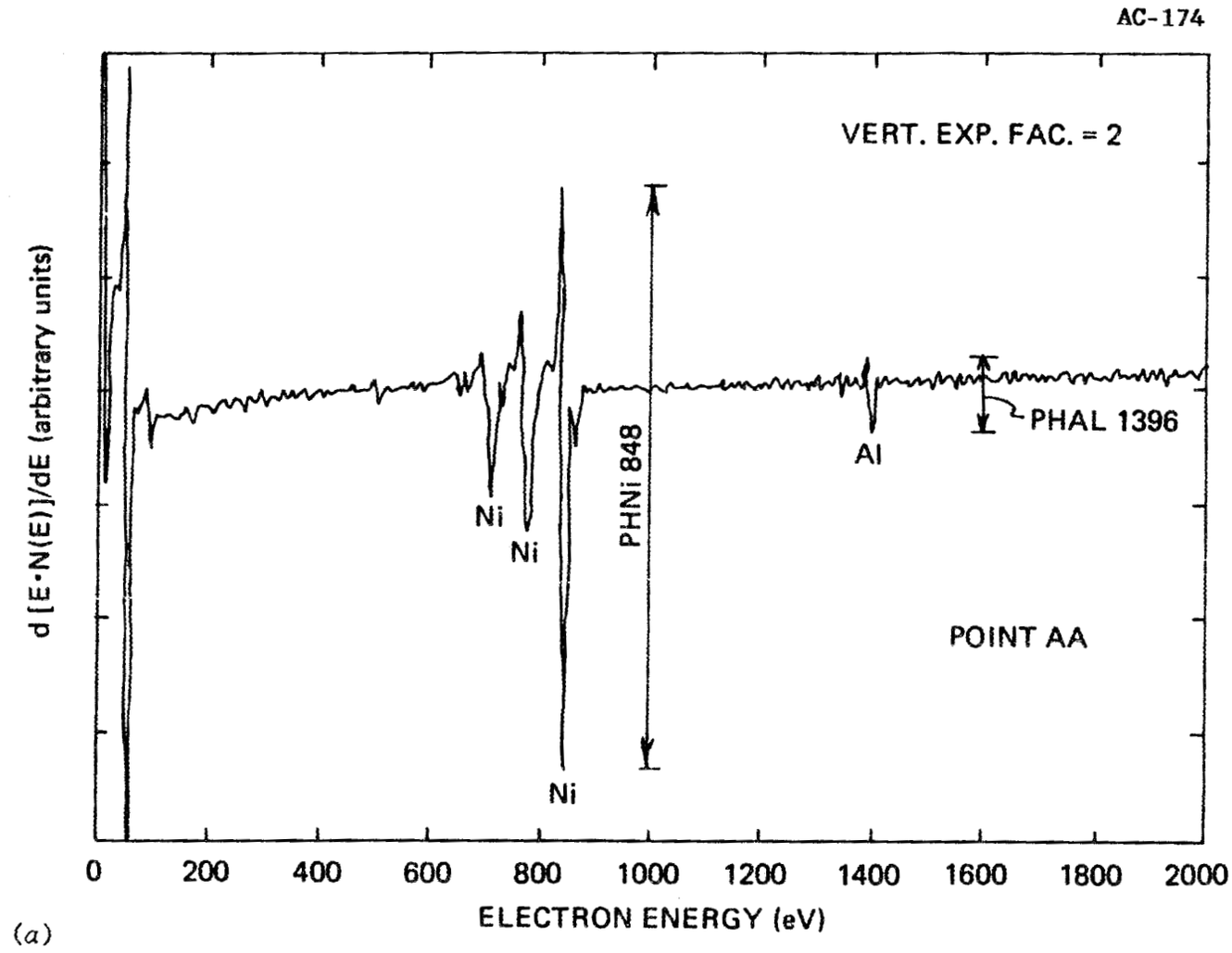

(*a*)

Figure B-2. (*a*) Typical 0 to 2000 eV differentiated Auger spectrum obtained from an intergranular point. Peak heights for elemental peaks are measured as shown. (*b*) The 0 to 300 eV region from (*a*), shown expanded (p. 288).

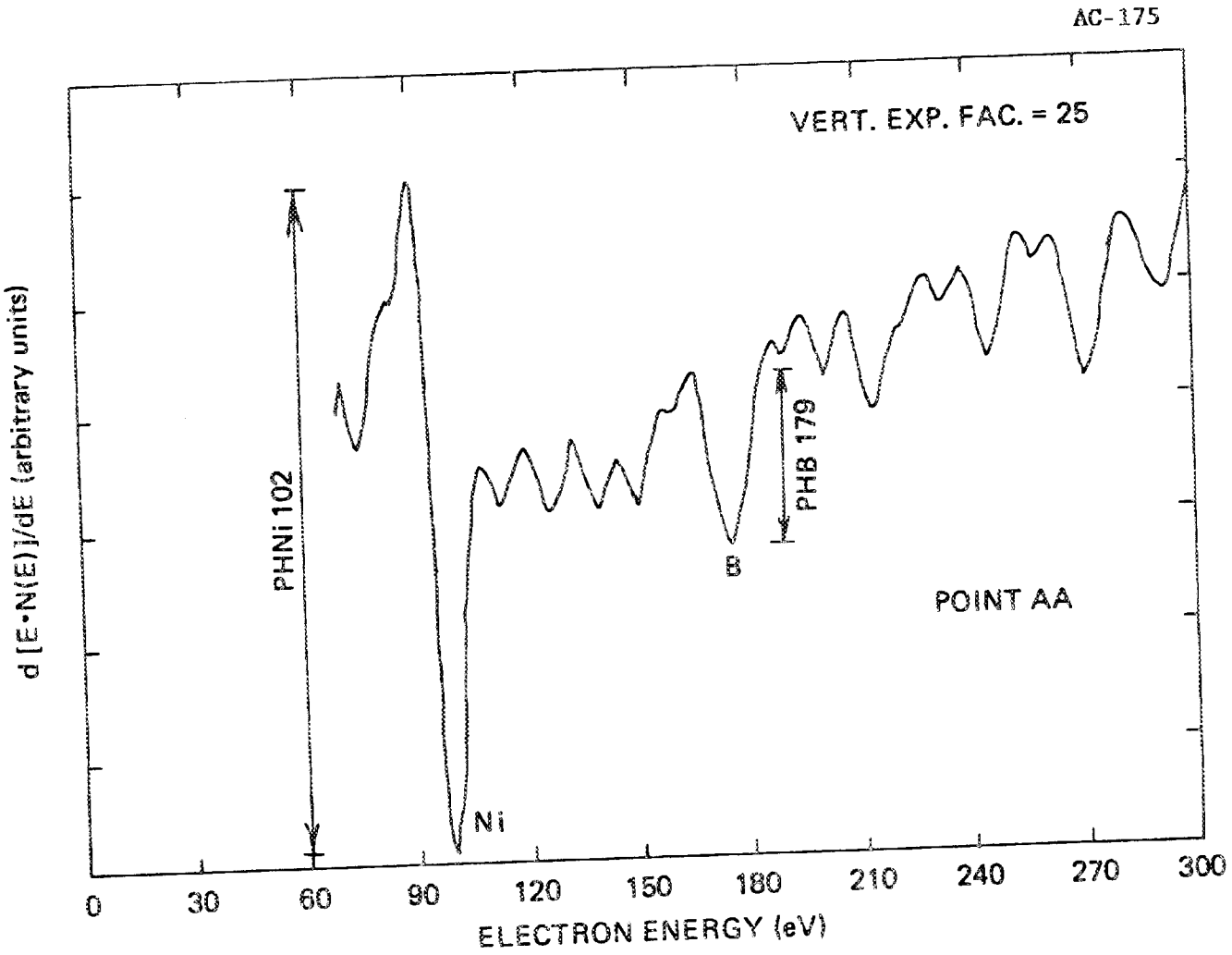

(*b*)

Figure B-2. (*b*) continued.

in Figure B-2(*a*). The vertical expansion factor of the printed spectrum is denoted as MAG2 (in this case it is 2.0). In the case of points where only 0 to 300 eV spectra have been obtained (Points A through X), PHNi102, PHB179 and MAG1 are similarly obtained. For this sample, the entire set of "raw data" is shown in Table B-1.

Table B-2 shows all the peak heights normalized to a vertical expansion factor of 1.00; e.g., if the normalized peak height for the Ni 102 eV peak is denoted as NPHNi102, then:

$$\text{NPHNi102} = \text{PHNi102/MAG1}$$

Similarly,

$$\text{NPHB179} = \text{PHB179/MAG1}$$

$$\text{NPHNi848} = \text{PHNi8484/MAG2}$$

$$\text{NPHA11396} = \text{PHA11396/MAG2}$$

III. ATOM FRACTION CALCULATIONS

As mentioned in Chapter 7, the sensitivity for the detection of Auger electrons depends both on the element being analyzed and the particular peak (energy level) under consideration. Also this elemental sensitivity factor varies (to a lesser extent) from analyzer to analyzer. In view of this a set of standard spectra were obtained to develop in-house sensitivity factors (Chapter 9). Let the sensitivity factors for the relevant peaks be denoted as:

$$\text{Ni 102 eV} = S1$$

$$\text{B 179 eV} = S2$$

$$\text{Ni 848 eV} = S3$$

$$\text{Al 1396 eV} = S4$$

Table B-1. Raw peak height data (in mm) for sample 860019D and vertical expansion factors

Point Name	PHNi102	PHB179	MAG1	PHNi848	PHA11396	MAG2
A	103.5	46	30			
B	85.5	20.5	30			
C	105.5	14	30			
D	86.5	27	30			
E	80	9	30			
F	70	11	30			
G	87.5	36.5	30			
H	91	37	30			
I	84	25.5	30			
J	93	24	30			
K	88	25	30			
L	103	18	30			
M	95	24.5	30			
N	98	17	30			
O	72	19	30			
P	76.5	18	30			
Q	73.5	17	30			
R	97	22.5	30			
S	88.5	35.5	20			
T	86.5	29.5	30			
U	78	23.5	30			
V	88	28	30			
W	80	32	30			
X	71	14.5	30			
AA	106	27	25	91	12	2

Table B-2. Peak height data from Table B-1 normalized to a vertical expansion factor of 1.0

Point Name	NPHNi102	NPHB179	NPHNi848	NPHA11396
A	3.45	1.53		
B	2.85	0.68		
C	3.52	0.47		
D	2.88	0.90		
E	2.67	0.30		
F	2.33	0.37		
G	2.92	1.22		
H	3.03	1.23		
I	2.80	0.85		
J	3.10	0.80		
K	2.93	0.83		
L	3.43	0.60		
M	3.17	0.82		
N	3.27	0.57		
O	2.40	0.63		
P	2.55	0.60		
Q	2.45	0.57		
R	3.23	0.75		
S	4.43	1.78		
T	2.88	0.98		
U	2.60	0.78		
V	2.93	0.93		
W	2.67	1.07		
X	2.37	0.48		
AA	4.24	1.08	45.50	6

Then the peak heights corrected for their sensitivity factors (as mentioned in Section V of Chapter 7) are:

$$CPHNi102 = NPHNi102/S1$$

$$CPHB179 = NPHB179/S2$$

$$CPHNi848 = NPHNi848/S3$$

$$CPHA11396 = NPHA11396/S4$$

For the sample being considered here these values are shown in Table B-3.

In the initial part of this research the level of intergranularly segregated boron was monitored in terms of the boron to nickel ratio (expressed as a percentage) at the grain boundaries. In terms of the quantities mentioned above, this ratio, denoted as E, is given as:

$$E = [(CPHB179 / CPHNi102) \times 100]$$

Table B-4 shows the values of E thus calculated for the sample being considered here.

Two important assumptions need to be mentioned at this point:

(a) While most of the spectra, in particular those from hydrogen charged samples, showed carbon and some oxygen at the grain boundaries, these have been neglected in this calculation. In other words, the concentrations of elements are based on the assumption that only Ni, Al and B are present at the analyzed points.

(b) The level of aluminum can strictly be determined only for a single grain boundary from each sample since a 0 to 2000 eV spectrum was obtained only from one grain boundary in each sample. The aluminum level for all grain boundaries in any given sample will be assumed to be this value. A similar assumption is made regarding the high energy (848 eV) Ni peak.

Table B-3. Peak height data from Table B-2 corrected for elemental sensitivity factors

Point Name	CPHNi102	CPHB179	CPHNi848	CPHA11396
A	32.857	0.575		
B	27.143	0.256		
C	33.492	0.175		
D	27.460	0.337		
E	25.397	0.112		
F	22.222	0.137		
G	27.778	0.456		
H	28.889	0.462		
I	26.667	0.319		
J	29.524	0.300		
K	27.937	0.312		
L	32.698	0.225		
M	30.159	0.306		
N	31.111	0.212		
O	22.857	0.237		
P	24.286	0.225		
Q	23.333	0.212		
R	30.794	0.281		
S	42.143	0.666		
T	27.460	0.369		
U	24.762	0.294		
V	27.937	0.350		
W	25.397	0.400		
X	22.540	0.181		
AA	40.381	0.405	45.500	26.549

Table B-4. The ratio of corrected peak heights for the boron 179 eV peak to the nickel 102 eV peak, the calculated atom fractions of boron and the enrichment ratios

Point Name	E	B1	B2	ENRAT1	ENRAT2
A	1.75	1.08	1.00	22.50	20.86
B	0.94	0.58	0.54	12.15	11.26
C	0.52	0.32	0.30	6.74	6.24
D	1.23	0.76	0.71	15.86	14.71
E	0.44	0.27	0.25	5.70	5.29
F	0.62	0.39	0.36	8.03	7.44
G	1.64	1.01	0.94	21.10	19.56
H	1.60	0.99	0.92	20.59	19.09
I	1.20	0.74	0.69	15.48	14.35
J	1.02	0.63	0.59	13.17	12.21
K	1.12	0.69	0.64	14.46	13.40
L	0.69	0.43	0.40	8.93	8.28
M	1.02	0.63	0.59	13.17	12.21
N	0.68	0.42	0.39	8.80	8.16
O	1.04	0.64	0.60	13.43	12.45
P	0.93	0.58	0.53	12.02	11.14
Q	0.91	0.56	0.52	11.76	10.90
R	0.91	0.56	0.52	11.76	10.90
S	1.58	0.98	0.91	20.33	18.85
T	1.34	0.83	0.77	17.27	16.01
U	1.19	0.74	0.68	15.35	14.23
V	1.25	0.77	0.72	16.12	14.95
W	1.57	0.97	0.90	20.21	18.74
X	0.80	0.50	0.46	10.35	9.59
AA	1.00	0.62	0.57	12.92	11.97
Count	25	25	25	25	25
Average	1.08	0.67	0.62	13.93	12.91
Standard Deviation	0.36	0.22	0.21	4.61	4.28

In terms of the second assumption stated above, the following terms may be defined:

$$C = CPHA11396 / CPHNi102$$

$$D = CPHNi848 / CPHNi102$$

For a given sample then, C and D are constant.

While the dominant peak for Ni is the 848 eV peak, most of the spectra in this research involved the low energy (102 eV) peak for Ni. Hence the atomic percent of boron at grain boundaries may be defined in either of two alternative ways:

$$B1 = [(CPHB179) / (CPHNi102+CPHB179+CPHA11396)] \times 100$$

$$B2 = [(CPHB179) / (CPHB179+CPHNi848+CPHA11396)] \times 100$$

In terms of the variables C, D and E mentioned above, it is simple to show that B1 and B2 can be calculated as:

$$B1 = [E / (100 + E + (100 \times C))] \times 100$$

$$B2 = [E / (E + (100 \times D) + (100 \times C))] \times 100$$

If the bulk level of boron in the sample is denoted as F (in at. %) then the enrichment ratios of boron at the grain boundaries are given as:

$$ENRAT1 = B1 / F$$

$$ENRAT2 = B2 / F$$

For the sample being considered here, the values of B1, B2, ENRAT1 and ENRAT2 are shown in Table B-4. Table B-4 also shows the number of intergranular points analyzed, the average values and standard deviations of these values.

ORNL/TM-10508
Dist. Category UC-25

INTERNAL DISTRIBUTION

1–2. Central Research Library
3. Document Reference Section
4–5. Laboratory Records Department
6. Laboratory Records, ORNL RC
7. ORNL Patent Section
8. L. F. Allard, Jr.
9. P. Angelini
10. P. F. Becher
11. J. Bentley
12. E. E. Bloom
13. R. A. Bradley
14. W. H. Butler
15. R. E. Clausing
16. J. H. DeVan
17. K. Farrell
18. E. P. George
19. G. M. Goodwin
20. L. Heatherly
21. J. A. Horton, Jr.
22. R. R. Judkins
23. E. A. Kenik
24. C. T. Liu
25. T. S. Lundy
26. M. K. Miller
27. W. C. Oliver
28. B. Onay
29. N. H. Packan
30. R. A. Padgett
31. G. S. Painter
32. W. D. Porter
33. A. C. Schaffhauser
34. C. J. Sparks, Jr.
35. J. O. Stiegler
36. R. W. Swindeman
37. M. Takeyama
38. P. F. Tortorelli
39. J. R. Weir
40. F. W. Wiffen
41. R. K. Williams
44. R. O. Williams
45. M. H. Yoo
46–48. P. T. Thornton
49. H. D. Brody (Consultant)
50. G. Y. Chin (Consultant)
51. F. F. Lange (Consultant)
52. W. D. Nix (Consultant)
53. D. P. Pope (Consultant)
54. E. R. Thompson (Consultant)

EXTERNAL DISTRIBUTION

55. DARTMOUTH COLLEGE, Thayer School of Engineering, Hanover, NH 03755
E. M. Schulson

56–57. GENERAL ELECTRIC COMPANY, Research and Development Center, P.O. Box 8, Schenectady, NY 12345
C. L. Briant
A. I. Taub

58. LOCKHEED PALO ALTO LAB, Metallurgy Laboratory, 3251 Hanover Street, Palo Alto, CA 94304-1187
T. G. Nieh

59. LOS ALAMOS NATIONAL LABORATORY, Los Alamos, NM 87545
J. E. Hack

60. MICHIGAN TECHNOLOGICAL UNIVERSITY, Department of Metallurgical Engineering, Houghton, MI 49931

    C. L. White

61. NAVAL RESEARCH LABORATORY, Code 6393, Washington, DC 20375

    K. Sadananda

62. NORTHWESTERN UNIVERSITY, Department of Materials Science and Engineering, Evanston, IL 60201

    J. R. Weertman

63. PACIFIC NORTHWEST LABORATORY, P.O. Box 999, Richland, WA 99352

    R. H. Jones

64. PETTEN ESTABLISHMENT, Postbus 2, 1755 2G, Petten, The Netherlands

    E. D. Hondros

65. RENSSELAER POLYTECHNIC INSTITUTE, Department of Materials Engineering, Troy, NY 12180-3590

    N. S. Stoloff

66. ROCKWELL INTERNATIONAL, P.O. Box 1085 Dept. 020 MS/A25, Thousand Oaks, CA 91360

    A. K. Ghosh

67. STATE UNIVERSITY OF NEW YORK AT STONY BROOK, Department of Materials Science and Engineering, Long Island, NY 11794-2275

    A. H. King

68. TOHOKU UNIVERSITY, Research Institute for Iron, Steel and Other Metals, Sendai 980, Japan

    K. Aoki

69. UNITED TECHNOLOGIES RESEARCH CENTER, East Hartford, CT 06108

    F. D. Lemkey

70-76. UNIVERSITY OF CALIFORNIA, Department of Mechanical Engineering, Davis, CA 95616

    A. Choudhury (5)
    J. Gibeling
    A. K. Mukherjee

77. UNIVERSITY OF PENNSYLVANIA, School of Engineering and Applied Science, Philadelphia, PA 19104-6391

D. P. Pope

78. UNIVERSITY OF PITTSBURGH, Department of Metallurgical and Materials Engineering, Pittsburgh, PA 15261

S. S. Brenner

79. UNIVERSITY OF TENNESSEE, Materials Sciences Department, Knoxville, TN 37916

C. R. Brooks

80–83. DOE, Division of Materials Sciences, Washington, DC 20545

J. B. Darby (ER-131, J321/GTN)
R. J. Gottschall (ER-131, J321/GTN)
F. V. Nolfi (ER-131, J314/GTN)
I. L. Thomas (ER-132, J321/GTN)

84. DOE, OAK RIDGE OPERATIONS OFFICE, P.O. Box E, Oak Ridge, TN 37831

Assistant Manager for Energy Research and Development

85–211. DOE, TECHNICAL INFORMATION CENTER, P.O. Box 62, Oak Ridge, TN 37831

☆U.S. GOVERNMENT PRINTING OFFICE 1988—548-118/60132